Technical Memorandum 33-777

10th Aerospace Mechanisms Symposium

April 22-23, 1976

NATIONAL AERONAUTICS AND SPACE ADMINISTRATION

Technical Memorandum 33-777

10th Aerospace Mechanisms Symposium

April 22-23, 1976

JET PROPULSION LABORATORY
CALIFORNIA INSTITUTE OF TECHNOLOGY
PASADENA, CALIFORNIA

July 1, 1976

PREFACE

The Tenth Aerospace Mechanisms Symposium, held at the Jet Propulsion Laboratory in Pasadena, California, April 22 and 23, 1976, was sponsored jointly by the National Aeronautics and Space Administration, the Lockheed Missiles and Space Company, Inc., and the California Institute of Technology. These symposia are meetings specifically devoted to the design, fabrication, test, and operational use of mechanisms, and provide a forum for interchange among those active in the field of mechanism engineering and technology.

As will be noted, contributions were from NASA Research Centers, and both United States and foreign industrial and research groups.

The Jet Propulsion Laboratory is operated by the California Institute of Technology under contract with the National Aeronautics and Space Administration.

ACKNOWLEDGMENTS

This report, representing a very successful Tenth Symposium, is a product of many individuals and organizations. In addition to the key role played by the Organizing Committee of the Aerospace Mechanisms Symposia, I wish to recognize the efforts of the arrangements committee at the Jet Propulsion Laboratory, which includes K. C. Curry, and J. D. Ferrera.

<div style="text-align: right">

Paul Bomke
Host Chairman
Jet Propulsion Laboratory

</div>

ORGANIZATIONS REPRESENTED
AT THE 10TH AEROSPACE MECHANISMS SYMPOSIUM

ABLE Engineering Company

Aeroneutronic Ford

Aeroject Electrosystems

Aerospace Corporation

Ames Research Center

Applied Research Laboratories

Astro Research Corporation

AVCO Corporation

Ball Brothers Research

Beckman Instruments

Boeing - Aerospace

Borg Warner

Cadillac Gage

California Institute of Technology

California Institute of the Arts

Design News

Dornier System

Engins - MATRA

European Space Agency

Fairchild Space and Electronics
  Company

General Dynamics Convair

General Electric Company

Goddard Space Flight Center

GTE - Sylvania

Hi Shear Corporation

Hughes Aircraft Company

Jet Propulsion Laboratory

Johnson Space Center

Kennedy Space Center

Langley Research Center

Lockheed Missiles Space Center

Martin-Marietta

Massachusetts Institute of Technology -
  Lincoln Laboratories

Motorola, Incorporated

NASA Headquarters

Northrop University

Paschall International Corporation

Planning Research Corporation

RCA

Rockwell International

Sandia Corporation

Santa Barbara Research Center

Schaeffer Magnetics, Incorporated

Stanford University

Thiokol Corporation

TRW

U.S. Department of Commerce -
  NOAA-NESS

CONTENTS

CONTENTS (Contd)

SPACE SHUTTLE TAIL SERVICE MAST CONCEPT VERIFICATION

By Robert T. Uda

Planning Research Corporation

ABSTRACT

Design studies and analyses have been performed to describe the loads and dynamics of the Space Shuttle Tail Service Masts (TSMs). Of particular interest is the motion and interaction of the umbilical carrier plate, lanyard system, vacuum jacketed (VJ) hoses, latches, links, and masthead (cart). A development test rig was designed and fabricated to obtain experimental data. The test program is designed to (1) verify the theoretical dynamics calculations, (2) prove the soundness of design concepts, and (3) elucidate problem areas (if any) in the design of mechanisms and structural components. This paper describes the design, fabrication, and initiation of TSM development testing at Kennedy Space Center (KSC).

INTRODUCTION

One of the last launch-critical pieces of ground support equipment that will be mated to the Space Shuttle Orbiter vehicle until lift-off is the T-0 umbilical. The LH_2 umbilical is connected to the left aft end of the Orbiter, and the LOX umbilical is on the right side. Retracting these umbilicals from the Orbiter's airborne umbilical interfaces and storing them within an enveloping blast housing to protect them from the high temperature environment of the exhaust plumes will be accomplished by two 32-foot tall TSMs. Figure 1 shows the two TSMs with relation to the Shuttle vehicle and Mobile Launch Platform.

The present concept involves retracting the T-0 umbilicals with the pulling force of a lanyard system connected to and actuated by a free-falling dropweight. Upon releasing the dropweight, the lanyard becomes taut, the collet locks are disengaged, and the umbilical carrier plate is rotated, disengaged, and retracted into the blast housing by a system of cables, flex hoses, and links which are connected to a mast which rotates within the blast housing. The rotating mast triggers the bonnet, which closes an instant after the carrier plate, and all attached equipment and components clear the TSM orifice. This entire process occurs within 1.1 seconds. Figure 2 illustrates the basic TSM operation and components.
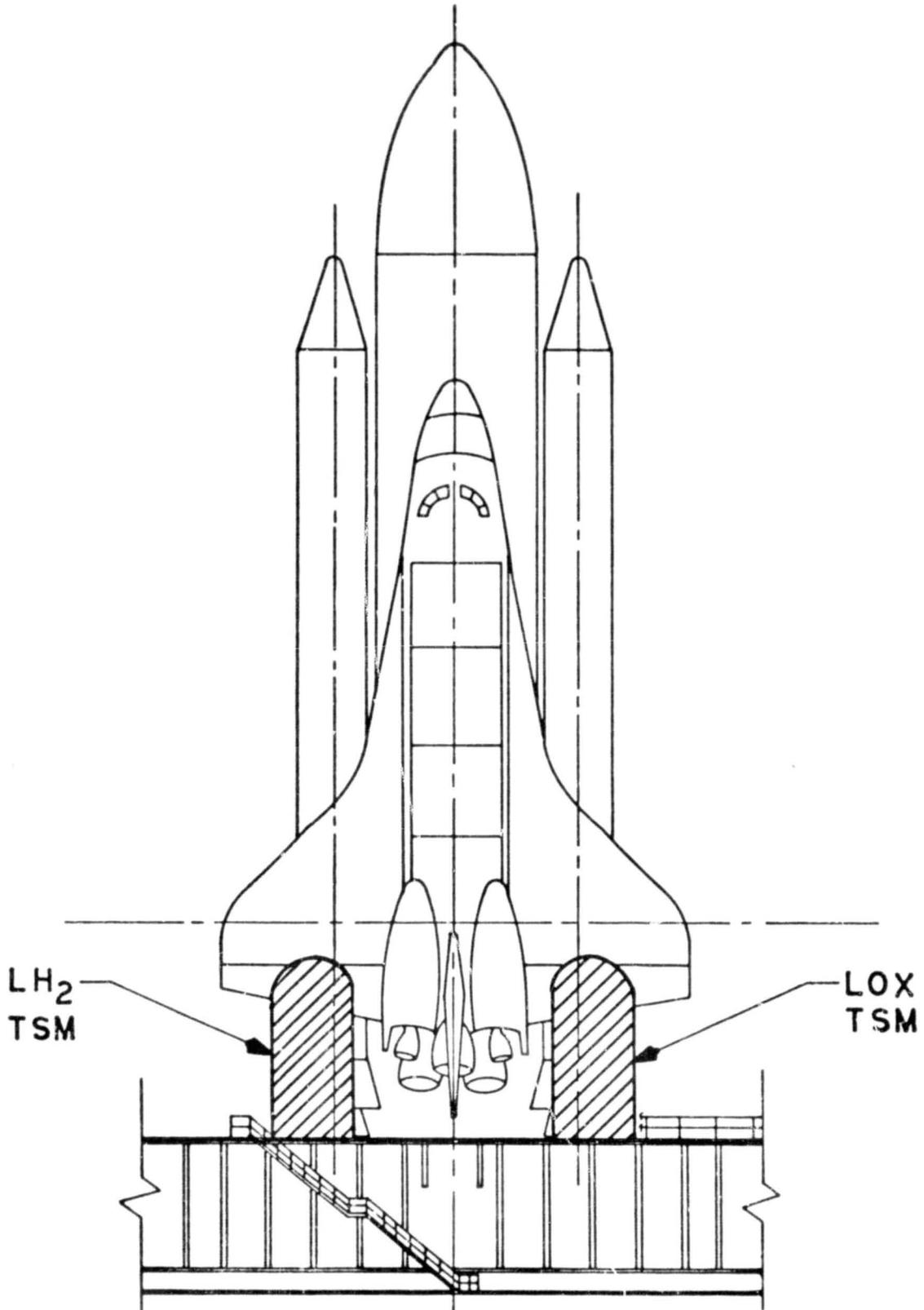
Figure 1.   The two TSMs in relation to the Shuttle
vehicle and the Mobile Launch Platform

BONNET IS 5'WIDE
COMPLETE ROTATION
IS APPROX. 70'

CARRIER

6'R

BONNET
PIVOT

M.A.

EXPLOSIVE
BOLT
RELEASE

DROPWEIGHT

MAST

FIRING POSITION

14°

8°

PIVOT

BONNET ACTUATION

BONNET

T1.1 SEC.
STOP

22°

RETRACT POSITION
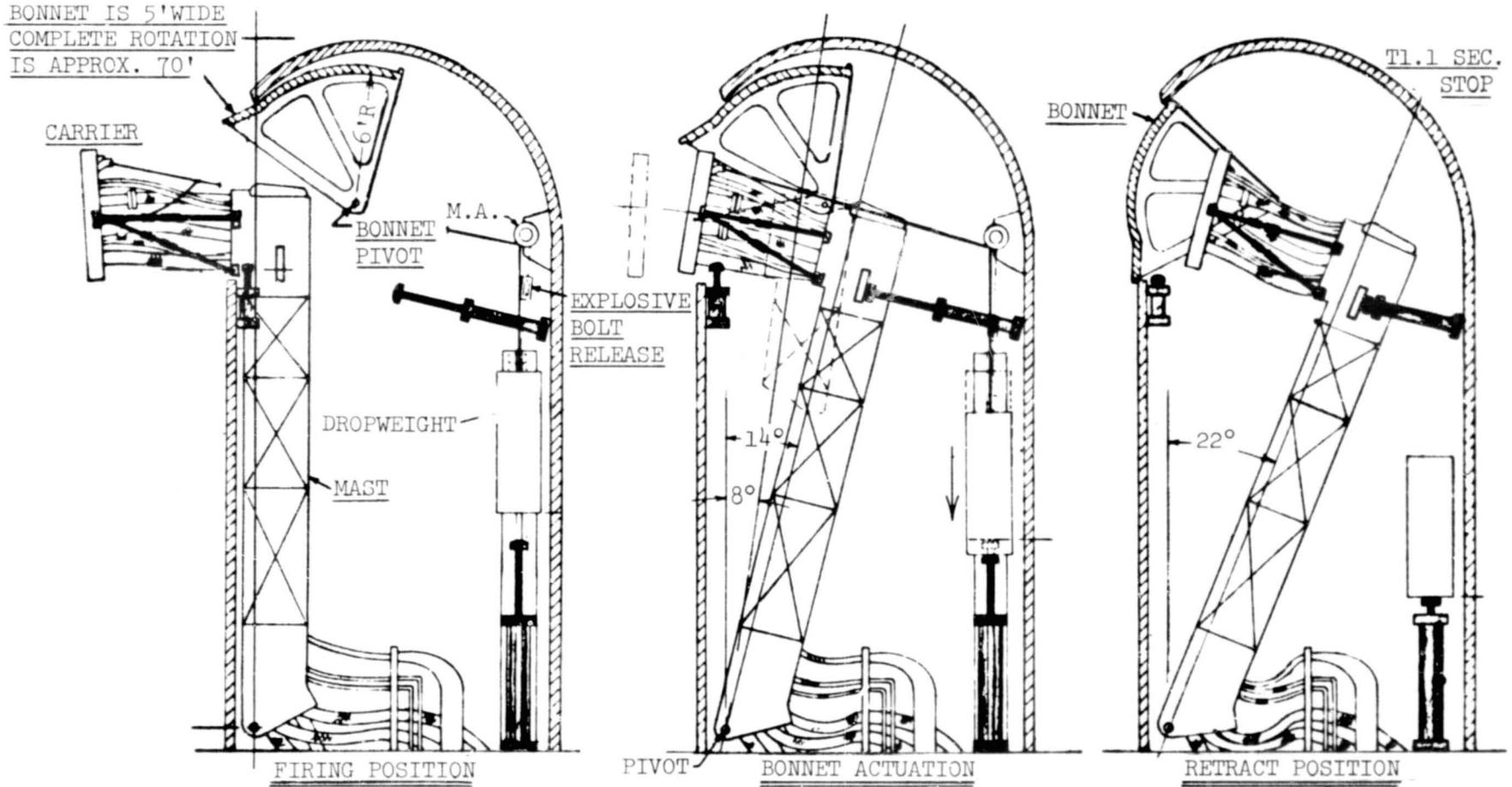
Figure 2.   The basic TSM operation and components

JUSTIFICATION FOR A CVT PROGRAM

Any redesign and retrofit after prototype fabrication (Figure 3) would be costly to the program in both time and dollars. Results from a development test would increase confidence is concepts and performance prior to committing large sums of procurement funds. Furthermore, the probability of redesign and retest later in the program would be greatly reduced, resulting in savings of time and dollars. Therefore, a concept verification test (CVT) program was initiated to design, fabricate, instrument, and test a development test rig at KSC to verify critical TSM design concepts and performance characteristics prior to prototype fabrication. Figure 4 shows the assembly drawing of the CVT rig.

PHYSICAL CONFIGURATION OF THE CVT RIG

To minimize costs, a structure which simulates only the top portion of the mast was designed and fabricated. Since the masthead traces an arc which is nearly a straight line, the design was simplified to allow the simulated masthead (cart) to translate on horizontal rails. Furthermore, instead of using a free falling dropweight, a hydraulic actuator was used to simulate the tension force in the lanyards.

Items that were designed included the floor assembly, mount support structure, masthead (cart), lanyard system, links, umbilical carrier plate, plate support assembly, VJ hose brackets, and instrumentation brackets. Off-the-shelf items that were used included the hydraulic actuator, VJ hose, shock absorber (decelerator), and various instruments (e.g., accelerometers, strain gages, potentiometers, load cells, extensometers, pressure transducers, microswitches, oscillograph recorders, high-speed photo-optics, etc.). Figure 5 shows the TSM CVT hardware setup.

DESIGN ANALYSES

The design of the TSM CVT rig was performed in accordance with NASA specifications, standards, and guidance documents. References 1-4 are the primary documents used in governing the design. The basic design criteria required that (1) the total weight of the moving assembly (cart/links/VJ hose/lanyard/plate) would not exceed 2268 kg (5000 lb) and (2) the moving assembly would accelerate at a maximum of 1 g. Sizing and selection of material were based on a safety factor between 3 and 5.

Studies and analyses were performed to establish design load limits. A static and dynamic link load analysis established the maximum tensile and compressive loads expected (Figure 6).
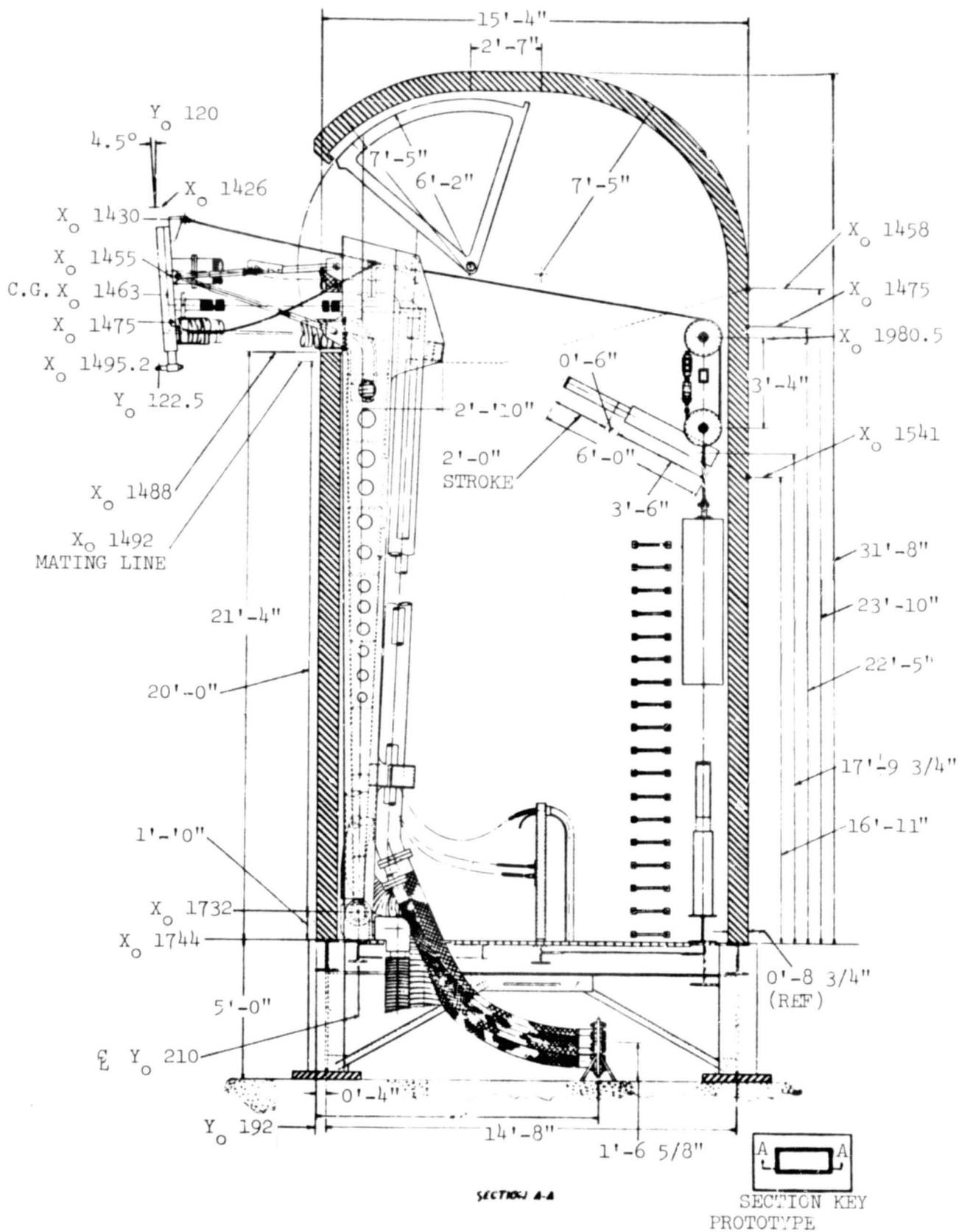
Figure 3. Assembly drawing of the prototype TSM

6

UPPER SUPPORT
SK-MDD-2-S-0-1/9/75-157-53
& 54 (SHT 2)

BRACKET 75M11501-1
MAY BE USED, 2 REQD

ROUNDWAY & RAIL INSTALLATION
SK-MDD-2-S-0/1/22/75-158

4 LOAD
CELLS

SK-MDD-2-S-0-1/22/75-159, UPPER & LOWER LINKAGE
ASSY & DETAILS; QUICK RELEASE PIN
SK-MDD-2-S-0-1/9/75-155-34 (SHT 2) CABLE ASSY
PIN SK-MDD-3-2-S-0-1/9/75-155)
MOUNTING BRACKET, 75M084-25-1
SHOCK ABSORBER, 76K30022-2
SEE SK-MDD-2-S-0-1/22/75-162
DETAIL 'B'

CYLINDER
75M06506-1

₵ ACTUATOR

8°

GROUND
LINE

₵ RAILS

₵ BUMPER

GROUND LINE

SEE SK-MDD-2-S-0-1/22/75-162
DETAIL 'A'

LOAD CELL
ARRANGEMENT

SK-MDD-2-S-0-/22/75-161
CARRIER PLATE ASSY AND
DETAILS, SHEET 1

BEARING, DUAL
ROUNDWAY

FLEX LINE VJ 8"
75M09788-203

PULLEY BRONZE McKISSICK 6-1

PULLY BRONZE McKISSICK 12-5

SK-MDD-2-S-0-1/22/75-160
MOUNT SUPPORT STRUCTURE

₵ RAIL

₵ RAIL

FLOUR ATTACHMENT ASSY
SK-MDD-2-S-0-1/9/75-156

Figure 4.   Assembly drawing of the TSM CVT rig
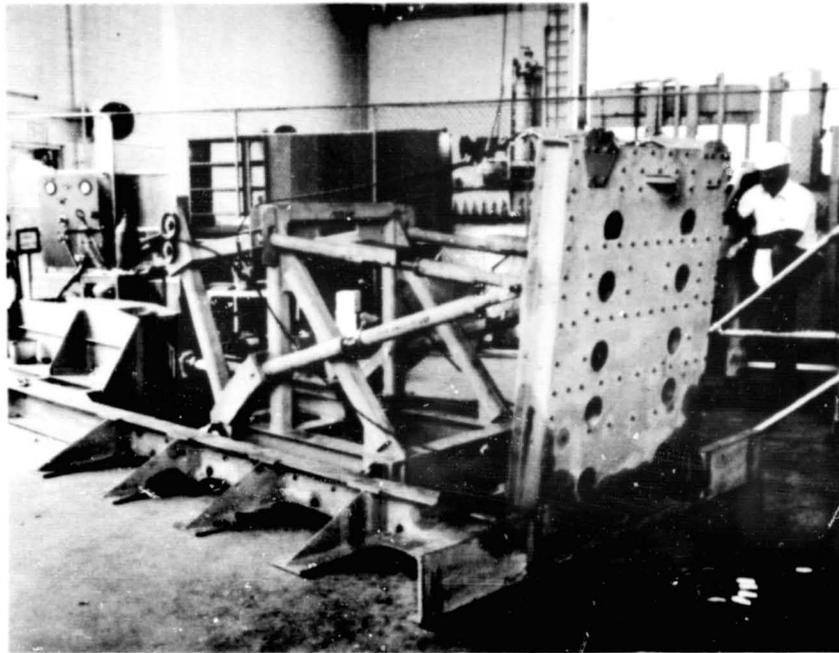
Figure 5.   The TSM CVT hardware setup
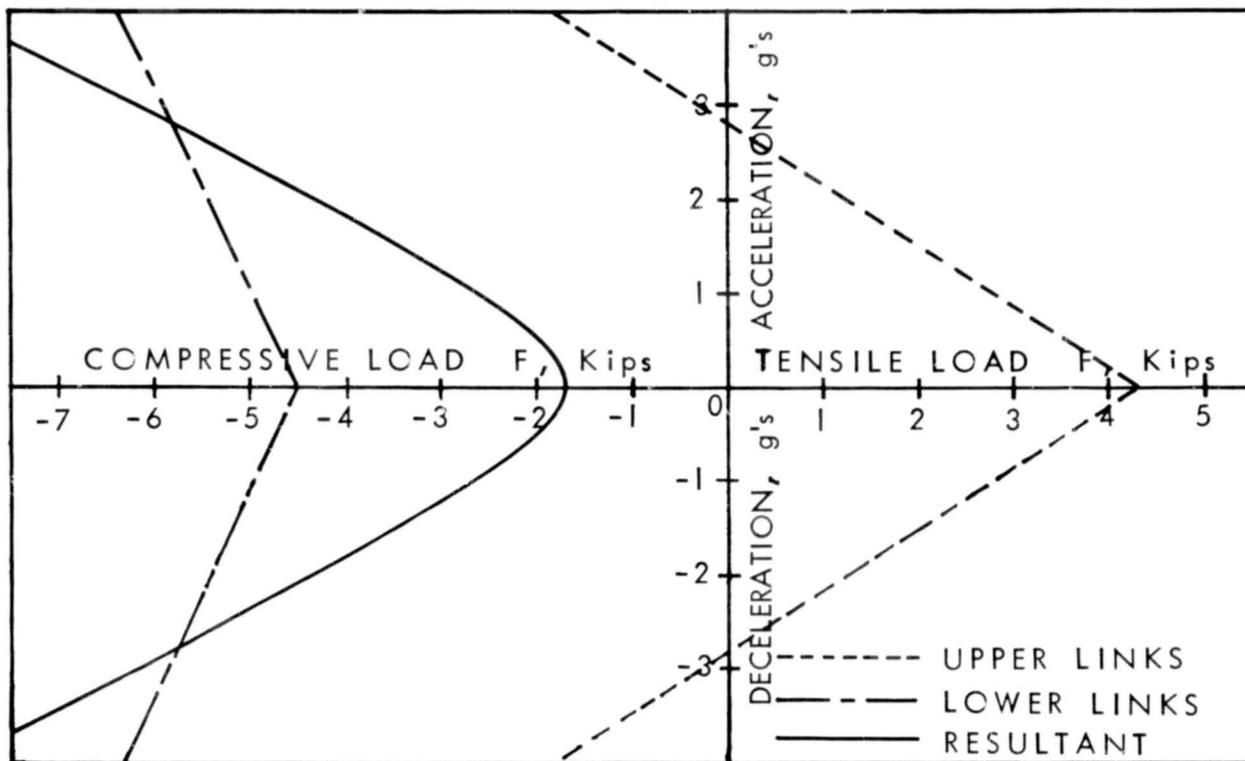
Figure 6.   Expected link loads

The tension limits on the lanyard system were analyzed and established. Wire rope and sheave sizes were determined from these limits. A study was performed to establish pre-load pressures and piston stroke for various cart accelerations up to 1 g. The kinematic rotational motion of the carrier plate was studied to establish performance parameters. Stress analyses were performed to select material and to size all weldments, fittings, and structural members. The functional flow block diagram shown in Figure 7 depicts the project's TSM development test process.

PROBLEMS ENCOUNTERED

Design. A major problem hindering the progress of the TSM design is the lack of firm information from the interfacing contractor. Interface criteria changes have occurred quite often which promulgated design changes and modifications. Consequently, program schedules were impacted. The design, however, must proceed, and costly revisions are tolerated since the flight hardware is the forcing function.

The design and development of the TSM CVT rig were originally planned as a "back yard" type of operation. Instead, sketches of detailed drawings were to be used in the fabrication process. However, as time elapsed, detailed drawings
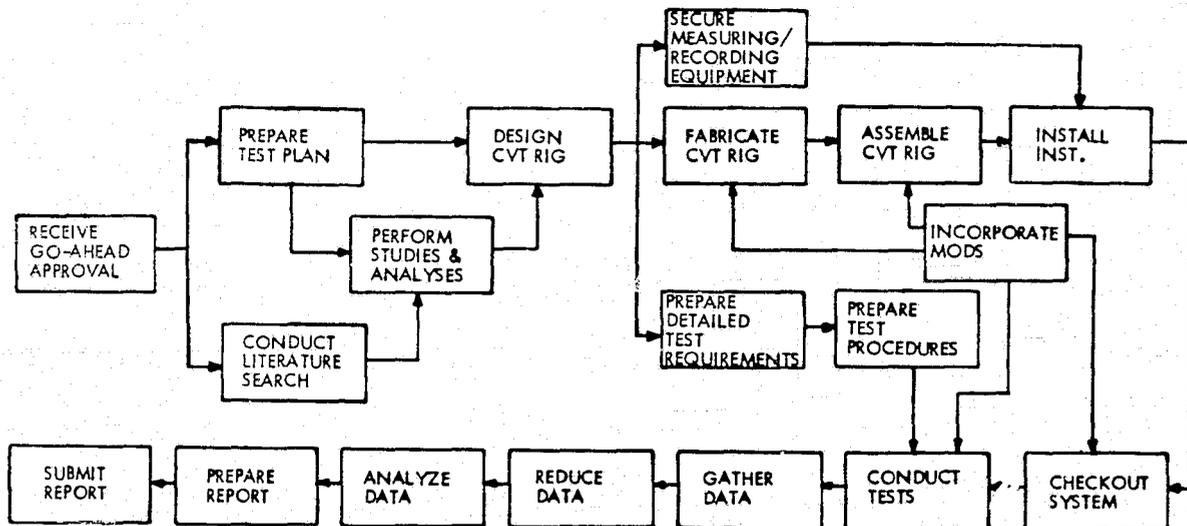
Figure 7. Functional flow process of the TSM CVT

were required, high tolerances and fabrication requirements were levied, and detailed test procedures were developed and employed. Furthermore, excess property was either unavailable or not applicable as initially anticipated. All of these occurrences contributed to test delays and increased cost.

Procurement. Extensive paperwork (red tape) through proper customer channels contributed to delays in receiving needed material and off-the-shelf items. Difficult to obtain (scarce) items, e.g., square T-1 steel tubing, contributed to delays in the fabrication process. Up to 17 vendors were contacted for T-1 steel tubing but without success. Ultimately, a different type of steel was used instead of T-1. It was determined that A-36, 4130, and 1018 steels are some of the more readily accessible ones. Whenever structural requirements permit, materials that are of lower strength, abundant, and of easy access should be used.

Fabrication. Quality control oversights caused refabrication and/or modifications which impacted the schedule. Concentrated scrutiny must be given to all drawings and fabricated parts to determine if proper dimensioning and tolerancing were used.

Test. Because funds were not approved for purchasing new or additional instrumentation, available instruments were used. Inconveniences of borrowing load cells from other on-going tests, using oscillograph recorders with insufficient number of channels to record all the "quick look" data desired, and using linear accelerometers to acquire angular accelerations had to be tolerated.

TEST PROGRAM

The umbilical carrier plate must be rotated at least 11 degrees before the carrier plate feet will be in a disengageable position. The lanyard system provides the forces which initially rotate the carrier plate and subsequently stops the rotation while translating the carrier plate. Carrier plate motion is transmitted to the masthead (cart) through a linkage system, which in turn supports the weight of the carrier plate during retraction.

The CVT program was designed to:

a. Verify that the lanyard system, which retracts the carrier after rotating it 11 degrees with the vehicle in the nominal "0" position, will prohibit over-rotation (beyond 15 degrees) when the vehicle is in the launch (up 7 inches) position. Over-rotation may damage or rupture the propellant flex hoses.

b. Verify that the impact of the carrier plate settling to the nominal retract position, when falling from a higher to a lower position, has little effect on mast dynamics.

c. Verify that the entire assemblage (carrier plate/lanyard/links/masthead) behaves in accordance with the time and motion and dynamics equations used to determine the energy requirements of the system.

d. Verify that the load on the umbilical carrier plate by the vacuum jacketed hose is not severe enough to present a bending moment problem.

CONCLUSION

Many lessons were learned during the design, fabrication, and assembly phases of this development project. A major change impacting the prototype TSM design involved the total redesign of the links. The telescoping concept was maintained but a fail-safe latching arrangement was developed. Also, constant force hydraulic shock absorbers were used instead of rubber pads.

A theoretical study was made to determine whether or not the carrier plate would flip over the masthead upon impact with the mast shock absorber. Though there would be no problem with the CVT test rig because it moves on horizontal rails, it was determined that there would be an overturning problem with the prototype TSM because the masthead/plate assembly traces an arc. Upon mast/shock absorber impact, the calculated overturning moment showed that the carrier plate would rise over the masthead. Therefore, a number of fixes are being devised to keep the plate rise from occurring. Other revisions resulting from this project which were incorporated in the prototype TSM design included cable size, sheave, and sling link changes.

REFERENCES

1. Space Shuttle Level II Program Definition and Requirements, Volume X, Revision A, Space Shuttle Program Flight and Ground System Specification, JSC 07700, Lyndon B. Johnson Space Center, Houston, Texas, January 2, 1974.

2. Space Shuttle Ground Support Equipment General Design Requirements, SW-E-0002, Lyndon B. Johnson Space Center, Houston, Texas, July 1974.

3. General Criteria for Design of New Equipment and Facilities to be Utilized at Kennedy Space Center, Revision 1, GP-863, John F. Kennedy Space Center, KSC, Florida, February 2, 1973.

4. Station Set Requirements Document, Volume 22, Mobile Launch Platform, K-SM-10.1.6, Revision 002, John F. Kennedy Space Center, KSC, Florida, January 31, 1975.

A MOBILE PLANETARY LANDER UTILIZING

ELASTIC LOOP SUSPENSION

By W. Trautwein

Lockheed Missiles & Space Company, Inc.
Huntsville Research & Engineering Center

ABSTRACT

Efforts to increase the cost effectiveness of future lunar and planetary rover missions have led to the mobile lander concept, which replaces the landing legs of a soft-lander craft with a compact mobility system of sufficient strength to withstand the landing impact. The results of a mobile lander conceptual design effort based on existing NASA-Viking '75 hardware are presented. The elastic loop concept, developed as a post-Apollo rover technology, is found to meet stringent stowage, traction, power and weight requirements.

INTRODUCTION

Future rover missions to the moon or to Mars must promise exceptional returns on the investment in order to successfully compete for funding in the constrained fiscal environment of the years ahead.

Mars exploration will intensify dramatically in mid-1976 when two stationary NASA-Viking spacecraft are expected to soft-land on the red planet and perform biological, photographic, geological and meteorological experiments at their landing sites. However, such localized spot checks can only scratch the surface of exploring a planet. The question arises: What type of follow-on mission will provide the highest and most cost effective scientific return after the first successful soft landings at isolated sites?

Through early 1974 NASA inhouse studies (Ref. 1) as well as several industry projects by Martin-Marietta Corporation (MMC) (Ref. 2) and by Messerschmitt-Boelkow-Blohm (MBB) (Ref. 3) pointed toward additional lander missions incorporating a small roving vehicle that would be stowed on top of and deployed from a slightly modified lander craft. The existing Viking Mars Lander and its entry capsule can accommodate four-wheeled rovers of 120 to 180 cm length and wheel diameters of 48 to 56 cm, where the larger size rover would require folding hinges for stowing the chassis inside the existing Viking capsule. A medium rover of 100 kg mass (Ref. 2) and an autonomous rover of 180 kg mass were studied in some depth (Ref. 3).

NASA estimates of the development cost of a piggyback rover were $80 million, which is considered to be too high for funding in the near future in view of the present constrained fiscal environment. Efforts to win the participation of the European Space Research Organization in a cost-sharing program for rover development were not successful.

THE MOBILE LANDER CONCEPT

Background and Basic Design Features

In efforts to improve the cost-effectiveness of planetary rovers, the Martin-Marietta Corporation (MMC) reexamined the idea of a mobile lander after earlier studies to mobilize the entire Viking Lander by conventional wheels had shown negative results (Ref. 4). NASA's Marshall Space Flight Center (MSFC), which was responsible for the Apollo Lunar Roving Vehicle development, was consulted by MMC in a search for lightweight wheels, tracks or rollers of high flotation. NASA-MSFC recommended use of elastic loops, which had been developed by Lockheed Missiles & Space Company in Huntsville under partial NASA-MSFC sponsorship for post-Apollo rover missions (Refs. 5 and 6). In design studies performed by Lockheed during the summer of 1974 in cooperation with MMC under NASA guidance the feasibility of mobilizing an entire Viking lander with minimum modifications to the lander and entry system was demonstrated. A candidate Viking mobile lander configuration is shown in Figure 1.

The lander's landing pads are replaced by a pair of elastic loops at the front (Figure 2) and single elastic loops at each rear leg. The elastic loop suspensions consist of one-piece self-supporting bands of high strength material and provide a large ground contact area with minimum stowage requirements. Their advanced state of development played a vital role in making the mobile lander concept credible. The following design guidelines had been established:

- The mobility system will attach to a landing gear similar to that of the current Viking '75 Lander and will be stowable in the volume available within the Viking '75 entry capsule.

- The mobility system will be deployed by the landing gear system.

- The lander craft will land on the mobility system. Landing loads will be transmitted through the carriages of the mobility system, which will be protected from the initial touchdown shock by shock absorbing pads.

- The ground contact area of the operational mobility system will be sufficient to limit sinkage in Martian loess material to 4 cm.

- The mission duration after landing will be 180 days.

- The mobility system will be designed for a range of 150 km and for night and day operation (temperature extremes $-84°C \leq T \leq +65°C$).

The development cost for a mobile lander based on an existing stationary lander craft has been estimated to be only one third of the cost of an autonomous "piggy-back" roving vehicle. A mobile Viking Lander mission has therefore been endorsed by NASA's Director of Planetary Programs as the logical next step in Mars exploration after the 1976 Viking landings (Ref. 7).

In the following sections major results of LMSC's design effort on a Mobile Lander based on the existing Viking landing craft will be summarized.

MOBILITY SYSTEM DESIGN

Selection of Concept

Since the mobility system of a mobile lander should fit within the aeroshell of an existing lander craft and take up not much more space than the landing legs which it replaces, compact stowage is the major design requirement. However, the ground contact area must be sized to ascertain sufficient traction and acceptable sinkage in the worst type of expected soil conditions. In a comparison of stowage volume, weight and mechanical complexity of wheels, tracks and elastic loops for specified footprint requirements, elastic loops and tracks are found to be substantially more compact than wheels. Elastic loops have the further advantage of lighter weight, simpler design and lower internal power losses over tracks as was demonstrated in NASA-sponsored prototype development and test programs (Refs. 5 and 8). A small three-loop test vehicle (Figure 3) built by Lockheed for NASA-MSFC demonstrated excellent rough-terrain mobility in soil bins and on obstacle courses. Yaw steering of the single loop, augmented in tight turns by differential speed control of the other loops, was found to provide good energy-saving steering response. A three-loop configuration with yaw steering of the front loop was therefore selected for the preliminary design. The three-legged Viking lander represented a perfect match for this configuration.

Loop Sizing

Extensive performance tests of elastic loop prototypes at MSFC's Wheel-Soil Interaction Test Facility and at the U.S. Army Engineer Waterways Experiment Station (Ref. 8) in lunar soil simulant provide a reliable basis for loop sizing. Loop sizes which satisfy the footprint requirements for the maximum landed mass of a 1979 Viking mission and yet allow stowage within the existing Viking entry capsule are listed in Table 1.

The penalty in weight, complexity and tractive efficiency of a dual-loop configuration could be justified for the front leg, which favors a short pair of loops for stowage and for yaw steering. For the rear legs, which do not require yaw steering, single loop support is more attractive.

Loop Fatigue Considerations

The two 180-degree sections of an elastic loop must provide sufficient bending stiffness to support the load without excessive deformations. Approximate stress-deformation formulas were derived based on a simplified theory which treats deformations of the transversely curved loops as inextensional bending distortions.

The specific loop strength is primarily dependent upon the flexural fatigue strength σ_f of the loop material evaluated for the required number of load cycles (2.3×10^5 cycles over 150 km range). Of several candidate loop materials glass fiber reinforced epoxy and titanium alloy ranked

highest in specific strength. Glass-epoxy composite material appears best suited for minimum weight loops. An experimental glass-epoxy loop for a 3300 N design load of only 11 kg mass is shown in Fig. 5 during fatigue testing in a moving belt dynamometer (Ref. 12). In order to minimize the amounts of organic material on the Viking Lander because of possible interference with the biological experiments, the high strength titanium alloy Beta III was chosen. Its specific fatigue strength is 76% of S-Glass epoxy. The manufacture of seamless loops by roll extrusion of forged ring blanks and subsequent hot forming was found feasible.

Loop Stowage, Deployment and Protection from Landing Impact

A candidate concept for loop stowage and deployment which is compatible with the existing Viking '75 aeroshell contours and the Viking '75 main strut is shown in Figures 2 and 4. The two front loops are sandwiched between the carriage bottom and a landing pad (Figure 4a) to prevent local deformations during the landing impact. By depressing the upper loop sections the stowed length is minimized and sufficient roll capability ±19 deg) is achieved for the carriage to adapt to the maximum expected slopes during touchdown without interference between loops and struts. Under the maximum expected landing loads the main strut will be compressed to the position shown in Figure 2 for the operational loops, which leaves at least 28 cm ground clearance. Upon separation of the landing pads after landing the loops will snap into their operational form with straight upper and lower sections. The front idler sprockets will swing forward and maintain permanent contact with the loops.

The energy absorbing landing pads have been designed to surround the lower loop sections completely during landing. Furthermore, the bottom surface of the carriage is contoured to closely match the loop shape in the stowed position as shown in Figure 2. The Viking '75 landing leg design loads are based on 200 g maximum vertical deceleration of the landing pads, which is attenuated by the main struts to a maximum of 30 g for the lander chassis by crushable honeycomb cartridges inside the main struts.

The preliminary landing pad design is based on the worst case conditions illustrated in Figure 6 (provided by R. J. Muraca, NASA-Langley). The face sheets at the bottom of the landing pads were assumed to distribute point loads from rock impact over an area $A_r = 470$ cm^2. The main strut force versus stroke characteristics indicate that the average crush force during the initial phase of the landing impact is $F_a = 4450$ N. The total energy to be absorbed by the landing pad to decelerate the mass $m_{\ell 3}$ of leg 3 (below main strut No. 3) is then

(1)
$$E_3 = 1/2 \, m_{\ell 3} \, v_o^2 + F_a x_p \, ,$$

where x_p is the stroke of the crushable landing pad. Neglecting the small initial energy absorption in the main strut during the force buildup to F_a, all energy absorption then occurs in the landing pad with crush strength p or

(2)
$$E_3 = A_r \, p x_p \, .$$

Substituting (2) into (1) and solving for the required crush stroke yields for $m_{\ell 3} = 15.4$ kg:

$$(3) \qquad x_p = 1/2\, m_3\, v_o^2 / (A_r\, p - F_a) = 4.2 \text{ cm} .$$

The allowable crushing stroke is 70% of the pad's thickness. The required honeycomb thickness is therefore $x_{hc} = 4.2/0.7 = 6$ cm. The maximum deceleration is encountered for a flat landing with uniform crushing of the full pad area. The selected crush strength and pad area must be sufficiently low to limit the deceleration to 200 g. The maximum allowable pad area A_o can be determined as follows: the maximum allowable pad load is $F_o = m_{\ell 3}\, g_{max} + F_a = 34.65$ kN. For the selected honeycomb material with crush strength $p = 24.1$ N/cm^2 the pad area should be $A_o \le F_o/p = 1438$ cm^2. However, the projected pad area for full protection of both front loops is $A_1 = 1768$ cm^2. Therefore the honeycomb must be "checkerboarded" leaving $A_1 - A_o = 330$ cm^2 of voids or a slightly softer honeycomb material must be found. Similar approximate calculations led to a required lateral pad thickness of 0.9 cm to protect the loops from side impact loads.

Drive System and Power Requirements

The drive system design requires trade studies between light weight and safe lubrication at the low temperature extremes. The present state of the art in bearing and gear lubrication requires dry lubricants for safe operation at -84°C. Since direct drive torque motors were ruled out due to heavy weight, brushless dc motors with gear reducer were chosen as primary candidates for further study. The gear ratio was chosen to limit the motor revolutions to 11 million over the operational life of the drive system. A 30:1 high efficiency roller-gear reduction was selected, which forms an integral part of the drive sprocket together with a brushless motor with parking brake and an emergency disconnect clutch. The weight of the complete drive sprocket/motor/gear/brake assembly is estimated at less than 3.5 kg.

Extensive performance tests of elastic loop prototypes at NASA-MSFC and at the U.S. Army Engineer Waterways Experiment Station (WES) (Ref. 8) provide a sound data base to predict power requirements. The Lunar Soil Simulant in the loose air dry test condition is very close to the assumptions made for Martian loess. The tests were performed for a wide range of slope angles up to 38 deg. Test results are documented in normalized form in Ref. 8 and can be readily applied to specific vehicle characteristics. For the mobile Viking Lander's weight on Mars of W = 2510 N the power requirements plotted in Figure 7 are predicted.

COMPARISON OF ROVER AND MOBILE LANDER MOBILITY CHARACTERISTICS

During development of the 4-wheeled Lunar Roving Vehicle (LRV) extensive performance tests of wiremesh wheels had been conducted at the

Waterways Experiment Station (WES) in Lunar Soil Simulant (Ref. 9). Since the majority of the elastic loop tests were performed in the same facility in identical soil conditions, the test results obtained for both concepts can be directly compared.

Slope Climbing Capability

In Figure 8 (taken from Ref. 8) specific energy and slope climbing ability are plotted for the LRV wheel and an elastic loop test unit tested in identical soft Lunar Soil Simulant. Between 0 and 10 deg slope angle wheels are found to require 30% more energy than elastic loops. For steeper slopes wheel performance rapidly deteriorates even more. The wheels spin out at 20 deg slope angle whereas elastic loops climb slopes up to 36 deg in this soft soil with propulsive efficiency peaking near 30 deg (η_{max} = 80%). For a moderate 10 deg slope the efficiencies of wheels and elastic loops are 45 and 63%, respectively. This superior soft soil performance of elastic loops can be attributed to the reduced sinkage, reduced slip and more uniform pressure distribution. The excellent traction of the loops not only improves slope climbing but also adds maneuverability by good response to pivot steering and braking commands.

Static Stability

Piggyback rovers are constrained in wheelbase and treadwidth by the limited stowage space on top of the lander craft. Even the additional complexity of a hinged chassis as proposed for the MBB rover (Ref. 3) results in vehicle dimensions which are substantially smaller than those of a mobile lander. These differences in vehicle geometry are reflected in the static stability limits plotted in Figure 9 for varying slope angles and assuming an additional rock under the uphill wheels (or loop). The three widely spaced lander legs provide exceptional static stability in roll, which, in general, is more critical than pitch stability.

Obstacle Negotiation

Good obstacle climbing capability is a key factor in reducing the risk of mission failure in an automated rover mission when unforeseen hazards are encountered. Furthermore, exceptional obstacle performance reduces the time and energy required to safely reach a given destination because minor obstructions can be negotiated without bypass maneuvers. The obstacle climbing of four-wheeled vehicles has been investigated in depth by Kuehner (Ref. 10) and more systematically by Rettig and Bekker (Ref. 11).

Vertical Obstacle Climbing

For all four-wheeled vehicles with all wheel drive and near uniform load distribution the rear wheels limit the vertical step negotiation. In the limiting condition (Fig. 10) the weight W, tangential and normal forces at front and rear wheels are in equilibrium. For small chassis pitch angles β this results in the following equation

$$(4) \qquad \left[(1 - \mu\beta) + \mu\lambda\right]\sin\alpha - \left[\gamma - \mu + \left(\gamma\frac{h_o}{s} - 1\right)\beta + \lambda\right]\cos\alpha = \mu\lambda$$

where $\lambda = D/2s$, $\gamma = (1+\mu^2)s_1/\mu s$, which must be solved for α and β, since $\alpha = \arcsin(1-2h/D)$ and $\beta = \arcsin(h/s)$ are functions of the wanted obstacle height h. For the piggyback rover proposed by MBB (Ref. 3), Eq. (4) yields a maximum vertical step height (assuming $\mu = 0,6$) of h = 8.1 cm ($\alpha = 41.5$ deg; $\beta = 5.2$ deg), whereas the solution for the smaller rover proposed by MMC (Ref. 2) is h = 5.7 cm ($\alpha = 51.3$ deg; $\beta = 5.4$ deg), which must be considered insufficient in view of the poor knowledge about martian surface details.

Obstacle heights of h = 26 cm were claimed in Ref. 3 without proof for both rover designs. NASA-sponsored obstacle climbing tests with the three-loop configuration of Figure 3 have shown (Ref. 5) that three-loop vehicles with pitch articulated loop suspensions as proposed for the mobile lander can climb obstacles which are 64 and 85% of the loop length in forward and reverse direction (single loop trailing), respectively. Reducing these test results from the test conditions ($\mu = 0.8$) to the assumed martian soil conditions ($\mu = 0.6$) the step heights decrease by 28% based on the analytical and experimental results in Ref. 5. In forward and reverse direction obstacle performance is limited by the rear loop pair. For the present length of the rear loops (L = 63 cm) the maximum step heights: $h_{fwd} = 0.72 \times 0.64 \times 63 = 29$ cm; $h_{rev} = 0.72 \times 0.85 \times 63 = 39$ cm result, which in the forward direction is consistent with the planned ground clearance of 28 cm and allows for safe negotiation of 22 cm high rocks expected in the landing area.

The major mass, size and performance data of the mobile lander and piggyback rovers are summarized in Table 2.

CONCLUSIONS

The compact size, light weight and large footprint of elastic loop suspensions was found to offer surface mobility for an entire planetary soft lander of the Viking class without major modifications of lander or entry system hardware. Compared with recent "piggyback" Mars rover designs the scientific value of a mobile lander mission is greatly enhanced because the complete science payload is mobile and the full power, communications, data processing and thermal resources of the lander are available for the science instruments. The larger vehicle dimensions add stability and obstacle climbing capability. Expected development cost is lower because most existing Viking subsystems including scientific instruments, cameras, communications, data, storage and handling and thermal control systems can be used without modifications while a piggyback rover requires separate subsystems, which for the most part will differ from the existing lander versions. The low weight required for lander mobilization should make the mobile lander concept very attractive for a Mars sample return mission, since more than one geological and ecological environment can be sampled, thereby greatly enhancing the scientific value of the samples collected for return to earth.

REFERENCES

1. Darnell, W. L., and Wessel, V. W., Conceptual Design and Operational Characteristics of Mars Rovers for Advanced Viking Science Missions NASA-Langley Working Paper 1113, June 1973.

2. Martin-Marietta Corporation, Viking '79 Rover Study Final Report. Summary Report, Vol. I, NASA-CR-132417, Detailed Tech. Rep., Vol. II, NASA-CR-132418, March 1974.

3. Koelle, D. E., Kokott, W., and Schultze, W., A Mars Rover Concept for Future Landing Missions, Raumfahrtforschung 18 (1974), pp. 224-235.

4. Martin-Marietta Corporation, Study of Application of Adaptive Systems to the Exploration of the Solar System, NASA-CR-132258, Vol. III, March 1973.

5. Costes, Nicholas C., Melzer, K-J., and Trautwein, Wolfgang, Terrain-Vehicle Dynamic Interaction Studies of a Mobility Concept (ELMS) for Planetary Surface Exploration, AIAA Paper No. 73-407, March 1973.

6. Costes, N. C., and Trautwein, W., Elastic Loop Mobility System — A New Concept for Planetary Exploration, J. of Terramechanics, Vol. 10, No. I, (1973), pp. 89-104.

7. Kraemer, R. S., Planetary Missions: Making Do, J. of Astronautics & Aeronautics, November 1974, pp. 10-12.

8. Melzer, K-J., and Swanson, G. D., Performance Evaluation of a Second Generation Elastic Loop Mobility System, Tech. Rep. M-74-7, U. S. Army Engineer Waterways Experiment Station, June 1974.

9. Green, A. J., and Melzer, K-J., Performance of Boeing LRV Wheels in a Lunar Soil Simulant, U. S. Army Engineer Waterways Experiment Station, Tech. Rep. M-71-10, December 1971.

10. Kuehner, K., Das Kraftfahrzeug Im Gelaende, ZVDI, 79 (1935) pp. 1019-1027.

11. Rettig, G. P., and Bekker, M. G., Obstacle Performance of Wheeled Vehicles, U. S. Army OTAC Rep. No. 29, 1958.

12. Trautwein, W., G. W. Fust, and J. A. Mayhall, Exploratory Development of Loopwheel Suspensions for Off-Road Military Vehicles, Final Report, Part 1, Contract N61331-74-C-0064, Material Selection and Structural Test Loop Design, Lockheed Missiles & Space Company, Huntsville, Ala., July 1974; Part 2, Contract N-61339-75-C-0090, Loop Core Fabrication and Testing, Lockheed Missiles & Space Company, Huntsville, Ala., December 1975.

Table 1. Loop data for dual- and single-loop support of Viking lander legs

Configuration	Overall loop Length cm	Width cm	Ground Contact Pressure N/cm^2	Loop thickness mm	Vertical Spring Rate[a] N/cm	Mass[b] kg
Two loops/leg	55	17	0.45	1.47	72	5.22 (2 loops)
One loop/leg	63	27	0.49	1.88	66	5.46 (1 loop)

[a]Based on 675 kg supported mass on Mars uniformly distributed over three legs.

[b]Mass of loop(s) required per leg, including inner drive lugs and outer grousers. Loop material: Titanium alloy Ti-4.5Sn-5Z4-11.5Mo (Beta III).

Table 2. Summary of major size, mass and performance characteristics of rover and mobile lander designs compatible with Viking aeroshell

	Piggyback rover designs by		Mobile lander design
	MMC (Ref. 2)	MBB (Ref. 3)	
Wheel base	60 cm	90 cm[a]	205 cm
Tread width	60 cm	94 cm[a]	235 cm
Total mass	108 kg	180 kg	675 kg
Mass of mobility system			50 kg
Mobile science payload	21 kg	55 kg	100 kg
Ground pressure	0.5 N/cm^2	0.75 N/cm^2[b]	0.47 N/cm^2
Ground clearance	22 cm	25 cm	28 cm
Max. obstacle height for $\mu = 0.6$	5.7 cm[c]	8.1 cm[d]	29 cm forward 39 cm reverse
Max. slope angle in Soft Soil Simulant[e]	20 deg	20 deg	36 deg

[a]Chassis requires folding for stowage inside Viking capsule.
[b]Considered too high for safe soft soil mobility.
[c]Can be improved to 12.4 cm by forward shift of c.g. to $s_1/s = 0.35$; however, front ground pressure then is 85% higher than rear.
[d]Can be improved to 13.2 cm in same way and with same penalty as (c).
[e]Based on NASA-sponsored soil bin tests (Refs. 8 and 9).
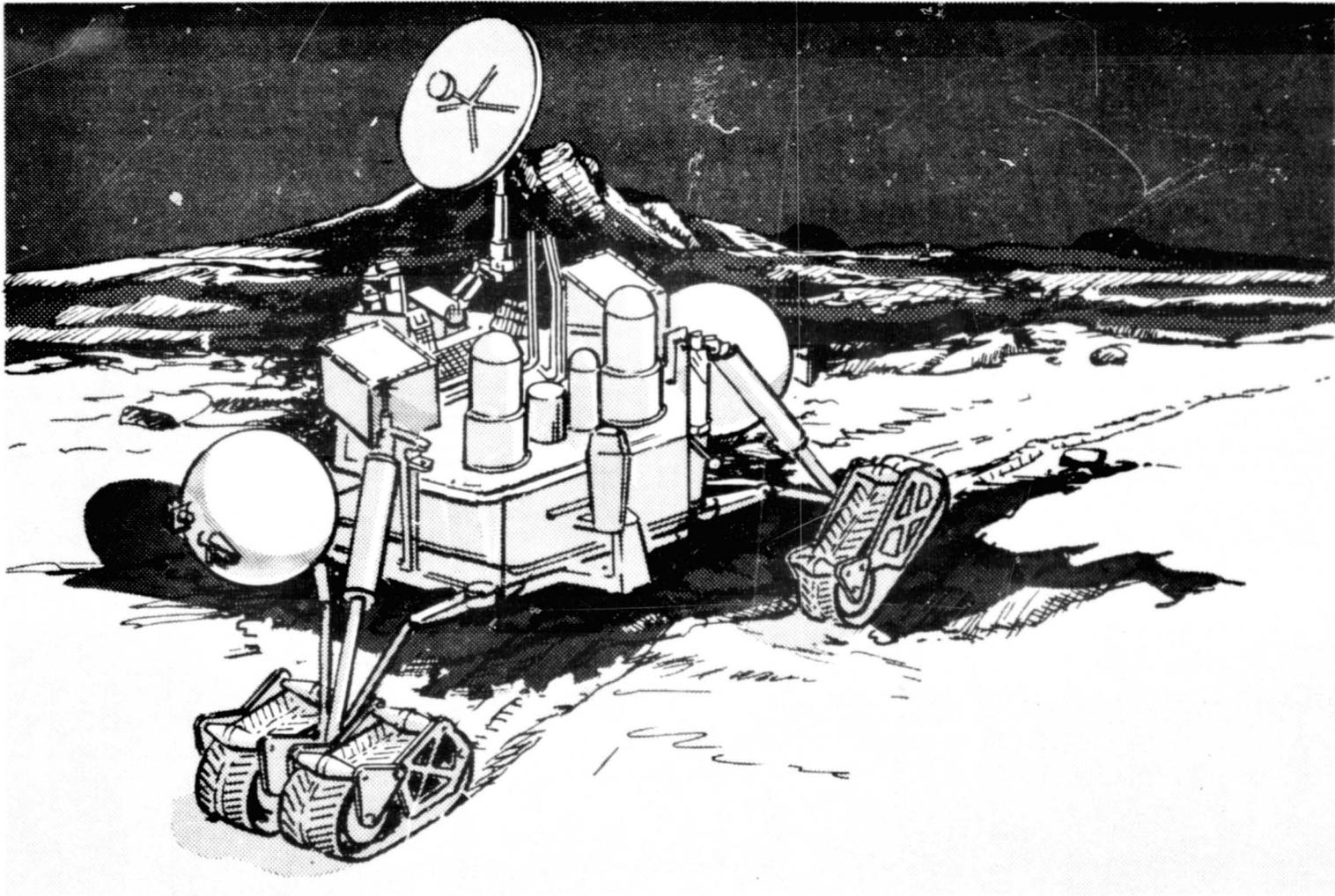
Fig. 1 - Candidate mobile Viking Lander configuration. A pair of steerable elastic loops supports front leg. Rear legs are supported by longer single loops.
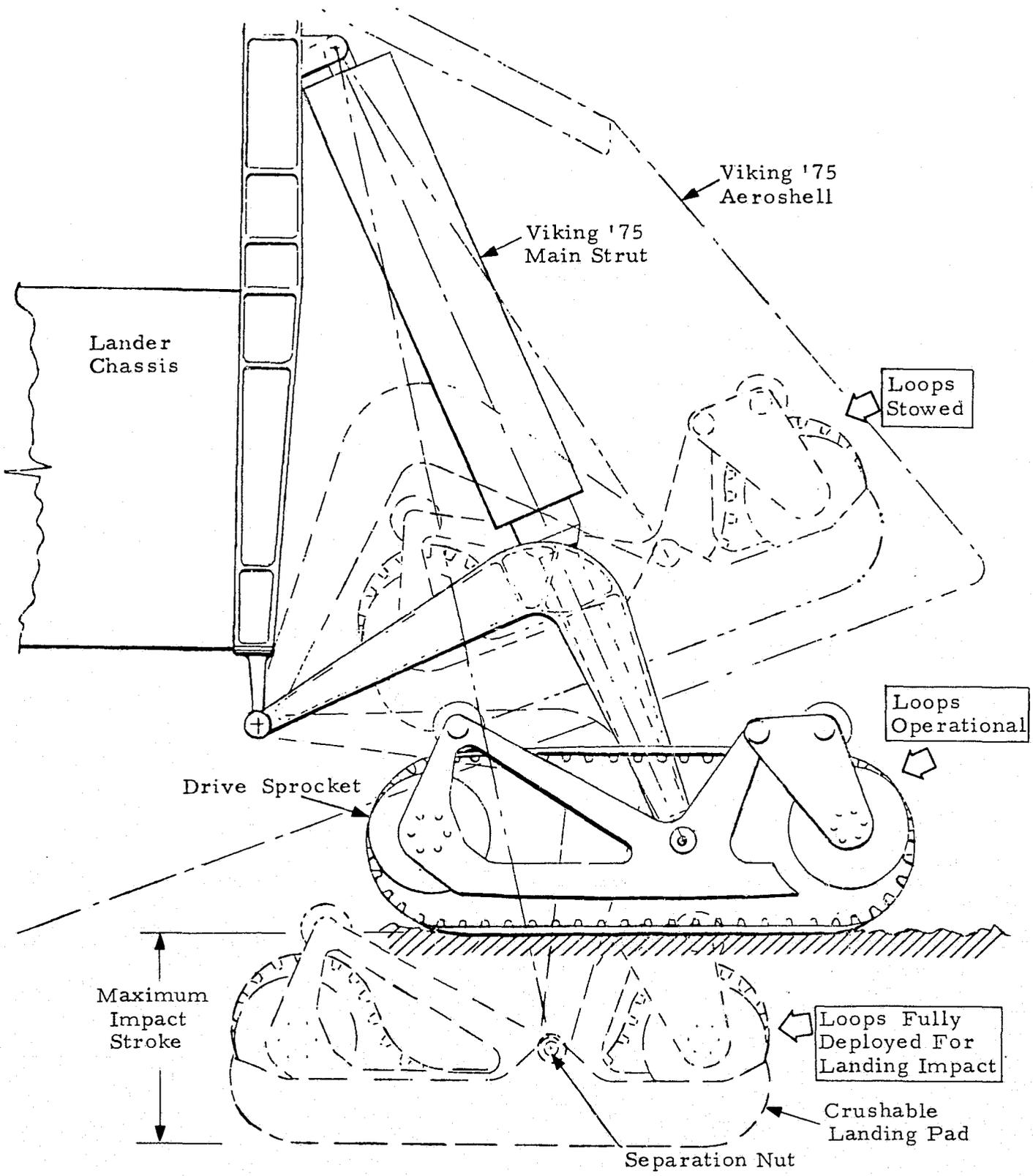
Fig. 2 - Side view of typical front loop suspension in stowed, fully deployed and cruise position.
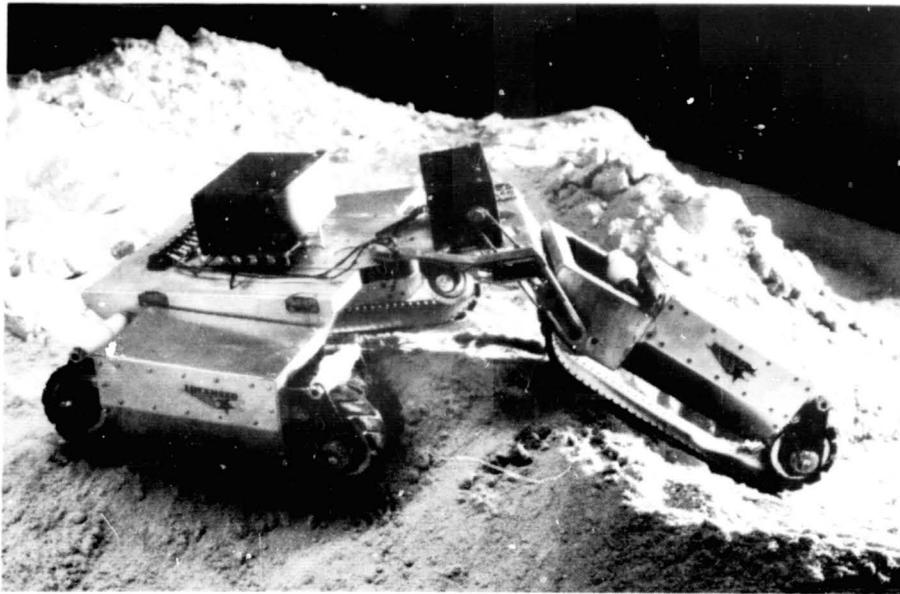
Fig. 3 - Sub-scale three-elastic-loop test vehicle with electric drive and remote control demonstrated high degree of rough-terrain mobility and maneuverability under NASA-sponsored test program.

a)

b)

Separation Nut

Contoured Honeycomb Bottom

Elastic Loop

Landing Pad (Crushable Honeycomb)

Face Sheet
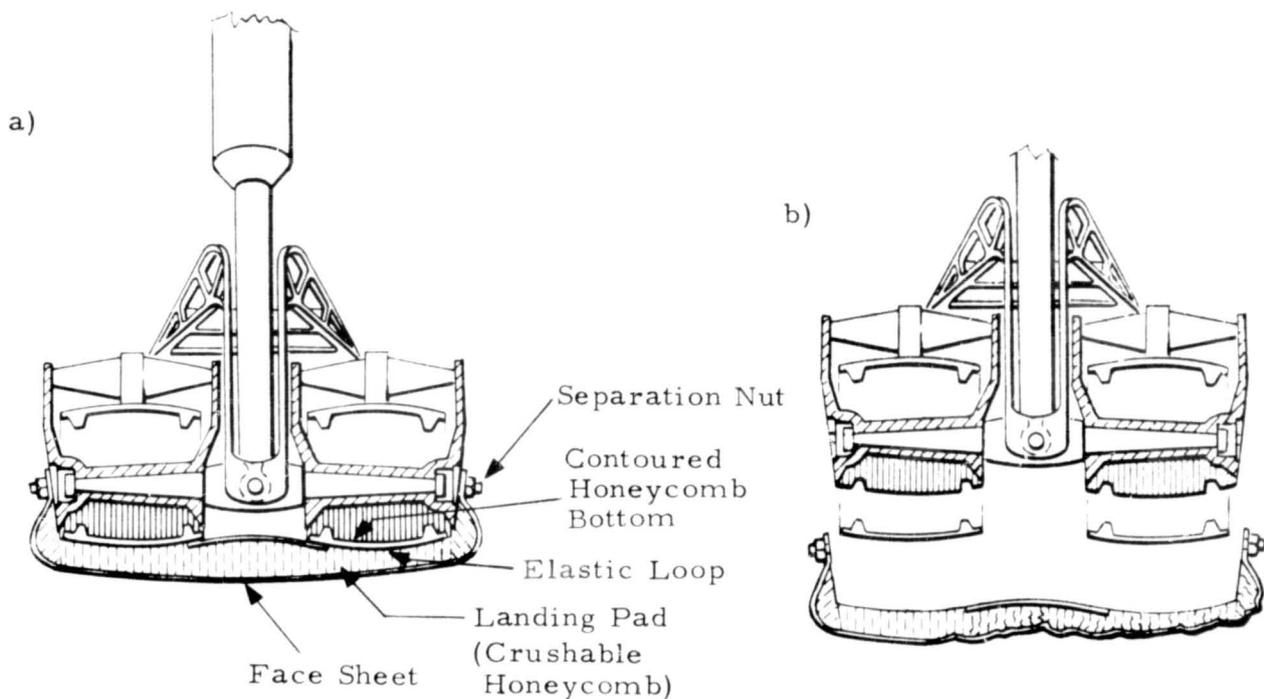
Fig. 4 - Loop protection during landing by contoured carriage bottom and crushable pad.
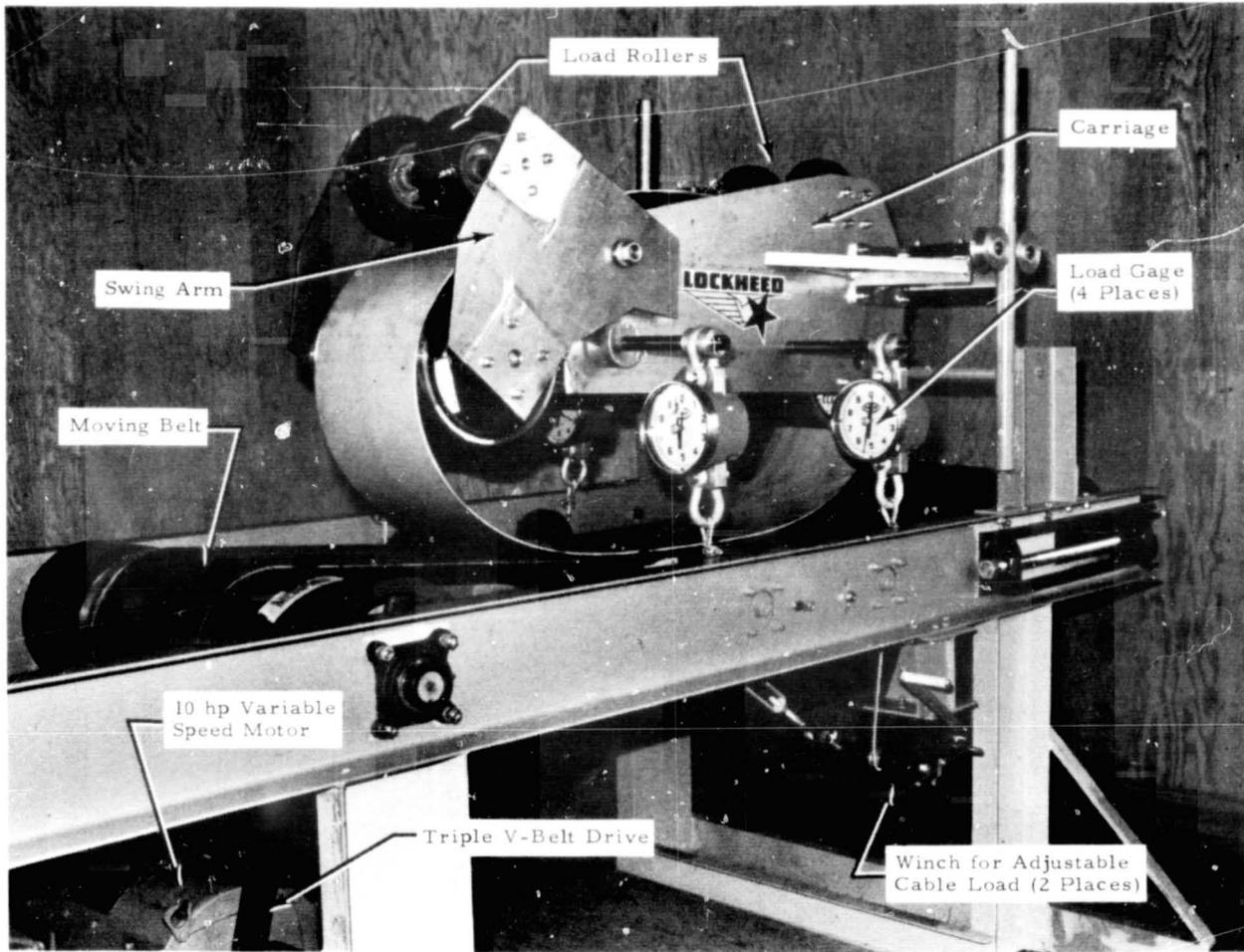
Fig. 5 - Fiberglass-epoxy test loop during endurance test on moving belt
dynamometer (Ref. 12).
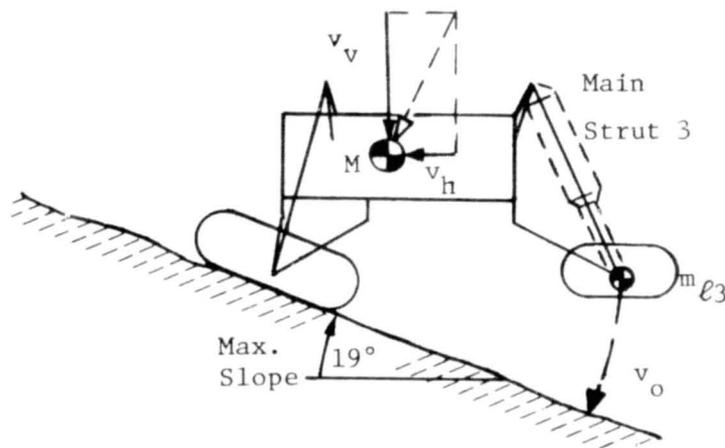
Worst Case:

v_v = 3.35 m/s

v_h = 1.22 m/s

Results In

v_o = 6.1 m/s At Leg 3

Fig. 6 - Side view of worst case landing impact. Load peaks at leg
3 due to "slap down" motion after initial simultaneous impact of
legs 1 and 2 into maximum assumed slope.
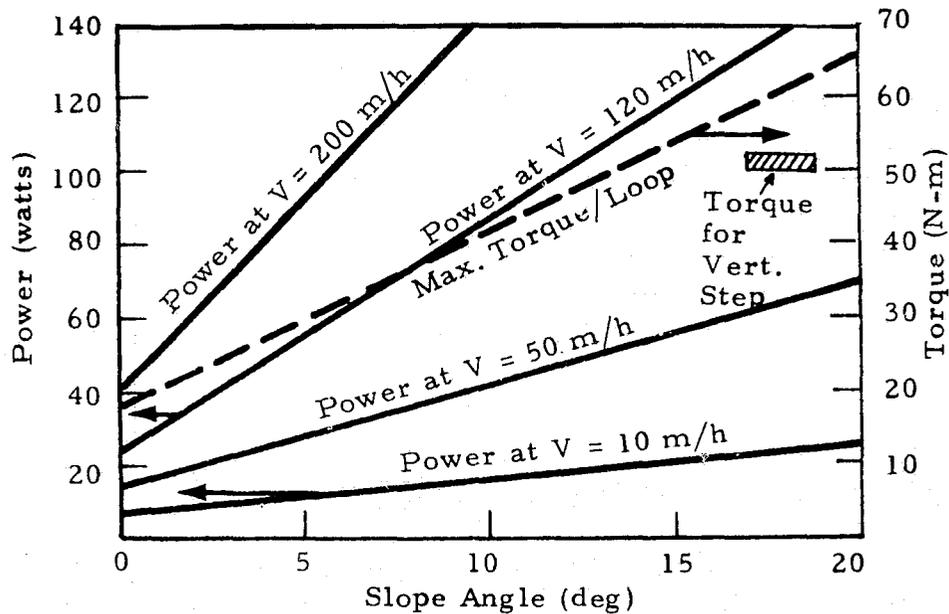
Fig. 7 - Total mobility power for mobile lander in martian loess based on loose soil tests (Ref. 8).

Notes: 1. Assumed efficiencies were $\eta_{motor/gear\ red.} = \begin{cases} 0.2 \text{ at } V = 10 \text{ m/h} \\ 0.4 \text{ at } V \geq 120 \text{ m/h} \end{cases}$

2. All power predictions multiplied by factor 1.25 to account for uncertainties and wear effects

3. Torque prediction includes load transfer to rear loops and $\eta_{gear\ reduction} = 0.8$
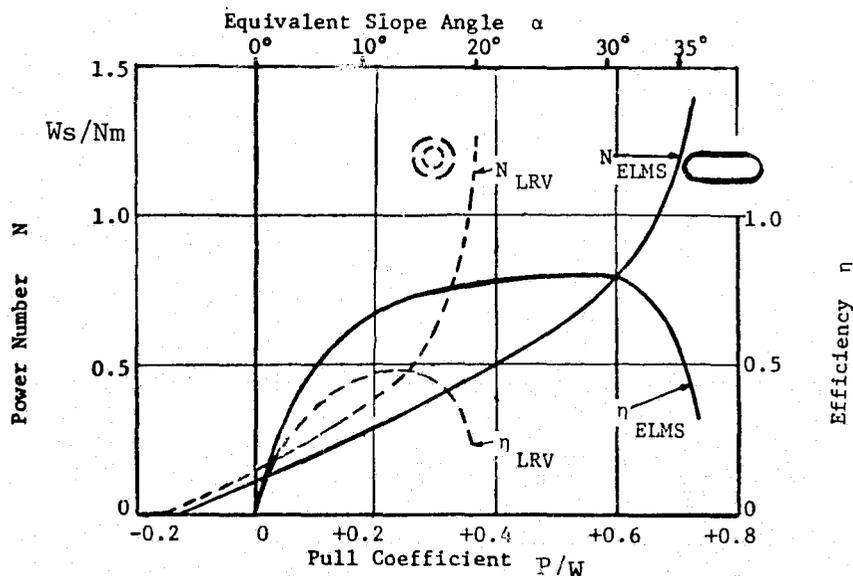
Fig. 8 - Comparison of power requirements and slope climbing capability of LRV-wheels (82 cm dia, 254 N load) and elastic loop mobility systems, "ELMS" (160 cm long, 46 cm high, 685 N load) tested in loose lunar soil simulant at WES (Refs. 8, 9); power number N = energy required (Ws) per newton load and per meter traveled; efficiency η = pull x speed/input energy.
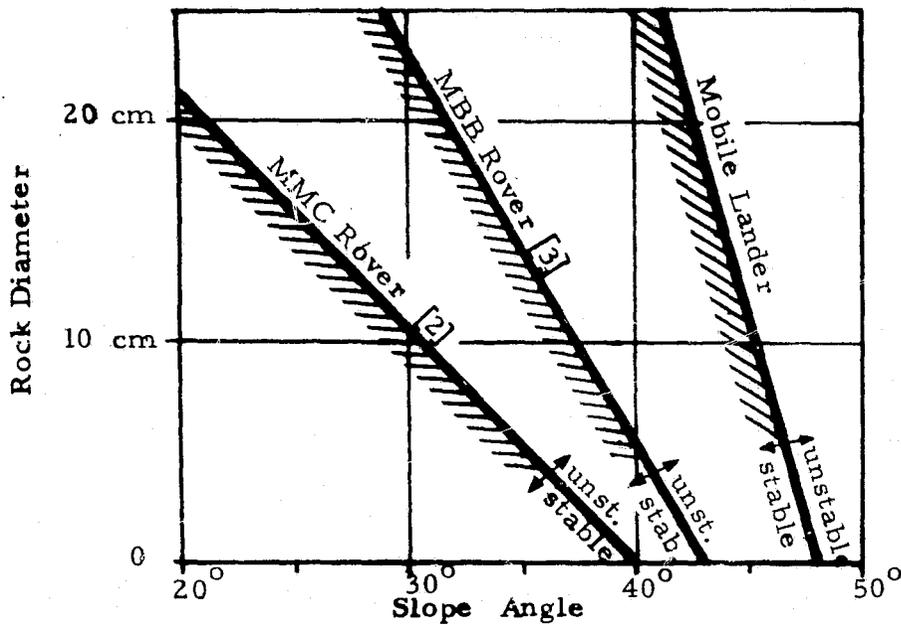
Fig. 9 – Static lateral stability boundaries for two four-wheeled rovers
and mobile lander as a function of slope angle and additional rock
under uphill wheels (or loops).
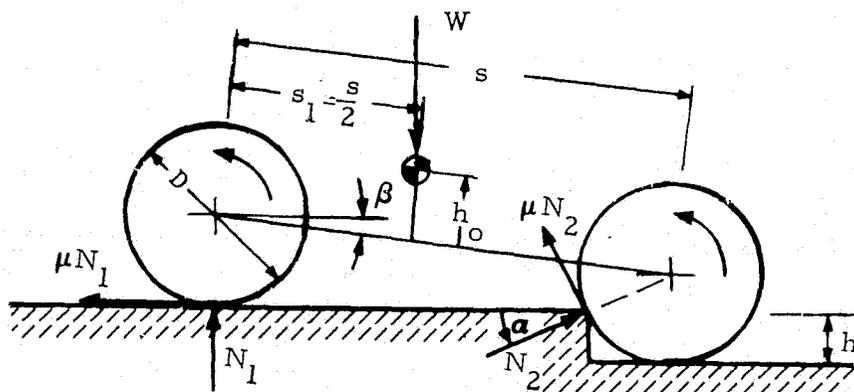
Fig. 10 – Forces acting on four-wheeled rover with all-wheel drive in
critical condition for step obstacle climbing.

APOLLO—SOYUZ TEST PROJECT DOCKING SYSTEM

By W.L. Swan, Jr.

SPACE DIVISION
ROCKWELL INTERNATIONAL

ABSTRACT

The United States and Soviet Union in July 1975 successfully completed a joint space mission utilizing each country's spacecraft and the compatible docking system designed and fabricated by each country.

This paper describes the compatible docking system and defines the extensive research, development, and testing leading up to the successful mission. It also describes the formulation and implementation of methods for breaking the language barrier, bridging the extensive distances for communication and travel, and adjusting to each country's different culture during the three-year development program.

INTRODUCTION

In the latter part of 1971, the United States and Soviet Union agreed to a joint space mission utilizing each country's spacecraft and a compatible docking system. This mission, called the Apollo-Soyuz Test Project (ASTP), was successfully conducted as planned in July 1975. The mission profile is shown in Figure 1. Hardware used in the mission is shown in Figure 2.

Docking system design, development, and test were governed not only by the Apollo philosophy but also the interface requirements generated jointly by the United States and the Soviet Union.

OBJECTIVES

The docking system for this mission provided for all facets of the mechanical docking between Apollo and Soyuz. Specific objectives were:

- Attenuate the forces caused by impact in docking the vehicles.
- Make the primary mechanical linkup (capture).
- Limit vehicle rotational excursions.
- Control vehicle misalignments before retraction.
- Draw the docking structural rings together (retraction).
- Structurally connect and seal the docking interface.
- Provide a clear passageway for intervehicular transfer without removing any part of the docking system.
- Abort and separate the vehicles at any stage of the docking operation.
- Provide capability for immediate emergency undocking and release.
- Provide repeated docking and undocking capability.
- Perform docking and undocking functions without the active aid of the other space vehicle.

DEVELOPMENT AND TEST

Basic philosophy for development and test of the system was joint testing for any facet affecting the interface (i.e., docking dynamics) and individual country testing for noninterface

aspects of the program (e.g., launch environments). This philosophy generated the joint test program outlined below.

Two-Fifths-Scale Model

In addition to full-scale hardware for test and flight, a two-fifths-scale model was fabricated to demonstrate the general concept of the docking system and to conduct joint dynamic tests and verification of interface compatibility with a similar scale model fabricated by the Soviet Union. This joint series of tests was conducted in Moscow.

Interface Seal

Interface seal testing initiated the joint full-scale hardware test series and established working methods and procedures for personnel, procedures for handling test hardware, and procedures for test conduct and documentation. This series evaluated several seal configurations and various shore hardness values. It considered seal capability at maximum misalignments, temperature extremes, and pressure variations. It further considered a gap between the metal interfaces. This test series was conducted at Rockwell International's Space Division headquarters in Downey, California.

Dynamic Testing

Six-degree-of-freedom dynamic tests were conducted with both development and qualification hardware to demonstrate satisfactory performance during docking operations. This testing utilized a dynamic simulator, which combined a computer and a relative-motion simulator, and exercised the docking system in specified dynamic modes to simulate actual space docking. High- and low-temperature docking system environments were provided during test. This test series was conducted at NASA's Johnson Space Center (JSC), Houston, Texas, on the Dynamic Docking Test System (DDTS). Verification of final hard docking dynamics (i.e., that phase from alignment pin/socket engagement through structural latch closure) was conducted on a simulator at the Space Division.

Mate Tests

Mate tests were conducted on the systems to demonstrate and verify final structural integrity and interface compatibility between the docking interfaces and provide capability for emergency undocking and release. This test series, involving both development and qualification hardware, was conducted at NASA JSC. A typical test setup is shown by Figure 3.

Preflight Mate Check

Preflight mate check tests were conducted to demonstrate satisfactory operation and interface compatibility of the two mating systems that were to dock in space. For this, the prime flight unit from each country was tested in conjunction with the prime flight unit and backup unit from the other country. For this test, both docking and undocking sequences were simulated. This test series was conducted in Moscow.

Test programs conducted by the U.S. on U.S. hardware for purposes of qualification were as follows (system-level tests only):

- Development environmental
- Development dynamic
- Qualification dynamic
- Qualification environmental

As may be expected, precedents were necessary because joint test programs had not been required in the aerospace industry prior to this time. The basic test philosophy used in the Apollo program was to be maintained; likewise, Soviet Union philosophy was not to be breached. This

naturally required mutual test conduct agreements which were defined during various working group meetings.

INTERFACE REQUIREMENTS

Soviet Union and United States personnel early in the program defined a clear method for control of all interfaces through documents entitled Interacting Equipment Documents (IED's). In essence, U.S. and USSR working-level groups met on a regular basis to develop, review, and concur on technical aspects of the project. Specific agreements and hardware interfaces were defined on the IED's which were prepared in both languages and in the metric system. Although interface configuration was jointly established, each country independently developed and designed hardware to satisfy these interface requirements. This naturally evolved to two distinctly different sets of hardware, as shown by Figures 4 and 5.

Joint interfaces were relatively straightforward on dimensional and load aspects but required additional coordination on technical terms not common to each country (e.g., dry lubricant and surface finish). An example of an IED prepared to define the structural latches is shown by Figure 6. Note that representatives from both countries verified both technical content and translation.

The English/Russian language differences did not produce any significant problem, although problems had originally been anticipated. The language difference did force each country to be totally objective in requirements, totally prepared prior to any technical discussions, and provided extreme incentive for making certain language was not a barrier in conduct of business. Although U.S. and USSR personnel attended classes in Russian and English, respectively, there was no attempt to rely on this training in conduct of technical meetings/reviews. For this, a technical interpreter was present and meeting minutes, as well as presented technical material, were in both languages.

SYSTEM DESCRIPTION AND OPERATION

The U.S. docking system for the ASTP is a self-contained unit mechanically attached to the docking module, which, in turn, is attached to the command and service modules. This is as shown by Figures 2 and 4. The Soviets attach their docking system to the orbital module at the end opposite the descent vehicle, as shown by Figures 2 and 5.

The docking system chosen for this mission was an androgynous system (i.e., any unit may be mated with any other unit of same or compatible design). Basic system design also dictated that each country's docking system have the capability of assuming active operational control.

The docking system is best described by the nomenclature of Figure 4 and the following sequence of docking operations (each component or subsystem is defined in greater detail later):

1. Guide ring is extended on the active docking system (as shown by Figure 4 and the upper system of the Figure 3 photograph) to provide impact attenuation upon initial contact with the passive vehicle. At this time, the passive docking system guide ring is in the retracted position (as shown by the lower system of the Figure 3 photograph).

2. Upon guide ring contact, the three capture latches (mounted on the active system guide ring) engage the passive system body-mounted latches. (This is defined as soft dock.) Impact energy is dissipated by the six hydraulic attenuators.

3. Following capture, the guide ring assembly of the active docking system is retracted until the structural mating surfaces of both docking systems meet.

4. The eight structural latch active hooks of the active docking system are then engaged with the passive hooks of the passive system. (This is defined as hard dock.)

5. During final phase of guide ring retraction, alignment is provided by engagement of alignment pins and sockets mounted on each structural ring.

6. The mating surfaces of each spacecraft's structural ring have two concentric seals which, compressed on each other during final retraction and structural latch engagement, are to provide a pressure seal to the tunnel area when it is pressurized.

7. The indicating system provides a continual status of the operation during actual usage. It defines position of guide ring, guide ring contact, structural ring contact, and gearbox readouts.

The undocking sequence normally is provided by the active docking system releasing the eight structural latch active hooks and then releasing the three capture latches. Spring thrusters mounted in the structure provide force to assure undocking with a positive separation force.

In an emergency, undocking may also be accomplished by either the active system disengaging by a redundant system or the passive system disengaging its passive structural latch hooks and its body latch hooks.

COMPONENT DESCRIPTION

The U.S. docking system consists of subsystems performing all sequences of docking and undocking as described below.

Base Structure

The docking system utilizes a basic structure on which all components are mounted. This structure, in turn, attaches to the docking module by an annular series of fasteners. To obtain maximum strength properties using conventional materials, a roll forging of 7075 aluminum alloy was utilized to produce a circular grain flow pattern. The machined forging size is approximately 1530 mm (60 inches) outer diameter, 760 mm (30 inches) inner diameter, and 510 mm (20 inches) wide. Initial temper is T411; final temper immediately prior to final machining is T73 with intermediate heat treatments to preclude warpage and maintain critical surface flatness requirements at sealing surfaces. All components attach to this structure by Slimsert inserts.

Guide Rings

This structure provides three equally spaced guides designed for aligning the mating systems in lateral and angular direction. These guides are set at a 45-degree angle slightly tapered at the tip. Construction is of an aluminum ring, machined from a roll forging, with mechanically attached guides.

Capture Latch

Each of the three capture latches (Figure 7) is mounted flush with the guide surface with two protruding hooks (with roller surfaces) for engagement with the mating body latches. Each capture latch has redundant mechanisms and redundant electrical linear solenoid release actuators. A unique feature is vector sensitivity to allow automatic release of a single latch in the event all three latches in the system are not engaged. Release of a capture latch is provided by two independently operated linear solenoids mechanically linked so that either of the two solenoids releases both hooks. Load

capability for each latch (single hook) is 600 kilograms (1320 pounds) in the vertical direction. To prevent engagement of all six capture latch/body latch combinations at any docking, the guide ring assembly (hence the capture latches) on the passive system is drawn down beyond the engagement reach of the body latches.

Structural Latches

Structural latches, providing final latching between the two systems, are shown in Figure 8. Each latch, in turn, has an active hook, mating and locking with the passive hook of the passive system, and a passive hook, remaining inactive (hence not locking) on the active system. All latches are interconnected by a corrosion-resistant steel, impregnated with solid dry film lubricant, cable system. Structural latch power to lock and provide interface preload as well as to unlock latches for separation is provided by an electric motor drive (described later). An emergency release system is provided to release the eight passive hooks. These structural hooks are also interconnected by an independent cable system powered by the electric motor drive.

Retract and Attenuation Systems

Early design and development trade-off studies indicated that the most feasible method for design of both attenuation and retraction was to handle each in separate systems rather than as one mechanism for both purposes. This evolved to a concept of: (1) six independent hydraulic attenuators for guide ring extension and to attenuate the impact of the spacecraft during initial contact; (2) a steel cable for retraction of the guide ring, as shown in Figure 9; and (3) guide ring extension via internal springs within each attenuator. Six attenuators are mounted in pairs beneath each guide.

Cables, similar to those used on the structural latches, attach at the guide ring via load bungees configured to compensate for different cable lengths and to a base-mounted actuator drum. This system is driven by an electric motor drive.

Body-Mounted Latches

Each of the three body-mounted latches (Figure 7) mounted on the base structure consists of a single hook operated by redundant rotary solenoid release actuators. Body-mounted latches are normally static devices unlatched only in the event of backup release. Maximum load capability is 600 kilograms (1320 pounds) in the vertical direction.

Electrical Indication Systems

These systems provide the necessary power and control for actuators, solenoids, and operation of the indication/sensing systems. System power is from redundant 28-volt dc; indicator power is from redundant 5-volt dc systems hardwired from the command module. The indication system's 32 status switches provide talk-back for all operations for continued crew and system monitoring.

A unique electrical load sensing cell was used to indicate interface preload during structural latch engagement. These cells, approximately 25 mm (1 inch) by 76 mm (3 inches) by 6 mm (1/4 inch) thick, are sandwiched between each latch and structure and hardwired back to the command module.

Actuators

The three electrical motor drive actuators provide power for structural latches and guide ring retract. Each has redundant electric motors and a gear train reduction assembly, including integral brake and full differential, so that with one motor inoperative, the actuator output is the same and operation time is doubled. In addition, each actuator has drive capability in both directions. Output requirements are:

1. Guide ring retract: 1950 kilograms (4300 pounds)
2. Structural latch active drive hook: 1361 kilograms (3000 pounds)
3. Structural latch backup drive: 234 kilograms (515 pounds)

Interface Seals

Two concentric interface seals mating with two seals on the mating system provide pressure integrity within the transfer tunnel region. These seals of silicon material are shown in Figure 10.

Thermal Control System

Considerable analyses were required for a thermal control system that would be totally passive. These analyses resulted in special surface exterior finishes and coatings as well as bagged-beta insulation on the tunnel interior for adequate crew interface temperature. Exterior coatings are:

- Attenuators
  - 260-degree segment facing outward to space
    - Electroless nickel, $\alpha_s/\epsilon = 0.37/0.15 = 2.5$
  - 100-degree segment facing base assembly
    - Gray polyurethane, $\alpha_s/\epsilon = 0.84/0.92 = 0.9$
- Guides (backsides)
  - Two guides facing cold side
    - Finch paint $\alpha_s/\epsilon = 0.35/0.35 = 1.0$
  - Guide toward CM
    - Black polyurethane to preclude glare (not thermal requirement)
- Capture latch sides
  - Finch paint $\alpha_s/\epsilon = 0.35/0.35 = 1.0$
- All remaining component surfaces: no special coatings required

CONCLUSIONS

Actual flight performance of the docking system on each spacecraft was normal. During the flight, two dockings and two undockings were conducted—first with the Apollo operating as the active system and second with the Soyuz as the active system. The docking systems of Apollo and Soyuz performed perfectly during all phases of docking and undocking operations.

Joint documentation developed during the preflight period proved adequate for resolving all problems in preparing and conducting the mission. In addition, working group disciplines adapted for joint operations proved successful.

With proper management, documentation, and program control, docking hardware may be fabricated individually by two foreign nations for a joint space venture.
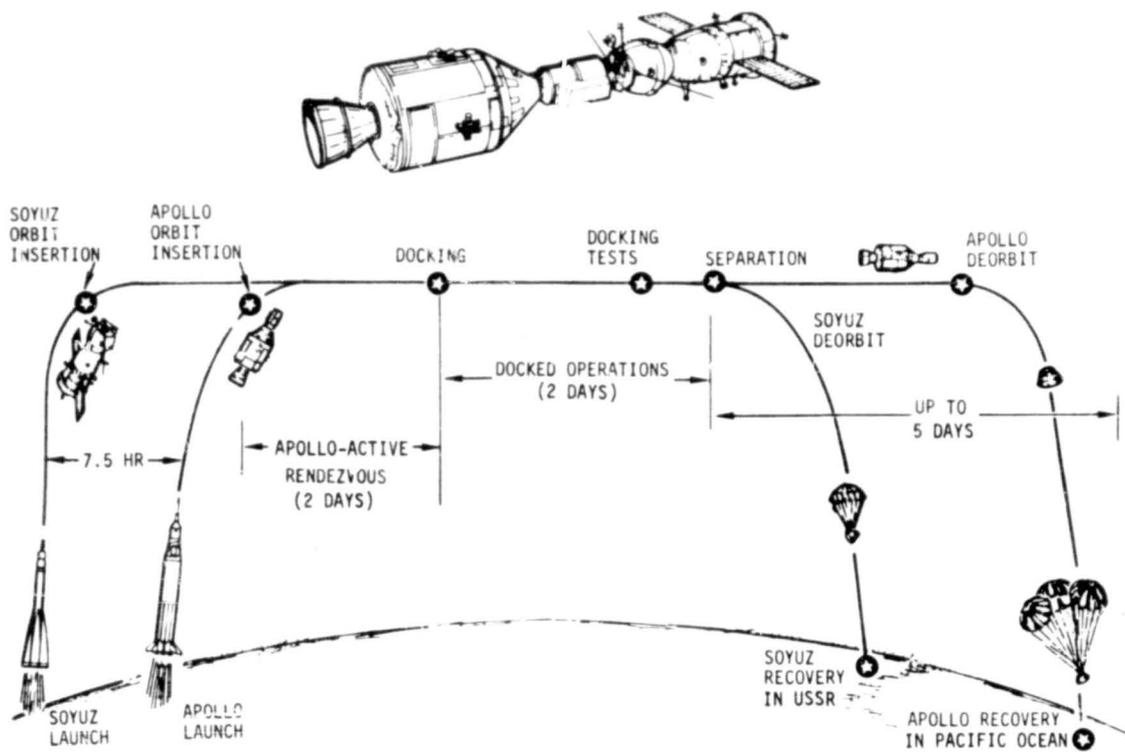
Figure 1. Basic Mission Profile
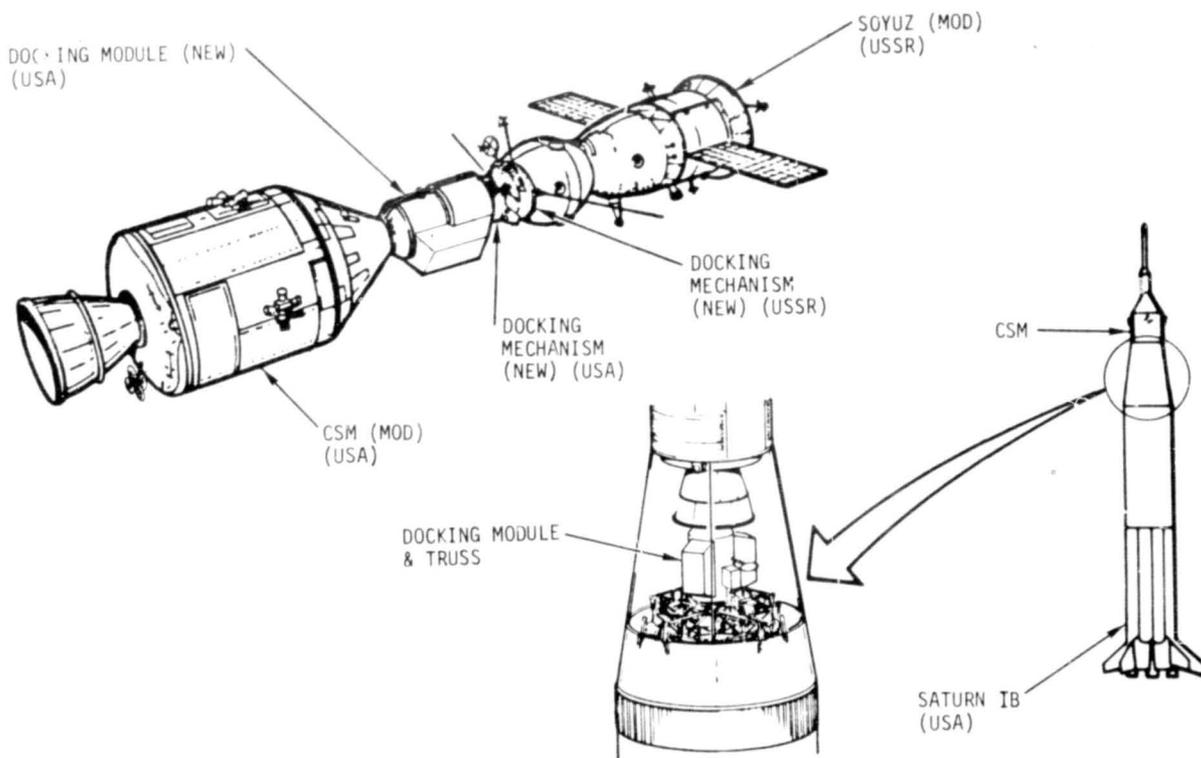
Figure 2. ASTP Major Hardware
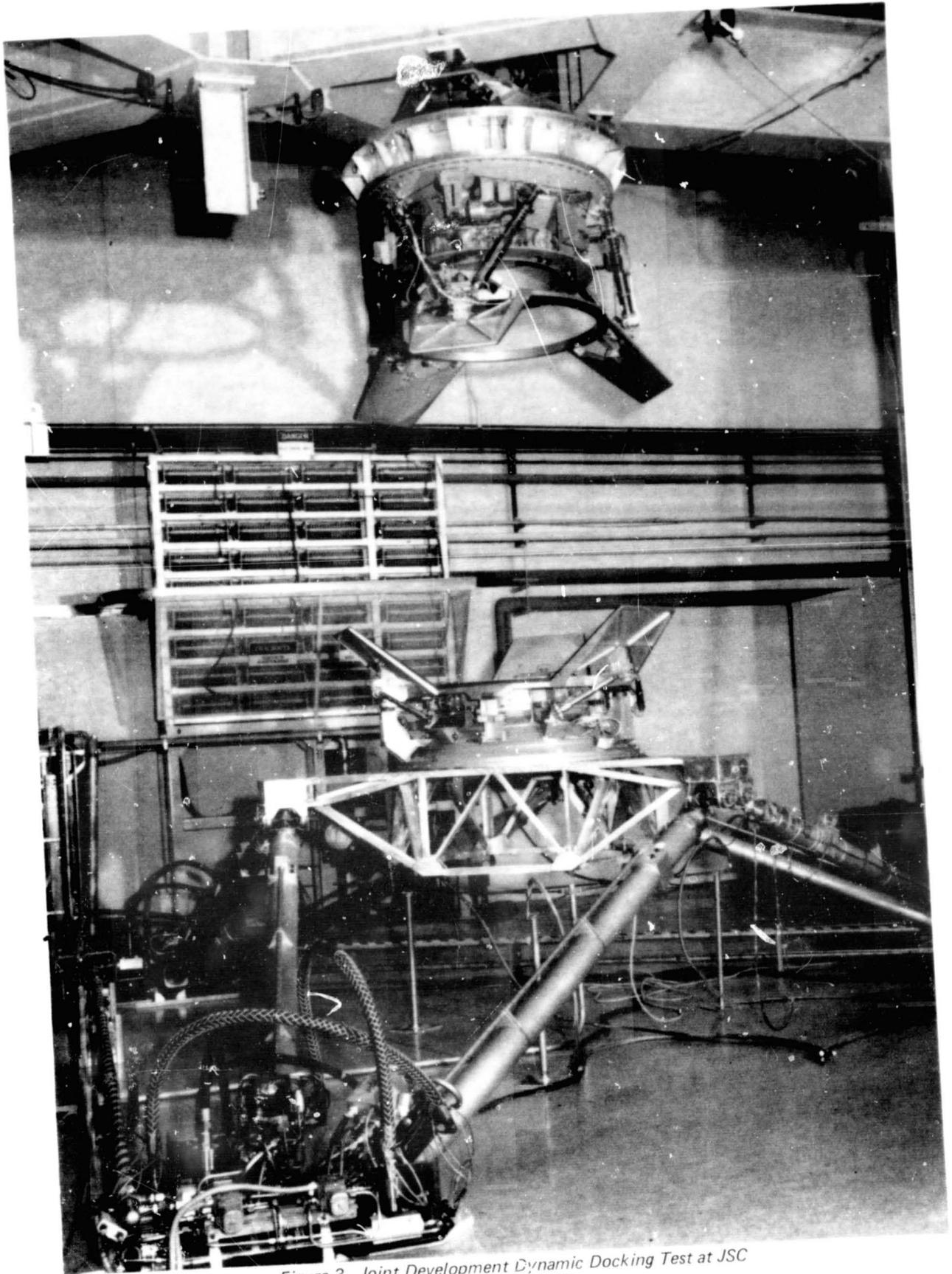
Figure 3. Joint Development Dynamic Docking Test at JSC

CAPTURE
LATCH

GUIDE

GUIDE RING
(EXTENDED)

ALIGNMENT
PIN

INTERFACE
SEALS

TUNNEL
INSULATION

UMBILICAL
DOOR

SPRING
THRUSTER

BASE
ASSEMBLY

BODY LATCH

GUIDE RING
RETRACT
SYSTEM

CABLE
GUIDE
TUBE

STRUCTURAL
LATCH
SYSTEM

ALIGNMENT
SOCKET

ATTENUATOR
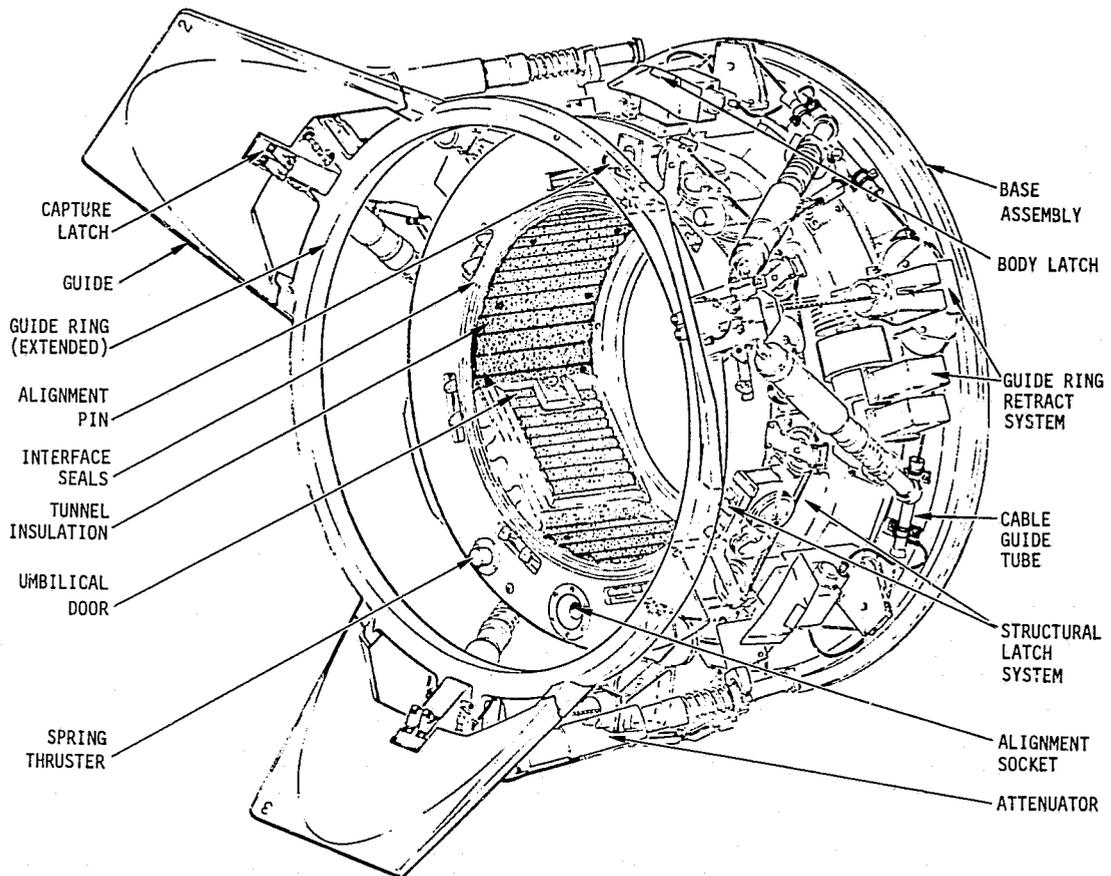
Figure 4. U.S.A. Docking System
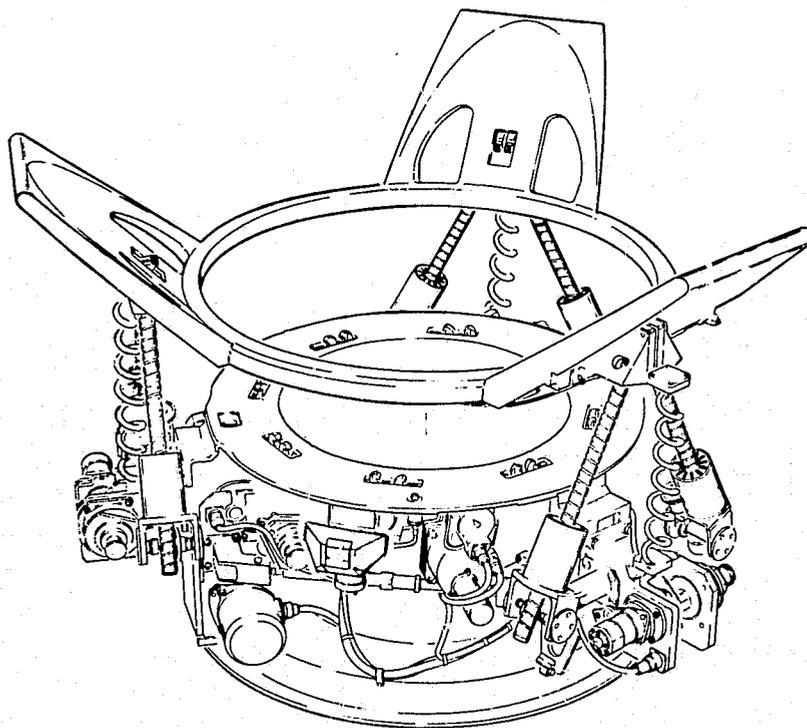
Figure 5. USSR Docking System

Figure 6. Interacting Equipment Document Example

- CAPTURE LATCH

  - TWO HOOKS, TWO SOLENOID RELEASE ACTUATORS

  - MAX LOAD 1320 LB
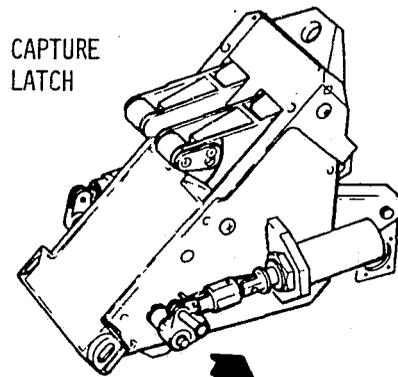
CAPTURE LATCH

- BODY-MOUNTED LATCH

  - SINGLE HOOK, TWO SOLENOID RELEASE ACTUATORS

  - USED FOR BACKUP RELEASE

  - MAX LOAD 1320 LB

BODY-MOUNTED LATCH
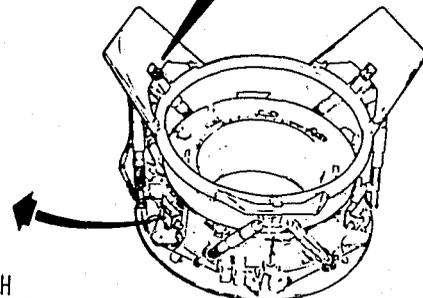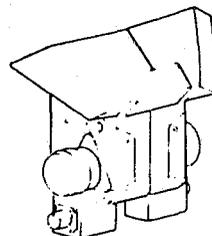
Figure 7. Docking System Capture/Body Latches

- EIGHT LATCH ASSEMBLIES

  EACH INCLUDES PASSIVE & ACTIVE HOOKS

- ACTIVE HOOK OF ACTIVE SYSTEM MATES WITH PASSIVE HOOK OF PASSIVE SYSTEM

- INTERFACE LOAD/HOOK COMBINATION = 4370 LB MIN, 7374 LB MAX

- OVER-CENTER LATCHING

ACTIVE HOOK DRIVE GEARBOX

BACKUP HOOK RELEASE DRIVE GEARBOX

IDLER PULLEY ASSY

INTERFACE PLANE

LOAD CELL

STRUCTURAL RING LATCH PASSIVE HOOK

STRUCTURAL RING LATCH ACTIVE HOOK

LOAD CELL
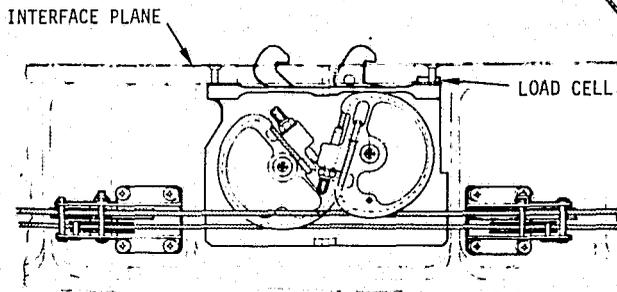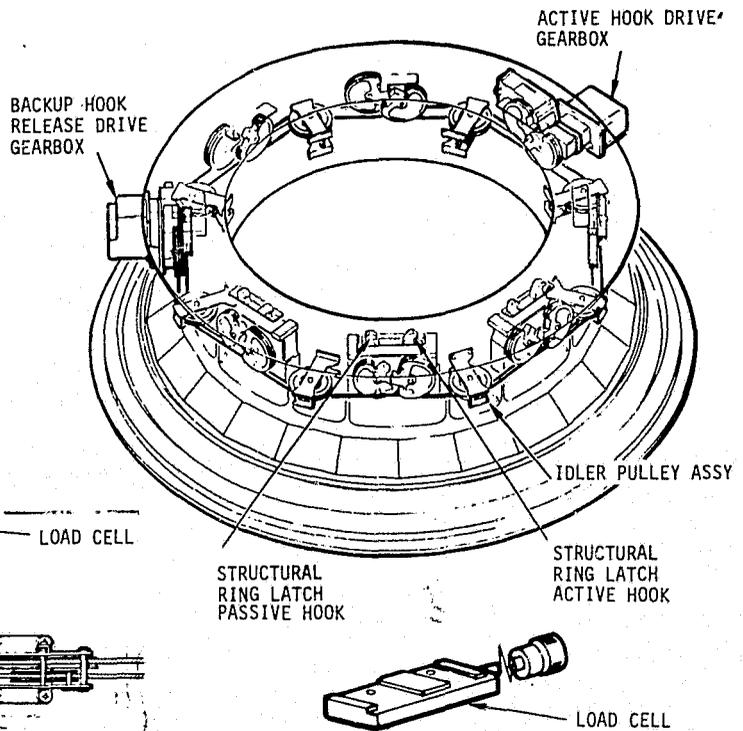
Figure 8. Docking System Structural Ring Latch

BELLEVILLE SPRINGS
(BUNGEE ASSEMBLY)
3 PLACES

ACTIVE MODE

RETRACT
GEARBOX

CABLE LOADS
1350 LB PER CABLE NORMAL
OPERATION
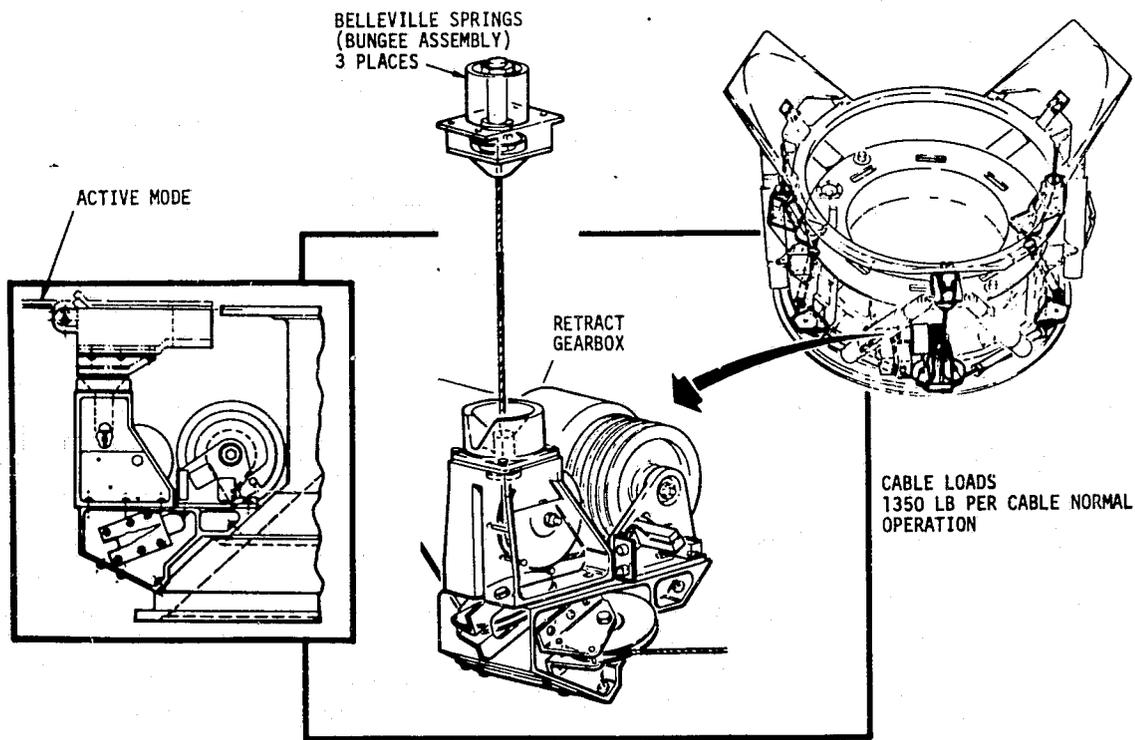
Figure 9. Docking System Guide Ring Retract System

TUNNEL

USSR

0.329 IN.

USA

SEALS   NOMINAL SEAL HEIGHT
0.041 IN. - 0.065 IN.

RETAINER
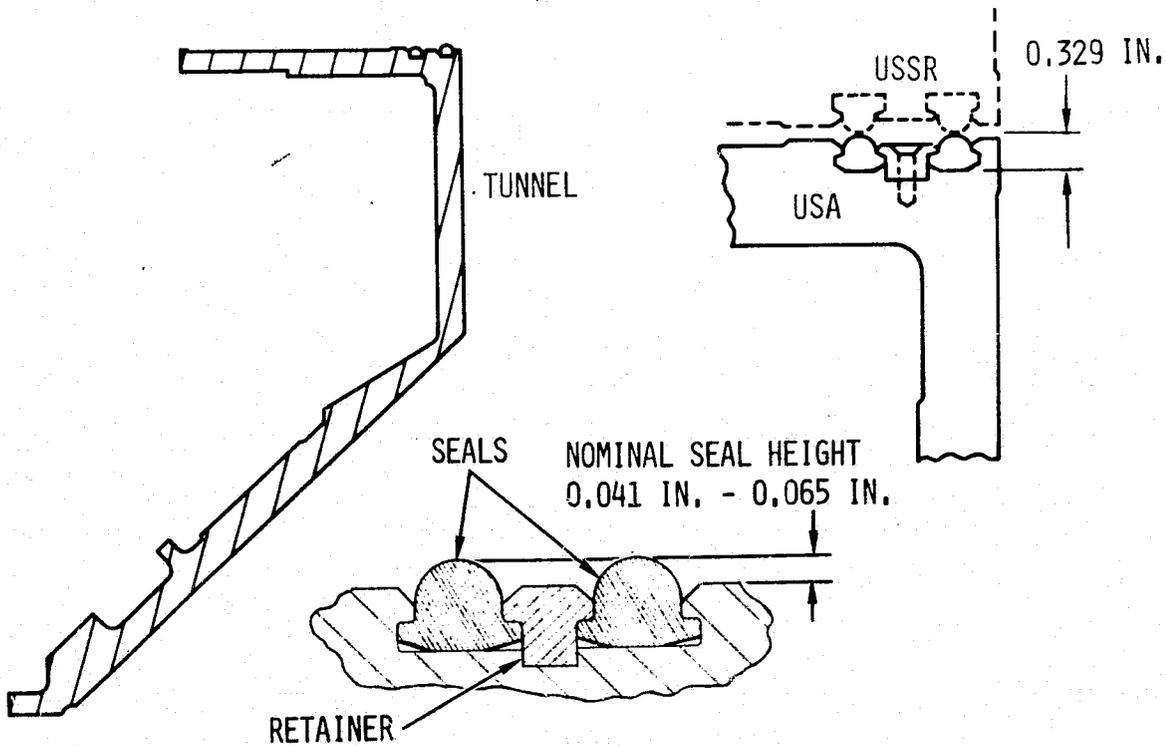
Figure 10. Diagram of Docking System Interface Seals

SHAPE OPTIMIZATION OF DISC-TYPE FLYWHEELS

By Richard S. Nizza

Lockheed Missiles & Space Company, Inc.

ABSTRACT

Recent developments in the field of flywheel powered electrical energy storage systems has prompted the need for a better understanding of the varied design and analytical criteria that must be considered in the selection of a flywheel. Techniques have been developed for presenting an analytical and graphical means for selecting an optimum flywheel system design, based on system requirements, geometric constraints and weight limitations. The techniques for creating an analytical solution are formulated from energy and structural principals. The resulting flywheel design relates stress and strain pattern distribution, operating speeds, geometry, and specific energy levels. The design techniques incorporate the lowest stressed flywheel for any particular application and achieve the highest specific energy per unit flywheel weight possible. Stress and strain contour mapping and sectional profile plotting reflect the results of the structural behavior manifested under rotating conditions. This approach toward flywheel design is applicable to any metal flywheel, and permits the selection of the flywheel design to be based solely on the criteria of the system requirements that must be met, those that must be optimized, and those system parameters that may be permitted to vary.

INTRODUCTION

This paper describes a procedure for designing an optimum flywheel shape based on the constraints of geometry, speed and stress so as to maximize energy density. The design procedure described relies on the application of linear elastic structural mechanics and the laws of conservation of energy and momentum. Little work has been reported in maximizing the energy density of solid disc flywheels. Much work however has gone into the design of turbine blades and discs, and electric generators and motors, which are perhaps the closest entity to the energy storage flywheel. The basic structural laws under which flywheels, turbine blades, generators and motors behave are the same but their functions, based on different design objectives, are different.

The energy density of a flywheel is represented by the simple relationship:

$$E = K_S \frac{\sigma}{\rho} \tag{1}$$

where E = energy density

K_S = flywheel shape factor (dimensionless)

σ = material working stress

ρ = material density

Flywheel shape factors for several geometries are shown in Table 1. For disc flywheels the shape factor can approach 1.00. The disc shaped flywheel that produces this high a shape factor has constant stresses throughout. This is attributed to the fact that each unit volume of material is stressed equally to a predetermined working stress level and therefore produces the largest amount of energy possible. The flywheel shape that produces this constant stress is exponential in profile.

Equation (2) expresses the summation of forces in a flywheel (Reference 2).

$$\frac{d(XY\sigma_r)}{dX} - Y\sigma_t + \frac{\rho}{g} W^2 X^2 Y = 0 \tag{2}$$

For uniform strength the tangential and radial stresses must be equal and of constant value throughout.

Therefore,

$$\sigma_t = \sigma_r = \sigma = \text{constant}$$

Equation (2) can be restated as

$$\frac{d(XY)}{dx} - Y + \frac{\rho}{g\sigma} W^2 X^2 Y = 0 \tag{3}$$

and by integrating,

$$\ln \frac{Y}{Y_o} = - \frac{W^2 X^2 \rho}{2g\sigma} \tag{4}$$

Applying the boundary conditions, at $X = X_R$, $Y = Y_R$

$$\frac{\rho W^2}{2g\sigma} = \frac{1}{X_R^2} \ln \frac{Y_o}{Y_R} \tag{5}$$

Substituting Equation (5) into Equation (4),

$$\frac{Y}{Y_o} = e^{-\left(\frac{X}{X_R}\right)^2 \ln\left(\frac{Y_o}{Y_R}\right)} \tag{6}$$

where   X   = radius

Y   = thickness at radius X

Y_o = hub thickness

Y_R = tip thickness

X_R = tip radius

Equation (6) gives the normalized thickness as a function of the normalized radius and the hub-to-tip thickness ratio. This equation represents the profile configuration for the constant stress flywheel geometry. According to Equation (6), the disc, even though with infinitely decreasing thickness, is prolonged to infinity. But practically, the disc is limited by a cylindrical boundary or radius X_R at which it has a thickness Y_R. Although the theoretical flywheel of infinite diameter would have a shape factor of 1.00, the practical flywheel of finite radius X_R would have a shape factor less than 1.00. In order to improve the shape factor of this exponentially shaped finite diameter flywheel, the author has chosen to take some of the material that theoretically existed between the finite diameter and infinity and place it near the rim of the flywheel producing a constant thickness section running from a point on the surface to the rim. The utilization of a flat tip as the means for improving the flywheel shape factor, in lieu of an exponentially flaired tip, was chosen for two reasons: number one, the shape factor difference between a flaired and a flat tip was found to be insignificant, and secondly, the manufacturing and machining operations are considerably simplfied by having a flat tip rather than a flaired tip. The question of how much constant thickness material should be added to the flywheel must now be determined. Since it is the objective to improve the shape factor as much as possible, it is necessary to solve Equation (1) in terms of the shape factor, K_S, for the various stresses and energy densities associated with each flatted tip flywheel that is generated for each hub-to-tip thickness ratio used in Equation (6). An analytical evaluation must first be performed to evaluate the resulting stresses and energy densities for each flywheel geometry.

One such analytical method developed at Lockheed Missiles & Space Company utilizes a computer program based on two dimensional stresses and strains developed in rotating machinery. These relationships were then expanded (Reference 3) and culminated in the computer program. A typical set of results are shown in Table 2. Tangential stresses, radial stresses and flywheel thicknesses are presented for various radii starting at the rim and extending to the hub. Once the stresses are determined the program then utilizes Equation (1) to calculate the shape factor from the calculated kinetic energy and maximum flywheel stress. A maximum shape factor is then obtained for each hub-to-tip thickness ratio by iteratively evaluating different flatted tips that begin at different percent radii.

Figure 1 represents the results of the relationship between the flywheel shape factor and the hub-to-tip ratio. The point at which the optimum

flat begins has an optimum value which varies with the hub-to-tip thickness ratio. By applying the appropriate flat tip as the means for optimizing the flywheel shape factor for a particular hub-to-tip ratio, it can be recognized that for hub-to-tip ratios less than 1.00, the appropriate flat tip would extend from the tip to the hub, and the flywheel shape would be that of a flat unpierced disc having a shape factor of 0.606.

FLYWHEEL PARAMETRIC TRANSFORMATIONS

By increasing the hub-to-tip ratio, the shape factor is improved and becomes 1.00 at a hub-to-tip ratio of infinity. There are instances when a high hub-to-tip ratio may not be practical, such as when geometric constraints limit the axial length of the hub. It is therefore desirable to determine the effects of changing parameters on the rest of the system. A set of parametric relationships for relating flywheel diameters, speeds, weights, kinetic energy levels, operating stresses and thicknesses permits an easy determination of the effects on each parameter when one or two are changed. Equations (7), (8), and (9) express these relationships, and can be used for the flywheel shapes generated by Equation (6) having fixed hub-to-tip ratios.

$$\frac{\sigma_N}{\sigma_o} = \left(\frac{D_N}{D_o}\right)^2 \left(\frac{W_N}{W_o}\right)^2 \tag{7}$$

$$\frac{THK_N}{THK_o} = \left(\frac{W_o}{W_N}\right)^2 \left(\frac{D_o}{D_N}\right)^4 \left(\frac{KE_N}{KE_o}\right) \tag{8}$$

$$\frac{WT_N}{WT_o} = \left(\frac{THK_N}{THK_o}\right) \left(\frac{D_N}{D_o}\right)^2 \tag{9}$$

where σ = working stress

D = flywheel diameter

W = flywheel speed

KE = kinetic energy

THK = flywheel thickness

WT = flywheel weight

A specific example is used to demonstrate the application of these equations for a flywheel having a kinetic energy of 12 kilowatt-hours. This is shown in Figure 2 for several flywheels from three to four feet in diameter. The stagger of the data points is caused by the quantizing error in selection of either 75 or 80 percent flat value for the optimum hub-to-tip ratio. Since the optimum flat lies between these two values a smooth curve in actuality joins the optimum points.

The curves represent a family of varying diameters for a particular kinetic energy level. It is reasonable to assume that the kinetic energy requirements are already known for a desired application. The requirements for the operating speed, or the maximum flywheel stress will further restrict the number of available flywheel design selections. If we permit the flywheel speed to vary, we can superimpose a family of flywheel speeds on Figure 2 indicative of a specific kinetic energy and operating stress level. This was done for an operating stress level of 100 ksi. By utilizing a series of plots similar to Figure 2, reflecting various operating stress levels, a more complete selection of flywheel geometries is possible. These curves represent a means for selecting an optimum geometry flywheel based on the kinetic energy requirements, volumetric limitations, and desired flywheel life (reflected through operating stress level). Once a selection is made, a stress profile may be performed using the two dimensional stress program of Reference 3, which produces results similar to those of Table 2. If upon examination of the results of this initial computer run, the flywheel selected is found to be satisfactory, a much more rigorous, three dimensional, stress-strain examination can be performed using a finite element computer program. A process of contour mapping of the stresses and strains developed under rotating conditions for each and every point within the flywheel can then be made. Figures 3 through 6 show contours for radial, tangential, axial, and axial shear stresses for a quarter section view of a 12 kilowatt-hour flywheel. Figures 7 and 8 show the radial, tangential, axial and axial shear stress distribution along an axis of symmetry, perpendicular to the axis of rotation. The graphs are plotted from right to left. The radial and tangential stresses are maintained at the maximum for almost 80% of the radius and decrease only at the tip.

These techniques permit a very accurate determination of all stresses throughout a homogeneous flywheel, and provide all the quantitative information necessary to perform sensitivity tradeoff studies. This allows a flywheel to be geometrically optimized for a given application in a precise, quick, and economical fashion. The desirability of a constant stress and homogeneous material was assumed; however, in manufacturing thick forgings the metallurgical composition can vary considerably from the core to the surface as well as from the hub to the rim. The effects of the resulting stress pattern variations, developed within the material, must be taken into account and applied to the optimization procedure presented. Such methods have been developed at Lockheed Missiles & Space Company in the form of additional computer programs that evaluate the effects of non-homogeneity of the flywheel material.

REFERENCES

1. Lawson, L. J., "Design and Testing of High Energy Density Flywheels for Application to Flywheel/Heat Engine Hybrid Vehicle Drives," Intersociety Energy Conference, P-38, Paper 719150, New York: Society of Automotive Engineers, Inc., 1971.

2. Stodola, H., Steam and Gas Turbines, Vol. 1. McGraw-Hill Book Co., Inc., New York, 1927.

3. Gilbert, R. R., et al., Flywheel Feasibility Study and Demonstration, Final Report to Environmental Protection Agency/Air Pollution Control Office, under contract EHS 70-104, April 30, 1971.

Table 1.   Flywheel shape factors for various geometries

Flywheel Geometry	Shape Factor K_S*
Constant-stress disc (OD ⟶ ∞)	1.00
Modified constant-stress disc (typical)	0.931
Truncated conical disc	0.806
Flat unpierced disc	0.606
Thin rim (ID/OD ⟶ 1.0)	0.500
Shaped bar (OD ⟶ ∞)	0.500
Rim with web (typical)	0.400
Single filament (about transverse axis)	0.333
Flat pierced disc	0.305

*From Ref. 1.

Table 2. Flywheel geometry and stress distribution

FLYWHEEL PARAMETERS

```
SPEED ----------------------- 1382 RAD/SEC
MATERIAL DENSITY ------------ .285 LBS/CU-IN
POISSONS RATIO -------------- .30
YOUNGS MODULUS -------------- 30000.0E+03
TEMP. EXP. COEFFICIENT ------ 7300.0E-09
TOTAL TEMP. DIFFERENCE ------ .0 DEG-F
OUTSIDE RADIUS -------------- 21.0000 INCHES
```

FLYWHEEL DESIGN FACTORS

```
MEAN TANGENTIAL STRESS ------ 108721 PSI
MOMENT OF INERTIA ----------- 400.453 LB-IN-SEC+2
KINETIC ENERGY -------------- 382417805 IN-LBS
                             12.0022 KWH
WEIGHT ---------------------- 1062.41 LB
ENERGY DENSITY -------------- 359954.08 IN-LBS/LB
                             11.3 WH/LB
SHAPE FACTOR ---------------- .9280
RADIAL GROWTH --------------- .463714E-01 INCHES
```

RADIUS (IN)	THICKNESS (IN)	TEMPERATURE (DEG-F)	TANGENTIAL STRESS (PSI)	RADIAL STRESS (PSI)
21.0000	1.2658	.0	66242	0
20.5000	1.2658	.0	72139	13118
20.0000	1.2658	.0	77789	86025
19.5000	1.2658	.0	83184	38725
19.0000	1.2658	.0	88314	51240
18.5000	1.2658	.0	93168	63569
18.0000	1.2658	.0	97734	75727
17.5000	1.2658	.0	101999	87728
17.0000	1.2658	.0	105946	99589
16.5000	1.3466	.0	107729	104940
16.0000	1.4914	.0	108023	105571
15.5000	1.6467	.0	108285	106128
15.0000	1.8124	.0	108519	106621
14.5000	1.9885	.0	108729	107058
14.0000	2.1748	.0	108917	107446
13.5000	2.3712	.0	109086	107791
13.0000	2.5772	.0	109238	108099
12.5000	2.7923	.0	109375	108373
12.0000	3.0158	.0	109499	108619
11.5000	3.2471	.0	109610	108838
11.0000	3.4850	.0	109711	109035
10.5000	3.7287	.0	109802	109211
10.0000	3.9769	.0	109885	109369
9.5000	4.2283	.0	109959	109511
9.0000	4.4815	.0	110027	109639
8.5000	4.7350	.0	110088	109753
8.0000	4.9870	.0	110144	109856
7.5000	5.2360	.0	110194	109948
7.0000	5.4802	.0	110239	110031
6.5000	5.7178	.0	110279	110104
6.0000	5.9470	.0	110316	110170
5.5000	6.1659	.0	110348	110229
5.0000	6.3728	.0	110377	110281
4.5000	6.5660	.0	110403	110326
4.0000	6.7438	.0	110425	110366
3.5000	6.9047	.0	110444	110400
3.0000	7.0472	.0	110461	110429
2.5000	7.1701	.0	110474	110454
2.0000	7.2722	.0	110484	110474
1.5000	7.3527	.0	110491	110490
1.0000	7.4107	.0	110493	110505
.5000	7.4457	.0	110465	110543
.0000	7.4574	.0		
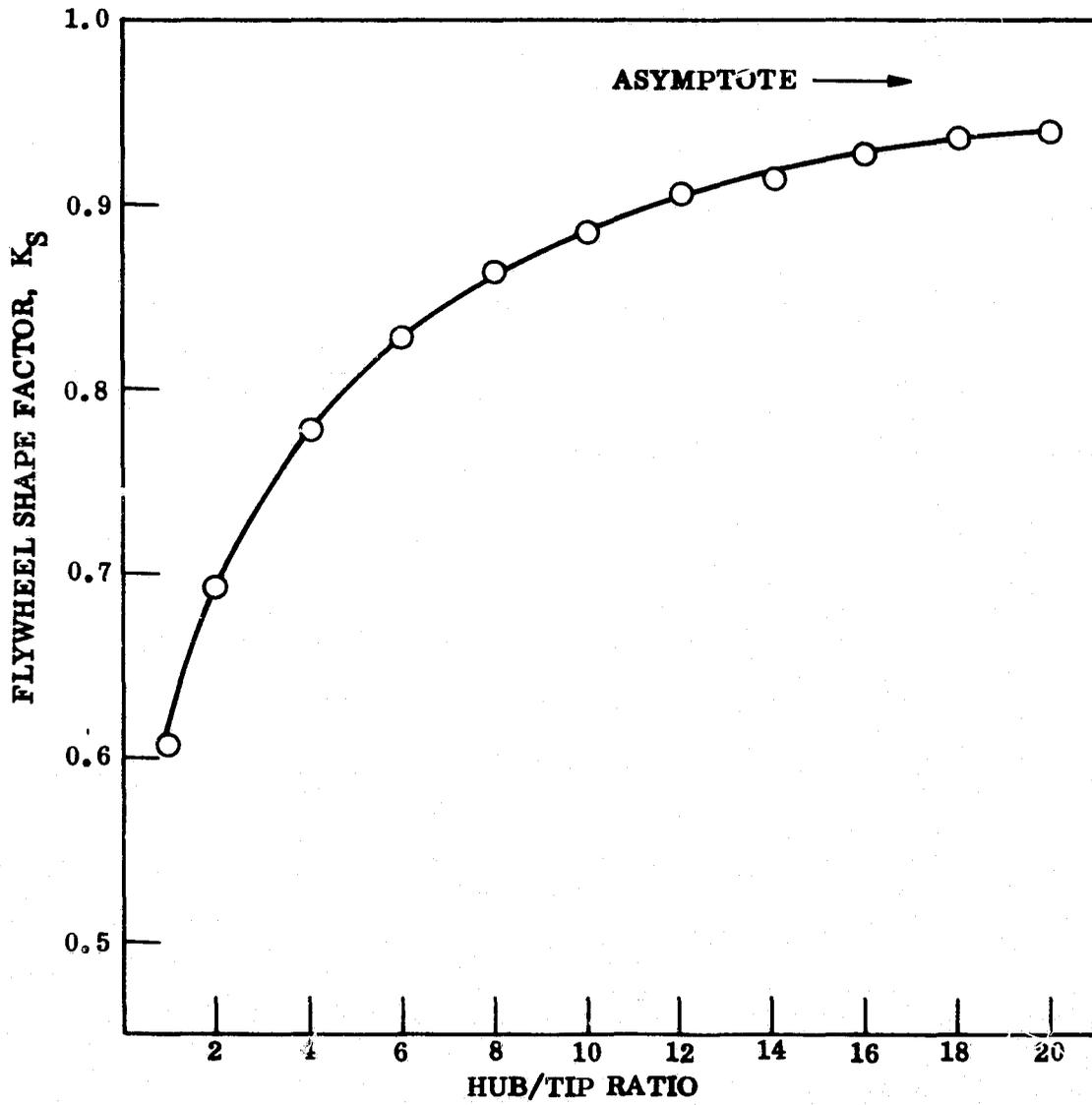
Fig. 1. Flywheel shape factor vs. flywheel hub/tip thickness ratio
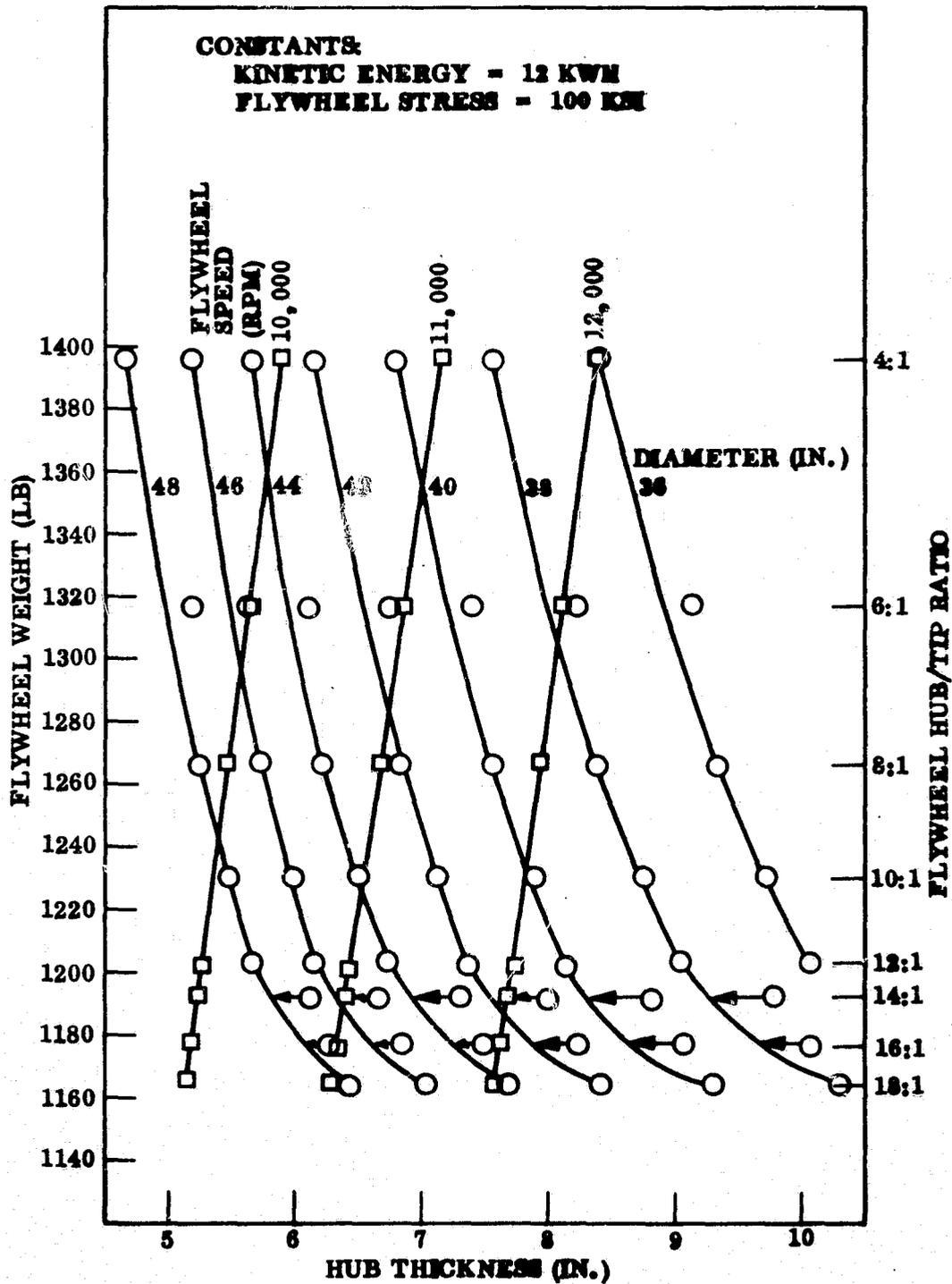
Fig. 2.   Flywheel weight and hub/tip ratio vs. hub thickness
for several flywheel diameters
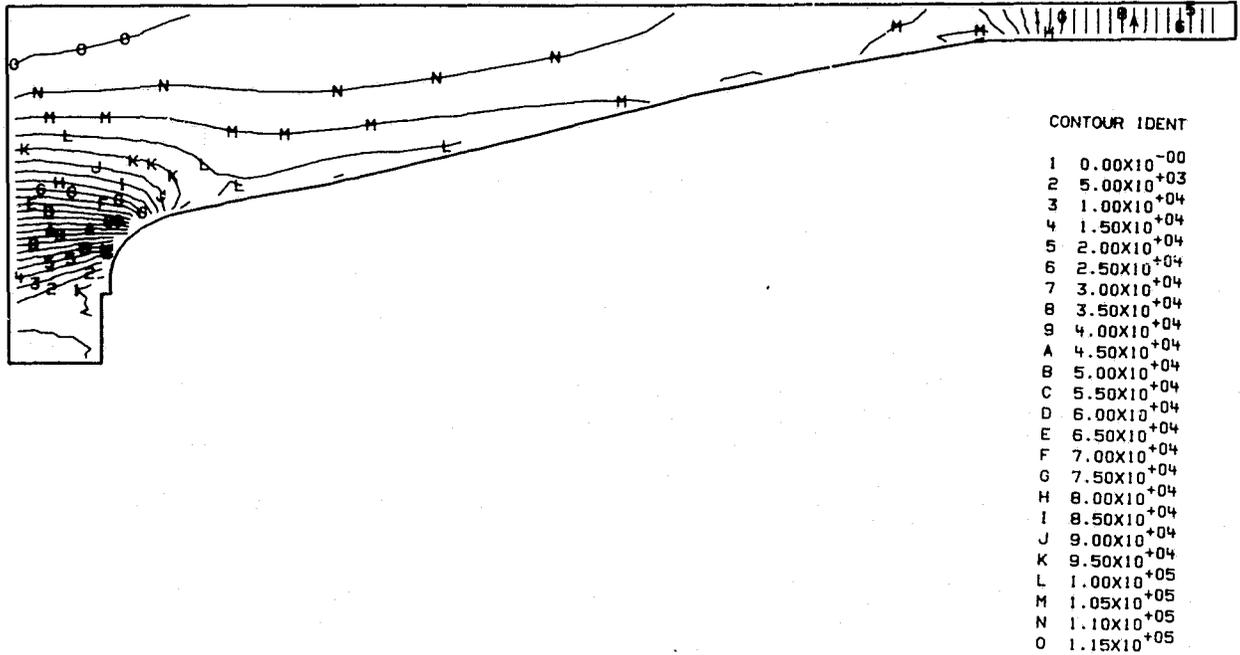
Fig. 3.   Contour map of R-stress
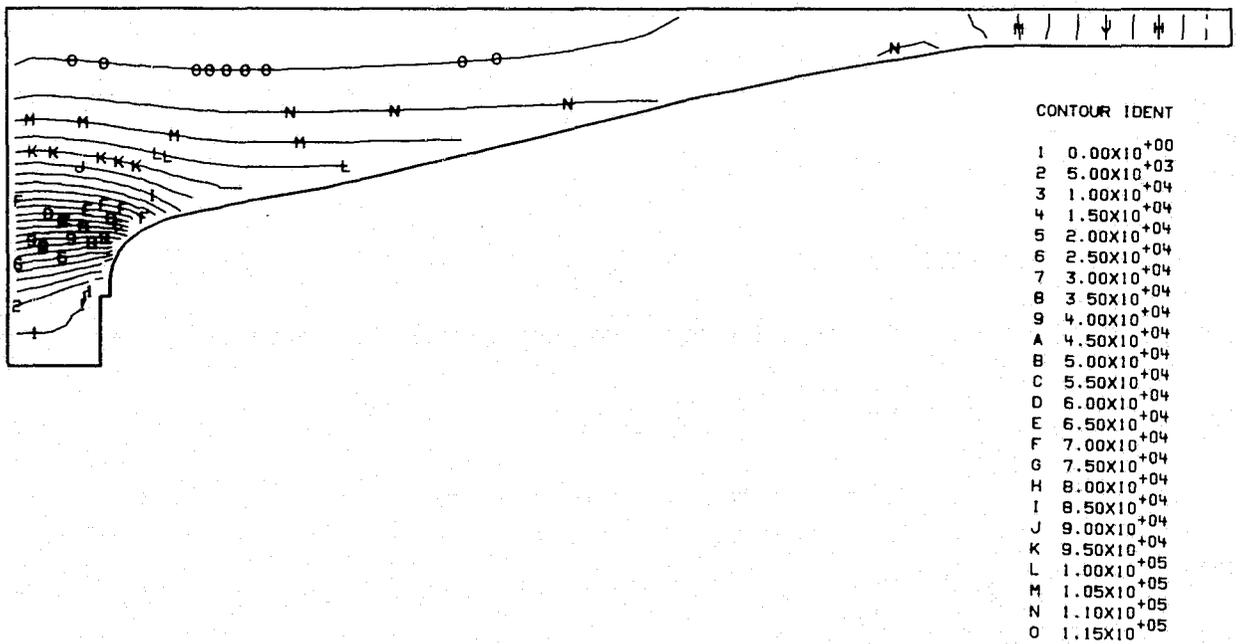

Fig. 4.   Contour map of T-stress
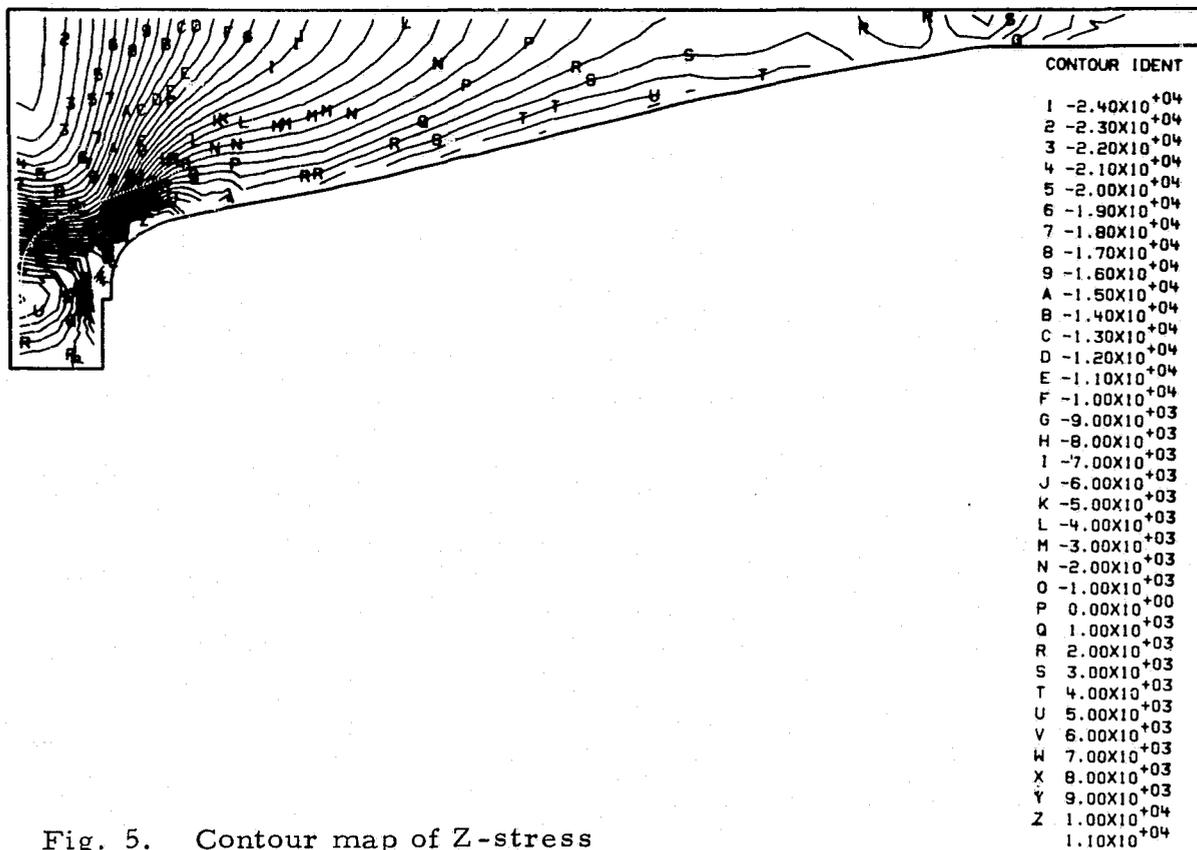
Fig. 5.   Contour map of Z-stress
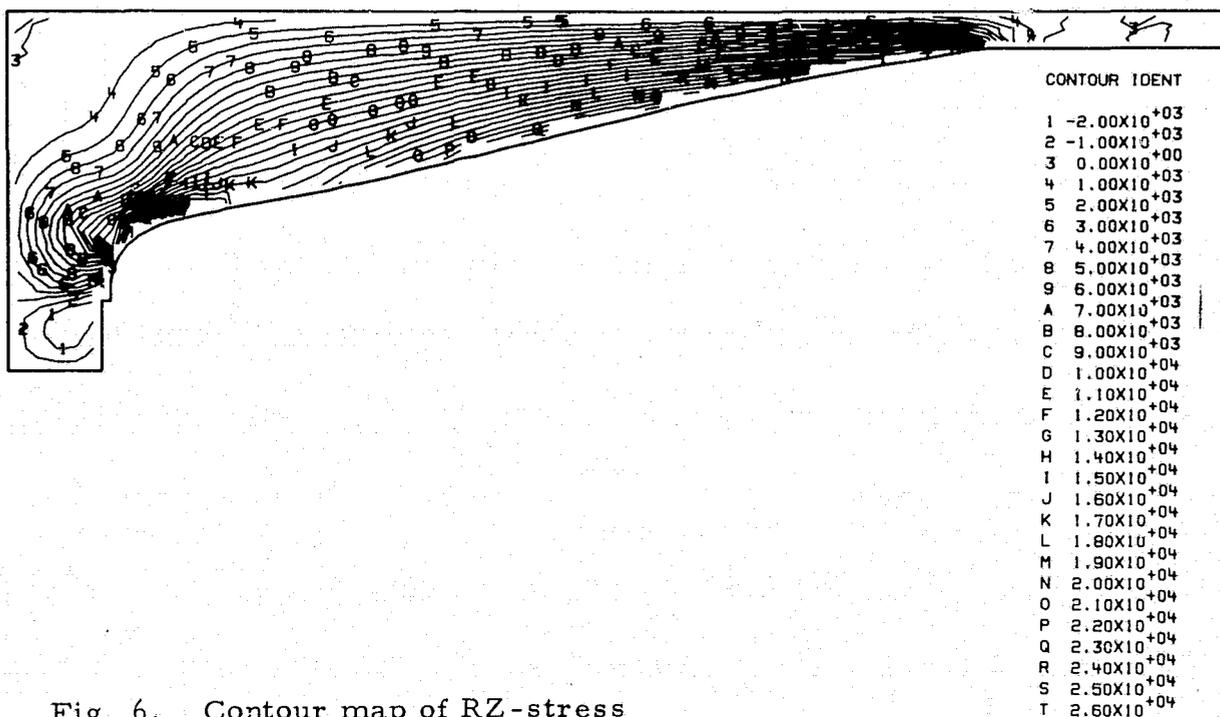
Fig. 6.   Contour map of RZ-stress
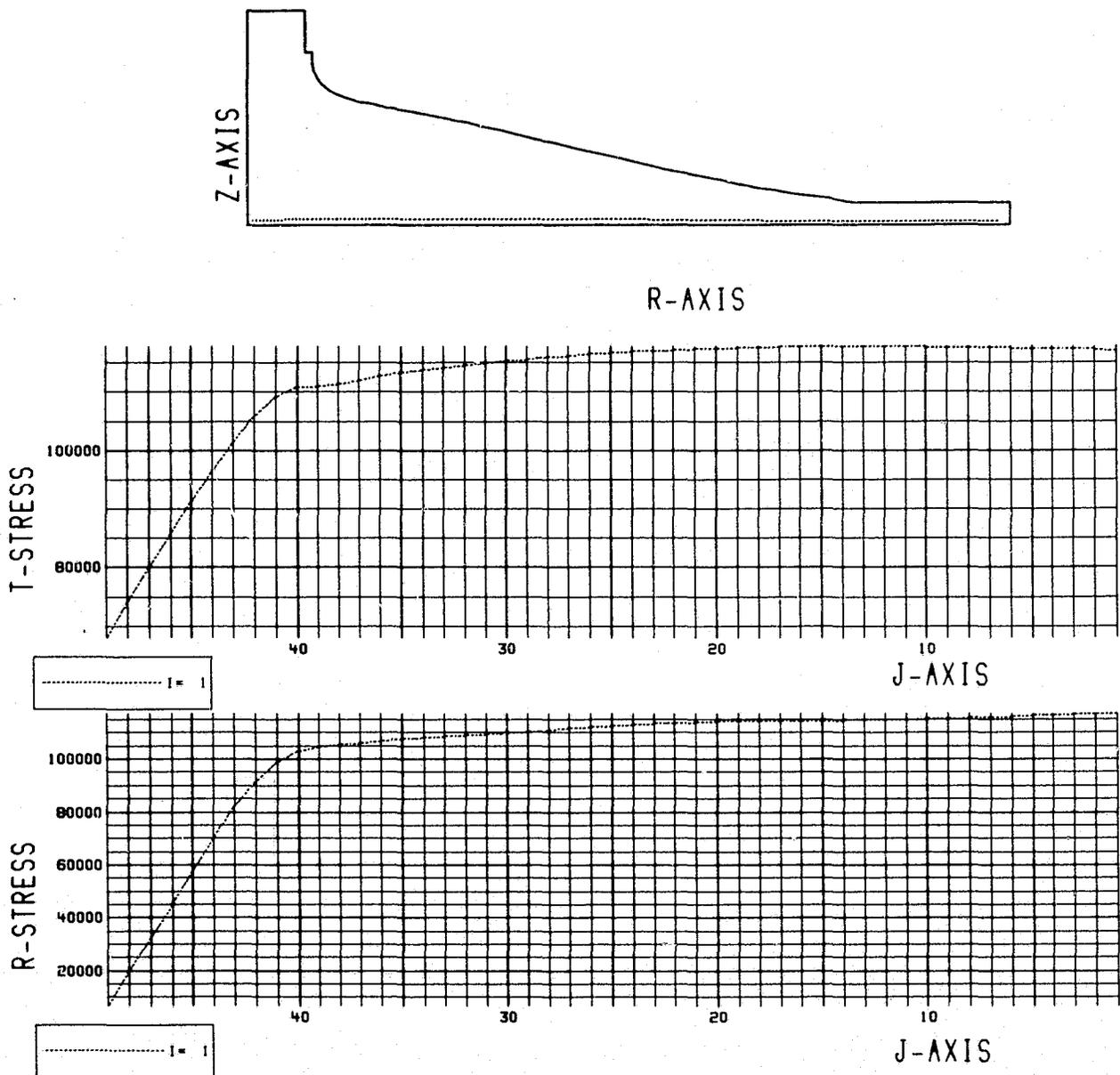
Fig. 7. Radial and tangential stress distribution
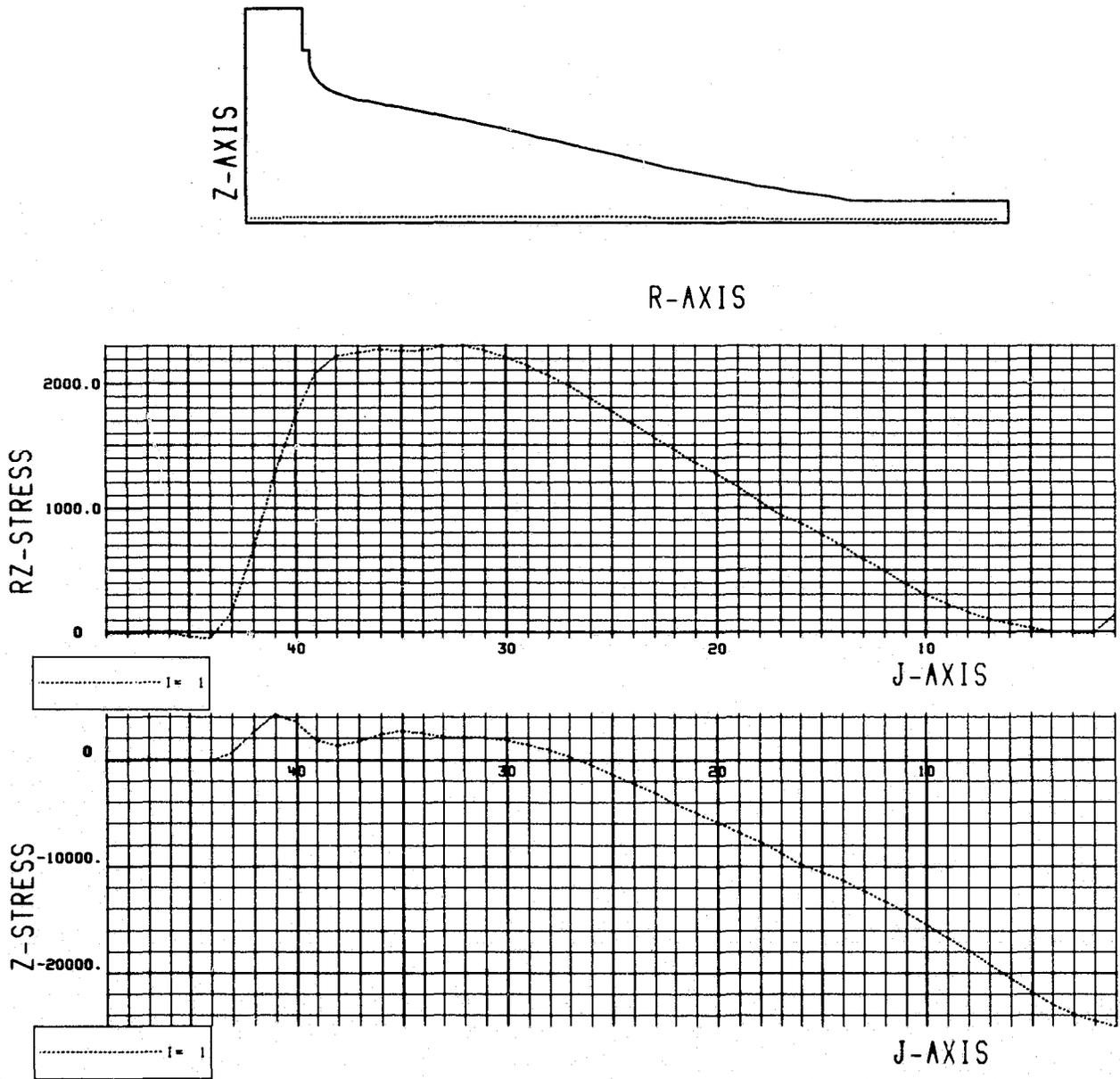
Fig. 8. Axial stress and axial shear stress distribution

DESIGN PRINCIPLES OF A ROTATING
MEDIUM SPEED MECHANISM

by: R.G. Hostenkamp, Dr.E.Achtermann (Dornier System) and Dr.R.H.Bentall
(European Space Technology Centre)

SUMMARY

Design principles of a medium speed mechanism (MSM) are presented, including discussion on the relative merits of Beryllium and Aluminium as structural materials. Rotating at a speed of 60 rpm, the application envisaged for the MSM was as a despin bearing for the despun platform or despun antenna of a spin stabilised satellite.

The MSM has been built and tested to qualification level and is currently undergoing real time life testing at the European Space Tribology Laboratory.

INTRODUCTION

In 1971/72 the European Space Technology Centre commenced its supporting technology programme for the development of critical applications spacecraft components. At that time the satisfactory performance of the despin configured spacecraft had been demonstrated for satellite missions with medium power requirements. However a critical item of equipment in this configuration was the despin mechanism itself, both from the point of view of its own status as a single point failure and its effect on the stability of the satellite. Accordingly, Dornier System was awarded an ESTEC contract for the design and construction of a "medium speed mechanism" (MSM) capable of operating at despin speeds and suitable for use with either a despun antenna or platform. A central part of the design study was the choice of structural material, considerable thought being given to the use of Beryllium (Ref. 1).

The performance of the MSM and the environmental test requirements are summarised in Tables 1 to 3.

Table 1: MSM PERFORMANCE DATA

DESIGN LIFE:	$\geqslant$7 years
SIZE:	375mm long x 214mm dia. (hosing flange) 35mm bore
MASS:	10.7 kg
NOMINAL SPEED:	60 rpm (30 rpm to 150 rpm range)
POWER CONSUMPTION AT 20°C:	1 Watt (28V DC supply)
WOBBLE ANGLE:	7 arc seconds
RADIAL STIFFNESS:	1.9×10^5 Nm/rad
STATIC LOAD CAPACITY:	$>$1.5 kN
POWER TRANSFER:	4 x 1.25A channels giving 300 W at 60 V
SLIP RING NOISE:	$<$50 mV/A
SIGNAL TRANSFER:	5 channels 2 to 60 kHz at peak signal level of 15 V (see Fig. 5)
CROSS TALK:	-40 dB

Table 2:   MECHANICAL TEST ENVIRONMENT (at Dornier System)

The following were applied in all three orthogonal directions.

Static: + 20.000 N for 5 minutes
Contant Acceleration: + 18 g   for 5 minutes
Sinusoidal Vibration: 5 to 15 · Hz   9 mm   o - p displacement
                                15 to 200 Hz   8 g   o - p acceleraction
                                (2 octaves/minute)
Random Vibration: 25 to 100 Hz 3 dB/oct increasing to $0.2g^2$/Hz
                                100 to 2000 Hz $0.2g^2$/Hz flat (for 5 minutes)
                                notching to zero between 140 and 200 Hz for
                                lateral vibration
Pyrotechnic Test: all pyrotechnics fired twice
Ambient Integration: 50 hrs. operation with 150 kg and 150 kgm^2
                                inertia attached to shaft flange.

Table 3:   THERMAL VACUUM TEST ENVIRONMENT (at ESTL)

T_1 = Shaft-Flange, T_2 = Housing-Flange mounting and environment

Test No.	Duration (hrs)	T_1 °C	T_2 °C
1	8	+ 60	+ 50
2	8	+ 60	- 10
3	8	- 20	- 10
4	8	- 2	- 10
5[+]	72 runs and 100 runs	-5 to -17 to -5	+ 20
6[+]	72 runs and 100 runs	-45 to -2 to +45	+ 20

[+] in simulation of eclipse

DESIGN DERIVATION

Configuration

A fully modular concept (off-load system, bearings, motor, signals, power
slip rings) was rejected because of the inherent penalties of mass and length
and the limited available separation of the bearings, which prevented the
achievement of a required 20 arc second wobble angle. The bearing separation
chosen was 200 mm and the space between was utilized for the location of signal
transformers and motor/resolver location. A speed pick-up with a housing-
mounted carrier for redundant Gallium Arsenide photo diodes and a shaft-
borne slotted disc were arranged outside that space (Fig. 1). This module
therefore contained all the elements required for a despin antenna, including
a 35 mm bore for waveguide location.

The power slip rings, which would be required for the despun platform con-
figuration, were, however, contained in a separate module, outside the bear-
ing compartment and utilised a smaller diameter shaft for low friction and
long life.

The brushless D.C. motor and the contactless signal transformers were chosen so as to eliminate the possibility of wear debris contaminating the bearings. ABEC 9 angular contact ball bearings were used, made from cold temperature stabilised, consumable electrode vacuum melted 52100 steel.

The bearing off-load was integrated into the MSM shaft and housing flanges in order to maintain a direct load path between the spun and despun structures. Off-loading is achieved by the axial displacement of the shaft flange against a conical seating by the jamming action of a flat headed pin. Release is effected by two pyrotechnics (one being redundant) moving an intervening blocking ring which permits the pins to retract. Note that Fig. 1 is split along the MSM centreline showing the free and off-loaded configuration.

Extreme care in construction was necessary in the region of the central flange due to the tight wobble requirement. The eccentricity of the flange was measured and marked so that on assembly, the most favourable alignment could be attained.

The determination of wobble angle depends upon which part of the MSM (shaft or housing) is despun. References 2,3 and 4 discuss the effects of despin bearings on the stability of despun satellites, affirming that it is preferable that damping processes occur on the despun rather than the spinning structures. It is clear that the shaft, being inherently more compliant than the housing, should be despun for the achievement of maximum stiffness (see also Ref. 5). For this reason also the flexible bearing mounting is favourably placed on the shaft. Calculations gave the maximum shaft wobble as 17 arc seconds (measured later as 7 arc seconds).

Thermal Design

Bearing preload is maintained and limited by use of a radially stiff, axially compliant bearing mounting. The use of sliding fits to give tolerance to thermal expansion effects is now thoroughly discredited for despin mechanisms, both from the viewpoint of tribological failure and destabilising effects (Refs. 3 and 6).

However, problems of bearing compression due to thermal variations were not completely overcome by the use of flexible mountings especially when choosing between the light metals (Beryllium and Aluminium) necessitated by the requirements of weight optimisation. Steady state thermal model calculations yielded very similar temperature distributions for both materials. Consequently Beryllium appeared to have a slight advantage over the Aluminium due to the close match of its thermal expansion coefficient with steel. However if a temperature differential of 10°C is taken as a design case to cover transient conditions such as those occurring during eclipse the greater stiffness of the Beryllium can distort the bearing (the wall thicknesses are very similar for both Al and Be) since the fits are designed as interference fits for all of the steady state temperature cases required.

For a given bearing dimension the ratio of the contraction pressure to the radial interference $(p/\Delta r)$ permits a direct comparsion between the materials. Fig. 2 gives $p/\Delta r$ as a function of housing wall thickness for both materials. The shaded area indicates the practical range of wall thickness, consistent with stiffness requirements. It can be seen that the interference fit of an Aluminium bearing mounting can be a factor 2 or more down on that required

for Beryllium for the same compressive stress.

This advantage of Aluminium is offset by the greater influence of temperature gradients on the Aluminium/Steel fit. The worst temperature condition occurs when the shaft is hotter than the housing, when the outer housing (relatively) compresses the outer ring and the shaft (relatively) extends the inner ring. This thermal state is made less severe by the consequent implied condition that the bearing area is at a medium, near ambient temperature and thus that local thermal expansions are low. Further radial mismatches of this type are compensated by an enforced slight change in contact angle. At the lower bearing Beryllium is superior to Aluminium because the inner race is decoupled from the shaft by the flexible steel bellows mounting. However there the magnitude of the mismatch is less severe, contact angle variation being only about 1/3 of that of the upper bearing.

In order to further reduce the effect of radial thermal mismatch the outer bearing mount was cantilevered and tooth profiled to reduce its stiffness and tendency to distort the bearing.

Axial thermal mismatch is clearly less for Beryllium than Aluminium, but here it is a matter of design choice between reduced preload variation and increased stiffness of the flexible bearing mounting.

Structural Design

The stability of a despun satellite is critically dependent on the radial stiffness of its bearing (see Refs. 5 and 6). A figure of 5×10^4 Nm/rad has been taken as an acceptable figure.

Fig.3 gives the structural and deformation models from which the stiffness is derived. At the lower bearing, the deflections of shaft, housing, and bearing plus bellows are given by f_S, f_H and f_C respectively. In addition to their radial deflection the bellows are subjected to an angular deflection β so that they exert a resistive moment $M_B = \phi\beta$, which results in a deflection f_m. (ϕ is the angular stiffness of the bellows.)

The total deflection is therefore

$$f = f_S + f_H + f_C - f_M$$

Using the relationship $\alpha = f/l$, one can derive the relationship for the radial stiffness:

$$\phi_R = \frac{6EI \, C_L C_B \, \ell^2}{2 \, \ell^3 \, (1+1/K) C_L C_B + 6EI (C_L + C_B) - 3\phi \, \ell \, (C_L + C_B)}$$

were the stiffness of the shaft is EI and that of the housing is K (EI).

This relationship permits the examination of the influences of various parameters on the stiffness. Fig. 4 shows the angular stiffness as a function of bearing distance for different structural materials. The benefit of Beryllium is clearly demonstrated as are the advantages of a hybrid structure (Be-shaft, Al-housing). Alignment dictates indicated a bearing distance of 200 mm where the stiffness of the all Aluminium construction was sufficient.

Although both thermal and structural analyses showed the technical superiority of Beryllium, the design and spacecraft criteria were met adequately

by an Aluminium structure and this was chosen in place of the more costly and fragile alternative.

Lubrication System

Liquid lubrication for the bearings was chosen as the most reliable means of long life lubrication. At that time the solid lubricant systems based on metal films and mechanically bonded MoS_2 systems had not proved their reliability. The choice lay between the lubricants F50, Apiezon C and BP110.

Fig. 6 shows the results of film thickness calculations for these oils, covering the range of temepratures expected. The scatter in film thickness (vertical spread) is caused by the application of two film thickness formulas, based on point load and line load (Ref. 7).

The lower oil film thickness for the F50 led to the rejection of that lubricant and the BP 110 was chosen after consideration of the calculated friction torques, Fig. 7. Bearing friction was calculated from the formula given in Ref. 8. This friction characteristic is not representative at low temperatures since oil starvation results in a reduction of torque, albeit at the expense of oil film thickness.

The lubricant system chosen consisted therefore of 5 % BP2110 grease in the bearing tracks with BP110 oil impregnated in the phenolic cages and nylasint. These lubricants are described in Ref. 9. BP110 is a fine cut mineral oil, and is modified to the grease, BP2110, by the introduction of an oleophilic graphite - lead composite. The cages were boiled in chloroform and outgassed at 10^{-2} Torr for 2 hours at 90°C to disperse included monomers and impregnated with BP110 at 70°C and 10^{-2} Torr. This resulted in about 0.25 gms of oil per cage, an effective porosity of about 2.3 %. A similar cleaning and impregnation process on the reservoirs gave about 3.3 gms/reservoir (about 25 %).

With the intention of providing each bearing with its own enclosed lubrication system, the reservoirs were placed close to each bearing, one on the shaft and one on the housing to ensure that at least one reservoir was always at a higher temperature than the bearing.Narrow clearances relative to the moving counterpart for the Aluminium backed reservoirs and carefully applied anticreep barriers (Tillan M2, which is derived from FX 706 of 3M Company) were used to limit the loss of oil from the immediate bearing vicinity. The materials used in the slip ring module were $AgCuMoS_2$ compacts against a silver ring, a combination that has been extensively tested (Ref.10). Brush contact pressure was maintained by a soft spring ensuring uniform contact conditions throughout life.

TESTING PROGRAMME

The MSM successfully completed the tests specified in Tables 2 and 3, which were established at qualifiaction level (Ref. 11). The tests were not without incident, however: the MSM slip ring module required refurbishment after its shaft broke during vibration testing and failure occurred during an initial series of thermal vacuum tests. This latter failure was due to a tolerance being disregarded during the manufacture of the upper molecular seal and escaping detection during inspection. This caused jamming of the MSM during setting up of test 3 of Table 3 with the shaft temperature 32°C and housing temperature 8°C. This was a disturbing experience in view of the careful attention that had been placed on the thermal design of the MSM and is significant support for thermal vacuum differential temperature

testing at acceptance level (build standard), a test philosophy that could well have been applied with benefits for past despin mechansim programmes.

The MSM is now commencing its real time life test at the European Space Tribology Laboratory. The test will consist of alternating periods of six months with different levels of thermal gradient applied across the mechansim. Simulated eclipse testing will be performed at the end of each six month period.

REFERENCES

1. R.G. Hostenkamp et al.–Study Report of a Medium Speed Mechanism – Study Report of ESTEC Contract 2566 (1972).

2. A.J. Iorillo – Hughes Gyrostat System – Proceedings of Symposium on Altitude Stabilization and Control of De-spin spacecraft, Nov. 1967.

3. C.R. Johnson – Tacsat 1 Nutation Dynamics–AIAA paper No. 70-455 (1970).

4. P.Y. Willems – Effect of Bearing Flexibility on Dual-Spin Satellite Attitude Stability–J. Spacecraft and Rockets, Vol.9, No. 8, August 1972.

5. British Aircraft Corporation Dual Spin Stability Study – Phase II Final Report for ESTEC Contract 1030.

6. F.A. Glassow – Despin Bearing Technology and Applications for Communications Satellites–AIAA Paper No. 70-459 (1970).

7. C.M. Taylor – Calculation of Elastohydrodynamic Film Thickness in Ball Bearings Project Report for ESTEC Contract 1110 (1971).

8. T.A. Harris,– Rolling Bearing Anylysis – John Wiley and Sons Inc. (1966).

9. G.C. Friend, A.J.Groszek, W.A. Ware, and M.Warwick – Development of New Space Lubricants – European Tribology Symposium, Frascati, April 1975.

10. K.R.Dalley and P.J. O'Donnell – Design and Performance of Electrical Contacts for Use in Ultrahigh Vacuum – European Space Tribology Symposium, Frascati–April 1975.

11. A.I. Walton and D.A. Appleton – Thermal Vacuum Qualification Test on a Dornier Medium Speed Despin Mechanism – ESA (ESTL) 20 (1976).

Fig. 1 Medium Speed Mechanism

Labels (reading around the figure):

- Pyrotechnic
- Electronics (for Tests only)
- Radiator Cone (for Tests only)
- Housing Flange
- Locking Pin
- Resolver
- Brushless DC Motor
- Inductive Signal Transmitters
- Venting Valve
- Labyrinth Seal
- Power Slip Rings
- Optical Position & Rate Pick up
- Preload Flexure
- Oil Reservoirs
- Upper Bearing
- Labyrinth Seal
- Shaft Flange
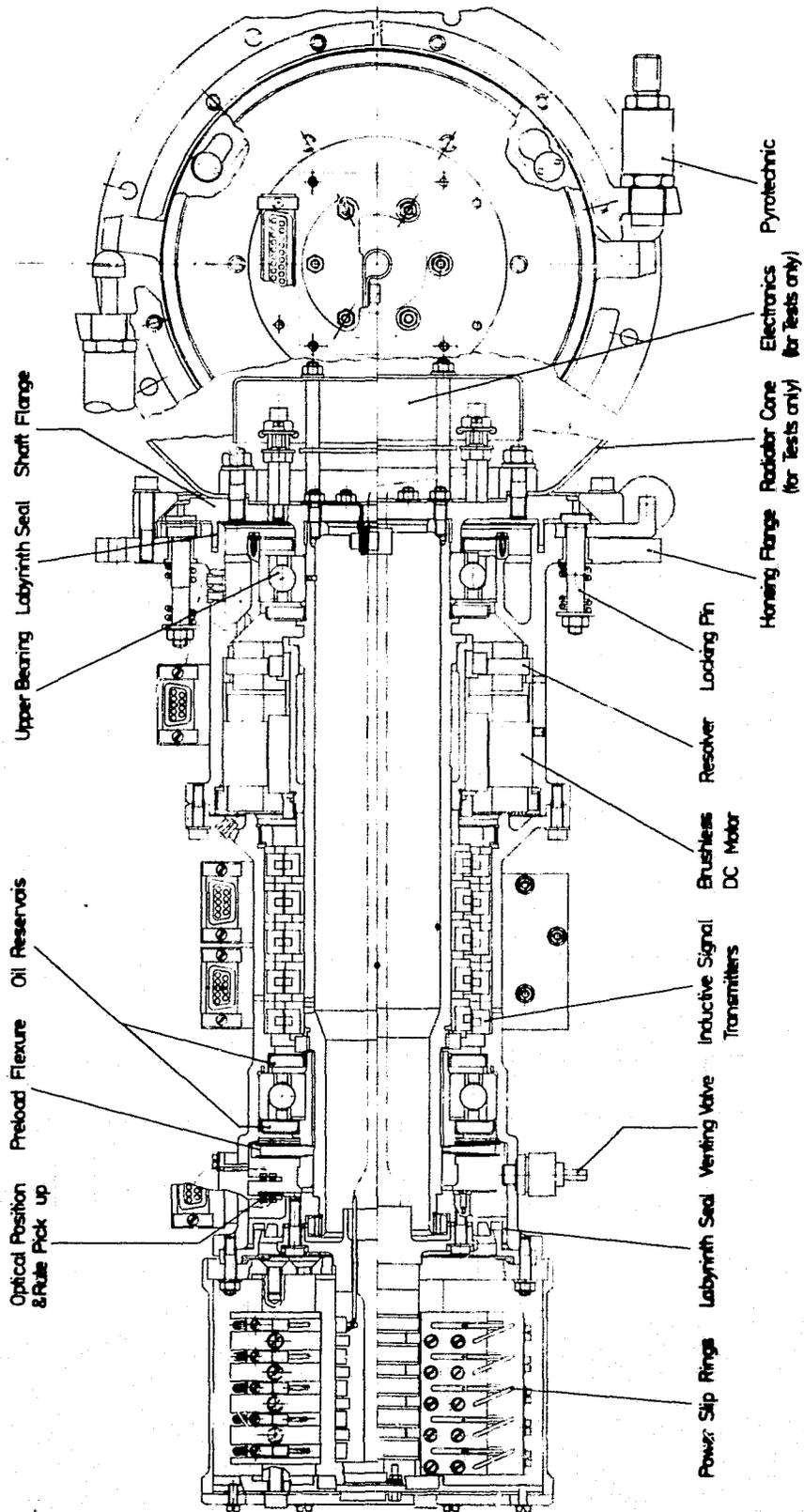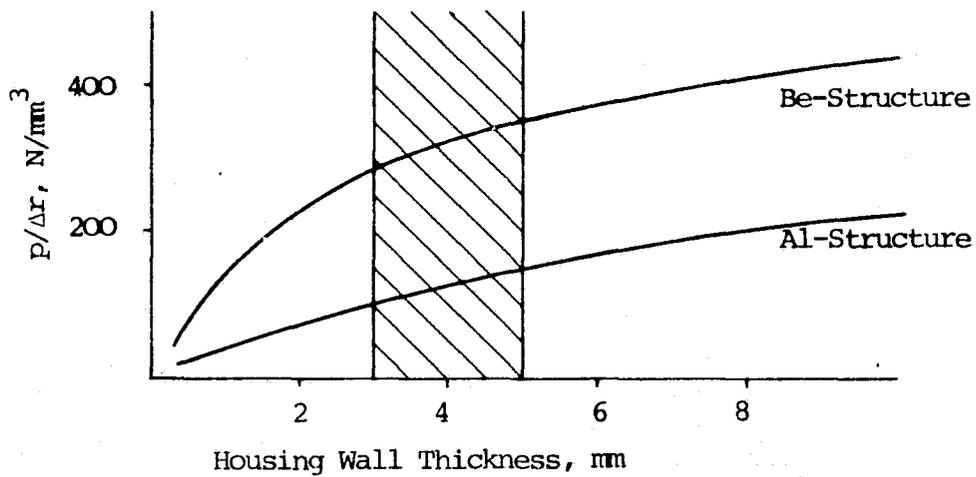
Fig. 2   Ratio of contraction pressure to interference p/Δr vs housing wall thickness
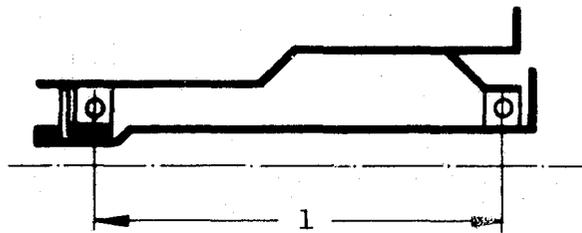
3.1 Structural Model
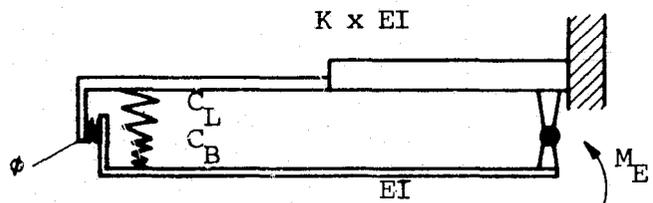
3.2 Stiffness Model
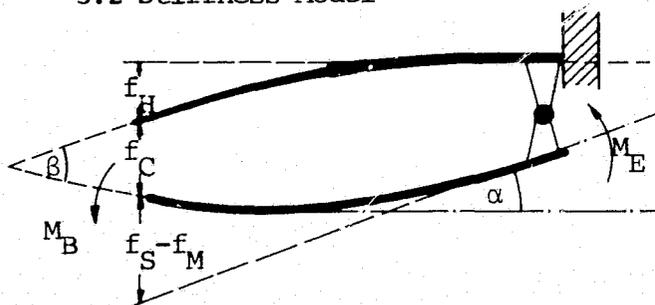
3.3 Elastic lines and deflections

Fig. 3   MSM stiffness model
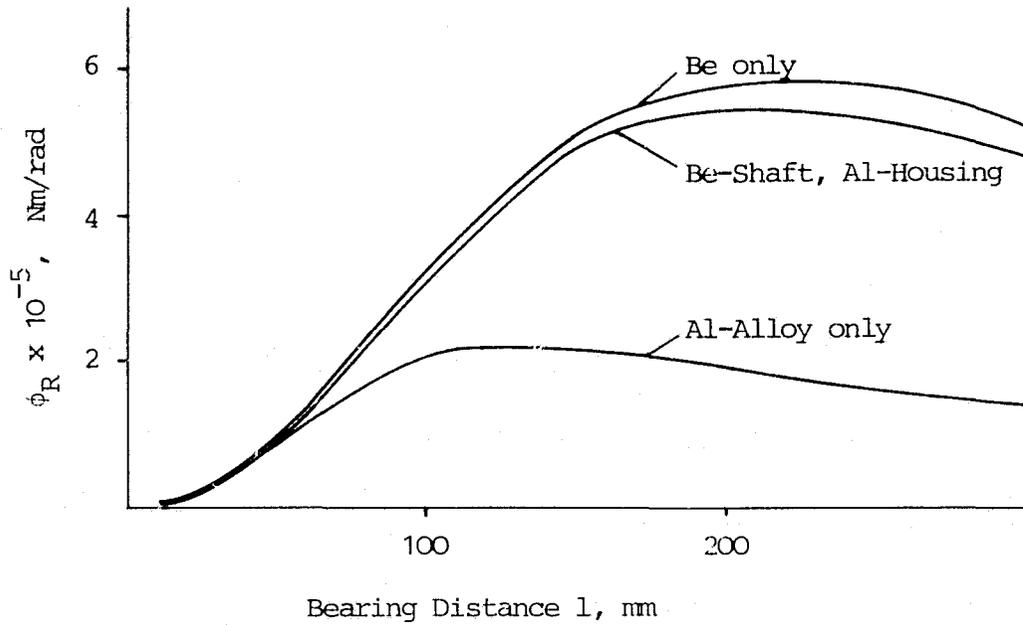
Fig. 4   Angular stiffness ϕ_R vs bearing distance for
         different structural materials
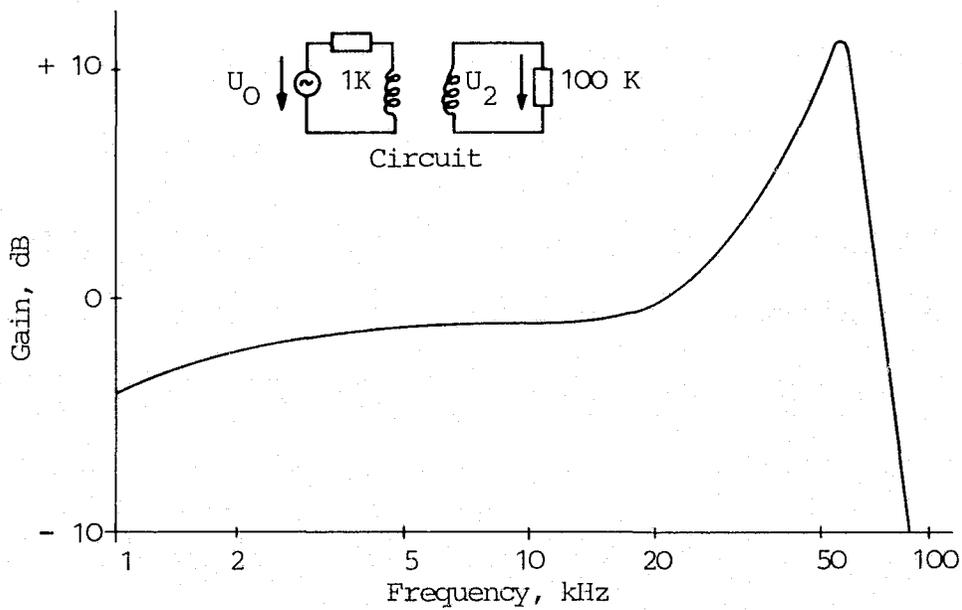
Fig. 5   Gain of inductive signal transmitters vs frequency

Temperature Range: 0 to 50°C
Bearing: 6011 GMN 55/90/18 (18 Balls)
Combined Surface Roughness: 0,12µm
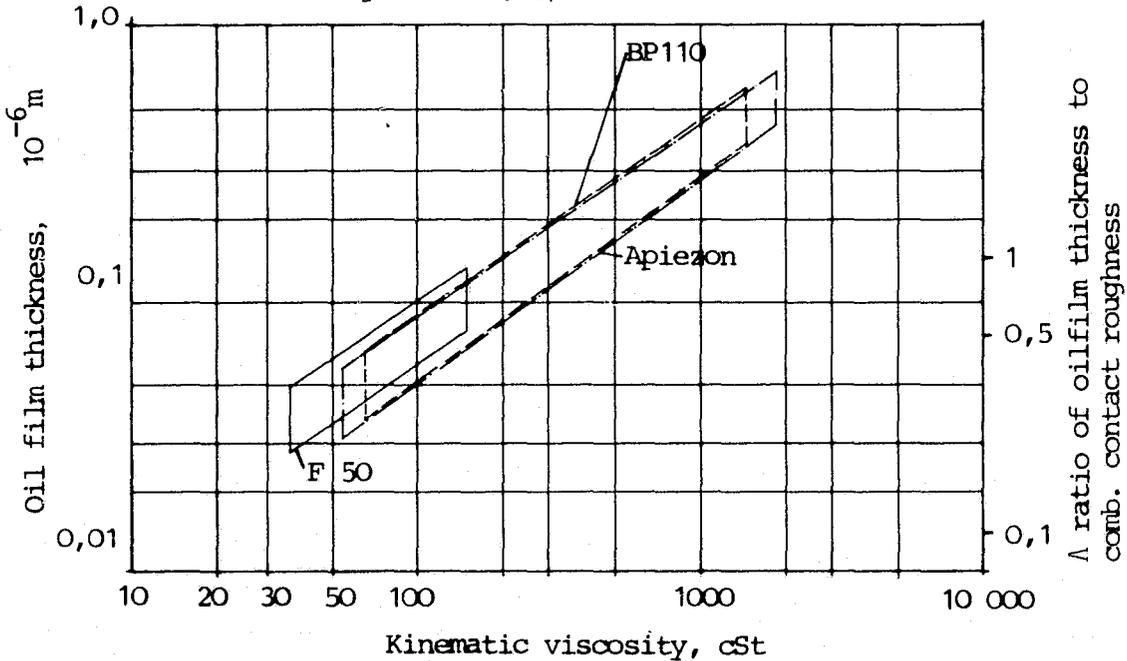
Fig. 6   EHD oil film thickness at 60 rpm
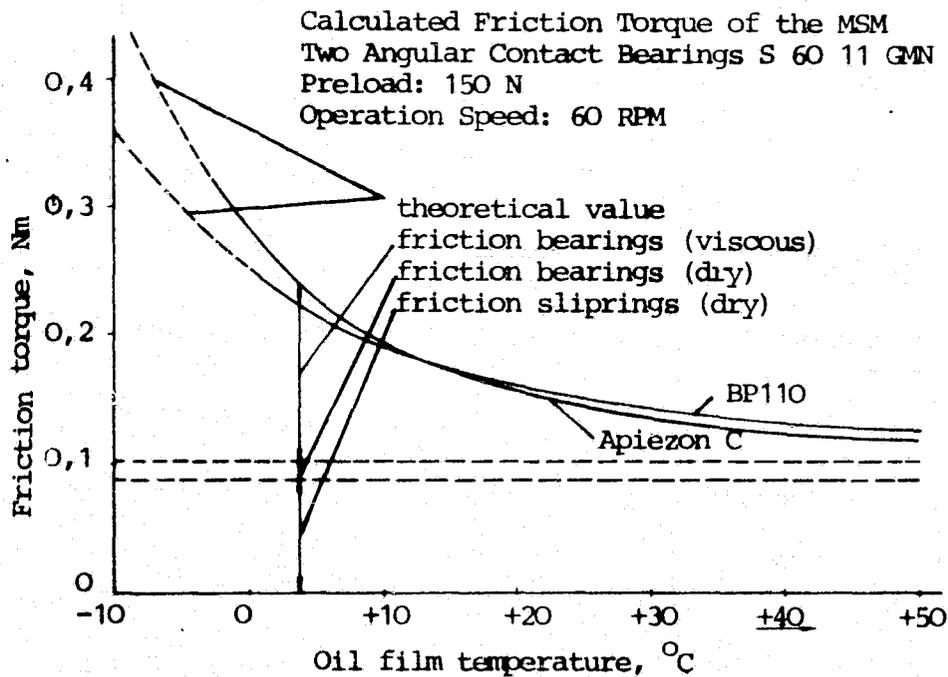
Fig. 7   Calculated friction torque of the MSM at 60 rpm

ROTARY MECHANISM FOR WIND TUNNEL

STALL/SPIN STUDIES

By Ronald E. Mancini, Dennis S. Matsuhiro,
and Wilbur C. Vallotton

NASA Ames Research Center

ABSTRACT

The critical problem of stall/spin characteristics of high performance aircraft and the need for experimental data in this area are reviewed. A rotary mechanism for obtaining this aerodynamic data in a conventional wind tunnel is presented. The intricacies of the drive systems and the articulation available through such a mechanism are described.

INTRODUCTION

With the advent of higher-performance aircraft, a great deal of research effort has been expended to improve the aircraft's performance capabilities and safety for the crew. One area of increased concern is in the stall/spin characteristics associated with highly swept, low aspect ratio, high angle-of-attack capabilities of current and future aircraft designs. A yearly toll of aircraft and human lives can be directly attributed to loss of attitude control resulting from a stall/spin entered during a high performance maneuver. With new military aircraft being designed for expanded flight envelopes that require even higher angles-of-attack for routine flights, a method of predicting the full-scale spin modes and recovery techniques is needed.

For years researchers have desired a method of obtaining experimental wind tunnel data from which a rigorous analytical approach could be devised for computing the spin characteristics of a given aircraft design. Early attempts at this approach included the building of a free-spin vertical tunnel facility at NASA Langley Research Center. However, these facilities are greatly limited in their Reynolds and Mach number capability. Furthermore, conventional wind tunnel test techniques, where realistic Reynolds and Mach numbers can be achieved, are not sufficient to fully describe the aerodynamic characteristics of an aircraft during a spin.

SYMBOLS

α	model angle-of-attack
β	model angle of side-slip or yaw
γ	offset angle of spin axis from air stream axis
ψ	axis for model positioning
φ	axis for model positioning
Ω	spin axis
CW	counterweight axis
HP	horsepower
GPM	gallons per minute
psi	pounds per square inch
rpm	revolutions per minute

ROTARY MECHANISM FOR DATA ACQUISITION

Because of the high Reynolds number capabilities of the NASA Ames wind tunnel facilities, a concerted effort was directed into the design of a rotary balance apparatus for use in a conventional wind tunnel. Such a device would enable aerodynamic data to be obtained under the same local flow conditions as in the full scale spin. The mechanism was to be capable of providing the motions required for generating the force and moment derivatives due to coning as well as damping in both pitch and yaw. Those configurations which are important in understanding the stall/spin problem are illustrated in Figure 1.

BASIC OPERATION

The "Dynamic Stability Rig," seen in Figure 2, supports and rotates an aircraft model inside a transonic wind tunnel test section. The angle of incidence of the model with respect to the air stream can be remotely varied to a maximum of 30°. This is accomplished through rotation about a set of axes (ψ,φ) which pass through the center of the model and intersect the spin axis (Ω). These axes are defined in Figure 2. By proper rotation about the ψ and φ axes, a particular combination of angle-of-attack (α) and angle of side-slip or yaw (β) may be obtained. The envelope of possible α-β orientations consists of discrete positions within a cone whose apex angle is 60°. This limitation of discrete rather than continuous positions will be discussed later. Using a rear-mounted straight sting model, the maximum α or β is ±30°.

However, by use of bent stings and top mounted models, this envelope can be expanded to meet the desired range in α of -5° to +100°.

Changes in model orientations will be made remotely and prior to spinning the balance in the airstream. The model position is set and the counterweight assembly (see Figure 3) is driven to a position which compensates for the unbalanced static moment about the spin axis (Ω). The entire apparatus is then rotated in the air stream at a rate from 0 to 400 rpm. This high rotation rate, much larger than the full scale spin, is a requirement resulting from one of the modeling parameters in which spin rate is inversely related to model size. For pure coning motion, the spin axis (Ω) of the mechanism is aligned with the tunnel stream axis. To obtain the moments resulting from damping in pitch and yaw, the spin axis (Ω) is slightly offset from the air stream axis by pitching the rotary balance assembly with the tunnel model-support system. This offset is shown as angle γ in Figure 3.

DRIVE ASSEMBLIES

The main drive for the spin rotation is powered by a servo valve controlled hydraulic motor operating a pinion and gear assembly (Figure 2). The motor is capable of producing 64 HP at approximately 1500 psi and 70 GPM.

The overall designs of the drive assemblies for the ψ, ϕ, and counterweight (CW) axes are illustrated in Figures 4 and 6. Figures 5 and 7 show the details of the assemblies. All three drives are similar in design. Rotation is powered by small D.C. electric motors incorporating planetary gear reducers and brakes. A roller chain couples a sprocket mounted on the motor output shaft to the sprocket-and-wave generator assembly of a harmonic drive speed reducer. The output of the harmonic drive is, in turn, mounted to the main shafts of the ψ, ϕ, and CW axes. Because of the large gear reductions involved, rotation rate about all three axes is approximately 30° per minute. All assemblies incorporate solid bearings for space saving considerations.

The CW and ψ drives include a sliding spline-lock mechanism. Centrifugal accelerations at high spin rates acting on particular orientations of the counterweight (CW) or the ψ-ϕ assembly-model combination can result in extremely high moments about the ψ and CW axes. A maximum torque of 70,000 inch-pounds is possible, this being several times the rated static capacity (10,000 inch-pounds) of the harmonic drive units. The remotely operated spline-locks relieve this load on the units by transmitting this torque directly to the main housings (see Figure 5). An internal threaded shaft, rotated by a chain - DC motor drive, operates the spline to engage or disengage the lock of the main shaft to the housing. Indexing for spline engagement is determined by a cam-switch position detector, incorporated in the main harmonic drive wave generator-sprocket assembly. Each revolution of the wave generator operates this cam-switch. The primary axis positioning device is the potentiometer coupled to the rear of the main shaft (Figure 5). When driving to a new position, the rough positioning is performed by use of the potentiometer. The fine adjustment is achieved by activating the cam-switch detector so as to allow alignment of the spline teeth for lock engagement. Spline position overtravel in either engagement or disengagement is prevented by a limit switch assembly, operated by a chain sprocket in the spline-lock drive system.

The ϕ axis drive (see Figure 7 for details) is similar to the ψ and CW drives described above. However, no spline-lock is included in this assembly. The torque load values from aerodynamic and inertia forces about this axis are within the static capacity of the harmonic drive unit. Shaft position again is determined by a potentiometer coupled directly to the main shaft.

Positioning the model in a particular α-β angle combination involves rotation about both the ϕ and ψ axes. The ϕ drive, which includes no spline-lock, is continuous and may assume any angular position. However, due to the discrete allowable positions of the ψ drive, to permit spline-lock engagement, angular motion about this axis is restricted to 2.25° increments or 160 possible lock positions per main-shaft revolution. This results in a limitation that only certain angular combinations of α-β may be obtained. The allowable incremental steps of α or β are dependent on the α-β combination desired.

Electrical power for the drive systems and balance-data acquisition is derived by use of a slip-ring assembly. This is a low-level signal slip-ring unit containing dual brushes and 72 channels. On the rear of the slip-ring unit is mounted an encoder for Ω axis position information and a tachometer for spin rate determination.

CONCLUDING REMARKS

The stall/spin characteristics of modern high performance aircraft and increased capabilities of future aircraft make it highly desirable to obtain experimental data which will enhance the use of analytical techniques for predicting these critical modes. This paper has described a rotary mechanism for wind tunnel studies which should provide the motions necessary for generating this aerodynamic data, specifically, force and moment derivatives, in support of stall/spin analytical programs.
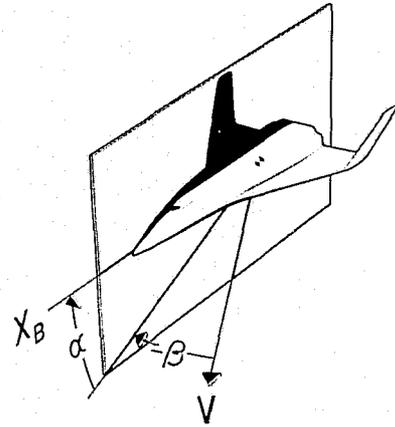
STEADY ANGLE OF ATTACK AND SIDESLIP
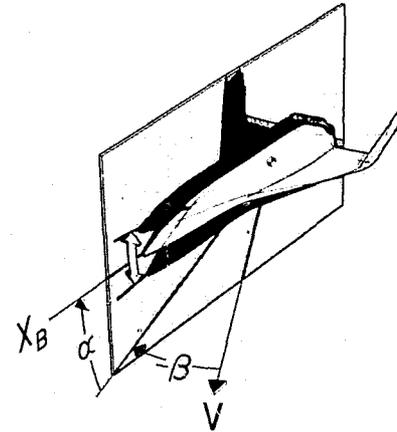
DAMPING IN PITCH
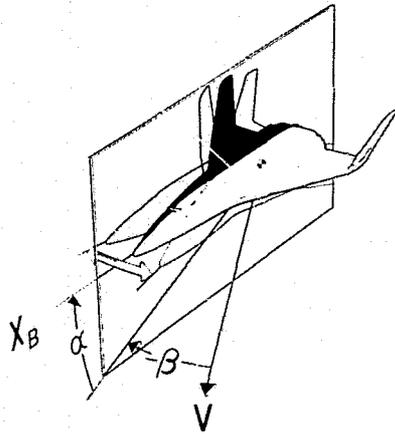
DAMPING IN YAW
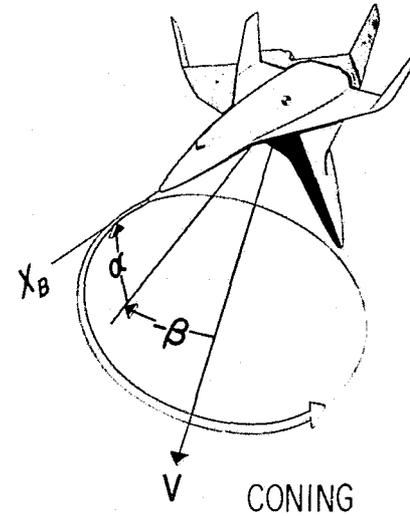
CONING

Figure 1. Motions in body axes of interest in stall/spin investigations

COUNTER WEIGHT

HYDRAULIC MOTOR

HYDRAULIC LINE

CW AXIS

MODEL

15°

15°

SPIN AXIS Ω

ψ AXIS

φ AXIS

WIND TUNNEL
STRUT-MODEL
SUPPORT SYSTEM

36"

SCALE
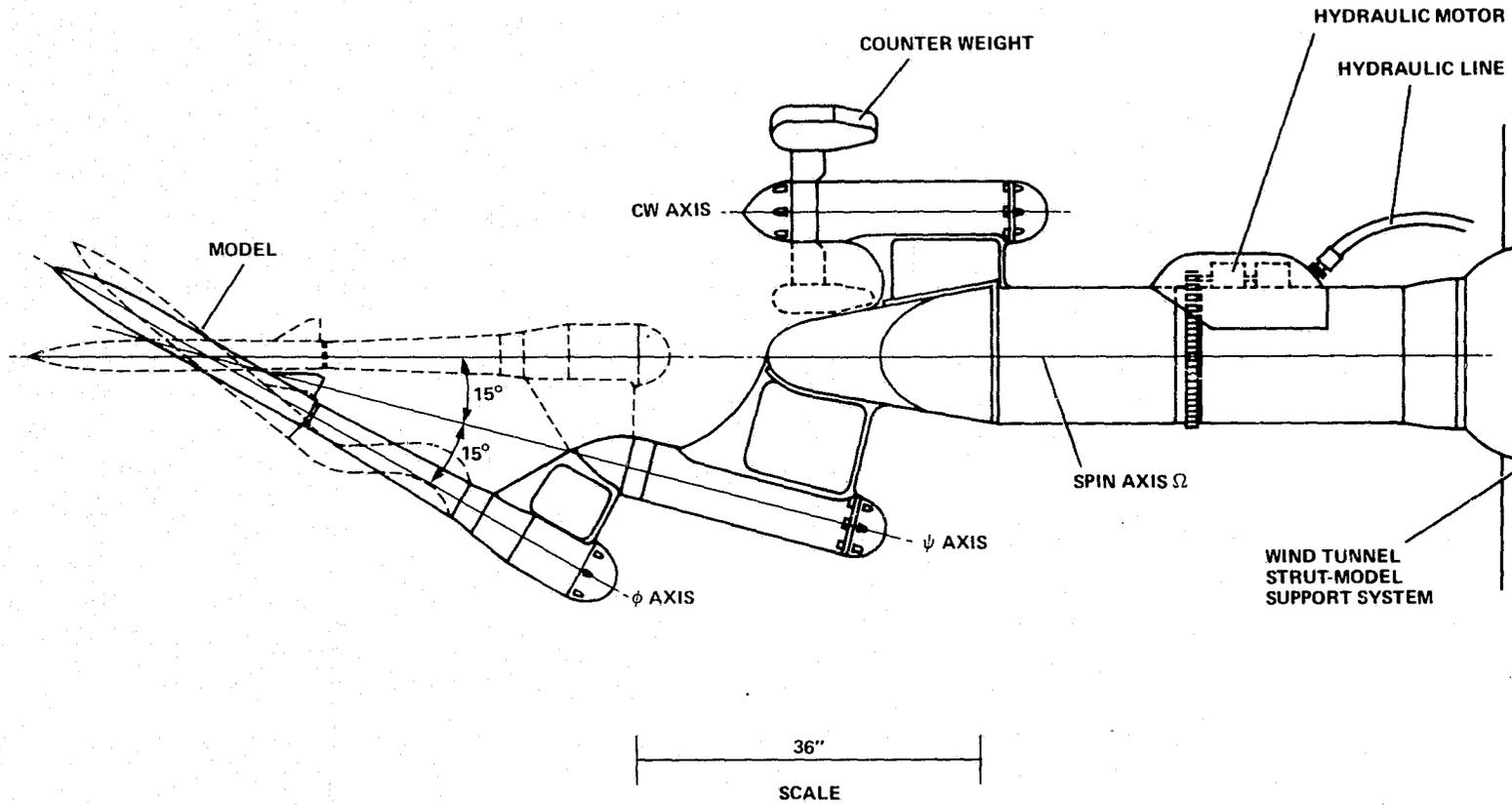
Figure 2. Axis definition and overall view of the
"Dynamic Stability Rig"

a = ANGLE OF ATTACK
β = ANGLE OF SIDESLIP
γ = ANGLE BETWEEN SPIN AXIS AND
     STREAM (SET WITH STRUT)

COUNTERWEIGHT

ROLL DRIVE

CW AXIS

a OR β CHANGE

ψ AXIS

SPIN AXIS

V

γ

ω

STRUT

ϕ AXIS

a - β RATIO CHANGE

Figure 3.   Spin axis is offset from stream axis for
            damping moment derivatives in
                      pitch and yaw
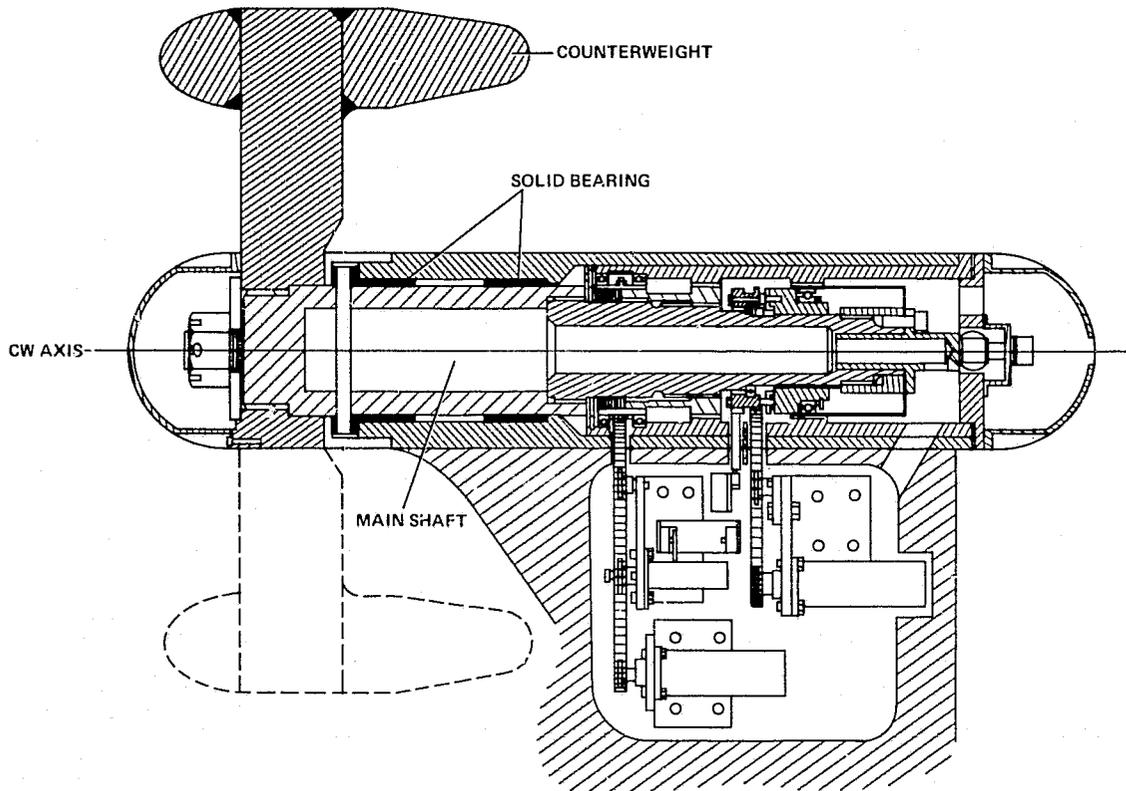
Figure 4. Overall view of CW axis counterweight drive
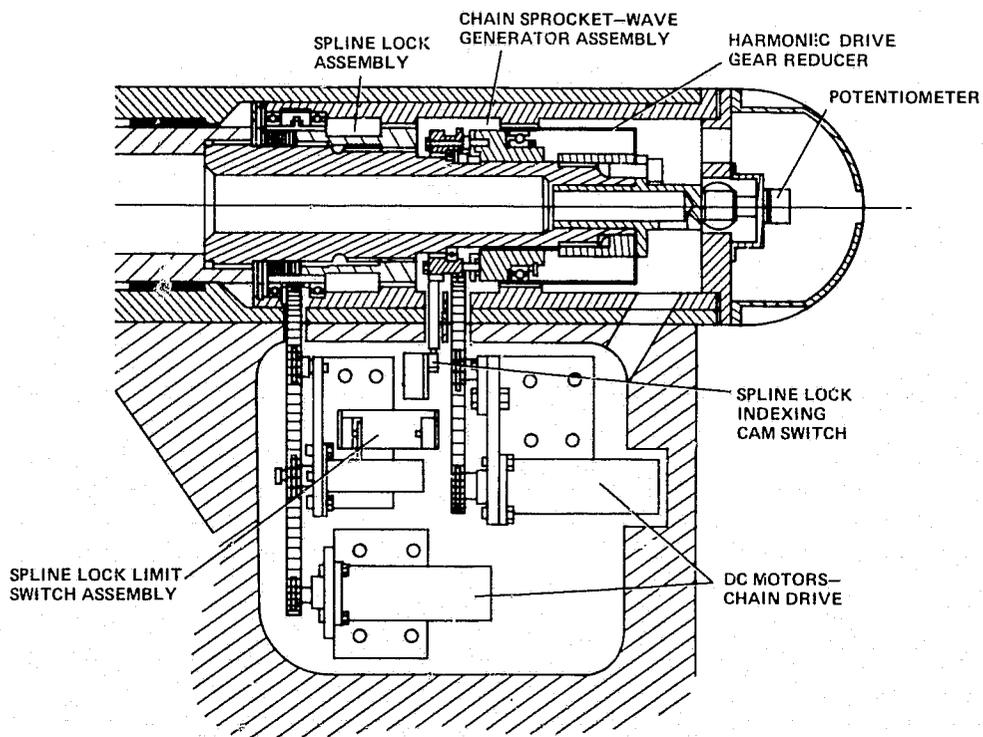
Figure 5. Counterweight or ψ axis drive details
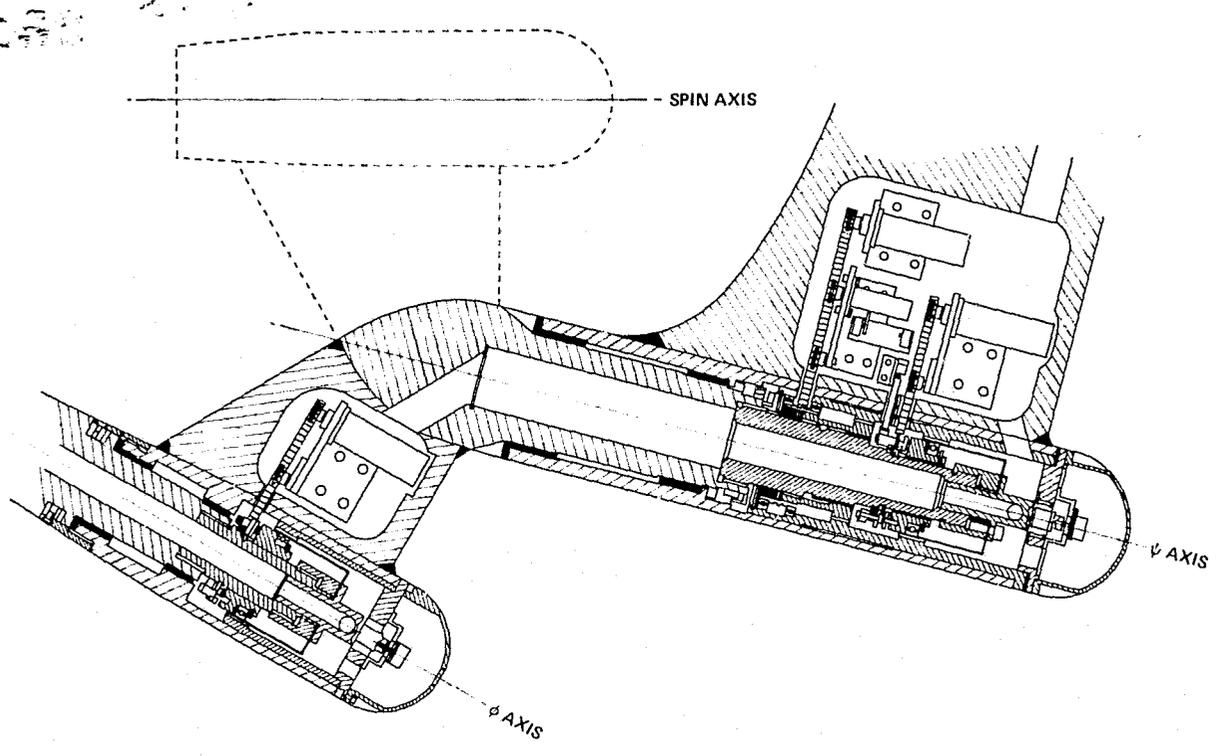
Figure 6.   Overall view of ψ and ϕ axis drives
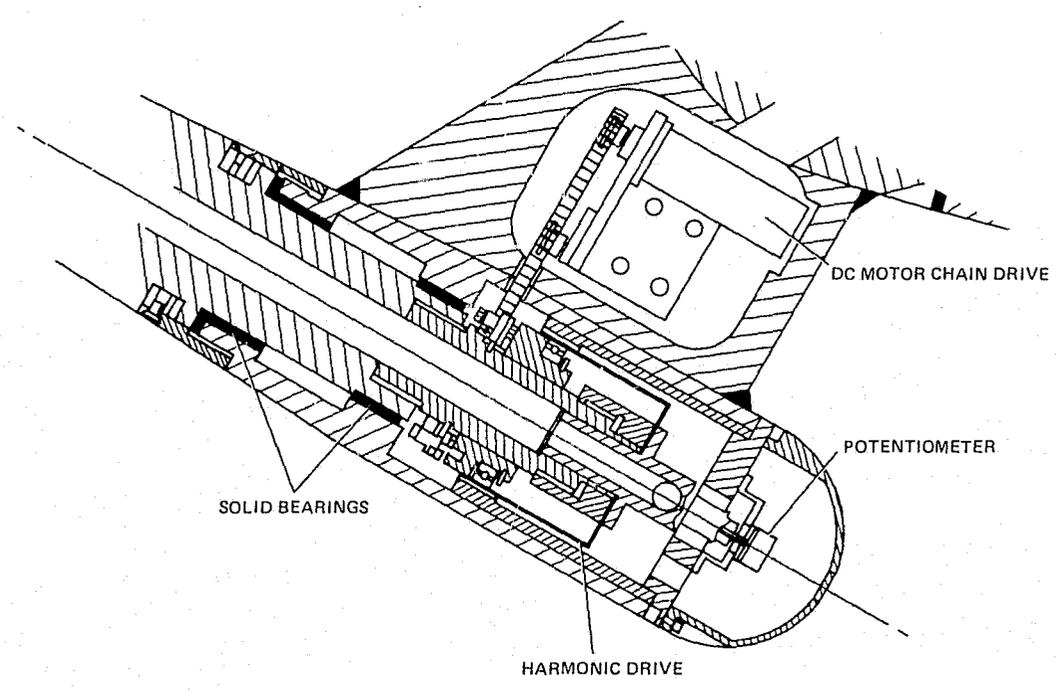
Figure 7. ϕ axis drive details

PIN PULLER IMPACT SHOCK ATTENUATION

By Gary F. Auclair, Barry S. Leonard, Richard E. Robbins,
and Wayne L. Proffitt

Lockheed Missiles & Space Company, Inc.

ABSTRACT

An investigation leading to the design of a pin arresting mechanism for a pyrotechnically actuated pin puller is reviewed. The investigative approach is discussed and the impact shock test results for various candidate designs are presented. The selected pin arresting design reduced the peak value of the shock response spectrum by five to one.

INTRODUCTION

Pin pullers have gained industry wide acceptance as a highly reliable release mechanism for spacecraft deployables. Frequently, the deployable is preloaded to the spacecraft primary structure to prevent excessive vibration amplification during ascent. Consequently, high energy pyrotechnic devices are required to overcome the high release pin friction accompanying the high preload. As a result, the pyrotechnic device imparts high level energy to the release pin, which usually must be stopped in a relatively short distance. The short stopping distance in conjunction with the high preload between the spacecraft and the deployable allows time for the pin arresting impact shock to be transmitted to the deployable before separation can be achieved. Many deployables, such as solar array panels for example, cannot tolerate high shock levels; hence, pin arresting mechanisms which effectively absorb shock energy are required.

This paper summarizes a brief investigation of a pin arresting mechanism which would meet a given set of shock spectrum requirements when applied to an existing pin puller design.

PIN PULLER IMPACT SHOCK

Pin Puller Design

The design of the release mechanism for which this investigation was conducted is shown in Figure 1. The mechanism has dual pin pullers, each of which is actuated by dual pyrotechnic squibs. At the end of the unit, the pin pullers release a toggle bolt which is holding the deployable to the spacecraft structure via a preload of 3100 pounds. The particular deployable in this case contained electronic circuits which were sensitive to shock spectrum in the 1 to 5 kilohertz range. The relatively long mechanism body between the deployable and the squib was intended to attenuate the impact shock transmitted to the deployable. However, as the data will show, resonance in this section actually amplified the impact shock.

The initial design of the pin puller arresting mechanism consisted of an aluminum ferrule impacting a swaging collar, as shown in Figure 2. Although this design had been satisfactorily proven in other uses, shock testing revealed that the shock spectrum transmitted to the deployable exceeded allowable levels by a factor of three. Hence, an investigation of alternate pin arresting mechanisms was initiated.

Investigative Approach

The investigation proceeded in four steps:

(1)   Formulation of pin arresting shock absorber design concepts.

(2)   Formulation of an analytical model to describe the process.

(3)   Static testing of candidate pin arresting mechanisms

(4)   Pyrotechnic tests of candidate mechanisms.

All of the various concepts considered can be approximated by a simple spring mass second order system model. However, it became rapidly obvious that accurate information on the various parameters in the model was not available, particularly the force-displacement time characteristic of the pyrotechnic squib when actuated. The model was useful, however, in conceptualizing pin arresting approaches, defining desired pin arresting characteristics, and identifying shock paths.

The initial design thrust was to use a linear absorber. However, since energy absorbed is proportional to the volume of material strained, it became obvious that geometric constraints would not allow the required volume. This led to the investigation of non-linear absorbers.

The selected design, as shown in Figure 2, consists of a soft aluminum tube with a lead insert which is readily adaptable to a standard pin puller housing. The output shaft of the combustion chamber piston impacts the lead insert following release. The lead is extruded past the shaft end while the aluminum tube is being stretched. The four inch long tube (approximately one half inch in diameter) is stretched about 0.4 inch. Since this elongation is far beyond the elastic limits of aluminum, a distinct non-linear force versus deflection curve is generated. The tube cross section area is sized to absorb the pin impact energy well before fracture would occur.

Test Results

Static testing was performed to determine the force-displacement and energy capacity characteristics of several candidate absorbers. Since the approximate pin energy was known from earlier tests, this allowed the geometry of each device to be scaled to absorb the pin energy within existing displacement constraints. Examples of the characteristics for the ferrule design and for the stretch tube design are given in Figure 3. The ferrule design produced a fast rising force level at the end of travel (to absorb the required energy) as the swaging process is completed. Alternate ferrule designs with greater material volume were considered but could not be accommodated within the geometric constraints of the existing release mechanism design. The stretch tube absorber design eliminates the high force at the end of travel, but still has a steep initial rise in the force-displacement curve. The lead insert, when properly sized, effectively eliminated the steep initial rise. This was later found to reduce the high frequency levels of the shock spectrum response.

Pyrotechnic tests were then performed to evaluate the performance of the prime candidate pin arresting mechanism designs. The tests were conducted using high frequency accelerometers to measure the transient shock response. A triad of accelerometers were mounted at both ends of the release mechanism, as shown in Figure 1. Accelerometer triad #1 essentially measured the shock at the pin puller while triad #2 measured the shock at the deployable. In all cases, the accelerometer transient shock data was processed through a spectral analyzer to obtain a shock response spectrum for comparison to response requirements.

It should be noted that observation of the transient shock response verified that the high shock levels were indeed due to the pin impact shock and not due to the shock from the pyrotechnic squib firing. The shock response spectrum data includes all effects; however, the pyrotechnic firing contributes little to the overall levels observed.

Figure 4 shows the shock response spectrum for the original pin arresting ferrule design at both the pin puller location and the deployable location. Only the high shock direction (Z) is shown. Figure 4 also shows the same responses for the selected design. Table 1 presents a summary of various design approaches and the shock levels that were measured.

As can be seen from Figure 4, the original design had considerable shock response amplification from the pin puller to the deployable. This occurred even though there was a significant distance from the shock source to the deployable (which was intended to attenuate the response). The selected design was successful in reducing both the pin puller shock level and in reducing the amplification, resulting in a five-to-one reduction in the peak shock response at the deployable. Significant reduction was achieved across the complete frequency spectrum of 200 Hz to 10,000 Hz.

CONCLUDING REMARKS

A simple pin arresting mechanism has been designed which effectively reduces the resulting shock spectrum levels and is easily adaptable to various pin puller designs. The design is based on the elongation of material, which is an effective and predictable method of absorbing impact energy.

A design approach consisting of simple modeling of the arresting mechanism followed by static tests of the energy absorption characteristics prior to relatively expensive pyrotechnic shock testing has been shown to yield satisfactory results. Shaping of the static characteristics was effective in reducing the shock spectrum response levels at all frequencies.

Although this investigation has relied primarily on an empirical testing approach, further development of the dynamical shock model would likely lead to additional improvements and should be the subject of future investigations.

Table 1. Summary of Pyrotechnic Shock Test Results

Test No.			Shock Response Spectrum Peak (G's)		Shock Response Spectrum at 1000 Hz (G's)		Stop Stroke (in.)
			Pinpuller (#1 Z)	Deployable (#2 Z)	Pinpuller (#1 Z)	Deployable (#2 Z)	
1.	Original Design – Aluminum Ferrule 0.3 in. long		7500	18000	4400	4000	0.20
2.	Same as 1 – also split body with splice plate[a]		7800	7000	4400	3100	0.20
3.	Aluminum Stretch Tube Design:						
	Tube Area in.^{2}	Lead Pellet Length (in.)					
3a.	0.091	0.20	9800	10000	3700	1900	0.47
3b.	0.180	0.40	4600	8100	1900	3100	0.31
3c.	0.139	0.20	5000	5600	1000	2000	0.21
3d.[b]	0.121	0.20	3100	3400	1600	1000	0.41
4.	Same as 3d – also split body with splice plate[a]		3000	2500	2700	1100	0.45

[a]Release mechanism body split (approximately halfway between pin puller end and toggle bolt end) and remated with splice plate and rivets. This provides shock path attenuation between the pin pullers and the deployable.

[b]Selected design. Average of 4 tests.

RELEASE FITTING

X
Z

X
Z

RELEASE ROD

EXTENSION ROD

PYROTECHNIC SQUIBS – ASI

|← 14.0 →|

DEPLOYABLE

NO. 2 TRIAXIAL ACCELEROMETER (TEST)

3100 -lb PRELOAD

DEPLOYABLE

FERRULE (ORIGINAL PIN ARRESTING DESIGN)

NO. 1 TRIAXIAL ACCELEROMETER (TEST)

Y

Y
Z

Z

SPACECRAFT STRUCTURE

TOGGLE AND BOLT

STRETCH TUBE (REVISED PIN ARRESTING DESIGN)
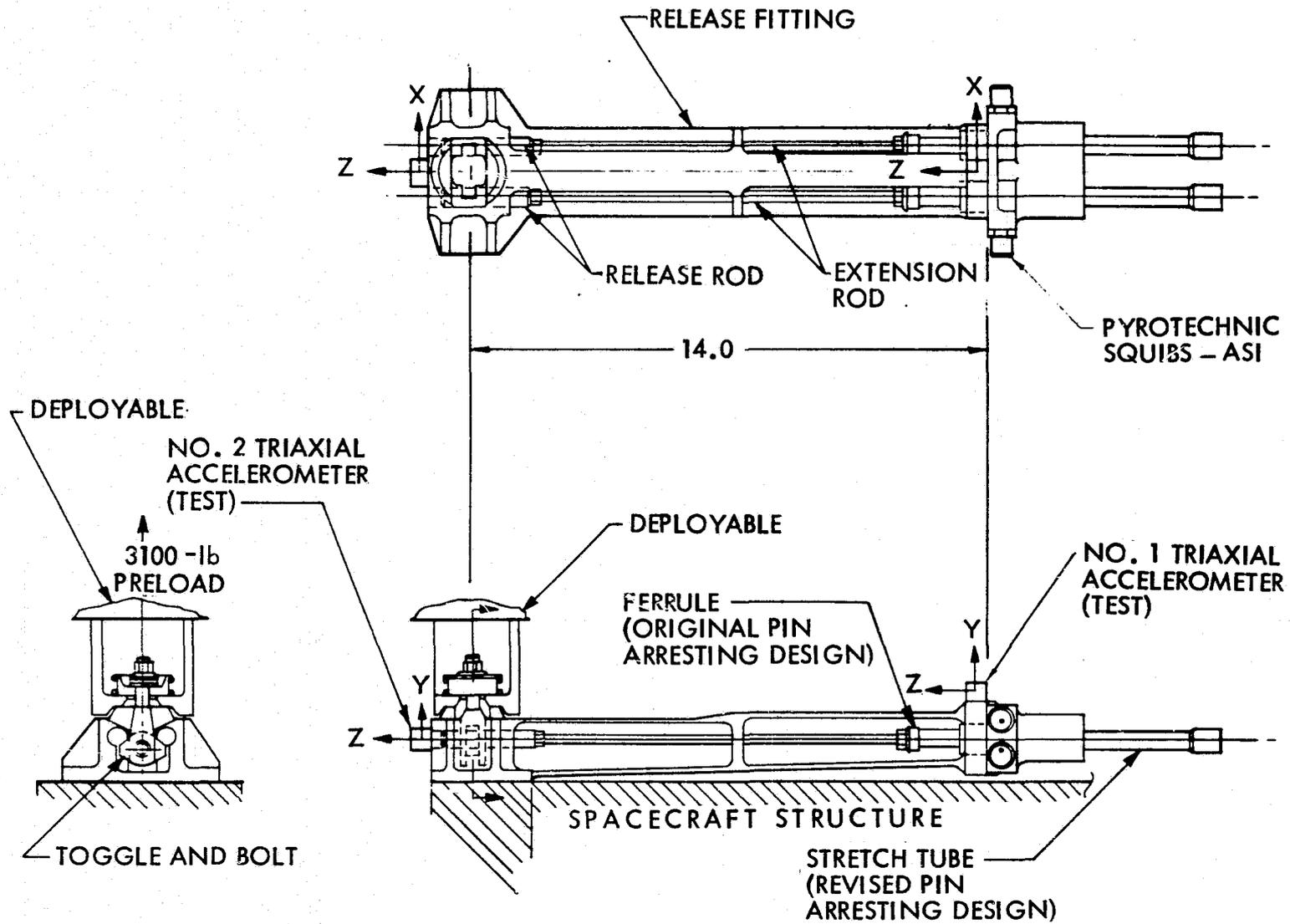
Figure 1.   Release mechanism design
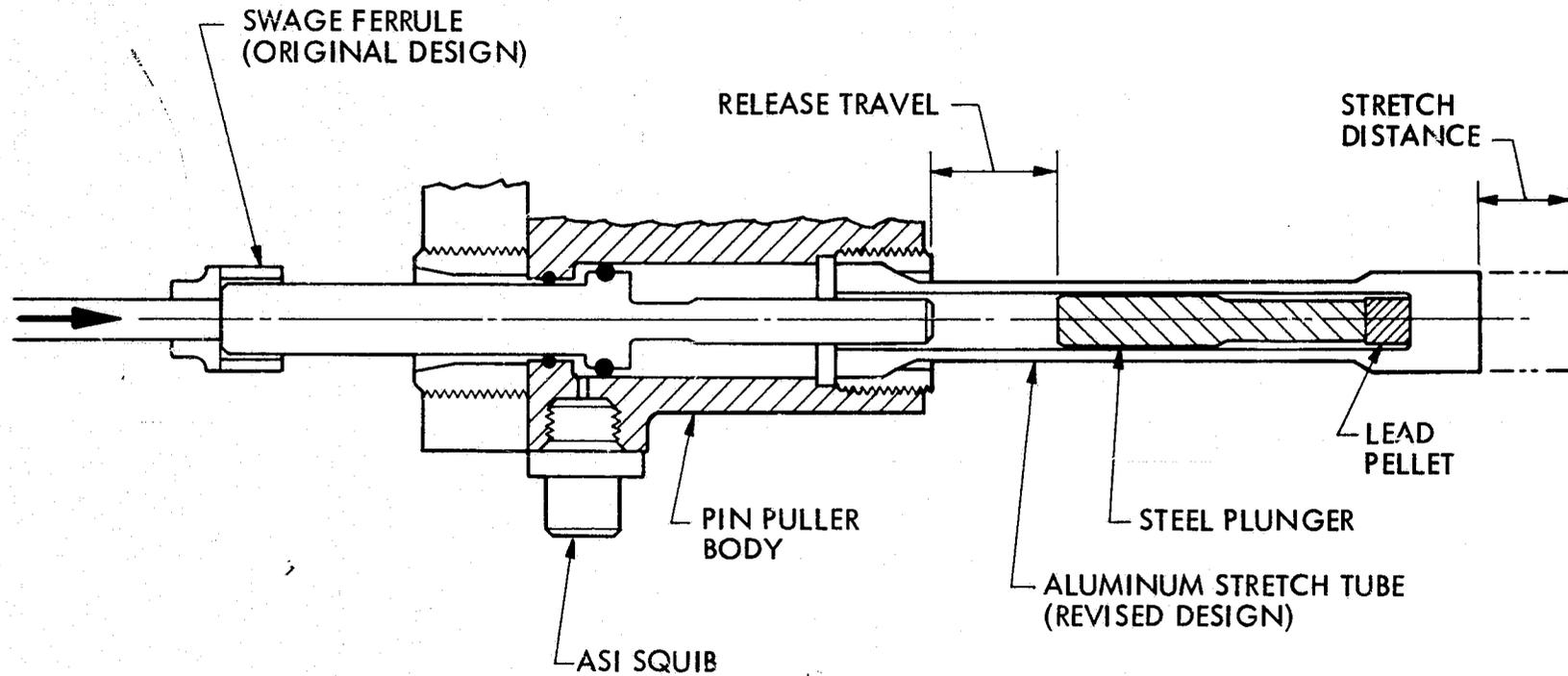
Figure 2. Details of pin arresting mechanism showing original (ferrule) and selected (stretch tube) designs

a. Characteristics of ferrule/swaging collar design

4000

FORCE, lbs

0

0   DISTANCE, in.   0.5

HIGH FORCE LEVEL AS FERRULE IS COMPLETELY SWAGED
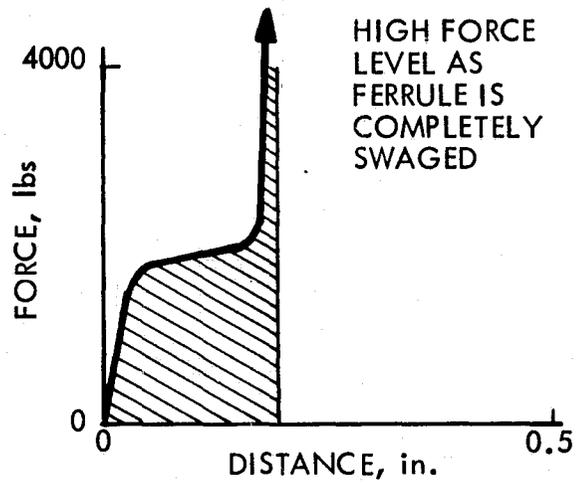
b. Characteristic of stretch tube design (high elongation material)

4000

FORCE, lbs

0

0   DISTANCE, in.   0.5

|←STOPPING DISTANCE→|
(ELONGATION)
YIELD POINT

X TUBE FRACTURE

AREA = ENERGY ABSORBED
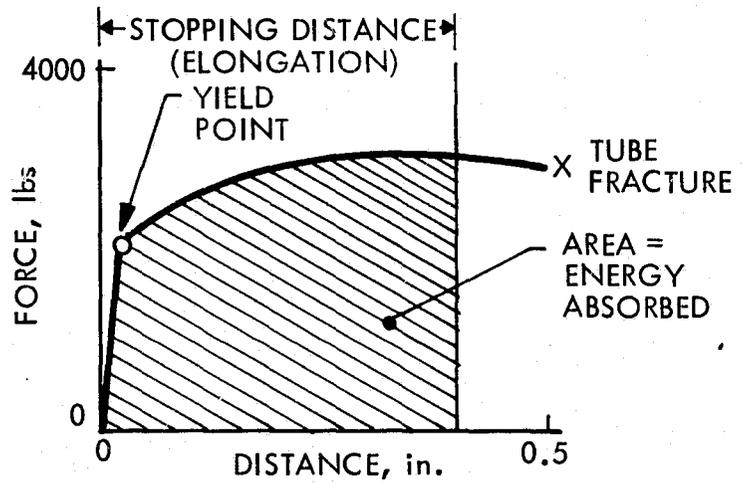
c. Characteristic of stretch tube design with addition of lead pellet (low modulus material) to reduce initial steep force rise.

4000

FORCE, lbs

0

0   DISTANCE, in.   0.5

LEAD EXTRUDING

X

ALUMINUM TUBE STRETCHING
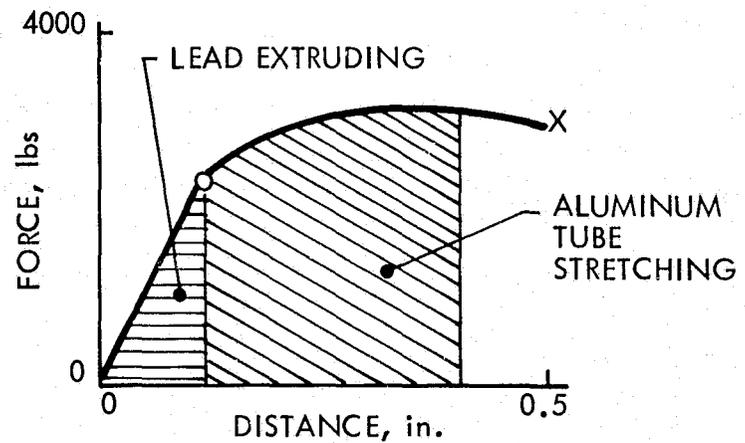
Fig. 3. Typical static force-displacement characteristics of absorber designs
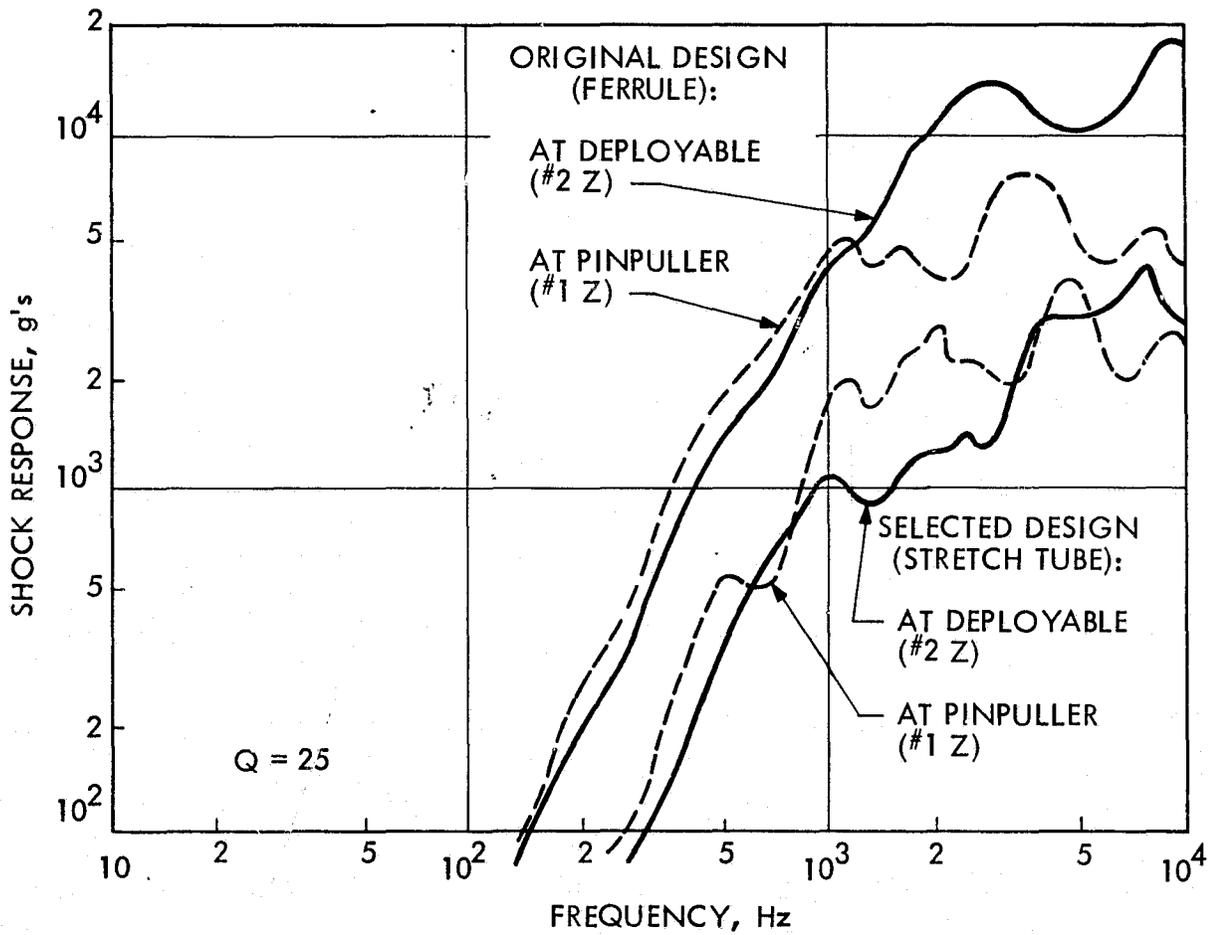
Fig. 4. Shock spectral response for original design and selected design

THE HELIOS MECHANICAL DESPIN DRIVE ASSEMBLY FOR THE

HIGH-GAIN ANTENNA REFLECTOR

by E. J. W. Müller, Dipl. -Ing.

DFVLR-BPT, Germany

ABSTRACT

The HELIOS mechanical despin drive assembly for the high-gain antenna reflector is described in this paper. HELIOS is the German-American solar probe which comes within 0.31 Astronomical Units (about 50.10^6 km) of the sun. A special thermal design and a dry lubrication system have resulted in successful operation up to now, with HELIOS having finished its first orbit around the sun.

INTRODUCTION

HELIOS is a German-American solar probe with an elliptical flight path around the sun. HELIOS A was launched on Dec. 10, 1974, and HELIOS B followed in Jan. 1976. Its aphelion is one Astronomical Unit (1 AU) and its perihelion 0.31 AU from the sun. The solar impact to the spacecraft varies between one and eleven solar constants. Figure 1 shows the orbits of earth and HELIOS around the sun. The HELIOS spacecraft is spin-stabilized at 60 rpm and has three antenna systems to achieve ground connection: a low-gain antenna for the near-earth part of the mission before the spacecraft spin axis is oriented orthogonal to the orbit plane; a medium-gain antenna, and a high-gain antenna for the main mission. The high-gain antenna is on the upper side of the spacecraft. It consists of an axial antenna feeder rotating with the spacecraft and a despun reflector, which is also pointed towards the earth. Figure 2 shows the spacecraft's configuration with its high-gain antenna system and the despin drive assembly (DDA). The flight time for one orbit is about six months; three months after launch, HELIOS reaches its closest distance to the sun, which is 46.10^6 km for HELIOS A and 43.10^6 km for HELIOS B. The launch vehicle — a Titan IIIe Centaur TE 364-4 combination, the varying thermal environment during the mission, and the ground testing time influenced the design of the reflector despin drive assembly.

The HELIOS Despin Drive Assembly

Figure 3 shows a photograph of the DDA. The design concept of the despin drive assembly had to take into consideration

    a)   the general HELIOS system aspects
    b)   the launch conditions
    c)   the orbit environments

The general HELIOS system aspects — including storage, shipment, and S/C system tests — called for materials which are corrosion-free and for a lubricant which operates in air as well as in vacuum. The launch conditions — acceleration, vibration loads, and acoustic noise — determined the mechanical design and the size of the bearings. The orbit environments — vacuum and an extremely changing thermal impact between one and eleven solar constants — dictated the kind of lubrication system used: dry film lubrication with self-replacement of the film by transfer.

The Mechanical Design of the Despin Drive Assembly

To accommodate the expected load impact during lift-off (14 g at 60 Hz), a three-inch angular contact bearing with 42 balls on each side was chosen. The contact angle varies between 18° and 25°, depending on the axial load impact. The lower bearing, supporting the axial load during the launch phase, is a "fixed" bearing with respect to shaft and housing. The bearing on the other end is preloaded via a preload spring to five pounds. The preload force was optimized during the tests to slightly more than the minimum force necessary to have the balls running in the same track. It was found out during the preselection tests at DFVLR, Munich, how the preload force influences the lifetime of the bearings. Figure 4 shows the DDA configuration, the arrangement of the bearings, and the materials used. The DDA is driven by a brushless DC motor which can overcome a drag torque of 30 oz-in. The nominal drag torque range is from 3.5 oz-in. to 6.4 oz-in. A magnetic pick-up device makes possible the pointing of the reflector towards the earth throughout the mission. The pointing accuracy is specified to be better than 0.7°.

The materials used for the DDA are:

- 440 C stainless steel for the high-precision bearings
- Aluminum for shaft and housing
- Titanium for the bearing seats (similar thermal expansion factor to 440 C)

These materials were chosen because of the wide range of expected temperatures and thermal gradients across shaft and housing.

The goal was not to jam the DDA under all possible flight conditions, which means not closing the radial or axial gap between top bearing and housing. Figure 5 shows the temperatures and thermal gradients necessary to close the radial gap between upper bearing and housing, and Fig. 6 shows the thermal gradient (housing versus shaft) required to close the axial gap. At a shaft temperature of -40 °C, a thermal gradient of 20 °C could be tolerated (assuming an isothermal housing and an isothermal shaft).

The Lubrication System

The lubrication system chosen is the dry film lubricant "Dry Vac Kote" of Ball Brothers Research Corporation (USA), which is based on molybdenum-disulfide (MoS_2) combined with a phenolic (RULON-A) retainer for

relubrication by transfer. The reasons for not using "common" oil or grease lubricants and going to a dry lubrication system are:

a) Expected bearing temperatures from -40 °C to +60 °C
b) Evaporation of oil at high temperatures in vacuum
c) Danger of contamination of spacecraft surfaces.

The Ground Testing of the HELIOS Despin Drive Assembly

HELIOS is the first civilian spacecraft which uses a dry film lubricant for such a mechanical device. Up to now, dry lubricants were used only for instrument size bearings. Because it was not possible to get lifetime data for these lubricants or even design data (e. g., temperature resistance across dry lubricated surfaces or lubricant break-away forces), various tests had to be carried out during the design and development phase of the HELIOS program. In the beginning, a functional support contract was established between the HELIOS project office and the DFVLR Institute for "Flugtreib- und Schmierstoffe" in Munich. The work done at DFVLR can be summarized as follows:

- Literature research
- Preselection tests of bearings, lubricants and separators
- Long-life tests of dry film lubricated bearings in UHV
- Long-life tests of dry film lubricated bearings in thermal vacuum
- HELIOS DDA thermal gradient tests in UHV
- Stand-by for trouble-shooting during the HELIOS mission using a HELIOS DDA in a thermal vacuum chamber which allows independent temperature settings at the shaft and the housing

Details about these tests and the results can be found in Ref. 1. In the following, the HELIOS DDA tests carried out at the subsystem and system levels at the supplier (Ball Brothers) and the HELIOS main contractor (Messerschmitt-Bölkow-Blohm) will be discussed.

HELIOS DDA Lifetime Test in Thermal Vacuum

In the beginning of the program, it was recommended by the HELIOS project office that a thermal vacuum life test be performed in real time on a complete DDA in addition to real-time tests on the DDA bearings. This would more nearly simulate the real environment for the bearings and provide a life test of all other DDA components. To simulate the real environment, a random vibration test (acc. level) was performed before the DDA was put into the thermal vacuum chamber. The lifetime test was done successfully between Apr. '72 and Nov. '73. Figure 7 shows the test history, including the measured torque values at the various temperatures. In order to complete the test in the allotted time, it was decided that the time lost through interruptions could be made up by operating at double speed.

HELIOS DDA Thermal Vacuum Tests

The next DDA system tests were the thermal vacuum tests of the prototype flight units one and two. During the prototype tests, it could be seen that the friction torque went up to 7 oz-in. at shaft temperatures between -40 °C

and -50°C. When the flight units were tested, the friction torque reached 12 oz-in. at the same cold temperatures. Many tests followed, with different bearing separators and different gaps between upper bearing and housing. Finally, it turned out that the drag torque was a function of the torque ripple which occurred due to an end plate (at the lower end of the DDA) misalignment at cold temperatures. During manufacture, the final machining was done with the end plate fixed to the housing. The rotational position of the end plate with respect to the housing was marked, and during the assembly of the DDA, the end plate was screwed on in the same position. During the thermal vacuum tests — especially during the cold phase — it turned out that the above-mentioned fabrication method was not the optimal one. A better way was to fabricate and machine each part by itself with close tolerances and to optimize by test the final position of the end plate on the housing. The resulting drag torque during the cold phase tests was about 5 oz-in. for both flight units.

HELIOS Spacecraft System Solar Simulation Test

The most important test to improve the thermal design of the spacecraft and its components was the HELIOS solar simulation test performed at the Jet Propulsion Laboratory (JPL, California). During this test, the DDA was operated by its motor to simulate flight conditions. The measured temperatures were nearly coincident with the calculated ones for the hot phase at 11 solar constants, but they deviated for the cold phase at 0.9 solar constant. Thermal gradients on the order of -40°C (shaft warmer than housing) were read out.

This was later explained by a heat leak in the area of the upper flange. As already mentioned, the maximum allowable thermal gradient is -20°C for the cold phase. Figure 8 shows a summary of the solar simulation test with respect to the behaviour of the DDA. One can see the influence of the temperatures on the friction torque, which influences the motor current and also the pointing accuracy.

The DDA Thermal Gradient Test

This test was necessary to simulate the JPL test and to check the design changes made to obtain warmer temperatures and lower thermal gradients during the cold mission phase. In the first step, the DDA temperatures were set to the JPL measured values. Then the following design changes were made:

a) The heat leak between reflector hub and DDA flange was closed.
b) A heater was added inside the reflector hub to warm up the upper part of the housing and thus to reduce the thermal gradient during the cold phase.

After implementation of these changes, a shaft temperature of -30°C and a thermal gradient of 8°C were measured for the cold flight condition.

Flight Data of the HELIOS DDA

Up to now, the performance of the HELIOS DDA has been excellent during the mission. Figures 9 and 10 show the performance of the DDA during the HELIOS A and B missions through March 1976. As can be seen, the measured friction torque (via motor current) is always within the specified values. As a result of the last design changes, the measured temperatures are warmer during aphelion and colder during perihelion.

Conclusion

The flight performance of the dry lubricated HELIOS despin drive assembly for the high-gain antenna reflector shows that the choice of the unusual lubricant was a good one. It confirms a concept which could be used not only for spacecraft but also in extreme earth environments.

References

1. E. Jantzen: A Dry Lubrication System for Spaceproofed Bearings. ESRO Proceedings, 1975.
2. BBRC, Calculation of DDA Endplay, March 1974.
3. MBB, DDA Design Specification.
4. MBB, Test Procedures for DDA.
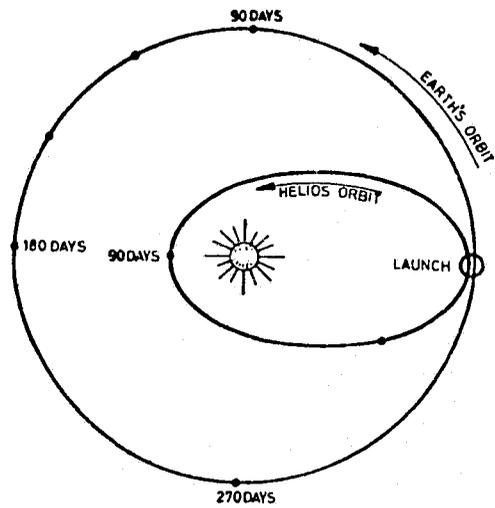
Fig. 1. Orbits of earth and HELIOS around the sun
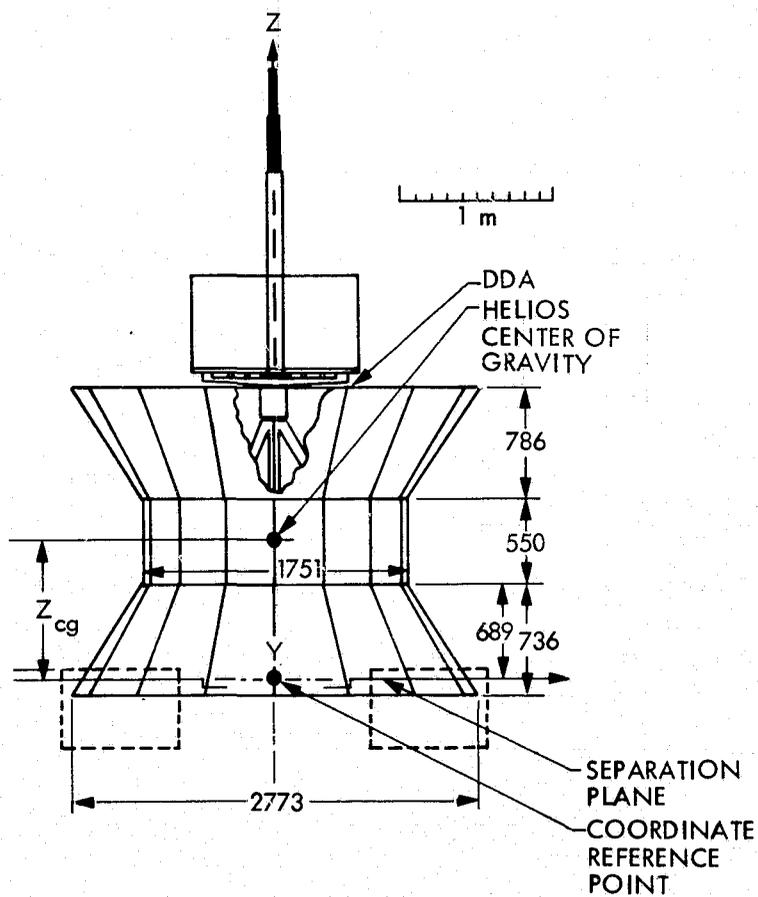
Fig. 2 HELIOS spacecraft dimensions

Fig. 3 The HELIOS despin drive assembly
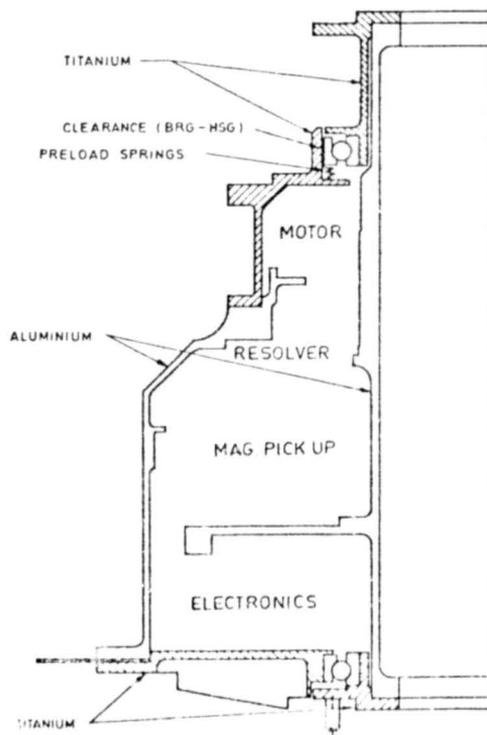
Fig. 4 DDA configuration
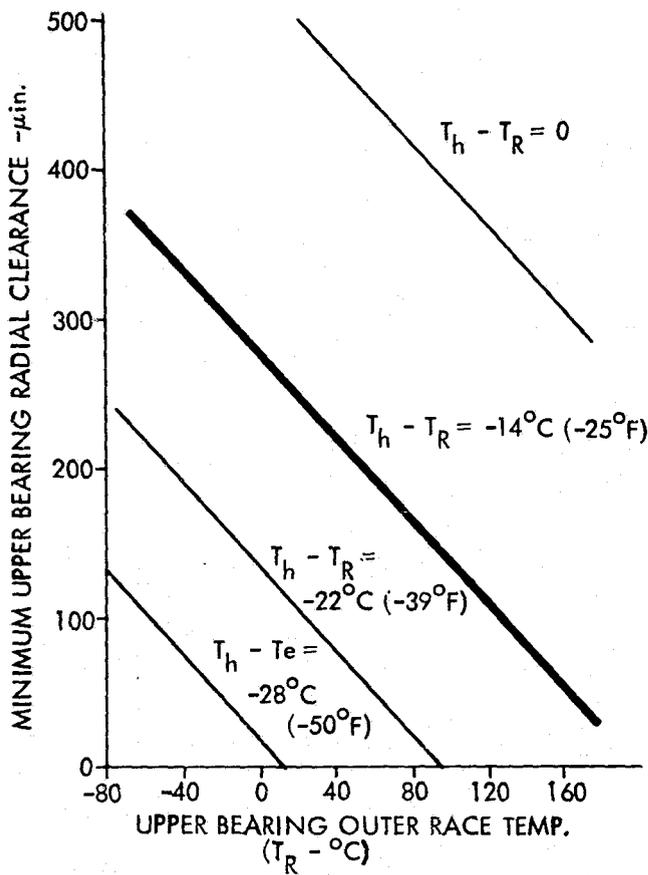
Fig. 5   Thermal gradient required to close upper
bearing radial gap
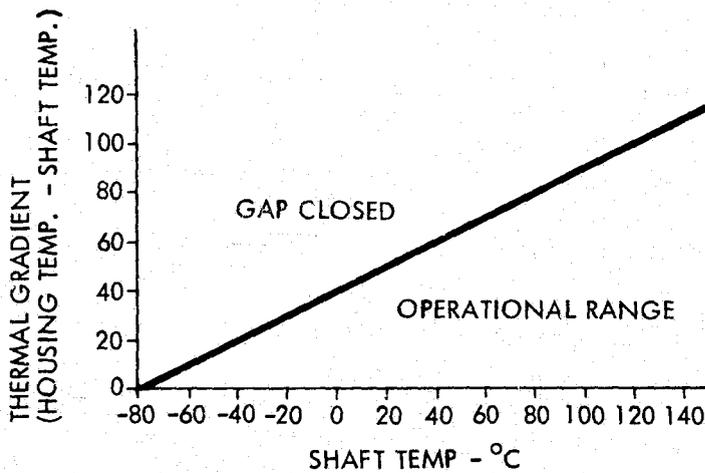
Fig. 6   Thermal gradient (housing vs. shaft) to close an axial gap of
0.0055 inch, assuming an isothermal housing and an isother-
mal shaft
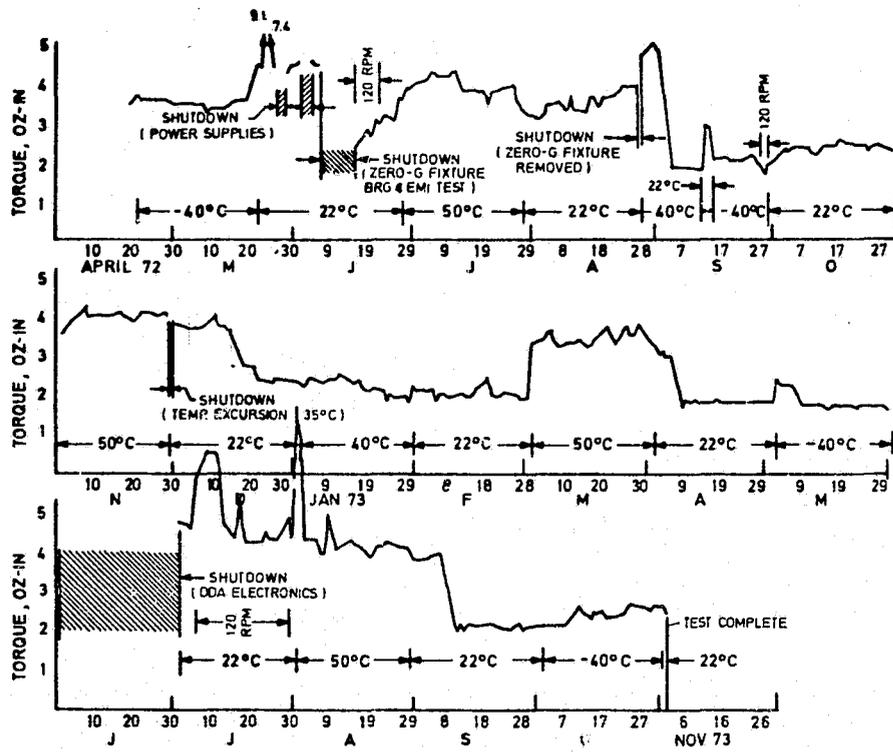
Fig. 7 Summary of DDA T/V life test
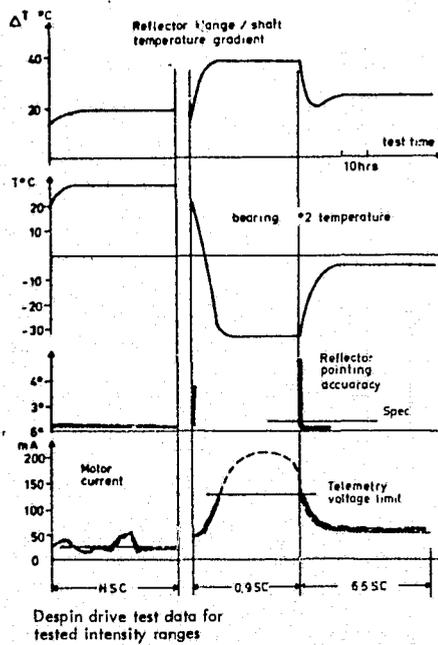
Fig. 8 Summary of HELIOS solar simulation test at JPL (for DDA)

HELIOS-A DESPIN DRIVE ASSEMBLY PERFORMANCE
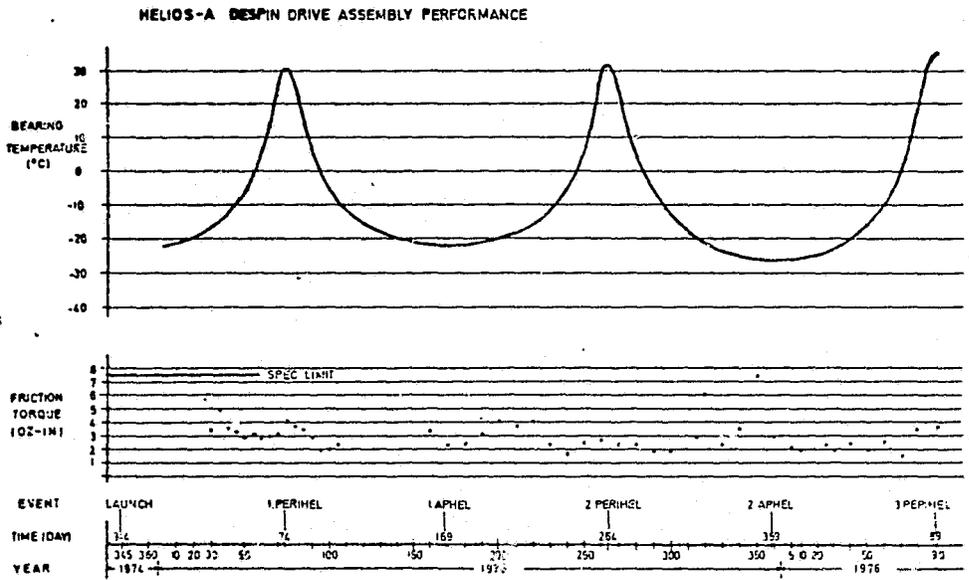
Fig. 9 HELIOS A DDA performance

HELIOS-B DESPIN DRIVE PERFORMANCE
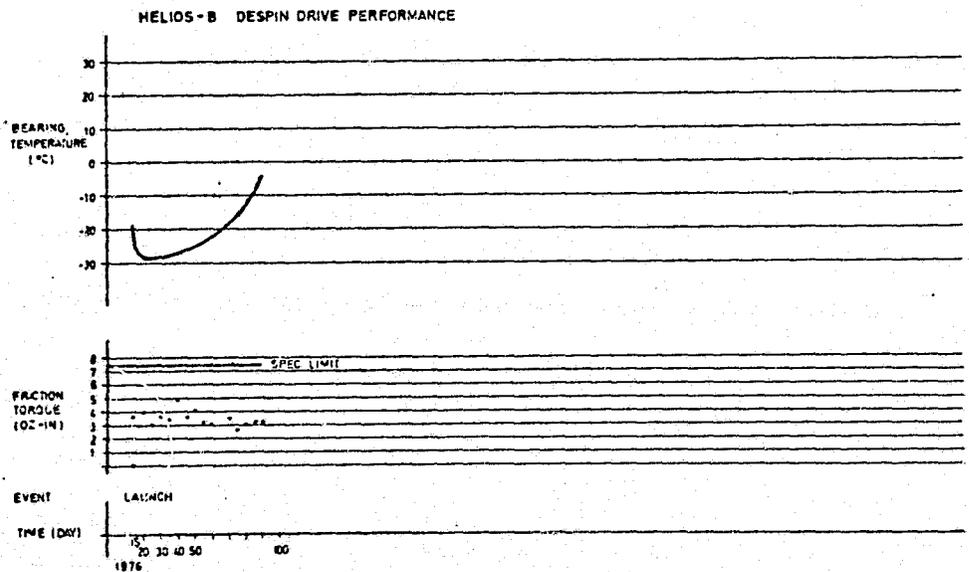
Fig. 10 HELIOS B DDA performance

ASSURANCE OF LUBRICANT SUPPLY IN WET-LUBRICATED

SPACE BEARINGS

By Frank A. Glassow

Hughes Aircraft Company

ABSTRACT

Recent research and development have made available two significantly new and different techniques for providing greater assurance of ample lubricant supply for bearings in despin assemblies and momentum wheels. Conventional lubrication techniques appear to be satisfactory, but rigorous proof of meeting a ten-year life requirement is lacking. One new approach provides additional lubricant only when commanded from ground control, while the other passively augments lubrication at all times. Each technique has specific advantages, and selection should be related to the application to obtain optimum performance.

INTRODUCTION

Early satellites were spin-stabilized and contained no moving parts, but advancing technology soon dispelled this state of simplistic bliss. Now we find that virtually all satellites contain critical applications of wet or dry lubricated ball bearings that are essential to meeting basic mission requirements. A modern satellite, by actual count, has as many as 52 ball bearings, many of which are in single-string failure locations with regard to mission performance. Some of the most important applications involve oil-lubricated ball bearings in the despin assemblies of dual-spin satellites or oil and grease lubricated bearings in momentum wheels of body-stabilized satellites. Unlike some ball bearing applications, despin and wheel bearings must rotate continuously for the life of the satellite, which is commonly expected to be as much as 10 years. In spite of relatively outstanding success in space, stringent life and performance requirements have aroused cause for concern and a desire for greater assurance of lubricant supply for these critical ball bearings.

Two techniques have been developed by the Hughes Aircraft Company for providing greater assurance of lubricant supply. Each technique, one active and one passive, is being applied to a flight program and has undergone extensive trade studies, qualification testing and life testing.

CONVENTIONAL LUBRICATION TECHNIQUES

Despin Bearings

Ball bearings employed in despin assemblies generally have bore sizes ranging from 60 to 150 millimeters and operate in the range of 5 to 100 rpm. They are usually lubricated with a hydrocarbon oil impregnated into porous cotton-phenolic ball retainers. Oil is fed by capillary action from the retainers as required by the ball bearings to maintain an equilibrium thin film of oil on the balls and races. Oil may also be contained in reservoirs of impregnated porous material located adjacent to the ball bearings (Ref. 1). Tests and measurements indicate that the value of reservoirs is dubious, and they are usually regarded as sources of oil which may escape through labyrinth seals of the assembly rather than a source of lubricant replenishment for the bearings. Since bearings are usually warmer than adjacent reservoirs, vapor and surface transport of oil tend to be away from the bearings.

Since despin bearings run at low speeds, a rather viscous oil and light preloads are preferred to ensure lubrication in the elastohydrodynamic regime. Lubricant life and life of the bearings are expended in three stages (initial film, equilibrium film, and boundary), the duration of which is determined as indicated in Table 1. Accordingly, the life profile of oil film thickness in Intelsat IV or IVA bearings is depicted graphically in Figure 1. This analysis indicates that there is ample margin to achieve the design life of 10 years in orbit.

Life of despin bearings in orbit is demonstrated by Intelsat IV satellites, the first of which has operated successfully for over five years. Three more vehicles of this series have demonstrated nearly four years each of continuous operation at approximately 50 rpm (Ref. 3). Hughes also has a complete despin assembly with 150 millimeter bore bearings that has operated in a chamber at high vacuum for five and one-half years.

Table 1. Lubricant/bearing life determination for Intelsat IVA despin bearings

STAGE	DESCRIPTION	BASIS FOR TIME DURATION	TIME YEARS
1	Reduction of initial oil film to equilibrium oil film.	Intelsat IV historical data.	2-4
2	Gradual reduction of oil film from initiation of equilibrium film.	o Loss of oil through evaporation/migration due to temperature differential. o TACSAT historical data. o Bearing and lubricant characteristics.	10
3	Progression of metallic wear in boundary lubrication regime after loss of EHD film (Ref.2).	o Composite roughness of balls and races. o Lubricant characteristics. o Calculation based on empirical data.	0.5

Wheel Bearings

Sizes of ball bearings used in mentum wheels vary according to the angular momentum of the wheel, but a large range of momentum is achieved by several wheel manufacturers with 12 millimeter bore bearings supporting the wheel. A typical bearing arrangement consists of two pairs of angular contact bearings mounted in face to face configurations within individual labyrinth sealed cartridges. The cartridges are spaced on a common shaft to provide a wheel base (Ref. 4). Another arrangement employs a single pair of angular contact bearings with precision spacers between the clamped races in a back to back configuration, thereby providing the wheel base.

Momentum wheels supported on ball bearings usually operate in a speed range of 3,000 to 4,000 rpm, but speeds within the range of 1,000 to 6,000 rpm have been used. This range of speeds, combined with commonly used lubricants, preloads, and ball and race finishes, ensures elastohydrodynamic lubrication provided the oil film is adequately maintained by the lubrication system.

In a manner similar to that used for despin bearings, cotton-phenolic ball retainers are impregnated with oil to supply part of the lubrication. Since the amount of this oil is only one to three milligrams per bearing retainer, it is not regarded as the primary lubricant source. Additional oil may enter the ball-race interface region by bleeding out of grease adhering to the bearing rings, or it may migrate from porous oil-impregnated reservoirs or grease-filled reservoirs suitably located within the bearing enclosure.

Since the ball retainer provides a minor contribution to the lubrication life in wheel bearings and the mechanism by which oil is resupplied to the balls and races is varied and ill-defined, life expectancy is based largely on performance history. Successful operation in orbit is known to have occurred for five to six years, and similar continuous operating periods have been achieved with wheels operating in vacuum life tests.

NEW TECHNIQUES FOR ASSURANCE OF LUBRICANT SUPPLY

Life demonstrations for both despin and wheel bearings are impressive and, when coupled with analytical techniques, provide high confidence of satisfying a 10-year requirement. Analytical methods for predicting life of despin bearings are probably somewhat more established than those applicable to wheel bearings because of the availability of fairly extensive data on torque, temperatures and performance from satellites in orbit. These data, derived especially from TACSAT and Intelsat IV satellites, build confidence that the despin lubricant systems can last for more than ten years. Nevertheless, the desire always exists to increase the margin or to back up the system with an alternate. Toward this end, Hughes has developed two lubrication techniques that provide basically different approaches to augmenting the lubricant supply for greater assurance of long bearing life.

Relubrication by Command

The specifications for the Intelsat IVA and Comstar I satellites required that the despin bearing assembly include a feature that would permit adding oil to the bearings on command from ground control. Prior to contract award Hughes had applied research to this subject, had developed a working engineering model of a commandable oiler and had confirmed its performance. The oiler was applied directly to the Intelsat IVA and Comstar I satellites following optimization of size, weight and power consumption.

Before selecting the relubrication approach, numerous ideas were collected, evaluated and finally narrowed to three models for experimental demonstration. One approach had no moving parts, consisting of an annular metal cartridge which contained porous material impregnated with oil and a heater to cause the oil to evaporate. This device was mounted immediately adjacent to a bearing and was found to transfer oil by evaporative means. The approach was dropped because of high power consumption

and poor efficiency; i.e., only about 35 percent of the oil given up by the cartridge reached the bearing. The method also suffered from indefinite control of quantity of oil transferred. The other two methods were both positive displacement types which delivered incremental quantities of oil with each stroke of a solenoid. Both of these approaches incorporated features to cope with cavitation or vapor lock, which occurred on an earlier feasibility model. This problem was solved in one version by employing a sealed bellows, the only outlet of which was a port normally closed by a check valve. The bellows was completely filled with degassed oil. Operation of the solenoid would cause a ratcheting mechanism to compress the bellows an incremental amount causing the check valve to open momentarily, allowing oil to pass through a duct to the bearing. This version of a solenoid-actuated oiler was abandoned for the following reasons:

o The bellows absorbed some of the impulse of the solenoid stroke, resulting in a low pressure for injecting oil into the bearing.

o The ratchet mechanism had wearing surfaces which required dry lubrication.

o The increment of oil ejected per stroke of the solenoid was larger than desired.

The selected oiler approach has a reservoir of oil contained in a chamber which includes a small cylinder. A piston, integral with the solenoid plunger, engages the cylinder when the solenoid is stroked. Since the moving plunger of the solenoid is contained within the oil chamber, the single moving part of the oiler is well lubricated. A quantity of oil equal to the volume of the cylinder (less leakage) is ejected from the oiler through a ball check valve at each stroke of the solenoid, thereby transferring oil in small known amounts. The oilers are oriented on the spinning bearing housing so that centrifugal force feeds oil from the chamber into the cylinder at all times. A breathing port on the oiler allows the escape of air from the interior of the oiler as the satellite enters the vacuum of space, but the port incorporates a series of fine-mesh screens which prevent the loss of oil during adverse orientation in earth's gravity. The oiler appears in cross-section in Figure 2, which illustrates the features described above. Table 2 provides design parameters of the oiler.

Table 2. Oiler functional parameters

Solenoid:

Stroke	.317 inch
Coil Resistance	17.3 ohms
Excitation	30.5 volts
Current	1.76 amps
Power	54 watts
Time to Stroke	90 milliseconds

Oil System:

Oil Supply	6.0 grams
Oil Pumped Per Stroke	45 milligrams
Strokes to Empty	130
Check Valve Opens	15 - 20 psig

General:

Weight	0.85 pound
Diameter	2.25 inches
Length	2.78 inches

In the Intelsat IVA satellite, the coils of the two oilers are connected to simple pulsing circuits identical to the type used for commanding attitude control jets. When the despin bearing assembly is built, ducts made of 1/16 inch stainless steel tubing are installed into the housing to carry oil from the mounting surfaces of the oilers to the forward and aft bearings, respectively. Oil leaves the formed end of either duct with a velocity and direction which cause it to deposit directly onto the outer raceways of the bearings. Since the bearing is rotating at about 50 rpm, the balls immediately pick up the new oil and distribute it throughout the bearing. Figure 3 illustrates the mounting of oilers on the Intelsat IVA despin assembly. Each oiler is separately commandable so that either bearing may be reoiled independently.

Since Intelsat IVA satellites are in geosynchronous orbit, every six months an eclipse season is encountered. During several days at the height of each season, the temperature at the despin bearings changes

about 15°F within a 24-hour period. Telemetry data on despin torque and bearing temperatures provide the inputs needed to calculate the oil film thickness in the bearings, and this result provides operators with an input for determining use of the oilers. (Ref. 3) Figure 4 is the torque-temperature profile of the F-4 satellite of the Intelsat IV series on 19 March 1972. These data indicated an oil film thickness of 500 microinches (early stage 1), which is sufficient to preclude use of oilers had they existed on the Intelsat IV. By March of 1975 the change in torque due to eclipse had reduced to much smaller values, indicating the initiation of stage 2. Similar conditions have occurred on other Intelsat IV satellites, indicating that they are following the classical lubrication profile.

Passive Relubrication

The cotton-phenolic ball retainer impregnated with oil has been a standard feature in wet-lubricated space bearings for many years. One of its shortcomings is the relatively small amount of retained oil ranging from about one to five percent by weight, a small fraction of which will actually feed to the bearing. This situation prompted Hughes to develop a ball retainer with much greater oil retention over the period 1971 to 1974. The result was the foam (nitrile acrylic copolymer) retainer illustrated in Figure 5 (Ref. 5). Retainers are illustrated with bearings having bore sizes of 60 and 12 millimeters, typical for despin bearings and momentum wheels, respectively. Foam retainers contain from 10 to 100 times more oil than cotton-phenolic retainers, and because of the small size of the capillaries which connect the numerous reservoirs within the foam cellular structure, the oil is metered to the bearing at a controlled rate to maintain the oil film. Thus, the foam retainer constitutes a passive oil replenishment technique with far greater capacity than the conventional approach.

The foam retainer has been applied to bearings having bore sizes of 150, 90, 80, 60, 12 and 6 millimeters. Vacuum life tests are presently running on four each of 60 and 12 millimeter bearings. The former, typical despin bearings, have been operating at 100 rpm for three and one-half years, and the latter, typical momentum wheel bearings, have been operating at 5,000 rpm for one year.

Because the capillaries in foam retainers average about 10 microns in diameter, they maintain a calculated 90 microinch thick film of oil on balls and races versus 20 microinches for cotton-phenolic retainers. This thicker film insures ample oil for elastohydrodynamic lubrication, but it also produces a higher oil churning torque. Consequently, despin bearings with foam retainers run at about a 20 percent higher torque than with cotton-phenolic retainers after equilibrium film has been established. The duration of stage 1 for despin bearings with foam retainers is comparable to that for bearings with cotton-phenolic retainers, but duration of stage 2 is calculated to be 122 years.

Figure 6 illustrates two momentum wheel fixtures, each containing four 12 millimeter bearings. One employs the baseline lubrication approach with cotton-phenolic retainers, while the other has foam retainers. As with despin bearings, the foam retainers maintain a higher equilibrium film of oil on the bearing metal than is the case with cotton-

phenolic retainers. This causes a more severe running torque penalty, 1.1 ounce-inches versus 0.5 ounce-inch, because of the much higher operating speed. Continuation of life testing is required to provide data leading to possible application of foam retainers to wheel bearings.

The extensive life testing and excellent performance of foam retainers in despin bearings has resulted in their adoption for the despin assembly of the Pioneer Venus satellite.

CONCLUSION

The two lubricant augmentation approaches provide totally different solutions to satisfy the desire for greater lubrication assurance of wet-lubricated space bearings. Each has been adopted for flight, one already in orbit and one scheduled on a flight program. Table 3 shows an attempt to compare the relative advantages and disadvantages of the two techniques. This evaluation reveals that a clear-cut overall advantage does not exist for either approach, but rather that the choice should be made with relation to specific requirements of each application.

Table 3. Comparison of Oil Augmentation Techniques

ACTIVE REPLENISHMENT COMMANDABLE OILER	PASSIVE REPLENISHMENT FOAM RETAINER
ADVANTAGES	
1. Preserves flight-proven ball retainer.	1. No added weight or volume.
2. Augmented oil supply reserved for emergency.	2. Oil replenishment is automatic.
3. Replenishment by conscious command allows thinner oil films, less torque.	3. Failure modes are virtually non-existent.
DISADVANTAGES	
1. Weight and volume penalty.	1. Departure from flight-proven ball retainer.
2. Command channel(s) required.	2. Viscous friction torque is higher.
3. Failure modes exist.	3. Thick oil films can cause more torque variation.

REFERENCES

1. Glassow, F. A., "Despin Bearing Technology and Applications for Communications Satellites," Paper No. 70-459, AIAA 3rd Communications Satellite Systems Conference, Los Angeles, CA, April 6 - 8, 1970.

2. "New Bearings Meet the Challenge of Speed, Load and Temperature", Product Engineering, August 1973, pp. 21 - 25.

3. Glassow, F. A., Hofmann, G., "Intelsat IV Despin Lubrication Performance," AIAA/CASI 6th Communications Satellite Systems Conference, Montreal, Canada, April 5 - 8, 1976.

4. Davis, P., Sutter, C., Reistad, K., "A Versatile New Reaction Wheel Used on Fleet Sat Com and Canadian CTS," IEEE Electronics and Aerospace Systems Conference, Washington, D. C., October 7 - 9, 1974.

5. Christy, R. I., "Evaluation of A Nitrile-Acrylic Copolymer As A Ball Bearing Retainer Material," Paper No. 74AM-5A-1, ASLE 29th Annual Meeting, Cleveland, Ohio, April 28 - May 2, 1974.
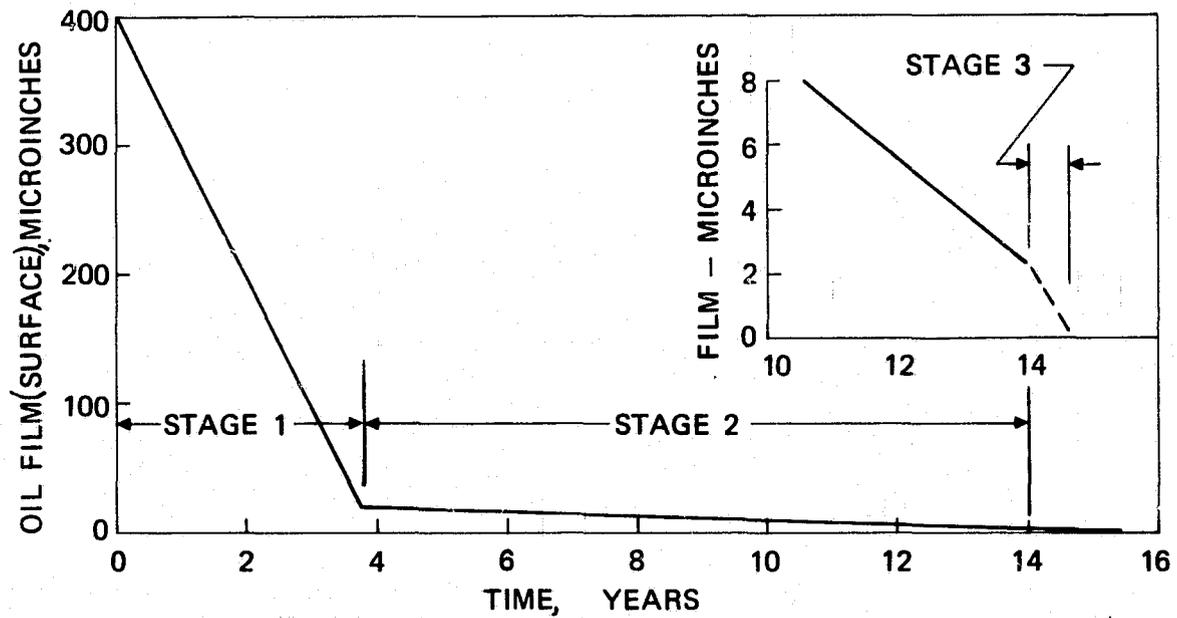
FIGURE 1. LIFE PROFILE OF OIL FILM THICKNESS IN DESPIN BEARINGS
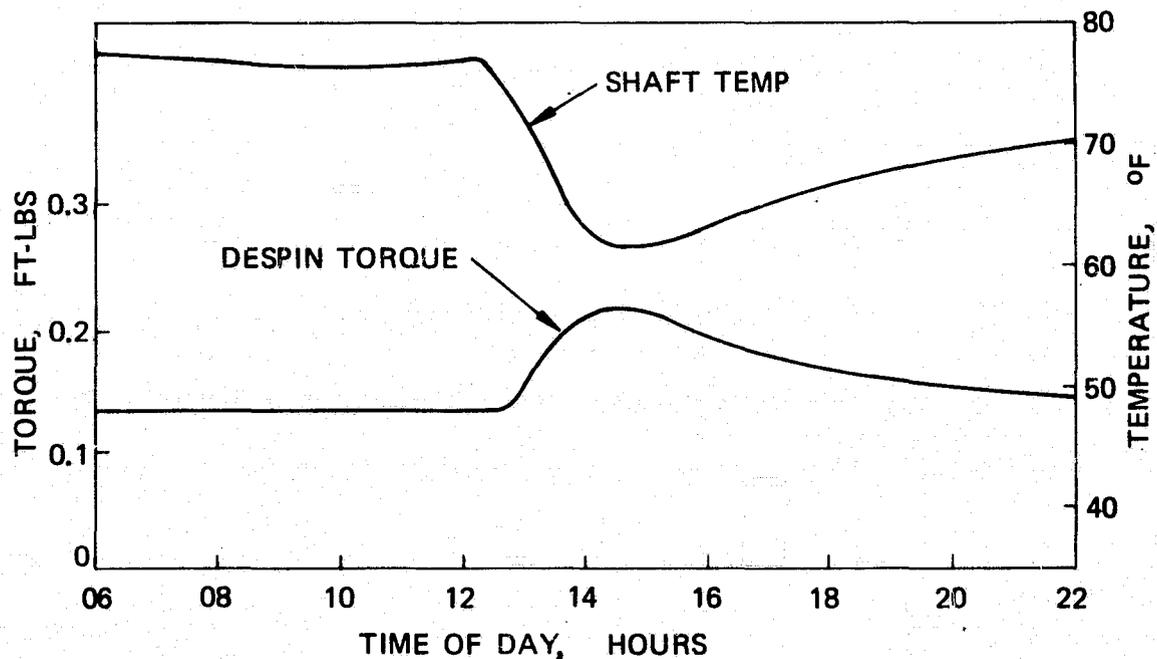
FIGURE 4. TORQUE/TEMPERATURE PROFILE OF INTELSAT IV,
F-4, ON 19 MARCH 1972 DURING ECLIPSE
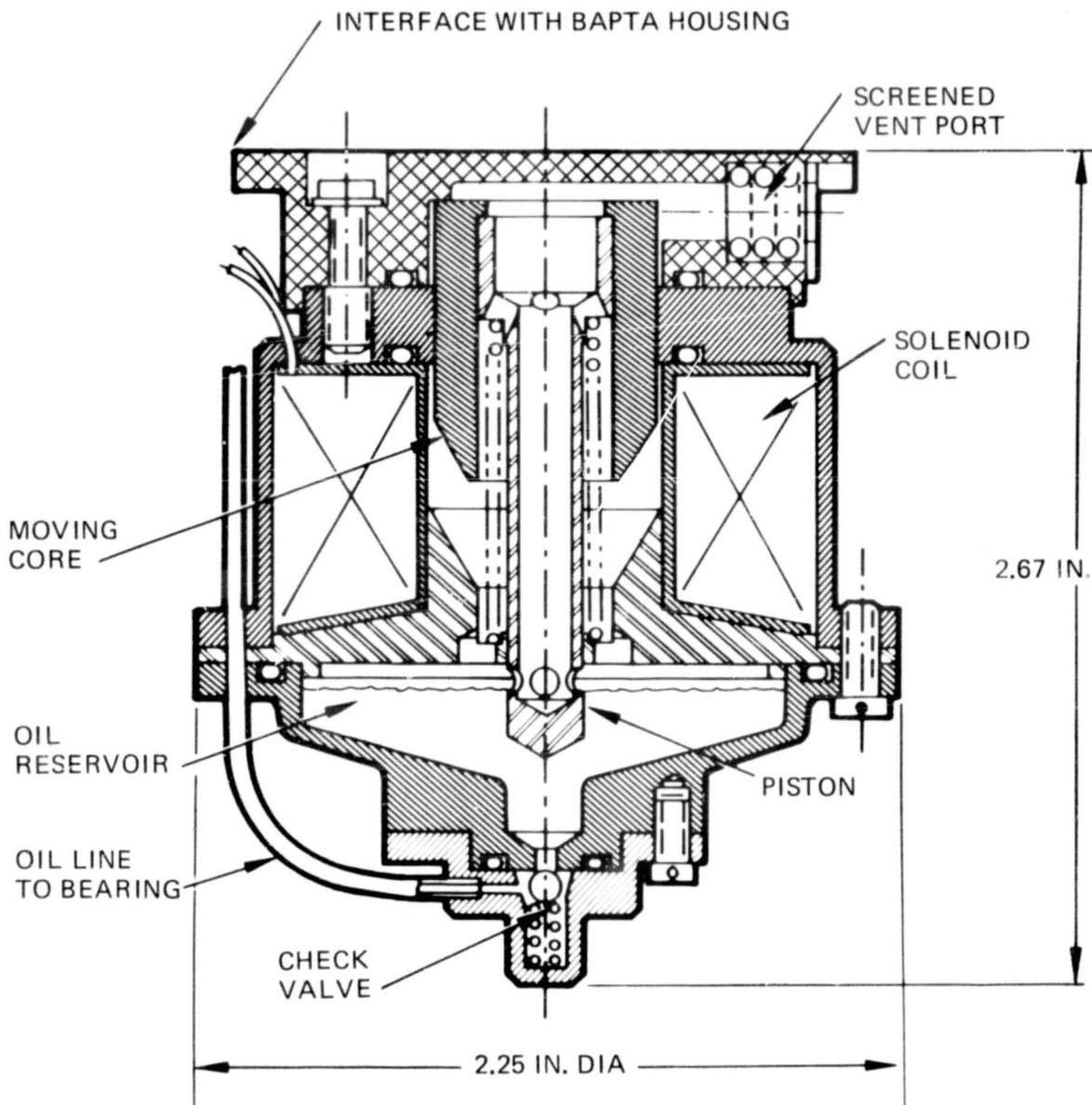
FIGURE 2. CROSS-SECTION OF SOLENOID-ACTIVATED OILER

The figure shows a cross-section with the following labels:
- INTERFACE WITH BAPTA HOUSING
- SCREENED VENT PORT
- SOLENOID COIL
- MOVING CORE
- 2.67 IN.
- OIL RESERVOIR
- PISTON
- OIL LINE TO BEARING
- CHECK VALVE
- 2.25 IN. DIA
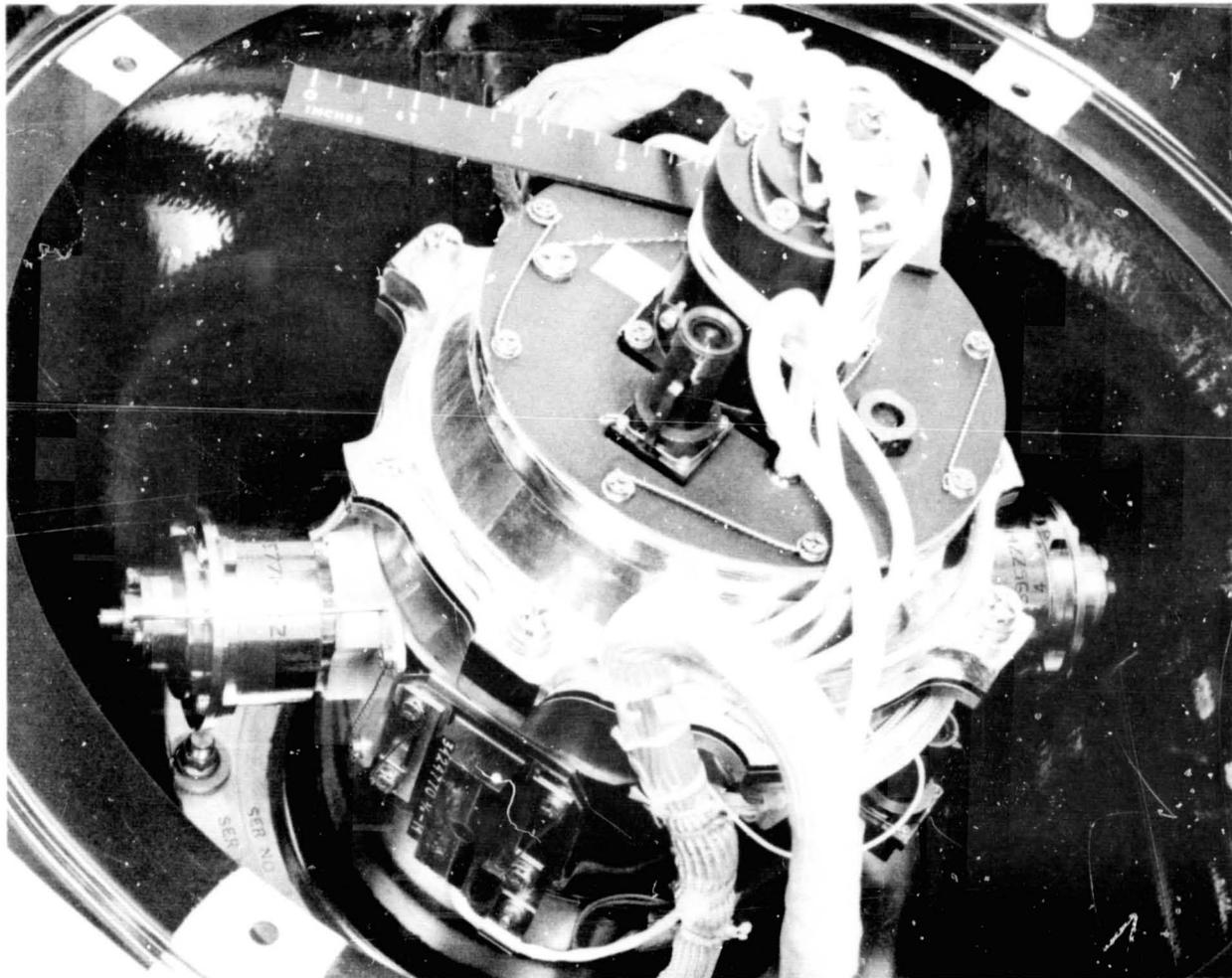
Figure 3.   Oiler Installation on Intelsat IVA Despin Assembly

Figure 5. Foam Retainers with 60 and 12 mm Bearings
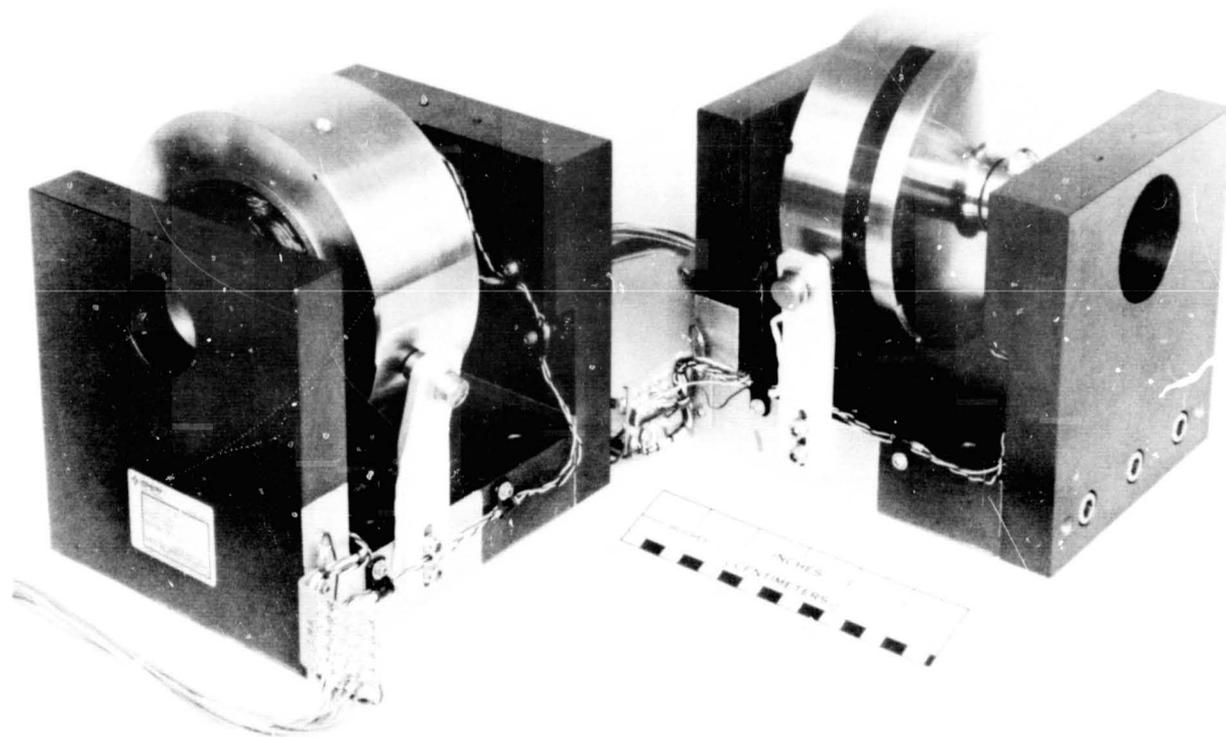
Figure 6.   Momentum Wheel Fixtures in 5,000 RPM Life Test

DESIGN OF MECHANISMS TO LOCK/LATCH SYSTEMS

UNDER ROTATIONAL OR TRANSLATIONAL MOTION

By Rohinton P. Billimoria

Planning Research Corporation

ABSTRACT

Several systems in the aerospace industry undergo rotational or translatioral motion. These bodies/systems need to be stopped and locked/latched at the end of their path. Some examples of these systems in the aerospace industry (including launch vehicle, spacecraft, and the ground support equipment) are the Command Module Access Arm, Service Arms, Docking Module of the ASTP and the Orbiter Access Arm for the Space Shuttle (Figures 1 and 2). This paper covers two major aspects: (1) various methods of latching and (2) selection of the optimum method for latching, depending on the application and the design requirement criteria.

INTRODUCTION

Before analyzing the design aspect of these mechanisms, it is worthwhile mentioning the major functions performed by them. Because of their critical functions of latching and unlatching, the mechanisms become part of the launch critical phase. For some applications, these functions are performed after the vehicle has begun lift-off.

Four major operations need to be performed by these mechanisms:

(1)   Stopping the system

(2)   Positive locking/latching

(3)   Maintaining the system locked due to loads on the mechanism

(4)   Positive unlatch

Each of these modes of the lock mechanism has to be designed depending on the critical modes of the application involved. However, the mechanism utilized to stop the systems may or may not be an integral part of the latch assembly. A brief discussion of all these modes of operation will be presented in the following paragraphs.

MODES OF OPERATIONS

The first major function to be performed is to stop the system under rotational or translational motion. Systems can be stopped by utilizing either shock absorbers or attenuators, or even by bringing them to a hard stop. However, most systems require deceleration before being brought in contact with the stop mechanism, i.e., by coupling the system to a cam mechanism or engaging a skid plate.

The next three modes involve mainly the latching and unlatching operations. Figure 3 illustrates various options that could be set up for the three phases of the locking mechanism. Studies and analyses have to be conducted to select the best possible option, depending on the critical modes of application involved.

DEVELOPMENTAL PHASES

The processes involved in the development of a product or mechanism are highly diversified and include a wide variety of detail. However, the typical detail in all these mechanisms involves four basic factors which should always be considered:

(1) Simplicity of design

(2) Ease of operation

(3) Extent of failure of the mechanism due to

    a) System failure, i.e., failure in the power system

    b) Component failure, i.e., failure in the linkages of the mechanism

(4) Developmental and manufacturing cost

After developing the concepts, selection of the kinematic scheme should be outlined. The decision as to the type or types of mechanism to transmit and transform the motion from the input to the output is an important one — for it may limit the selection of the components of the mechanism, it limits the capacity of the hydraulic or pneumatic power system, and it may determine the mechanical efficiency and cost of the latch mechanism.

Three concepts for the design of locks are briefly discussed below, with reference to Figures 4 through 8.

CONCEPTUAL DESIGN

Following the selection of the kinematic scheme and the
concept, further design can be incorporated. Three conceptual
designs are discussed below, with calculations and equations
shown for the locks utilized on the Command Module Access Arm
and one which will be used on the Orbiter Access Arm.

Figures 4 and 6 illustrate the Extend Stop and Lock mech-
anism used on the Command Module Access Arm. The main features
of this mechanism are the hard stop, automatic lock with over-
center latch and powered unlatch (system utilizing an hydraulic
cylinder).
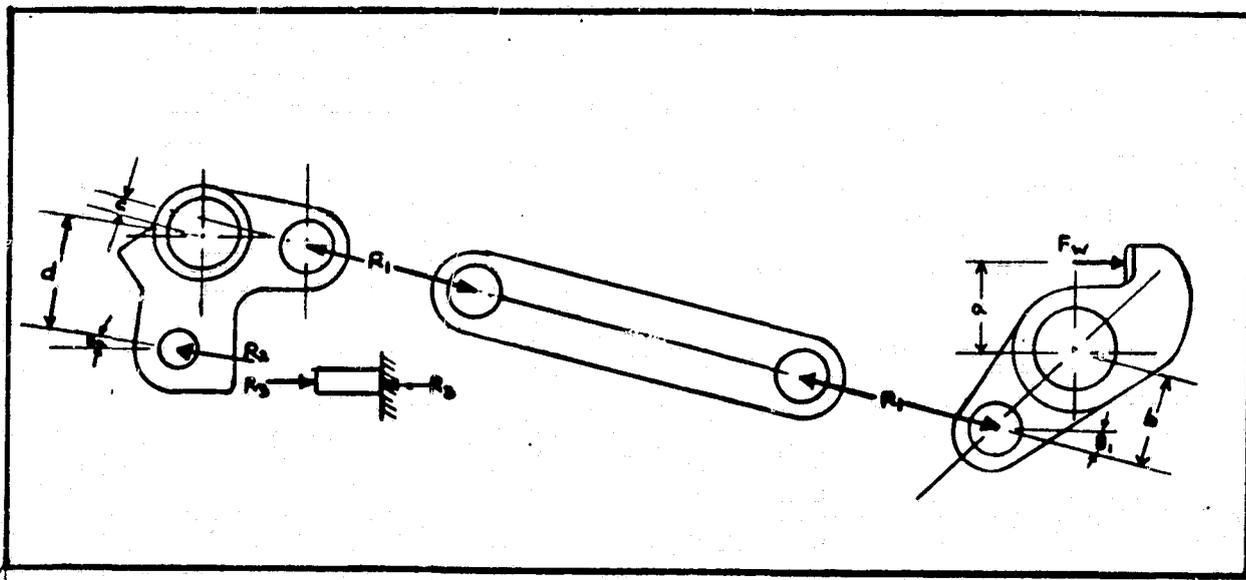
EXHIBIT A

The free body diagram of the latch mechanism is shown in
Exhibit A above. Once the links are in the locked position, the
kinematic scheme is so arranged that the links over-center. This
prevents the system from unlatching when a load is applied from
the system (i.e., the arm) onto the latch. The power required to
unlatch depends on the geometry of the links. Load on the latch
(when the arm is locked) is transmitted into the base block of
the latch weldment. This load on the base block could be deter-
mined by using the following equation:

$$R_3 = \frac{F_w \times a \times c}{b \times d} \cdot \cos \theta_2$$

where

F_W — load on the latch

R_3 — load on the base block

θ_2 — angle made by the actuator with the base block

a, b, c & d — geometric lengths on links

Figures 5 and 7 illustrate the latches used to hold the Apollo arms in the retracted condition. The main feature of this latch is the remote latching with a positive locking system (accomplished by holding the cam up against latch weldment). The arm is decelerated by riding it over a skid plate with the final impact absorbed by two shock absorbers. The cam roller principle for unlatching does not link the hydraulic/pneumatic power to the latch. This system can have a manual override for use in the event of system power failure. However, the force required to unlatch this mechanism is greater than that required by the Extend Stop and Lock mechanism (assuming that the forces on the latch for both the mechanisms are the same). This is due to the fact that the remote latch mechanism, shown in Figure 7, retracts towards the load and not away from it.

Figure 8 illustrates the lock mechanism to be used on the Orbiter Access Arm. The main features for this lock are hard stop, remote lock with over-center latch and powered unlatch (system utilizing pneumatic cylinder).
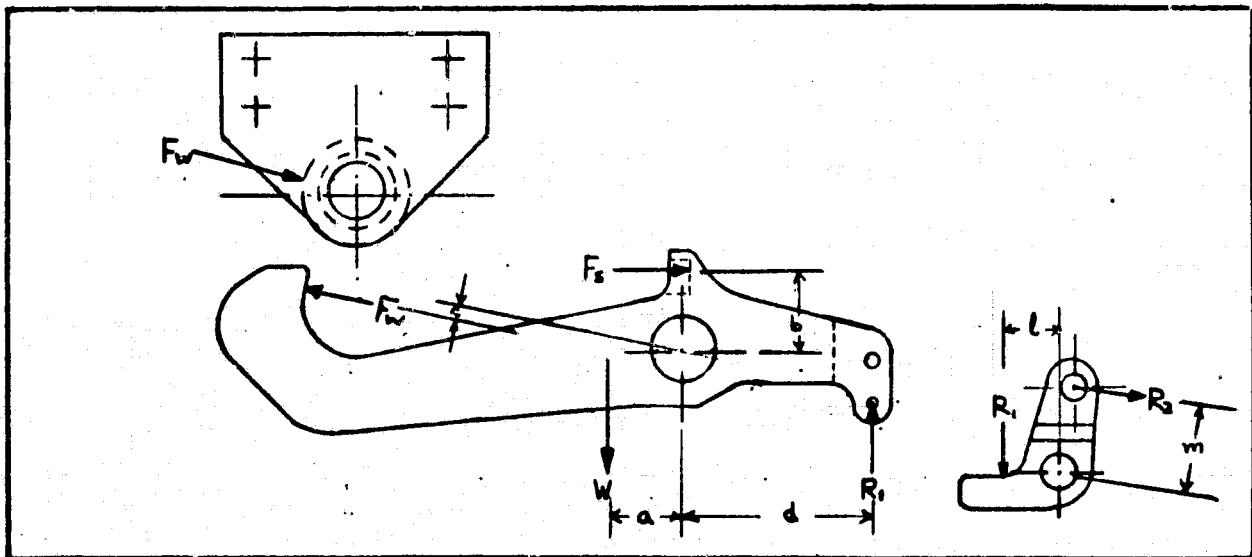

EXHIBIT B

Exhibit B illustrates the free body diagram of the latch mechanism. The cam roller arrangement gives the mechanism the ability to have a manual override, which can be used in the event

of system power failure. Another distinguishing characteristic of this type of kinematic scheme is that the force required to unlatch this mechanism is comparatively smaller than that required by the Extend Stop and Lock mechanism (Figure 6). The force required to unlatch can be determined by the following equation:

$$R_2 = \frac{F_w \times c + F_s \times b - W \times a}{d} \cdot \frac{1}{m}$$

where

R_2 — force required to unlatch

F_w — load on the latch

F_s — spring load on the latch

W — latch weight

$a, b, c, d, 1 \& m$ — geometric lengths on links

CONCLUDING REMARKS

In conclusion, one may realize that more than a cursory investigation is useful for final mechanism selection. Proper definition of requirements, with effective trade studies performed, would further aid in developing or selecting the right concept for a particular application. Furthermore, because of the complexity of detail design that arises, consideration should be given to whether the mechanism can be manufactured with minimum expense, can be assembled efficiently, and can be serviced and repaired easily.

REFERENCES

1. Beggs, Joseph Stiles: Mechanism, McGraw-Hill Book Co., N. Y.

2. Faires, V. M., and R. M. Wugren: Problems on Design of Machine Elements, The Macmillan Company, N. Y.

3. General Criteria for Design of New Equipment and Facilities to be Utilized at Kennedy Space Center, Rev. 1, AP-863, John F. Kennedy Space Center, KSC, Florida, February 2, 1973.

4. Technical Manual, Apollo/Saturn V, Mobile Launcher Service Arms Operations and Maintenance, TM-509, November 25, 1968.

DOCKING SYSTEM, ACTIVE

DOCKING SYSTEM, PASSIVE

Body-mounted latches

Thrusters

Attenuators

Guide pin

Docking seal

Z_5

Y_5

X_5

Structural latches

Docking seal

Docking interface

Supporting rod

Y_5

X_5

Z_5

Capture latches

Guide ring (extended)

Guide ring (retracted)

Docking system base

Socket
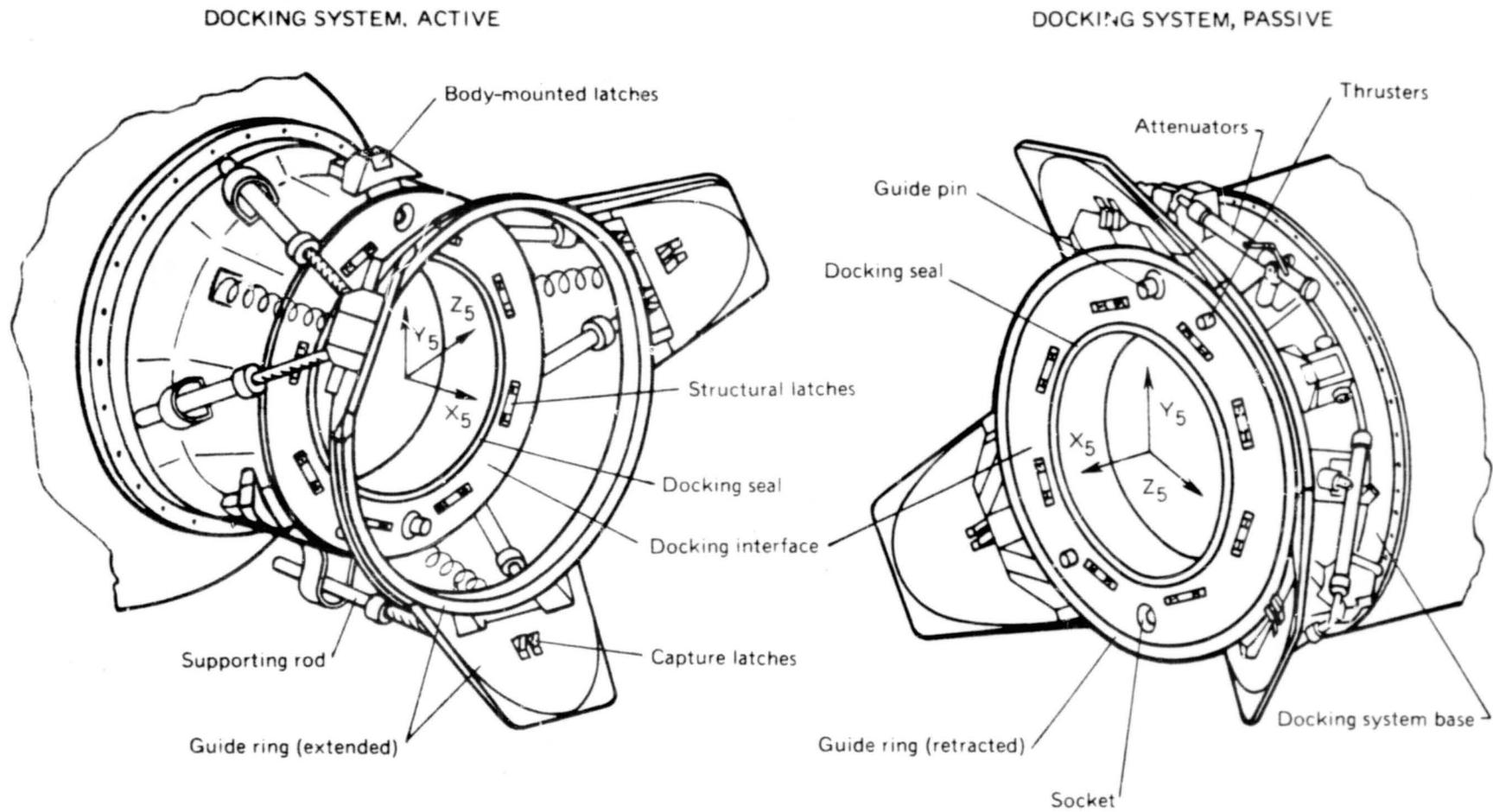
Figure 1.   Docking System---ASTP.

ACCUMULATOR RACK ·

CONTROL CONSOLE NO. 1

SHOCK ABSORBERS

MOBILE LAUNCHER (320-FOOT LEVEL)

LATCH ASSEMBLY

WATER QUENCH SYSTEM

COMMAND MODULE ACCESS ARM
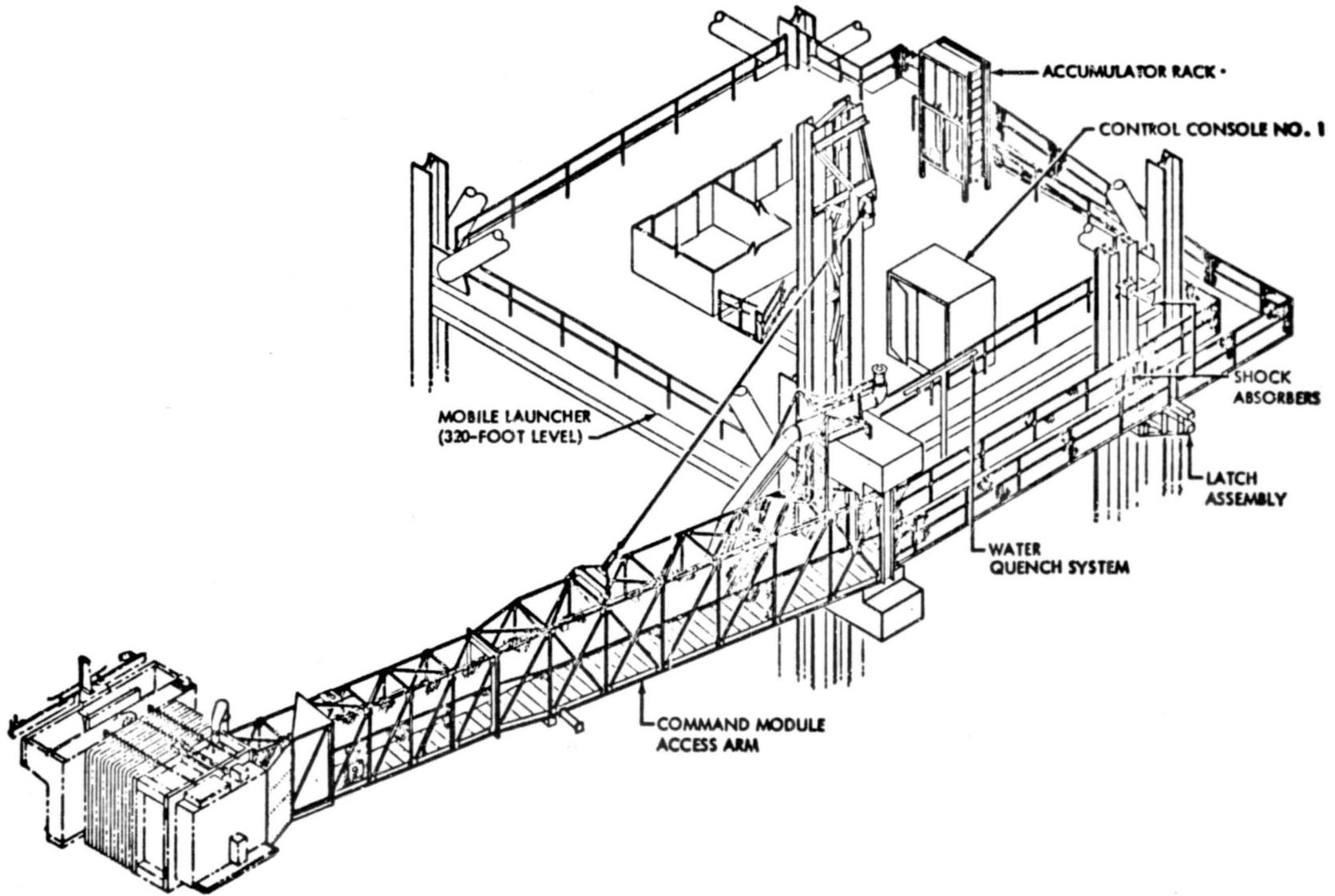
Figure 2.   Command Module Access Arm System.
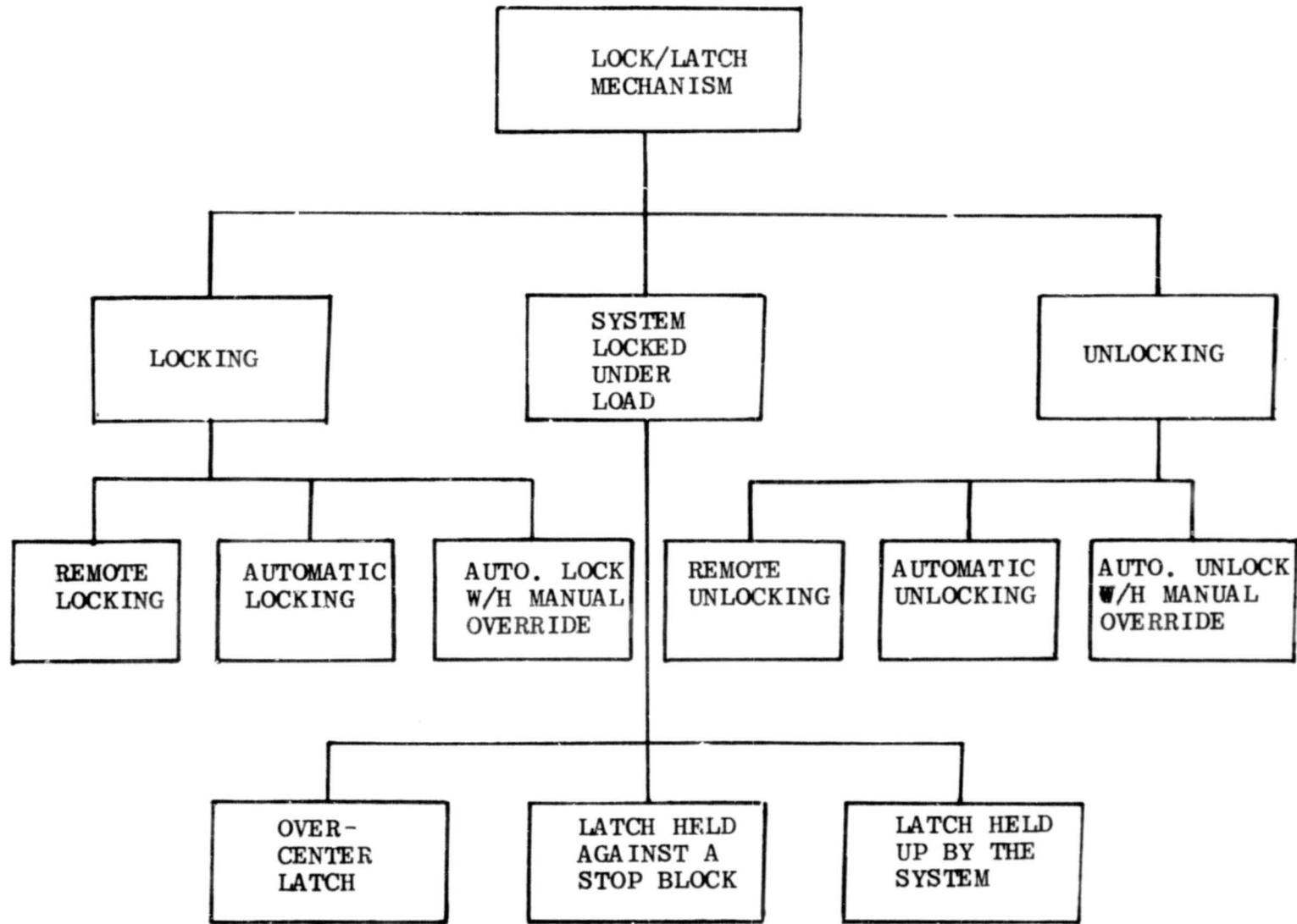
Figure 3.   Locking System Tree Diagram.
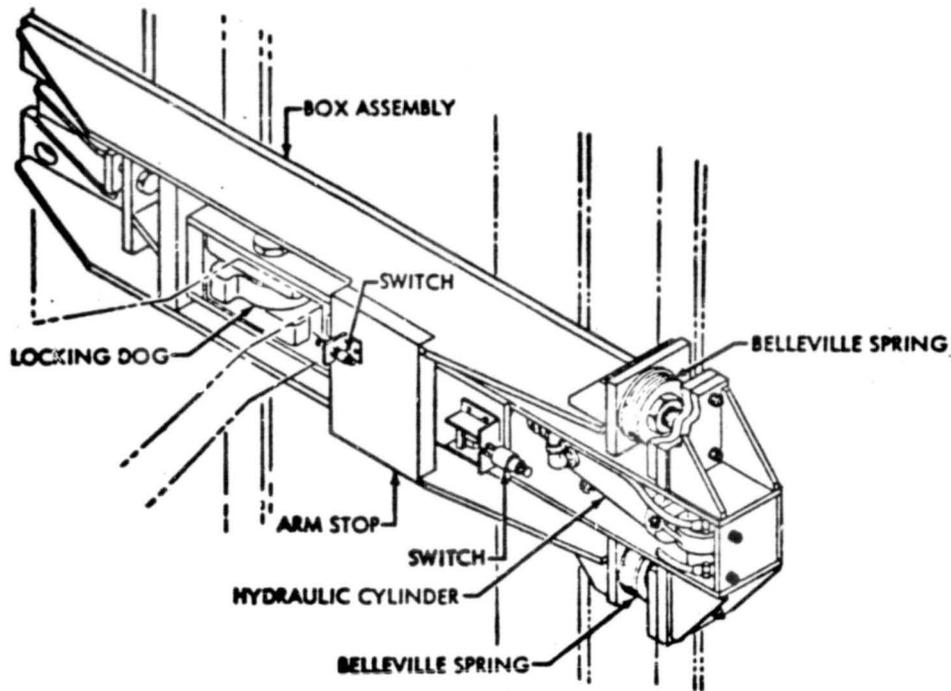
Figure 4.   Arm Extend Lock.
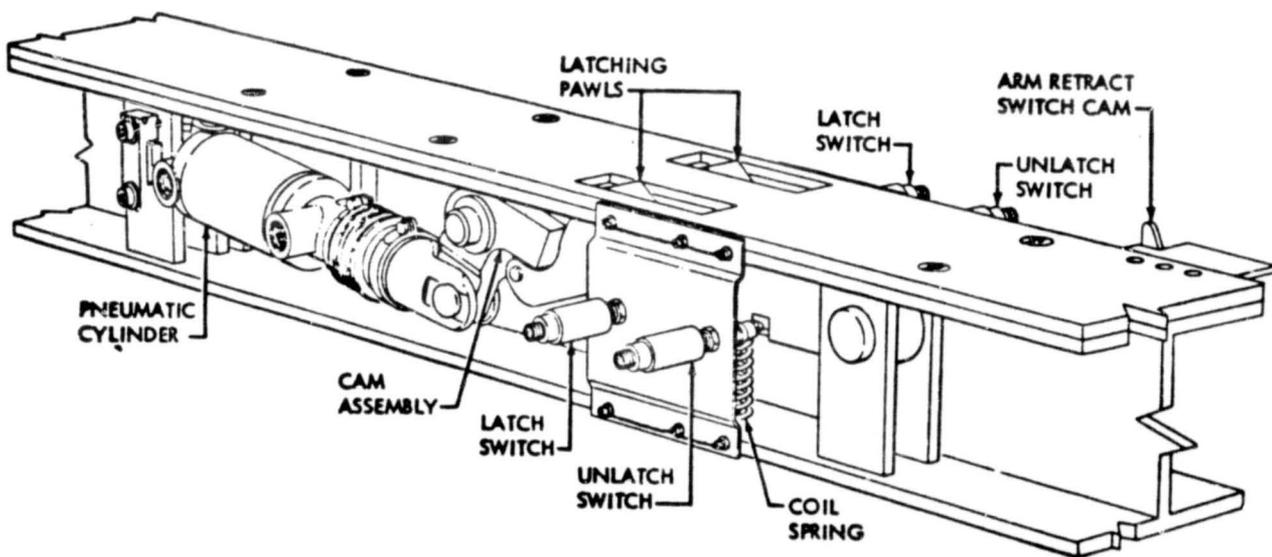
Figure 5.   Arm Latch Assembly.

CYLINDER ASSEMBLY

TOGGLE

LINK

LATCH

A

A

TOGGLE

LINK

LATCH

CYLINDER ASSEMBLY

SECTION A·A

Figure 6.   Arm Extend Lock.

CYLINDER — BELLOWS — CAM — SKID PLATE

ROLLER

CONNECTING EYE — LATCH WELDMENT — SPRING — LATCH
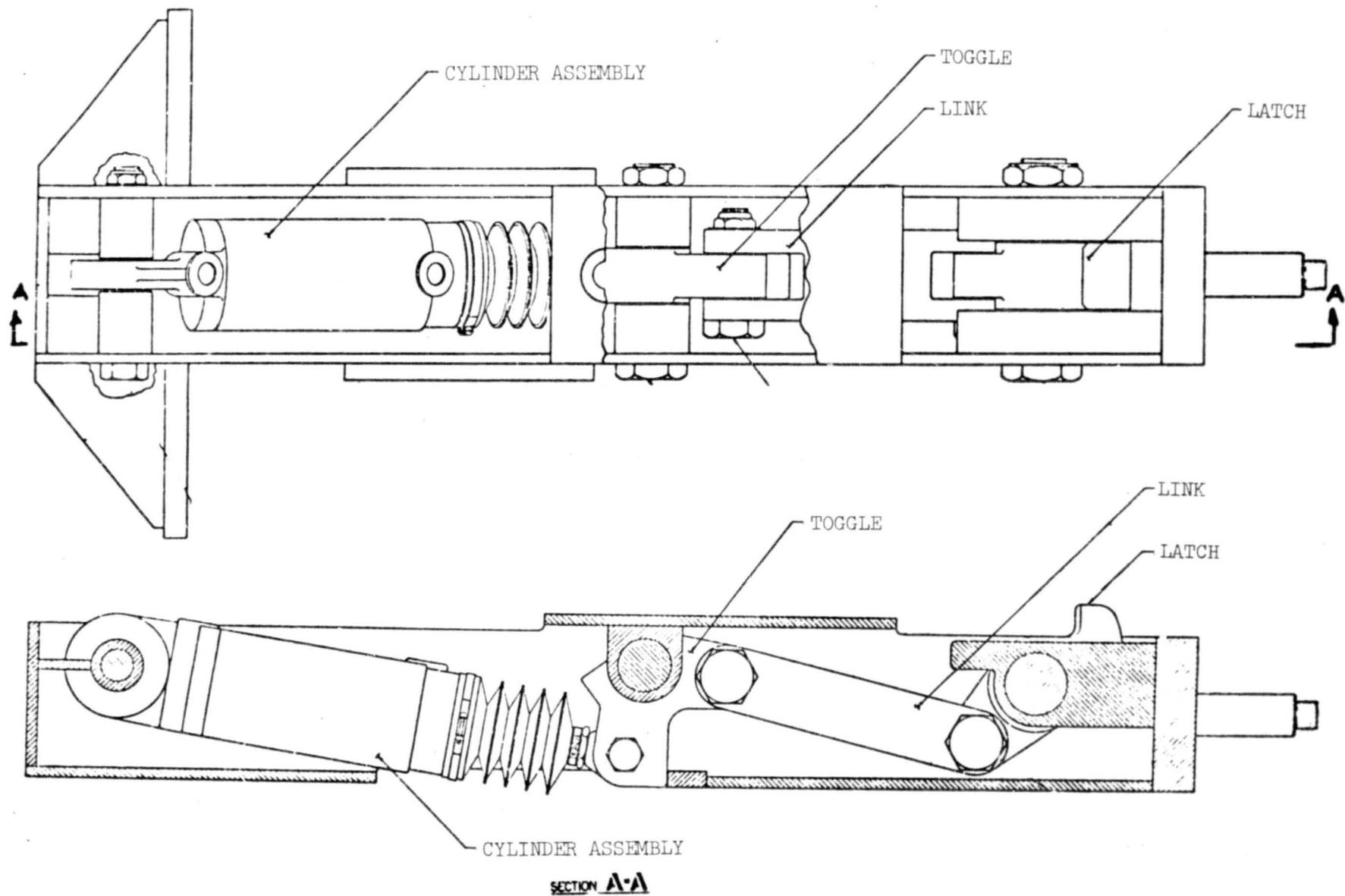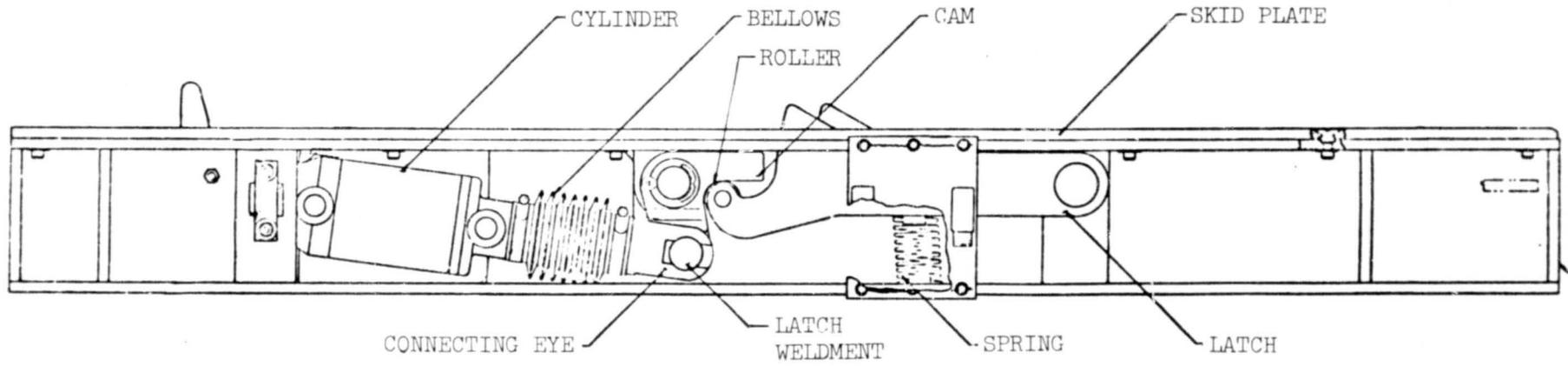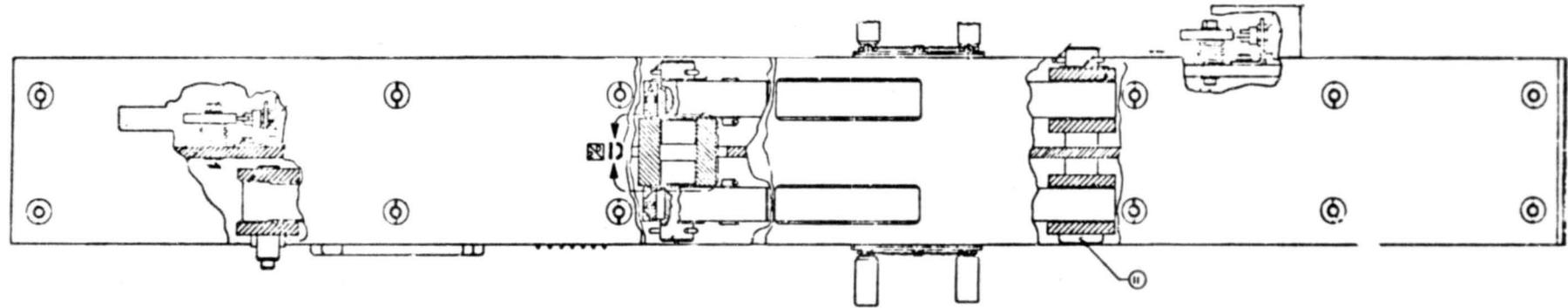
Figure 7.   Arm Latch Assembly.

Stop/Lock Weldment

Cylinder

A

A

A

A

Bearing

Hinge Post

Spring

Manual Overide Lever
Cam

Latch

Section A-A
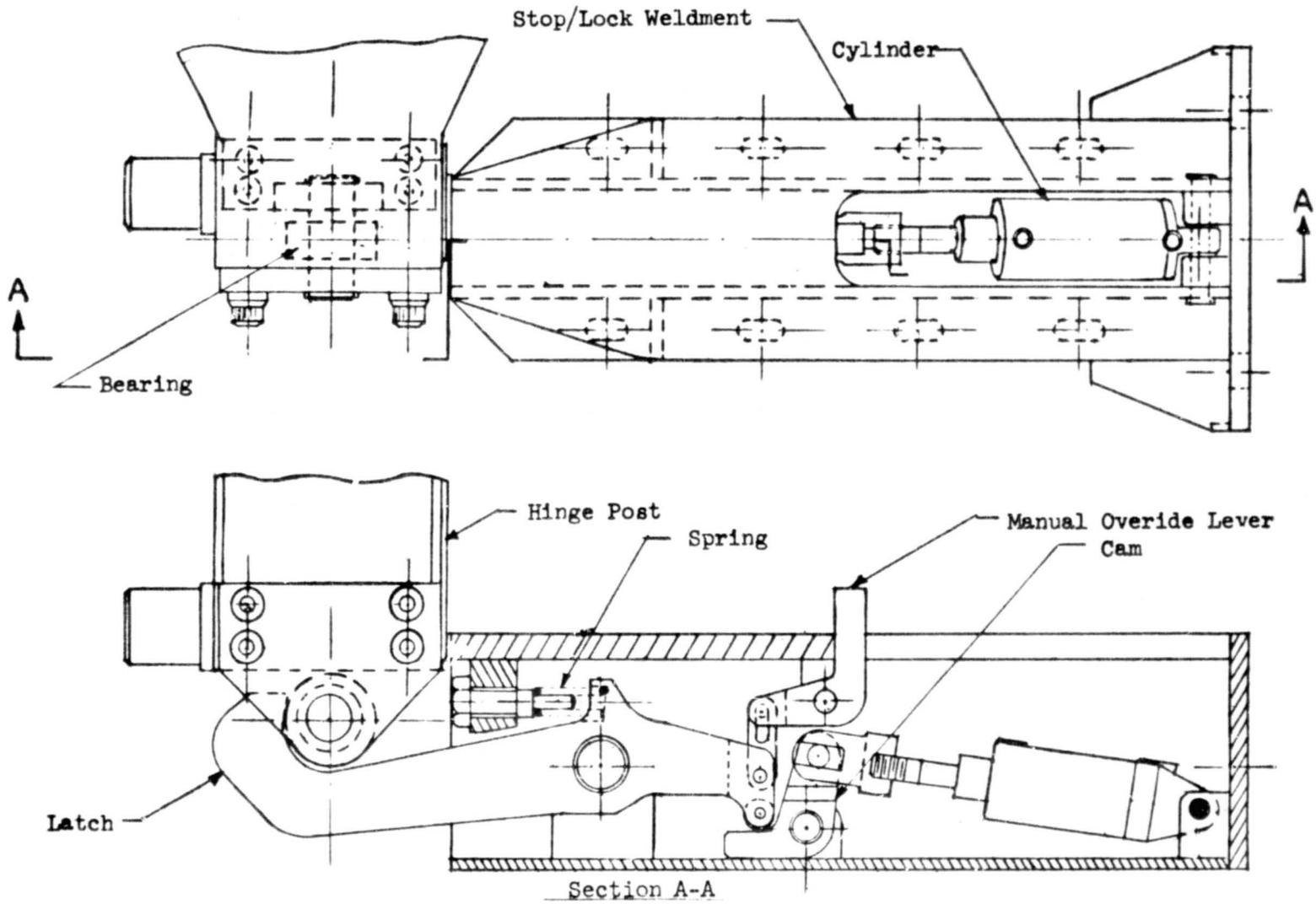
Figure 8.   Stop/Lock Assembly For The Orbiter Access Arm.

A HIGH RESOLUTION, ADJUSTABLE, LOCKABLE LASER MIRROR MOUNT*

By Dr. Curt H. Chadwick

GTE SYLVANIA, INC.
P. O. Box 188
Mountain View, California 94042

ABSTRACT

A description is given of a prototype high resolution, adjustable, lockable mirror mount suitable for use as a resonator end mirror mount in fieldable lasers. The prototype was vibrated to 15g levels, 10-2000 Hz, and was shown to be stable to within 1 arc second and settable to an accuracy of 10 arc seconds. Improvements to be made to the prototype are outlined which will significantly improve the accuracy without sacrificing the other attributes of the prototype.

INTRODUCTION

The advent of fieldable laser systems, such as satellite communications systems has mandated the construction of lasers that are capable of "HANDS , OFF" operation even in the presence of severe vibration and temperature cycling. Since the efficiency of a laser is highly dependent upon the maintenance of alignment of the two cavity end mirrors to a high degree of accuracy, the cavity end mirror mounts are critical items. Depending upon the optical design of the particular laser, this accuracy ranges from approximately 1 arc second to about 50 arc seconds. This means that these end mirrors must be adjustable to a very precise angular orientation and then locked with a minimal positional change during the locking process.

To satisfy these stringent requirements, a set of goals was formulated for the mirror mount. A prototype lockable mirror mount was then designed, fabricated, and tested. Most of the defined requirements, or design goals, were either met or exceeded by the prototype design.

DESIGN GOALS

The design goals are listed below in approximate order of decreasing importance.

Stability

As stated previously, the primary goal of the design was retention of alignment after severe vibration and temperature cycling.

Accuracy

The accura,y of an adjustment is defined as the precision to which the adjustment can be set in a single trial without overshooting the set point, plus the lockability (the maximum amount the adjustment may be disturbed when it is locked), plus the maximum amount that it may be disturbed when the adjustment mechanism is removed (in the case of removable adjustment mechanisms). In order to make the mount usable on as many lasers as possible, the mount was designed to a 1 arc second accuracy limit.

Adjustability

Adjustability is defined as the ease of adjustment of mirror orientation before locking. During the alignment of a laser, many mirror adjustments are required, especially in the case of the more developmental versions. This fact makes it very important to design the mount so that it is easily adjustable. To ensure this, it was decided that the mount would provide two perpendicular pivot axes intersecting at the center of the mirror face. This arrangement of pivot axes is the one providing the minimum theoretical"cross talk" between the axes of adjustment. In practice, other factors (mechanical tolerances for example) increase cross talk. The goal was set at 1% cross talk, a value determined to be very acceptable.

Another goal adopted to enhance adjustability was to minimize adjustment hysteresis to ensure a nearly one to one position relationship between the mirror position and adjustment knob setting.

Size and Weight

The advantages inherent in a lightweight and compact design for fieldable applications are obvious. However, there are tradeoffs to be made between this goal and the previous two goals, for a compact and lightweight design is commonly achieved by compromising accuracy and adjustability. With this in mind, a size of 2.5 inches in diameter by 1.0 inch thick was defined as the maximum envelope size which would allow the mount to conveniently mate with the greatest variety of laser structures. A weight of 8 ounces was arbitrarily chosen as an upper limit.

Range of Adjustment

The maximum range of adjustment needed in lasers is about $1.5°$ in either direction about each adjustment axis.

Proximity of Mirror Face to Front Surface of Mount

Since it is often desirable to mount other optical elements between the end mirrors, but close to a mirror face, it was determined that the mirror face should be located as close as possible to the front surface of the mount.

THE PROTOTYPE DESIGN

The prototype mirror mount is shown in Figures 1 and 2. The basic design approach used two gimbals and a frame connected by torsion bar pivots. The inner gimbal is connected to the outer gimbal by two torsion bars, while the outer gimbal is in turn connected to the frame by two more torsion bars (Figure 2). The frame is usually bolted directly to the laser structure. However in the case of the prototype, the frame was attached to the structure via four special flexures which allow for differential thermal expansion between the frame and the laser structure.

Torsional flexure pivots were used for their advantages of having no mechanical play, wear, or friction. These properties are essential in order to achieve low adjustment hysteresis and stability. The limited angular motion required permitted the use of these torsion bar pivots. An added benefit of the torsion bar pivots is that the adjustment return springs are provided by the torsion bars themselves. In the interest of stability, the two gimbals, the frame, and the four torsion bars are constructed as a unitary structure, machined from one piece of beryllium copper alloy, chosen for its good spring properties.

The adjusting screws (80 threads/inch) are threaded into bosses attached to the outer frame (Figure 1). The outer gimbal adjusting screw bears directly against the outer gimbal. The inner gimbal adjustment screw passes through the gimbals to bear on an adjustment tab (Figure 2) that is bolted directly to the inner gimbal. This is done to allow the point of contact to be nominally on the pivot axis of the outer gimbal, to minimize the cross talk. If the inner gimbal adjusting screw were mounted on the outer gimbal instead of the frame, there would theoretically be no cross talk. However, in practice, this causes severe cross talk due to random forces from the operator's hand being transmitted to the outer gimbal during adjustment.

After final machining, each pair of torsion bars is given a permanent two degree twist rotating each gimbal toward its adjustment screw. This provides the spring bias necessary for $\pm 1.5°$ rotation about the straight ahead position.

ADJUSTMENT KNOB
AND SCREW,
INNER GIMBAL

LOCK,
INNER GIMBAL
(2 PLACES)

LOCKING SCREW
INNER GIMBAL
(2 PLACES)

MOUNTING
FLEXURE
(4 PLACES)

LOCK,
OUTER GIMBAL
(2 PLACES)

LOCKING SCREW,
OUTER GIMBAL
(2 PLACES)

ADJUSTMENT KNOB
AND SCREW, OUTER
GIMBAL

MIRROR MODULE

OUTER GIMBAL

TORSION BAR,
OUTER GIMBAL

FRAME

INNER GIMBAL
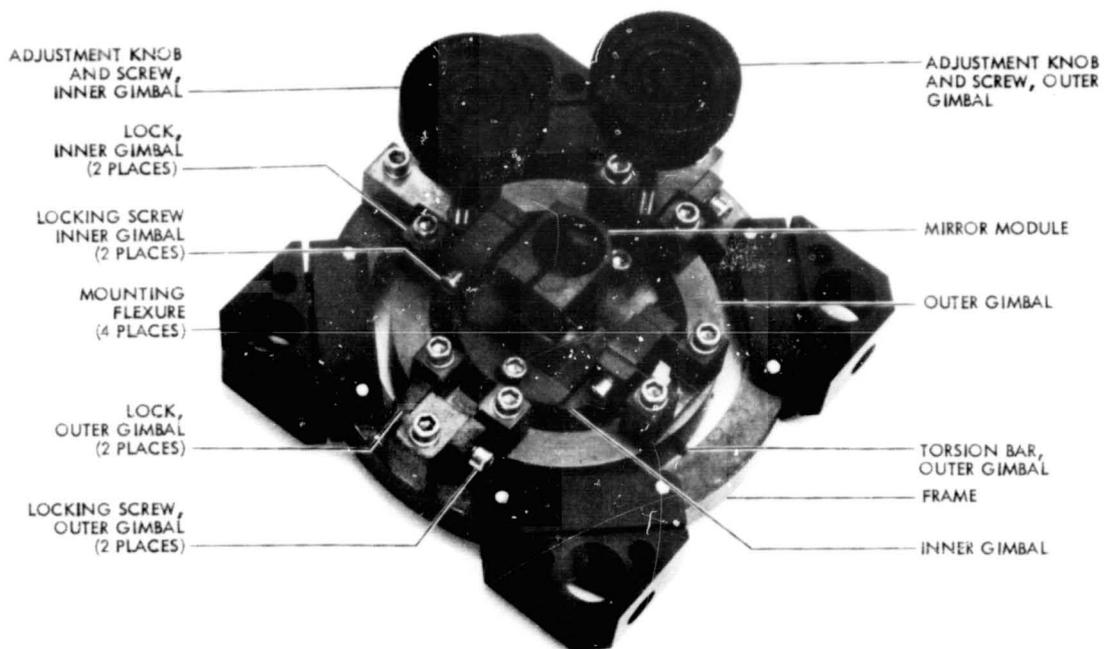
Figure 1. Back Side of Prototype Mirror Mount.
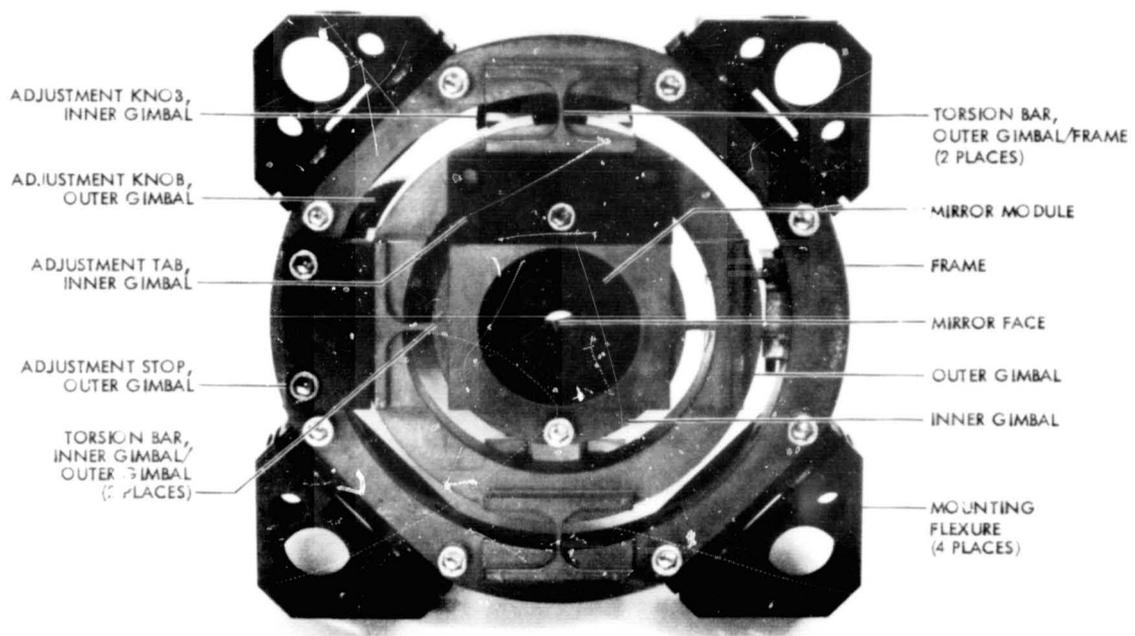
Figure 2. Front Side of Prototype Mirror Mount.

The torsion bars are 0.125 inch long with a rectangular cross section. This cross section is .050 inch by .025 inch with the longer dimension parallel to the adjusting screws. These dimensions were chosen to limit the axial translation of the mirror during adjustment to approximately 10^{-5} inch, while providing 3.5° of rotation and an acceptable spring rate. The maximum axial translation of the mirror over 3° of rotation is about 1.2×10^{-5} inch, while the torsional spring rate for a pair of torsion bars is 2.7 in.oz./deg. This design results in the pivot axes being only 0.025 inch behind the front face of the mount itself.

There are four locking mechanisms on the mirror mount, two to lock the inner gimbal to the outer gimbal, and two to lock the outer gimbal to the frame (Figure 1). Since all four mechanisms are essentially identical, only one, an inner gimbal lock, will be described in detail. This lock is shown in Figure 3. It consists of only three parts, a boss bolted to the inner gimbal, a clamp bolted to the outer gimbal, and a locking screw.

As the inner gimbal rotates within the outer gimbal, the boss translates up and down between the wings of the clamp as shown in Figure 3. When the locking screw is loose, the boss fits between the wings with approximately .0001 inch clearance on each side. This allows adjustments to be made with no friction being introduced by the locking mechanisms. The locking screw passes through a small clearance hole in one wing of the clamp, through a large clearance hole in the boss, and is threaded into the opposite wing of the clamp. When the locking screw is tightened, the wings are drawn together to clamp the boss between them. Each wing has a thin section to provide flexibility in the direction parallel to the locking screw. If the clearance between the wings and the boss is the same everywhere, there will be no net moments, or forces, exerted between the inner and outer gimbals as the locking screw is tightened. The only forces exerted on the boss will be the equal and opposite forces acting on each side of the boss in a direction parallel to the adjusting screw. For thermal stability, the clamps and boss are made of beryllium copper to match the gimbal and frame. The locking procedure consists simply of tightening the two outer gimbal locking screws followed by the two inner gimbal locking screws. After the locking screws are tightened, the adjusting screws are removed to create a smaller package and to avoid the screws shaking loose during vibration.

With the adjusting screws removed, the mount weighs about 5 oz., and is 2.5 inches in diameter and 0.7 inch thick overall.

EVALUATION OF THE PROTOTYPE

The prototype mount met or exceeded nearly all design goals. It was vibrated at 15g levels from 10-2000 Hz and temperature cycled through a 100°C temperature range with no change in setting observed using apparatus with a resolution of about 1 arc second. It is very compact (2.5 inches diameter, 0.7inch thick) and light (5 ounces). It has a 3 degree range of adjustment and the cross talk was determined to be less than 1% with a one to one relationship between adjusting knob position and the mirror settings. In addition
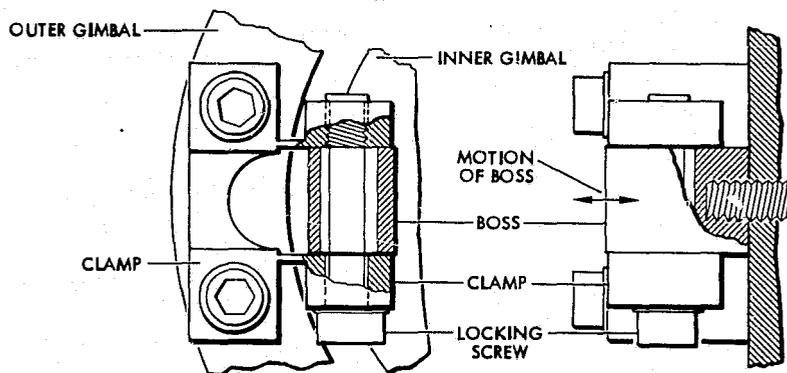
Figure 3.   Locking Mechanism, Inner Gimbal.

the mirror face is very close (.025 inch) to the front surface of the mount.

The adjustability of the mount is good and it is possible to set it to within one arc second without overshoot. However, when it is locked, a change in setting occurs which is greater than that desired, especially when locking the inner gimbal. In addition, when the adjusting screws are removed, further motion occurs. These effects combine to reduce the total accuracy of the mount to about 10 arc seconds. This accuracy makes the mount usable in most lasers but prevents its use in those requiring very accurate mirror settings.

The motion upon locking has been determined to be caused primarily by misalignment between the locking clamps and their respective bosses. The reduced performance of the inner gimbal locks as opposed to the outer gimbal locks is caused by the closer spacing of the inner gimbal torsion bars and locks. The torsion bars for the inner gimbal are only 1.2 inches apart and the two locking screws are only 1.0 inch apart. The problem is made evident when it is noted that, with the locks this close together, a motion of only 2.5 millionths of an inch at the lock causes the mirror to rotate about 1 arc second.

The motion resulting from the removal of the adjusting screw occurs as the load previously supported by the adjusting screw is taken up by the previously unloaded locks.

PROPOSED IMPROVEMENTS

A new revised design has been created that should improve the accuracy of the mount without compromising a significant number of the other goals. This design employs Bendix flexure pivots instead of torsion bars. These have a torsional spring rate about one order of magnitude smaller than the torsion bars used in the prototype. This will considerably reduce the load transferred to the locks upon removal of the adjustment mechanism. In addition the locks will be reconfigured to make them stiffer when locked and much easier to align.

Changes will be made in the configurations of the gimbal and the frame to allow all four pivots and locks to be located at the extreme edges of the mount. This at least doubles the spacing of each pair of locks and pivots. This change is allowed by the use of separate flexures which allows greater latitude in the design of the gimbals and frame. This change alone should increase the accuracy by at least a factor of two.

CONCLUSIONS

The prototype mirror mount discussed in this paper has passed severe environmental tests. It is lightweight, compact and easy to adjust so long as the accuracy required is no better than 10 arc seconds. The goal of one arc second accuracy should be reached by a new prototype that will be undergoing test at the time of publication of this paper.

CAGING MECHANISM FOR A DRAG-FREE SATELLITE

POSITION SENSOR

By R. Hacker[†], J. Mathiesen[‡], D. B. DeBra[‡]

Guidance and Control Laboratory
STANFORD UNIVERSITY

ABSTRACT

A disturbance compensation system for satellites based on the drag-free concept has been mechanized and flown, using a spherical proof mass and a cam-guided caging mechanism. The caging mechanism controls the location of the proof mass for testing and constrains it during launch. Design requirements, design details, and hardware are described.

INTRODUCTION

A navigation satellite launched by the Applied Physics Laboratory of Johns Hopkins University incorporated a device built at Stanford University for the compensation of external forces, e.g., atmospheric drag and solar radiation pressure, which perturb a satellite's orbit.

If we enclose an object (proof mass) in a housing which isolates it from the drag and solar radiation pressure, it will follow an orbit influenced solely by the gravitational field of the earth. If the satellite is constrained to follow the proof mass, it will follow a similar gravitational orbit. Such an orbit can be predicted for much longer times than the orbit for a satellite calculated on the best estimates of drag and solar disturbance [Refs. 1 and 2].

[†] Research Engineer.

[‡] Research Engineer at time of design; deceased.

[‡] Director, Guidance & Control Lab; Professor, Aeronautics and Astronautics, and Mechanical Engineering.

The accuracy of navigation on the earth's surface by ships or aircraft, and the extension of measurement resolution in the fields of aeronomy and geodesy are all areas which can benefit from the long-term predictable orbits made possible by DISCOS (Disturbance Compensation System).

The DISCOS consists of a spherical proof mass within a housing, a capacitive sensing system to detect proof mass position, a propulsion system to position the satellite relative to the proof mass, a caging mechanism to control the location of the proof mass for testing and launch, and the electronics necessary for operating the control system and providing telemetry information and receiving commands.

The satellite for which the DISCOS was designed was a three-body gravity-gradient three axis stabilized configuration with an overall length on orbit of 7.5 m (Fig. 1). The DISCOS was contained in the center body, a 300 mm diameter by 300 mm long cylinder attached to the other two bodies by folding booms.

DISCOS DESCRIPTION

The DISCOS is made up of five major components: the proof mass, proof mass housing, electronics, propulsion subsystem, and the caging mechanism (Fig. 2). These components are arranged in the cylindrical housing in a manner which tends to minimize the mass attraction force of the components on the proof mass; that is, the parts are kept as far away as possible and as symmetrical as possible. Our familiarity with mass attraction is, in general, limited to the earth's, i.e., the weight of objects around us. In the design of a drag-free satellite, however, the disturbance forces to which the proof mass is subjected must be kept smaller than the order of 10^{-11} g, which, for comparison, is the attractive force exerted on the proof mass by a 15 gm mass at a distance of 100 mm. For this reason, the size and location of all parts of the DISCOS had to be controlled and known to dimensions as small as 0.01 mm.

The most important and at the same time the simplest component of the system is the proof mass—a sphere 22 mm in diameter, mass of 0.11 kg, cast from a 70 — 30 gold-platinum alloy and lapped to size. The proof mass is contained in a beryllium oxide housing of 40 mm inside diameter. The caging

mechanism penetrates the wall of this housing to provide control of the proof
mass. The inside surface of the proof mass housing is coated with vacuum
deposited chromium in a pattern of three orthogonal pairs of capacitor plates.
The change in capacitance caused by motion of the housing relative to the
proof mass is sensed to obtain satellite position data. The other major items
of the DISCOS are the electronics and propulsion subsystems.

MECHANISM DESCRIPTION

The caging mechanism for the DISCOS performs two functions. First, it
is used to move the proof mass in a prescribed path inside the housing so that
the signals from the three pairs of capacitive plates can be checked. To a
degree, this is a simulation of the normal orbit condition where the proof
mass would be free to sense the motion of the satellite.

The caging mechanism serves the second purpose of securing the proof
mass against motion during launch and ascent to orbit. To meet this caged
position requirement, the mechanism was designed to exert a force of 54N
when securing the proof mass.

The caging mechanism (Fig. 3) is located below the proof mass housing,
and the caging rod, a beryllium oxide cylinder 12.7 mm diameter by 46 mm
long with a mass of 0.017 kg, extends upward into the housing. The lower
end of the caging rod is pinned to two circular springs, which are in turn
pinned to a transfer nut. The springs are fabricated from beryllium copper
and the transfer nut is 303 stainless steel. The transfer nut travels on
a 1/4"-16 Acme screw, also fabricated from beryllium copper. The lower end
of the caging rod follows a two-dimensional cam slot cut into two plates on
the side of the mechanism, thereby imparting the desired motion to the proof
mass for systems tests. The cam slot is designed to move the proof mass
along a path resembling a sinusoid. The beryllium oxide caging rod is fur-
nace brazed to a clevis end fitting of 17-4 PH stainless steel. Initially,
a titanium end fitting was tried but there were excessive voids in the joint
due to insufficient wetting. The procedure which finally was used was to
sputter approximately 4000Å of gold on the rod end, 10 μm of gold on the
end fitting, and vacuum braze at 850°C with a gold-copper alloy (Englehard
378). The brazing temperature was held as low as possible to prevent grain
growth in the beryllium oxide rod. In spite of this there was an increase

in the rod diameter requiring an additional lapping operation to resize.

The acme screw is driven by a size 9 permanent magnet d-c motor geared to produce 23 mm travel of the transfer nut in 30 sec. The motor bearings are Barden ball bearings with a self-lubricating composite retainer, and the gear box is lubricated with Microseal 100-1. The motor was being produced for a program which had a similar launch environment and was purchased off-the-shelf. A modified Oldham's coupling is used between the motor and the screw.

The frame on which the components of the mechanism are mounted was machined from a piece of 6061-T6 aluminum 62.5 mm diameter by 100 mm long. The surfaces contacted by the transfer nut were given a hard anodize to minimize wear. An assembly fixture was fabricated for use in obtaining alignment of the two cam plates with respect to each other, for checking the switch trip points, and for measuring the spring load.

During operation in the caging direction, the first 0.86 mm travel of the transfer nut relieves the spring load which has been applied by stretching the springs during the uncaging cycle. Free travel then takes place for 21.25 mm during which the cam slot is traversed. At the end of free travel, the proof mass contacts the proof mass housing and the two springs are compressed a distance of 1.17 mm. This produces the load of 54N giving a longitudinal acceleration capability of 43 g without motion of the proof mass away from its caged position. At the end of spring compression, a tab on the transfer nut contacts a limit switch and power is removed from the motor. A pair of switches arranged to operate independently is used at each end of the stroke. Thus, opening either switch of the pair will remove power from the motor. Should both switches fail to open, the transfer nut will contact a steel pin after an additional 0.25 mm travel and stall the mechanism. This is done to prevent cracking or spalling failures of the beryllium oxide housing and caging rod.

TESTING

The systems check-out and testing phase for the DISCOS required a number of caging and uncaging cycles for the determination of electronic signal strength and scale factors for the position sensing system. Tests were performed at ambient conditions, in vacuum at 45°C and −20°C both before and

after vibration testing. Several hundred caging and uncaging cycles were performed during the test period.

CONCLUDING REMARKS

One caging mechanism was fabricated to serve for both system qualification and the flight vehicle. At the completion of testing, the cycle time on the unit was within 1 sec of the desired time. Following launch and orbit injection, the mechanism remained in the caged position for eleven days, at which time it was uncaged by ground command.

ACKNOWLEDGMENTS

REFERENCES

1. Lange, B.O., "The Drag-Free Satellite," AIAA J., Vol. 2, No. 9, Sept. 1964, pp. 1590–1606.

2. Space Dept. of the Johns Hopkins University Applied Physics Lab., and the Guidance & Control Lab. of Stanford University, "A Satellite Freed of all but Gravitational Forces: 'TRIAD I'," J. Spacecraft and Rockets, Vol. 11, No. 9, Sept. 1974, pp. 637–644.
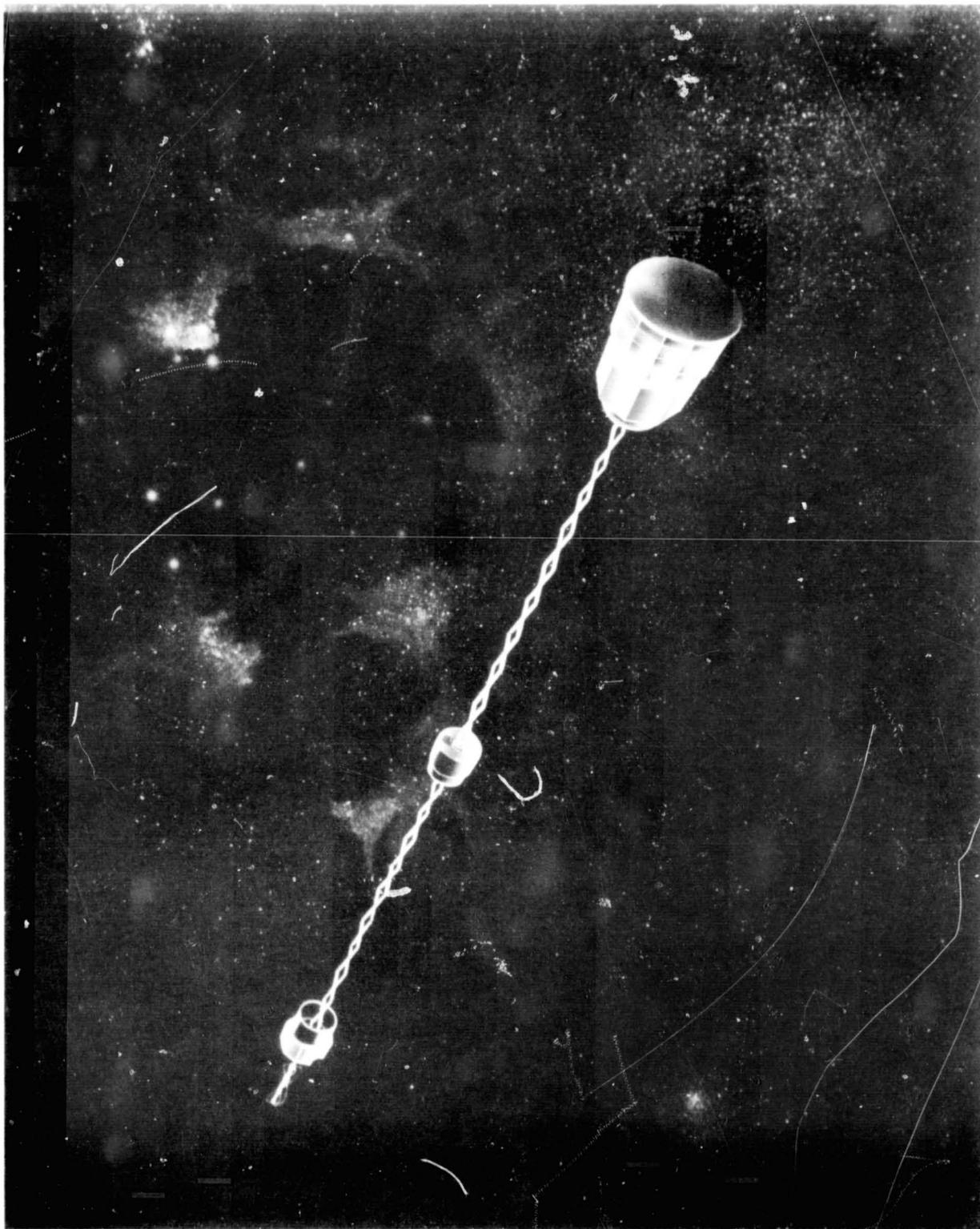
FIG. 1   NAVIGATION SATELLITE WITH DISCOS HOUSING IN CENTER.

PROPULSION
SUBSYSTEM

PROOF MASS
HOUSING

PROOF MASS
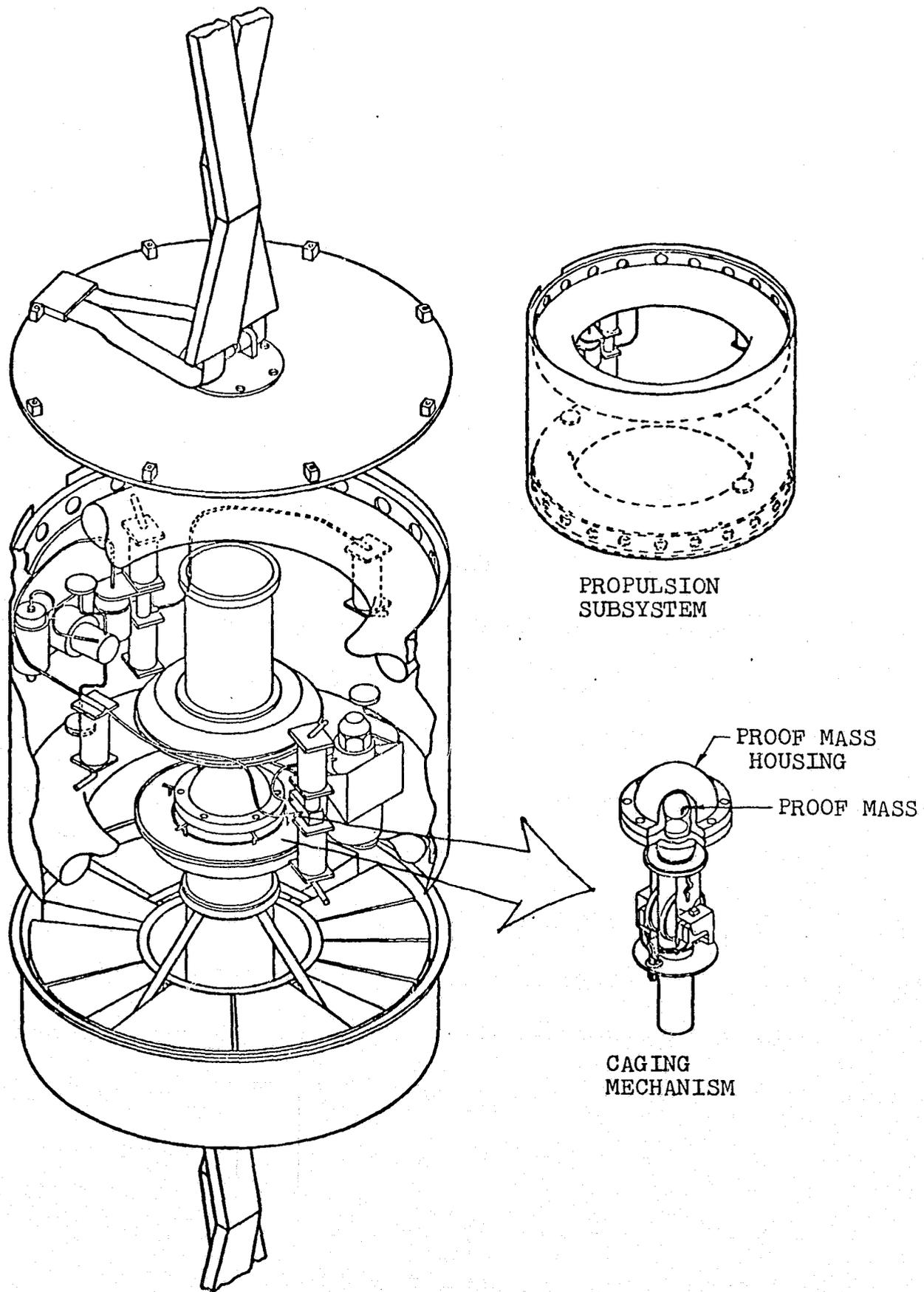
CAGING
MECHANISM

FIGURE 2   DISCOS SHOWING LOCATION OF CAGING MECHANISM.
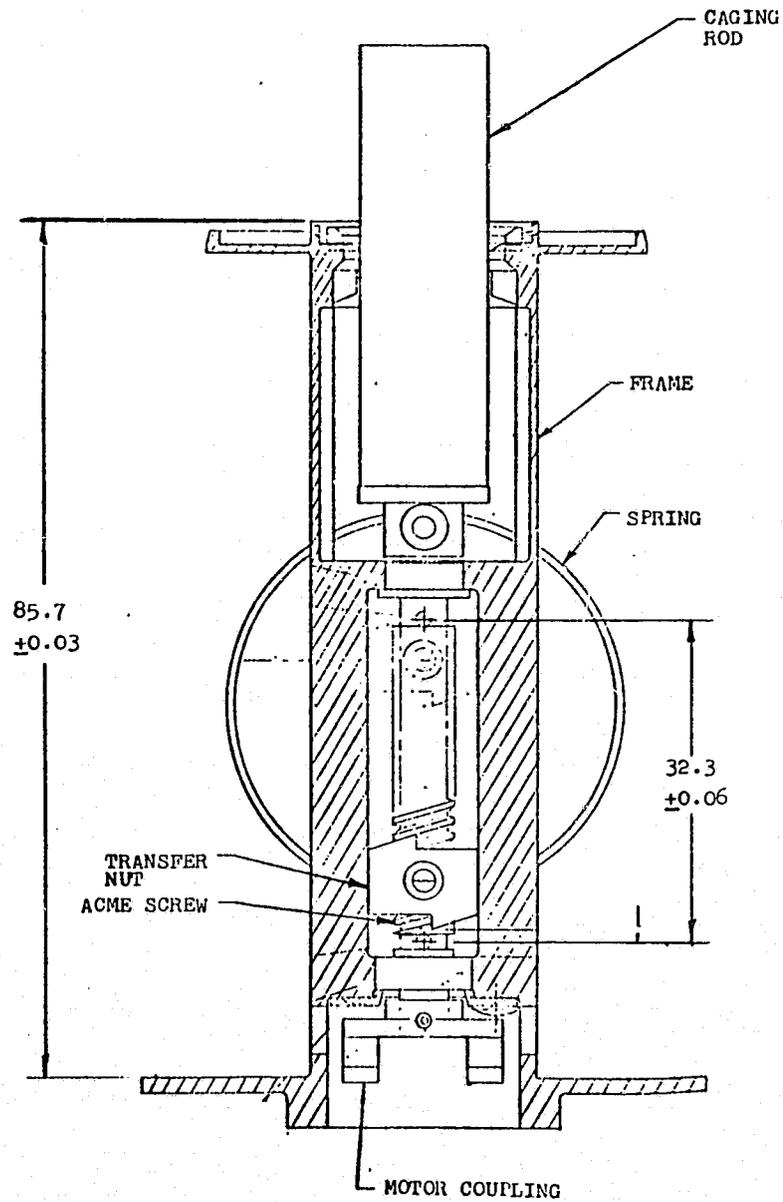
FIGURE 3   CROSS SECTION OF CAGING MECHANISM.

The figure shows labels: CAGING ROD, FRAME, SPRING, TRANSFER NUT, ACME SCREW, MOTOR COUPLING, with dimensions 85.7 ±0.03 and 32.3 ±0.06.

THE HELIOS EXPERIMENT 5 ANTENNA MECHANISM

by E. J. W. Müller, Dipl. -Ing.

DFVLR-BPT, Germany

SUMMARY

This paper describes the Experiment 5 Antenna Deployment problem on board HELIOS A, the failure analysis, and changes in design, test, and operation which led to a successful deployment of both antennas during the early HELIOS B mission phase.

INTRODUCTION

The two Experiment 5 antennas are installed normal to the axis of rotation close to the equatorial plane. The antennas form a dipole which is used by the Plasma and Radio Wave Experiment. It was planned to deploy both antennas at once, about 3 hours after the launch of HELIOS A. However, the observed anomalies:

- Only one of the motors was switched off automatically by the end switch
- The spacecraft spin rate change due to the change in the spacecraft spin moments of inertia was from 52.966 rpm to 51.072 rpm instead of 49.36 rpm
- One antenna element was grounded to the spacecraft structure

indicated that only one antenna was deployed to the full length of 14.75 meters.

Description of the Antenna Mechanism

Figure 1 shows the simplified antenna drive system. Each antenna mechanism is powered by an AC motor and inverter which drives the antenna storage spool and the pinch drive rollers. The pinch drive rollers are geared to deploy the antenna material at a rate faster than it can be unwrapped from the driven spool. A slip clutch in the gear train makes this possible. The intent is to keep any slack material from developing between the spool and the pinch drive rollers by keeping tension in the antenna material. A one-way clutch permits the pinch rollers to free wheel during antenna retraction. A potentiometer with a range of five volts is driven by the rotating storage spool. Microswitches with arms riding against the antenna material shut the motor off automatically at full extension or retraction. This shut-off is accomplished by having a slot cut near each end of the antenna material. As the slot passes under the microswitch arm, the arm drops through the slot and opens the circuit to the motor. These switches are located outboard of the pinch drive rollers in an area where the antenna material is forming into a cylinder around a form; therefore,

the antenna exhibits some stiffness in this area — it is not a flat ribbon. The antenna itself is a 0.0038 cm (0.0015 inch) thick Be Cu strip heat-treated to form a 0.673 cm (0.265 inch) diameter cylinder along the longitudinal axis of the strip. After forming into a cylinder, the edges of the strip overlap each other by approximately 90°; there is no interlocking feature. The outboard of the mechanism housing contains an ion guard approximately two meters long when fully deployed. This ion guard consists of a thin rubber sleeve expanded around a relatively long, weak coil spring, i.e., a glorified vacuum cleaner hose about 5.1 cm (2.0 inches) in diameter. During and prior to launch, the ion guard is compressed into a housing about 25.4 cm (10 inches) long and held in place by a fitting on the end of the retracted antenna. Upon deployment of the antenna, the free end of the ion guard follows the antenna out until the ion guard has extended to its full length. The inboard end of the ion guard remains fixed to the front end of the mechanism housing. The antenna then continues to deploy through the extended ion guard until the antenna is fully deployed. The mechanism is enclosed in thin sheet aluminum dust covers to provide an RF shield between the antenna and noise originating inside the spacecraft. The antenna itself is also isolated electrically from the remainder of the mechanism.

Failure Analysis

The commands to deploy both Experiment 5 antennas were properly received and executed by the spacecraft; however, due to a malfunction within unit S/N006, the antenna element of this unit was not properly deployed. The analysis performed was based on the following parameters:

- Telemetered antenna length readout
- Solar aspect angle information
- Science data of Experiment 5
- Spacecraft spin rate information

The telemetered antenna length readout of S/N006 shows some unsteady behaviour during the early deployment phase. But looking into all transmitted data, it is obvious that the motor and gear train of S/N006 started up and operated until the 10-turn potentiometer was driven against its mechanical stop, which indicated an 18 cm longer antenna element. The nonessential bus current monitor provides information on the total current drawn by all consumers fed by this bus. Besides the experiments, the E-5 antennas also are powered from this line. The current is sampled by the A/D converter for short time intervals only. This, together with the current chopping caused by the D3A 400 Hz inverter, provides a very unsteady current reading.

From this information, it can be deduced that both units drew approximately the predicted current (0.4 A each) and that one unit automatically switched off after a run time of 32.5 min. These data also show clearly that the second unit did not switch off automatically. Only when the power disable command for the antenna units was executed did the current reading drop to the value it had prior to antenna deployment. The solar aspect angle changed during the deployment by 0.2°, which also indicates a malfunction of one antenna element because both antennas are mounted about 10 cm

above the center of gravity plane. During deployment of the E-5 antennas the experiment was collecting data. The noise spectrum obtained shows two distinct changes: 3.4 minutes after the deploy initiation command the noise went down, while at 7.1 minutes after initiation the noise went up to approximately its original level. The spacecraft spin rate data turned out to be the best tool for locating the failure. Figure 2 shows the relative spin rate variation as a function of the deployed antenna length. The upper dashed line shows the variation for a nominal simultaneous deployment of both antennas, the center line shows the variation in spin rate for deployment of one antenna only, and the lower line indicates the actual measured spin rate change as a function of the transmitted antenna length read out. As can be seen by looking at all observed anomalies, the failure must have occurred in the early deployment phase during the simultaneous deployment of the ion guards with the antenna elements. In subsequent meetings, the possible failure modes were discussed, and the following were seen as the most probable failure modes:

A)   Failures based on the interaction of ion guard and antenna element:

   -   The turns necessary to fold the ion guard affected the boom element during the first phase of deployment when the ion guard rotated back.

   -   Ion guard jammed during element deployment; suddenly it came free, hit the antenna tip mass, and damaged the antenna element or tip mass.

B)   Failed mechanism:

   -   Clutch on the drive roller failed, then antenna element bloomed up between spool and drive roller device.

   -   Element damage caused high friction between moving element and ploy; again blooming up of the boom either between spool and drive roller or between drive roller and ploy.

   -   Loss of load on the pinch roller caused element blooming up between spool and drive roller due to slippage between drive roller and antenna element.

   -   Loss of alignment due to a bearing failure or misalignment after relubrication at Kennedy Space Center (KSC).

   -   During lubrication at KSC, some lubricant (grease) was put on the drive roller, causing slippage between drive roller and antenna element.

   -   Wrong lubricant in the worm gears: silicon lubricants tend to creep. Suggestion was made to change to the Krytox 243 grease for lubricating the worm gears.

As the outcome of the discussions, a test sequence was set up to simulate the possible failure modes. It was decided to perform the tests with specimens S/N001 and 002. Units 003/004/005 were reserved as flight and spare units. The following tests were performed at Fairchild in early March 1975:

1. Test sequence for S/N 001/002

    1.1 (S/N 002) Deploy element to 1.2 mark. At his point, release ion guard instantaneously (element pointing down, motor in operation).

    1.2 (S/N 002) Store ion guard with "4-turn twist." During deployment, measure rotation of element tip and ion guard tip.

    1.3 (S/N 001) Twist element on stationary mechanism. Observe reaction of element on ploy and microswitch travel.

    1.4 (S/N 001) Stall element during extension. Observe buckling of element between drive roller and ploy.

    1.5 (S/N 001) Check pressure between drive and pinch roller.

    1.6 (S/N 001) Determine torque range of clutch for proper deployment, with no pull force acting on element. When clutch fails (at minimum torque setting), continue mechanism operation for 80 sec minimum and record status. Attempt "retract" of antenna element.

    1.7 (S/N 002) Determine clutch setting and roller pressure.

    1.8 (S/N 002) Run full extend/retract load cycles:
2 cycles, room temperature, min/max load
4 cycles, -20°C, min/max load
4 cycles, +50°C, min/max load
Operation in air, load ±50% of nominal, retraction under nominal load.

    1.9 (S/N 002) Determine clutch setting and roller pressure.

2. Component tests and other matters

    2.1 Measure torque versus temperature performance for a clutch set at center of acceptable torque range. See test 1.6 (S/N 001) and callout on respective drawing.

    2.2 Regarding the intended deletion of the ion guards, it was clearly stated that antenna deployment will be achieved

3. Test sequence for S/N 003/004/005 (spare unit)

   3.1 If deployable ion guards are deleted, remove detent spring.

   3.2 Check torque setting of drive roller clutch and check pressure between drive and pinch roller.

   3.3 Perform full-length element extension at ambient pressure and -20 °C and +50 °C ambient temperature, respectively. (If wear-out was shown to be a problem by test 1.8, only the cold cycle deployment is to be performed.) Perform visual inspection of element when fully deployed.

Results of the Failure Investigation Tests

The most probable failure mode which could have caused the problem on HELIOS A was found in tests No. 1.2 and 1.3 when the effect of the ion guard on the antenna element was determined. When the ion guard and the antenna system are assembled for S/C integration, the ion guard is compressed to about 30 cm for storage. During storage, it is additionally twisted axially through two to four turns due to the normal rotation of the helical spring inside the ion guard. When the ion guard deploys (simultaneously with the antenna element), it imparts a torque to the antenna element transmitted by the friction between ion guard end flange and antenna tip mass. When the direction of the ion guard torque is such that the antenna cross section tends to open, the antenna element is caused to bind at the end of the ploy. As a result, a blooming or buckle occurs between the drive roller and the ploy. When this effect was detected at Fairchild, approximately 5 seconds had elapsed between stall of element and power switch-off. The 5-second delay was enough to damage the antenna element. A possible explanation was that one antenna worked properly and that it was impossible to overcome the failure on board HELIOS A by retracting and deploying maneuvers of the S/N 006 unit. Figure 3 shows a close-up view of the failed mechanism after test step 1.2.

Modifications

A) Design Modifications

Based on S/C noise data obtained by Experiment 5a on board HELIOS A, the experimenter requested the elimination of the foldable ion guard. It should be replaced by a rigid electrically conducting tube of 10-cm diameter and 0.8-m length to provide electrostatic shielding of the antenna base from noise originated by the spacecraft solar array. This modification completely eliminated the interaction between ion guard and antenna element. Together with the elimination of the foldable ion guard, the detent spring inside the mechanism could be removed. This spring was necessary to hold the antenna element in its stored position during vibration loads, because of the pulling force of the ion guard on the antenna element.

B) Test Modifications

Two full extension/retraction tests were added on a system level: one prior to the spacecraft vibration test and one after all mechanical system tests, prior to encapsulation at Cape Kennedy.

C) Operational Modifications

A new operational procedure was worked out that makes it possible to stop the deployment if any anomaly occurs. It was planned to deploy both antennas on board HELIOS A at once. The new procedure was the following.

Before starting antenna deployment, operations E5 and E4 shall be turned on and S/C telemetry shall be in science data mode to monitor S/C spin rate for possible antenna short to ground and indication of motor current flow. It shall be monitored continuously, displaying nonessential bus current, antenna potentiometer reading, antenna motor switch status, S/C spin rate, E5b scientific data, and E4 scientific data. One operator shall continuously plot the above parameters on a chart which has the predicted values plotted on it. Deviations from predicted values will be cause to stop antenna deployment operations. A pre-arranged command shall be at the instant ready, stowed in the command queue, to turn off the antenna motor current.

Sequence of E5 Antenna Deployment

Step 1

Deploy the +Y antenna element to a length of 1 m, where it is possible to detect a change in the S/C spin rate and monitor all parameters.

Step 2

Deploy the -Y antenna element analogously to step 1.

Step 3

Deploy the +Y antenna element from 1 m to 2.5 m.

Step 4

Deploy the -Y antenna element from 1 m to 2.5 m.
Time for bow shock measurements.

Step 5

Deploy the +Y antenna element from 2.5 m to 14.4 m.

Step 6

Deploy the -Y antenna element from 2.5 m to 14.4 m.

Step 7

Deploy the +Y antenna element to the full length in steps of 50 to 60 mm, which correspond to a running time of 10 to 12 seconds. Monitor all parameters and perform an impedance measurement after each step. Deployment commands shall be terminated after a step increase of the impedance measurement or closure of the end switch.

Step 8

Deploy the -Y antenna element analogously to step 7.

The Inflight Deployment of the HELIOS B Experiment 5 Antennas

Steps 1 to 6 of the deployment were performed successfully on the first day of the HELIOS B mission. All above-mentioned parameters were monitored and plotted and did not deviate from the predicted values. Figure 4 shows the plot of the spacecraft spin rate and solar deviation angle as function of deployed antenna length. Steps 7 and 8 were performed successfully during the third Goldstone pass on the third day of the mission.

Acknowledgement

The author thanks Gordon Smith and Richard Kramer of Fairchild Industries and Dr. Wunderer of Messerschmitt-Bölkow-Blohm for the excellent cooperation which made it possible to locate the problem and introduce, in a short time, changes to prevent a similar failure on board HELIOS B.

References

1   MBB Procurement Specification Extensible Antenna, HELIOS Spacecraft.

2   Dr. Wunderer (MBB), Failure Analysis D3A S/N 006.

3   E. Angulo/W. Sours (GSFC), Memorandum, "Summary of the HELIOS Experiment 5 Antenna Problems."

4   E. Müller (GfW), E5 Antenna Problem Investigations.

5   Fairchild/MBB, Test procedure for failure investigation tests with S/N 001/002.

6   E. Müller, Test report of failure investigation tests.
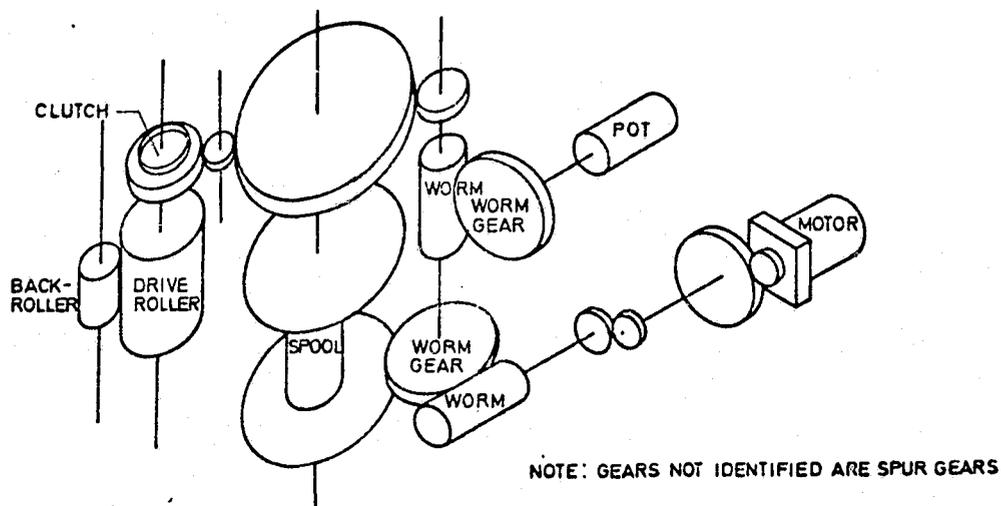
Fig. 1   Antenna drive system
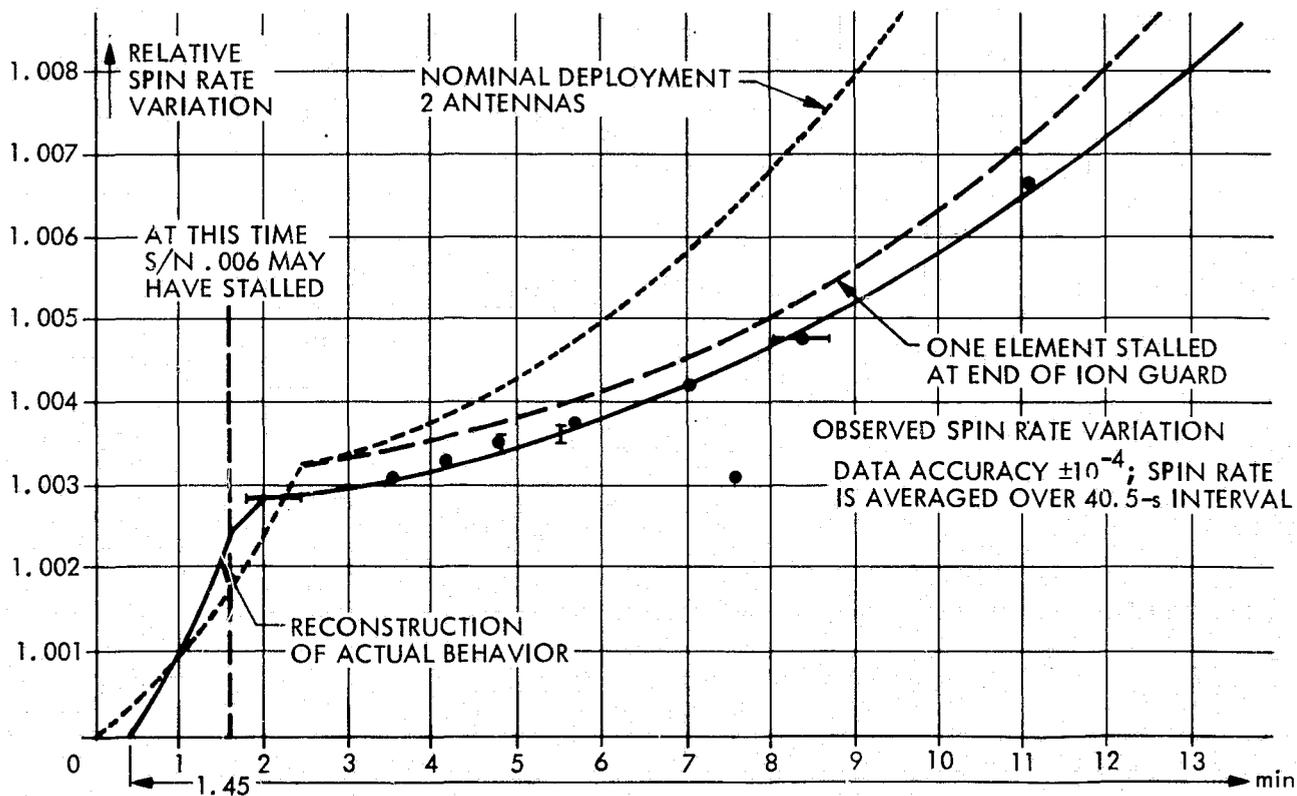
Fig. 2   Spin rate variation on board HELIOS A
as function of time

CLUTCH

DRIVE ROLLER

FOLDED ANTENNA
ELEMENT

ANTENNA ELEMENT

SPOOL

Fig. 3   Close-up view of the failed mechanism
after test step 1.2

HELIOS-B   E-S ANTENNA DEPLOYMENT

STEP 1   DEPLOY + Y ANTENNA TO 1m
STEP 2   DEPLOY - Y ANTENNA TO 1m
STEP 3   DEPLOY + Y ANTENNA FROM 1m TO 2,5m
STEP 4   DEPLOY - Y ANTENNA FROM 1m TO 2,5m
STEP 5   DEPLOY + Y ANTENNA FROM 2,5m TO 14,4m
STEP 6   DEPLOY - Y ANTENNA FROM 2,5m TO 14,4m

MEASURED SPINRATE DECREASE DURING E-S ANTENNA DEPLOYMENT

CALCULATED
FOR 50 rpm INITIAL
SPINRATE

HIGH STABILITY DEPLOYABLE BOOM

by

Gordon A. Smith, Thomas G. Berry and Lamont DiBiasi

Fairchild Space and Electronics Company

ABSTRACT

Meaningful magnetic field vector measurements in space require accurate placement of a magnetometer beyond the magnetic fields of a spacecraft. This paper describes the design and development of a deployable boom which ensures accurate deployment of an instrument package and maintains high stability after extension.

INTRODUCTION

Predictability of boom alignment and stability of the boom after deployment were the driving design requirements. Specifically, these requirements were:

1.   The alignment of the boom after deployment shall be predictable within 20 minutes of arc in both twist and deflection.

2.   Boom twist shall not exceed 5 minutes of arc and boom deflection shall not exceed 15 minutes of arc from all sources, including thermal effects from solar radiation and air drag at altitudes above 200 Km.

These stringent stability requirements, coupled with a 6.8 Kg weight limitation for a 6 meter boom that can be stowed into a volume of 0.057 m^3 (2 ft^3), dictated the following features for the boom design:

- Largest closed cross section possible, consistent with the stowed volume constraints.

- Construction using a framework truss which will receive nearly equal thermal input throughout.

- Minimum play in the boom truss and linkage joints.

- Use of non-magnetic, lightweight materials having very low thermal coefficients.

To meet these requirements, an adaptation of a Fairchild patented folding box beam was designed and is described in the following sections.

DESIGN DESCRIPTION

The basic building block of the high stability deployable boom is a modular bay, and the length of the boom is determined by the number of modules linked together in series. Each module consists of two side truss panels supported and deployed between two synchronized scissor linkages. When the boom is fully deployed, as shown in Figure 1, the side panels, which are hinged along their transverse center lines, lock into position and form two sides of a box beam. Shear capability is inherent in the truss panels whereas the shear continuity in the two opposite sides of the box is furnished by the links themselves. Both the links and the truss panels are of sandwich construction using low density (2-3 lb/ft^3) aluminum honeycomb with Graphite Fiber Reinforced Plastic (GFRP) face sheets. This construction provides for maximum strength, minimum weight, and low thermal distortion.

Flexure hinges are used where each truss folds or is attached to its neighbor. The flexure hinges serve three functions: (1) as a hinge, (2) as a deployment spring, and (3) as a deployment lock. As shown in Figure 2, the flexure hinge has a configuration similar to that of a carpenter's rule, with a radius of 19 mm. The hinges are made from GFRP and a significant test program was conducted to achieve acceptable hinge properties. The results of the test program are discussed under a separate heading.

As stability in the deployed boom is a critical requirement, all bearings at the extremities and centers of the scissors links are close tolerance (0.0002-0.0005 inch radial clearance) ball bearings. For magnetic cleanliness reasons, these bearings are manufactured from beryllium copper.

It can be seen that any play at the base of the boom after it is deployed will adversely affect boom deflection. To prevent this, a system for deployment was designed as shown in Figure 3. A ball screw, one half with a left-hand lead and the other half with a right-hand lead, is located across the center of the housing at the base of the boom. Depending on the direction in which the screw is turned, two carriages, one on each end of the screw, will simultaneously move toward or away from each other. Rotation of the carriages is prevented by parallel rods positioned on either side of the ball screw as shown in Figure 3. The degree of tolerance between the linear bearings and the rods determines to a large extent the amount of boom deflection. The lower extremities of the four scissors links at the base of the boom are pinned to the clevises which are an integral part of the carriages.

The engineering model is deployed using a hand crank; however, the design is flexible enough to accommodate a drive motor. In addition, for flight booms, the drive assembly will be designed for minimum weight.

FLEXURE HINGE DESIGN

The most critical component in the boom design is the flexure hinge. Its primary purpose is to provide a stiff lock between side panels after the boom is fully deployed and a secondary function is to provide a spring force to aid in boom deployment. Important characteristics of the flexure hinge are.

- A high value of EI for stiffness

- Good spring properties

- Flexibility

- Made from non-magnetic material

- Made from material with a low thermal coefficient

It is evident that, because of the flexibility requirement, the hinge must be made from a thin strip of material. Therefore, for stiffness, the strip is configured similar to a carpenter's rule to increase the area moment of inertia of the cross section.

A preliminary review of available material for the hinge indicated beryllium copper as the most likely candidate. However, a thermal analysis showed that there would be an unacceptable distortion of the boom unless the maximum temperature difference between a sunlit portion of the boom and a shaded hinge is held to 69.5°C. It must be realized that the flexure hinges comprise about 20% of the length of the deployed boom.

Various schemes to limit the temperature differential across the boom were then evaluated including the use of beryllium copper conductor straps placed along the inside of the panel diagonals. An alternative solution, and the one that was implemented, was the use of GFRP as the hinge material. It can be seen from Table 1 that the tensile modulus, E, is very close to that of beryllium copper, but the big advantage of GFRP is its thermal coefficient, a minimum of 20 times less than that of beryllium copper.

Before the feasibility of using GFRP for the flexure hinge could be established, an experimental test program was performed to evaluate the following:

- Optimum lay-up configuration

- Best bonding agent

- Degree of flexibility

- Minimum bend radius (for minimum stowed volume)

Table 1. Physical Properties of GFRP

Property	Lay-Up		
	*90° Cross-Ply	Isotropic	Unidirectional
E	17×10^{6} psi	10.6×10^{6} psi	20×10^{6} psi
G	$.65 \times 10^{6}$ psi	4.0×10^{6} psi	$.65 \times 10^{6}$ psi
75°F to + 300°F	$.42 \times 10^{-6}$ in/in/°F	$.80 \times 10^{-6}$ in/in/°F	$-.49 \times 10^{-6}$ in/in/°F
75°F to -225°F	$.06 \times 10^{-6}$ in/in/°F	$.35 \times 10^{-6}$ in/in/°F	$-.16 \times 10^{-6}$ in/in/°F

*Two longitudinal plies and one transverse

For test purposes, flat strips of GFRP were laid up in widths of 0.5, 0.75 and 1.0 inches for each configuration of A through J as shown in Table 2. Two plies were considered optimum, each ply being approximately 0.005 inches thick and made from AS3501-5 GFRP. Kapton was included in some samples because it was thought that this would inhibit the tendency of the strips to delaminate.

Each sample was tested to determine the shortest practical length and the minimum bend radius for each configuration. The results are given in Table 2, and it can be seen that for one ply oriented 30° to a longitudinal ply, a bend radius of 4.3 mm can be achieved with a strip 70 mm long. It was found that neither strip width nor Kapton had any significant effect on the bend properties.

Another grade of GFRP material (HMS3501-5) was tested and found to be much more brittle. However, it can be seen that the possible variations in material and configuration are considerable and it is not claimed that the 0°/30° lay-up of two plies of AS3501-5 provides the best hinge material. Further testing is required to determine the optimum parameters.

Using the 0°/30° two-ply lay-up, flexure hinges were heat treated, five at a time, in the tool illustrated in Figure 4. The force versus deflection characteristics of the resulting hinges are shown in Figures 5 and 6. As expected, the spring force is much greater when the flexure hinge is bent round with its normal concave surface as the outer bend radius.

CONCLUDING REMARKS

The purpose of this paper is to present a unique boom design for deploying instruments from spacecraft and maintaining the instruments in a stable configuration under all combinations of space environments. Of prime importance to the stability of the boom is the flexure hinge design. The need for a material with an extremely

CONFIGURATION	OUTER PLY[a]	MID PLY	INNER PLY[b]	RESULTS
A	GFRP	None	GFRP at 0°	MIN. RAD. = 10 mm FOR A 120 mm LG ELEMENT
B	GFRP	None	GFRP at 15°	MIN. RAD = 6.4 mm FOR A 102 mm LG ELEMENT
C [c]	GFRP	None	GFRP at 30°	MIN. RAD. = 4.3 mm FOR A 70 mm LG ELEMENT
D	GFRP	None	GFRP at 45°	MIN. RAD. = 7.9 mm FOR A 102 mm LG ELEMENT
E	GFRP	None	GFRP at 90°	MIN. RAD. = 10.2 mm FOR A 120 mm LG ELEMENT
F	GFRP	None	KAPTON 3 MIL	THE USE OF KAPTON HAD NO APPRECIABLE EFFECT ON THE COMPOSITE
G	GFRP	None	KAPTON 5 MIL	F & G COMPARED TO A,
H	GFRP	GFRP at 90° [b]	KAPTON 3 MIL	H & J COMPARED TO E
J	GFRP	GFRP at 90° [b]	KAPTON 5 MIL	

a FIBERS RUNNING LONGITUDINALLY

b WITH RESPECT TO OUTER PLY

c .75 mm WIDE ELEMENT TESTED

TABLE 2. Flexure Hinge Experimental Results

low coefficient of thermal expansion influenced the choice of GFRP and therefore instigated a hinge development program. As stated earlier, the hinge configuration used in the engineering model meets all requirements for its intended use but there is obviously room for further development.

Fabrication of an engineering model of the boom is currently underway at the time of writing. Deployment and solar simulation test results may be available at the 10th Aerospace Mechanisms Symposium.
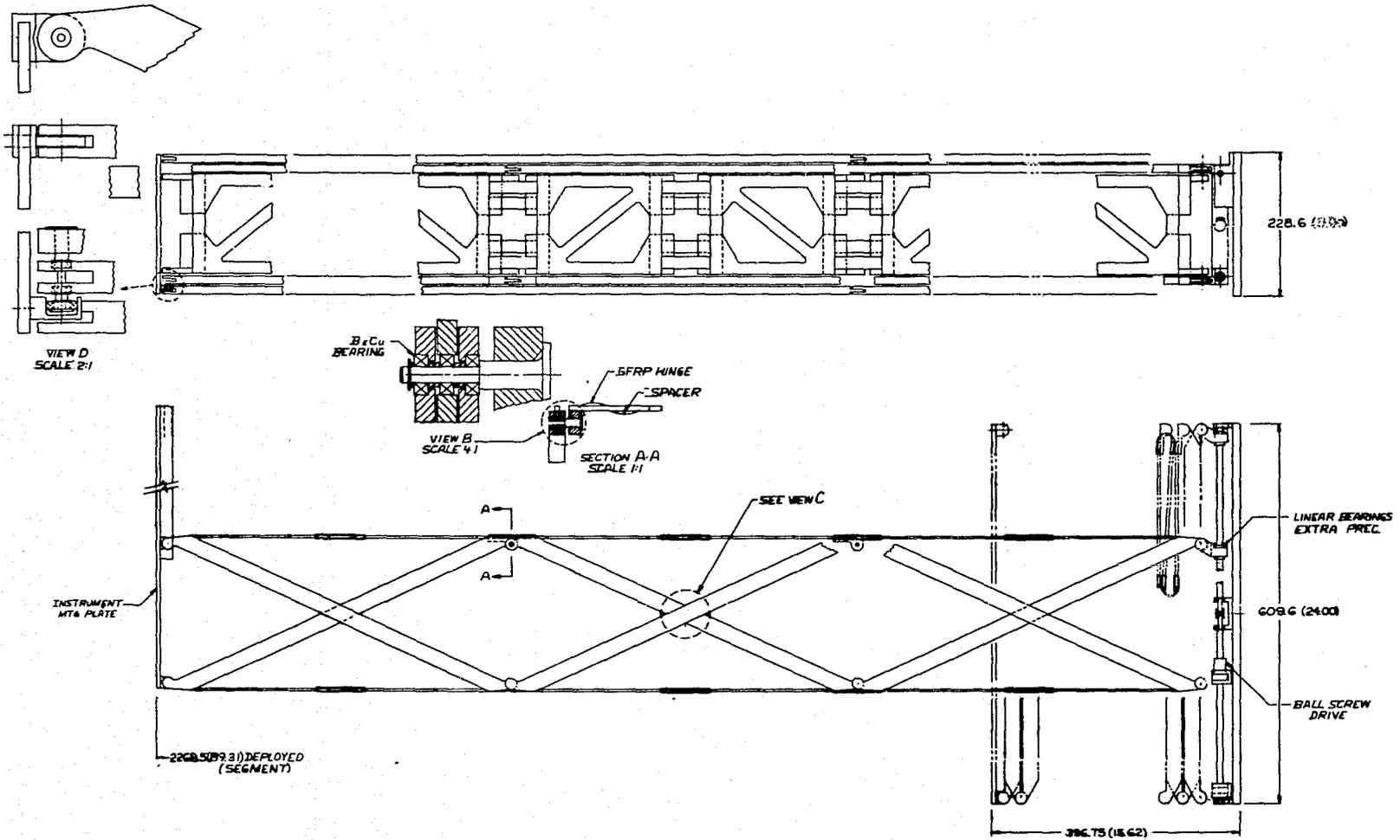
Figure 1. High Stability Boom

Fiber Orientation

30°

25.4

19.05

.31

43°

l

All dimensions are in mm.
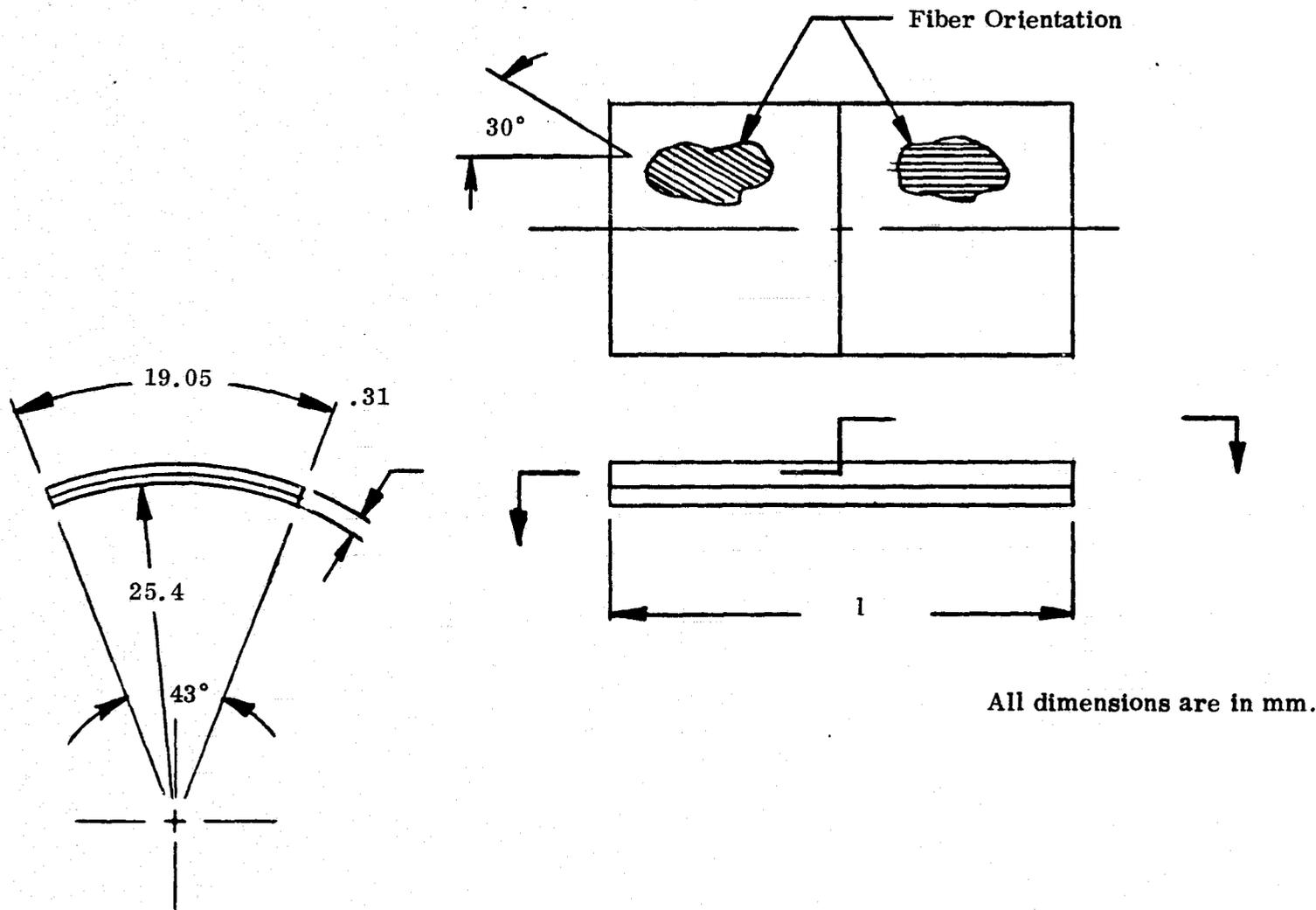
Figure 2.   Flexure Hinge Configuration

Drive Block

Ball Screw

Ball Nut

Linear Bearing
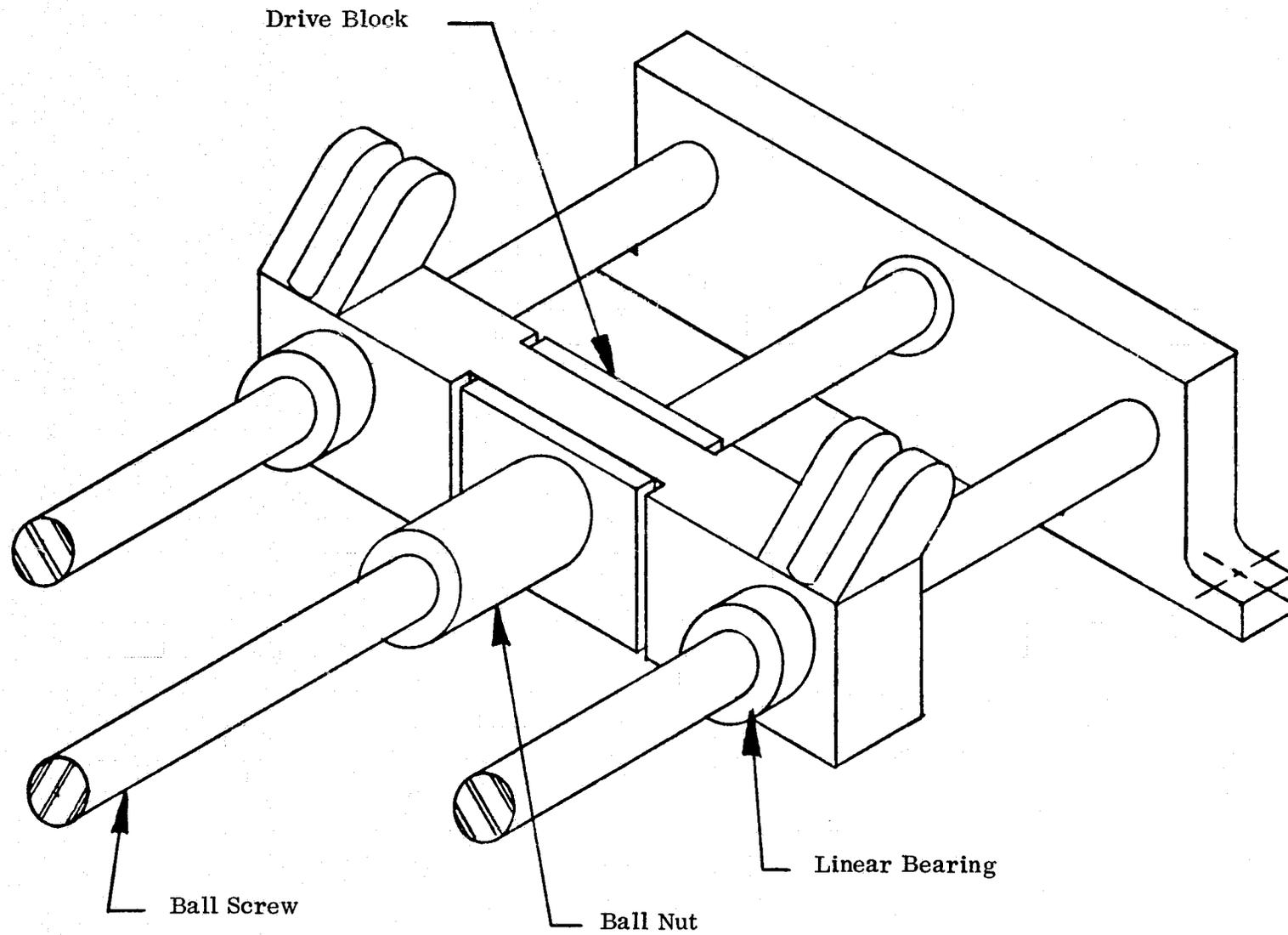
Figure 3.   Deployment System
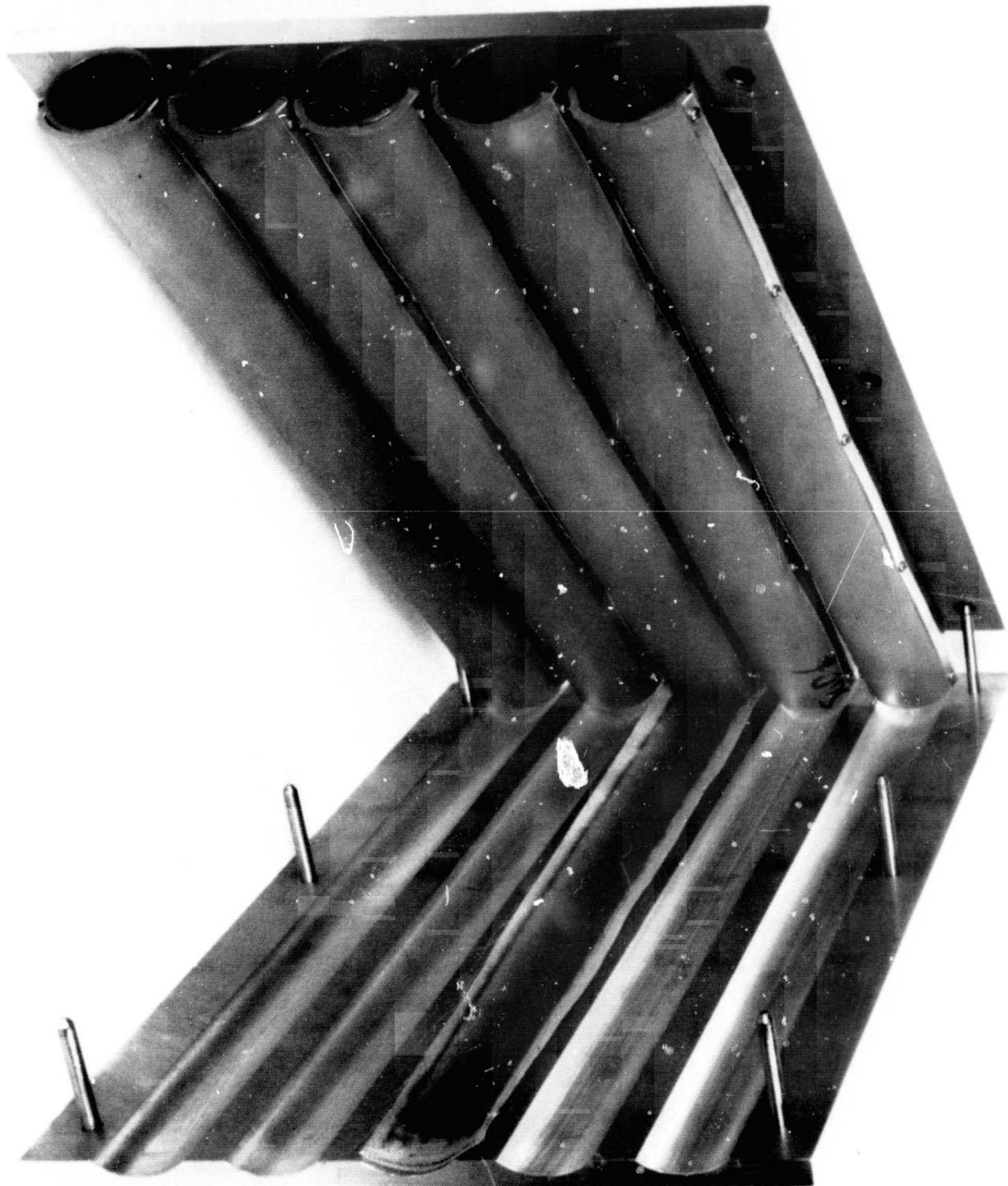
Figure 4. Flexure Hinge Heat Treat Tool
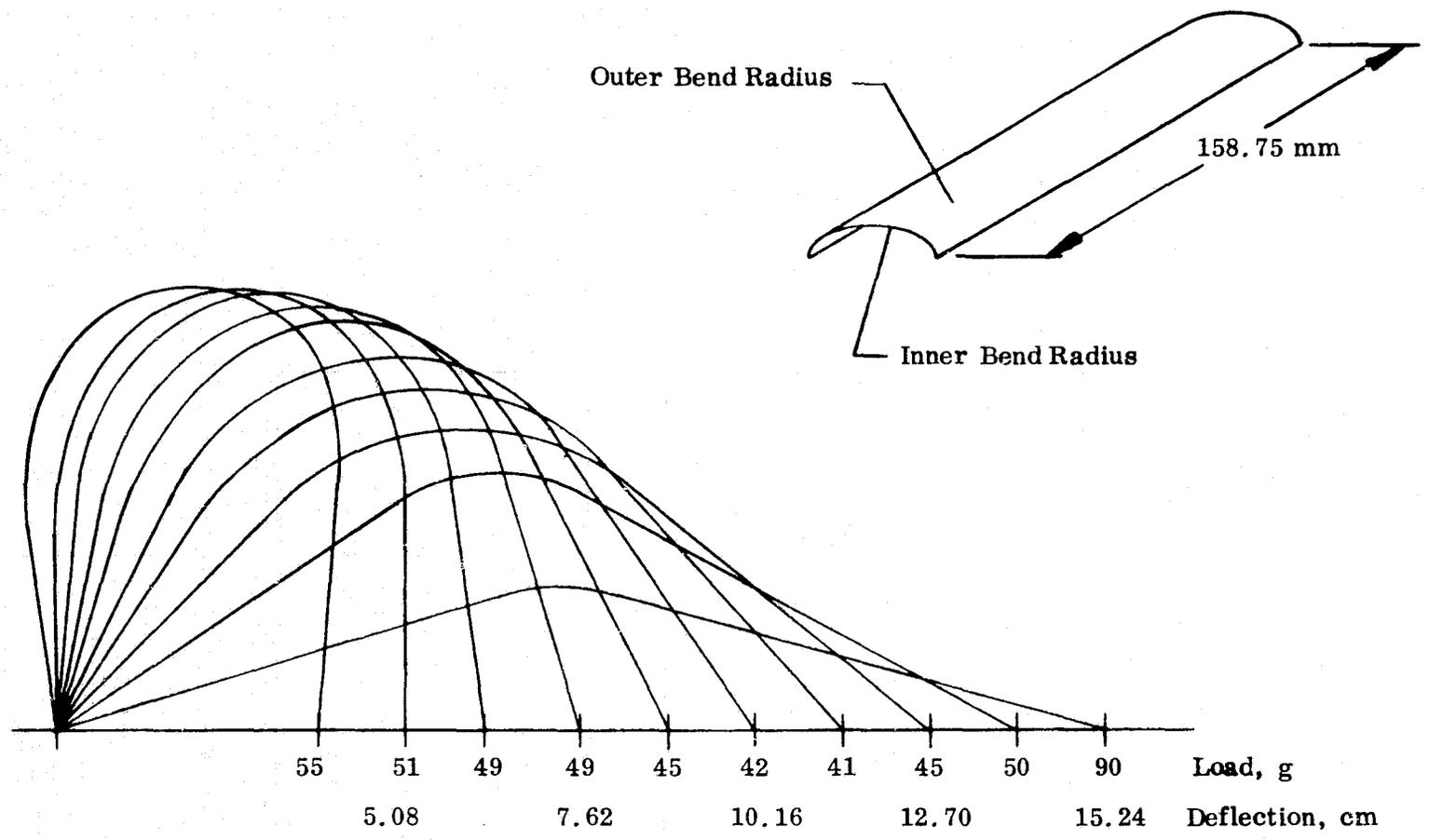
Figure 5.   Flexure Hinge Force vs Deflection Characteristics

Outer Bend Radius

158.75 mm

Inner Bend Radius

| 85 | 80 | 78 | 72 | 68 | 62 | 60 | 60 | 60 | 70 | 140 | Load, g |

| 0 | 2.54 | 5.08 | 7.62 | 10.16 | 12.7 | 15.24 | Deflection, cm |
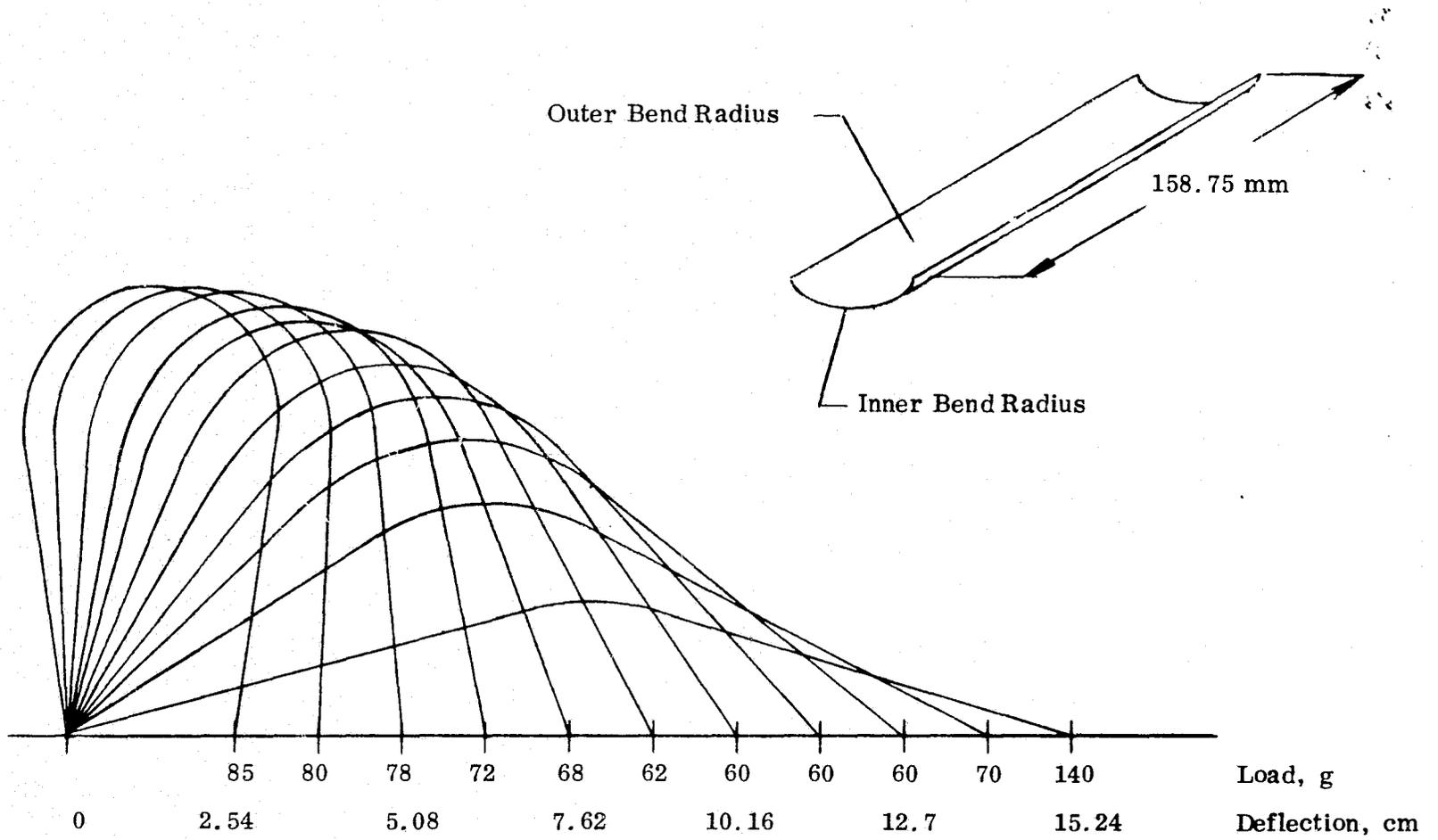
Figure 6. Flexure Hinge Force vs Deflection Characteristics

MECHANICAL DESIGN OF NASA AMES RESEARCH CENTER

VERTICAL MOTION SIMULATOR

By David F. Engelbert, Allan P. Bakke
Mladen K. Chargin and Wilbur C. Vallotton

NASA Ames Research Center

ABSTRACT

NASA has designed and is constructing at the Ames Research Center a new flight simulator with large vertical travel. Several aspects of the mechanical design of this Vertical Motion Simulator (VMS) are discussed, including the multiple rack and pinion vertical drive, a pneumatic equilibration system, and the friction-damped rigid link catenaries used as cable supports.

INTRODUCTION

Existing flight simulators are inadequate for a number of critical tasks. Among these are simulation of aircraft flare and touchdown, particularly for V/STOL and carrier aircraft landings, and control with degraded longitudinal stability. Extended vertical travel is necessary to accomplish this class of simulations with sufficient fidelity. To meet this need, NASA has designed the Vertical Motion Simulator (VMS), which is now under construction at the Ames Research Center.

GENERAL DESCRIPTION

The VMS motion generator provides six degrees of freedom for a fully out-fitted cab. The motion generator will be installed in a tower that is approximately 22m (73 feet) long by 11m (36 feet) wide by 34m (110 feet) high. Vertical motion is the primary degree of freedom. A vertical platform is the basic structure driven vertically and all other degrees of freedom are assembled on top of it. The vertical platform, fabricated primarily from aluminum plate and angles, spans the tower and is supported by two vertical drive columns spaced to minimize deflections. Eight DC servo-motors drive the platform vertically for a total usable travel of 18m (60 feet) through gear reducers, pinions, and racks which are attached to the columns (see Figure 1 and Table 1).

Principal design calculations used the English system of units.

Table 1. Vertical Motion Simulator Parameters

Item	Value	
Vertical Travel, m (feet)	18	(60)
Lateral Travel, m (feet)	12	(40)
Maximum Vertical Acceleration, m/sec^2 (ft/sec^2)	10	(32)
Maximum Lateral Acceleration, m/sec^2 (ft/sec^2)	7	(24)
Effective Mass for Vertical Acceleration, kg (lb_m)	5×10^4	(1.1×10^5)
Mass for Lateral Acceleration, kg (lb_m)	1.2×10^4	(2.6×10^4)
Maximum Vertical Velocity, m/sec (ft/sec)	6	(20)
Maximum Lateral Velocity, m/sec (ft/sec)	3	(10)
Equilibrator Pressure, MPa (lb/in^2)	2.41	(350)

Four torque tubes mounted in bearings at the tower floor extend out to the drive columns. The vertical drive racks engage pinions on the ends of the torque tubes forcing them to rotate as the platform moves vertically. The torque tubes synchronize the columns driving the platform and react roll moments induced when the cab is off the center position.

Two guide rails attached to the east and north walls of the tower provide continuous support points for the horizontal loads on the vertical platform. Wheel assemblies on the vertical platform transfer these loads to the rails.

Lateral motion capability of 12m (40 feet) is provided by a lateral platform which is driven across the vertical platform. Four DC servo-motors on the lateral platform drive through gear reducers and pinions to a fixed rack on the vertical platform.

A commercially available six degree of freedom motion generator will be mounted on the lateral platform to provide longitudinal and rotational motions. The hydraulic power supply for this unit will be installed in a separate room adjacent to the tower. Hydraulic and electrical power and signals are transmitted through lines mounted in two catenaries linking the lateral platform to the tower walls (Figure 1).

An equilibration system, used to uncouple gravity forces from the vertical drive, uses air pressure inside the drive columns to provide a constant upward force equal to the effective weight of the vertically moving components of the simulator.

VERTICAL DRIVE

Each tubular vertical drive column is 35m (81 feet) long and is loaded by internal air pressure as well as by mechanical loads from the drive and torque tube pinions. Two racks are attached to each column. The pinions which engage them are mounted in diametrically opposed pairs. Pinion separating forces are then balanced, eliminating the need for heavily loaded guide rollers. A small (eight degree) pressure angle rack reduces squeeze on the column from pinion separating forces.

The drive columns are critical components of the simulator from a safety standpoint. Failure of a column would be catastrophic. For this reason extra care in analysis of the stresses was needed. Flanged connections were designed using the ASME Boiler and Pressure Vessel Code (Reference 1), and stress levels were further checked by finite element analysis using the NASTRAN program. The tubular part of the columns was sized using hand calculations, but the complicated geometry of the rack attachment and multiple pinion load points resulted in a decision to refine that analysis through the finite element approach.

All pinions for each column are mounted in a carrier which encompasses the column and reacts the separating forces internally (Figure 2). The column is positioned laterally relative to the pinion carrier by polyurethane coated guide wheels mounted in the pinion carrier. Pinion carriers are gimbal mounted on the floor to accommodate small angular misalignments and crookedness of the columns. Axial alignment of columns with their pinion carriers is also achieved by the guide wheels. Pinions are flexibly spline-mounted on their shafts to assure tooth contact across the full 10cm (4-inch) rack width. Drive motors, reduction gears, and torque tubes are mounted rigidly to the floor and connected to the pinion shafts by gear couplings.

One of the design criteria for the VMS is to provide a mechanically stiff system in order to keep its fundamental frequency well above the desired servo-controlled operating frequency of about 2 Hz. Individual components were designed to have a frequency of about 15 Hz, recognizing that when they are combined in a single structure their combined compliances would result in a lower resonant frequency. A NASTRAN analysis was done to find the frequencies and mode shapes for the complete VMS structure, giving a first natural frequency of 7.5 Hz. Figure 3 shows the undeformed and deformed plots of the vertical platform for the 7.5 Hz fundamental frequency.

<center>EQUILIBRATION SYSTEM</center>

The purpose of the equilibration system is to support the dead weight of the simulator so that the drive system sees nearly identical inertial loads whether driving up or down. The effective weight of the vertically moving parts of the simulator is about 4.9×10^5 newtons (110,000 lb). Equilibrating forces for the VMS arise from pressurized nitrogen gas contained inside the drive columns. Each drive column fits over a stationary inner tubular column which is connected by piping to a gas storage volume of 28 m^3 (1000 ft^3). A sliding seal at the bottom of each drive column allows vertical motion with little gas leakage. Changes in volume of the gas container resulting from vertical motion are relatively small ($\pm$ 5% from mid-travel position) resulting in a nearly uniform equilibrating force.

<center>FRICTION DAMPED CATENARIES</center>

<center>Description</center>

The total vertical and lateral excursions of the VMS motion system are

22m (72 feet) and 14m (46 feet) respectively. A number of schemes to provide electrical power and control cables, instrumentation leads, and hydraulic lines to the lateral carriage from various points in the tower were investigated. The chain-like apparatus shown in Figures 1, 4 and 5 was selected as the best candidate for the job. The two flexible "conduits" are suspended between the support structure on the lateral carriage and two pivot points which are located 16m (52 feet) above the floor on the north and south tower walls. The two catenaries are constructed much the same as a roller chain. The links are approximately 0.9m (3 feet) long from pin to pin and wide enough to provide 0.6m (2 feet) of clear space for the attachment of cables and hoses. In order to prevent the catenaries from whipping and oscillating as the motion system goes through its various gyrations, spring loaded brake discs will be installed at the hinge points of each link. They are arranged as shown in the exploded view and section in Figure 4.

Urethane bumper pads and stops will be installed at each of the hinge points on both sides of the links to prevent the catenaries from reversing curvature during large, downward, vertical excursions when the acceleration is greater than one "g". (This is outside the scope of the present motion generator but within the scope of an upgraded version.)

The catenaries consist of 24 links each and have a total length, from the pin joint on the tower wall to the pin joint at the lateral carriage, of 22m (73 feet).

DYNAMIC ANALYSIS

Concern about the dynamic behavior of the catenaries during various simulator motions resulted in the concept of the coulomb friction damped catenaries described above. Extraneous forces from whipping and flailing cables and hoses would produce severe negative effects on servo-system performance. The purpose of the dynamic analysis was to give assurance of adequate performance by the catenary system.

A numerical analysis was performed using the idealized model described in Figure 5. Masses are considered to be lumped at the joints of the 24-link catenary. The links are all of equal length and are considered rigid.

K_i represents the torsional spring coefficient in a joint. The spring stiffness is derived from the cables and from the "anti-reverse curvature" urethane bumpers. Figure 6 shows the variation of the spring stiffness as a function of $\Delta\theta_i = \theta_i - \theta_{i-1}$.

$$K_i = \frac{K_p + K_N}{2} + \frac{K_p - K_N}{2} \text{ sign } (\Delta\theta_i)$$

Springs mounted on the building wall to cushion impacts of the joints with the wall were also included in the model, but details of their incorporation are omitted for brevity.

Frictional damping in the joints is denoted by C_i. Because of the discontinuous nature of friction force with reversing velocity and numerical

analysis considerations, the following function was used to represent friction torque versus $\Delta\theta_i = \theta_i - \theta_{i-1}$:

$$F_T = T_0 \left(\frac{2}{\pi}\right) \arctan [S(\Delta\theta_i)]$$

X (t) and Y (t) are the prescribed motions of the last joint. In reality, X and Y can be any functions of time that the simulator servo-system can generate. In this case $X = A \cos \omega_1 t$, $Y = B \cos \omega_2 t$ were chosen because of the mathematical simplicity of the functions. With the simultaneous application of X and Y motions and appropriate selection of A, B and $\omega_{1,2}$ the extremes of displacement, velocity, and acceleration can be obtained.

Lagrange's equation was used to obtain the differential equations of motion for each joint, resulting in a system of 24 second order, non-linear differential equations. These were converted to 48 first order equations and solved numerically.

Although printed output was obtained, the most interesting and useful results were the 16 mm movies of the computed joint trajectories. They were generated by plotting joint positions at 1/96 second intervals resulting in movies with the motion slowed by a factor of 4.

After analyzing cases with and without friction damping and anti-reverse curvature springs, it appears that incorporation of these concepts will result in satisfactory operation of an otherwise ill-behaved cable support system, using only about 15% of the 110 newton-m (1000 in-lb) friction damping torque available at each joint.

REFERENCES

1.   ASME Boiler and Pressure Vessel Code, Section VIII, Division I, Appendix II, Part B, 1971
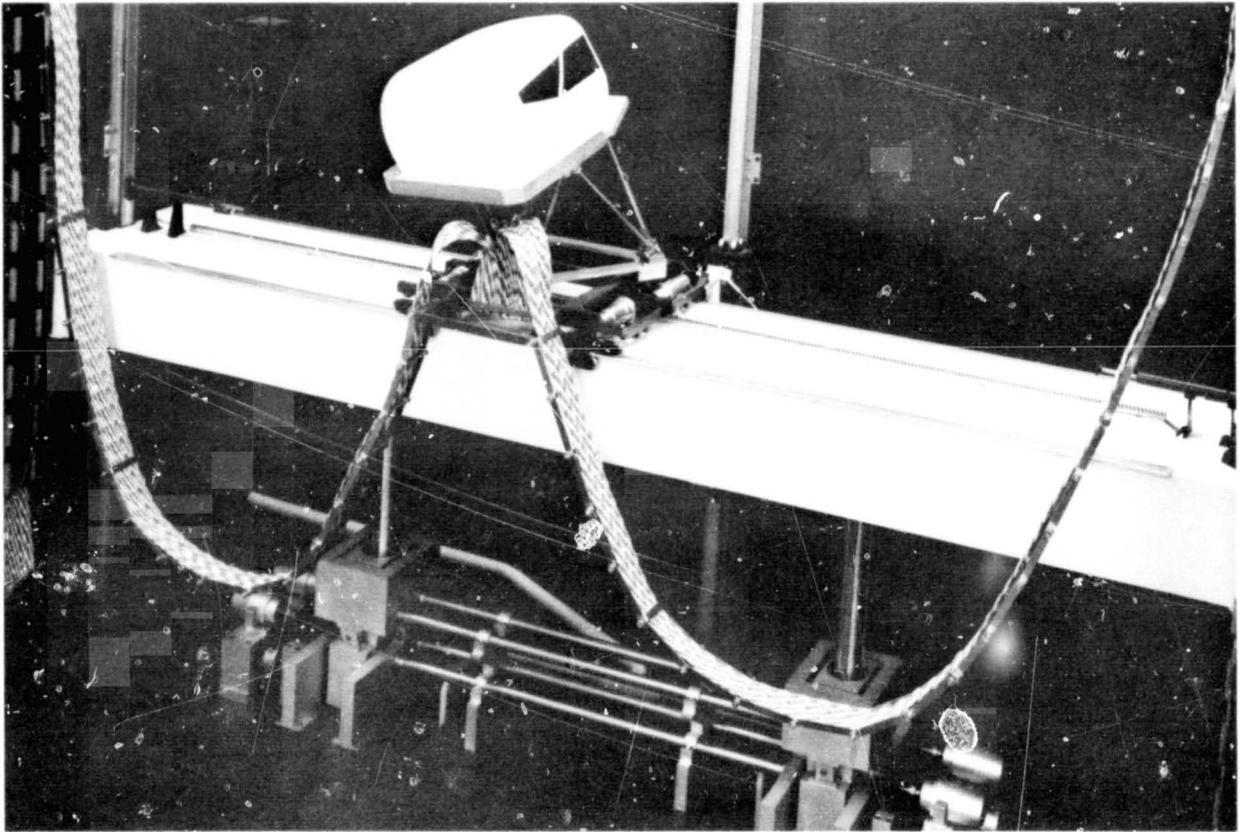
Figure 1. Scale model of Vertical
Motion Simulator
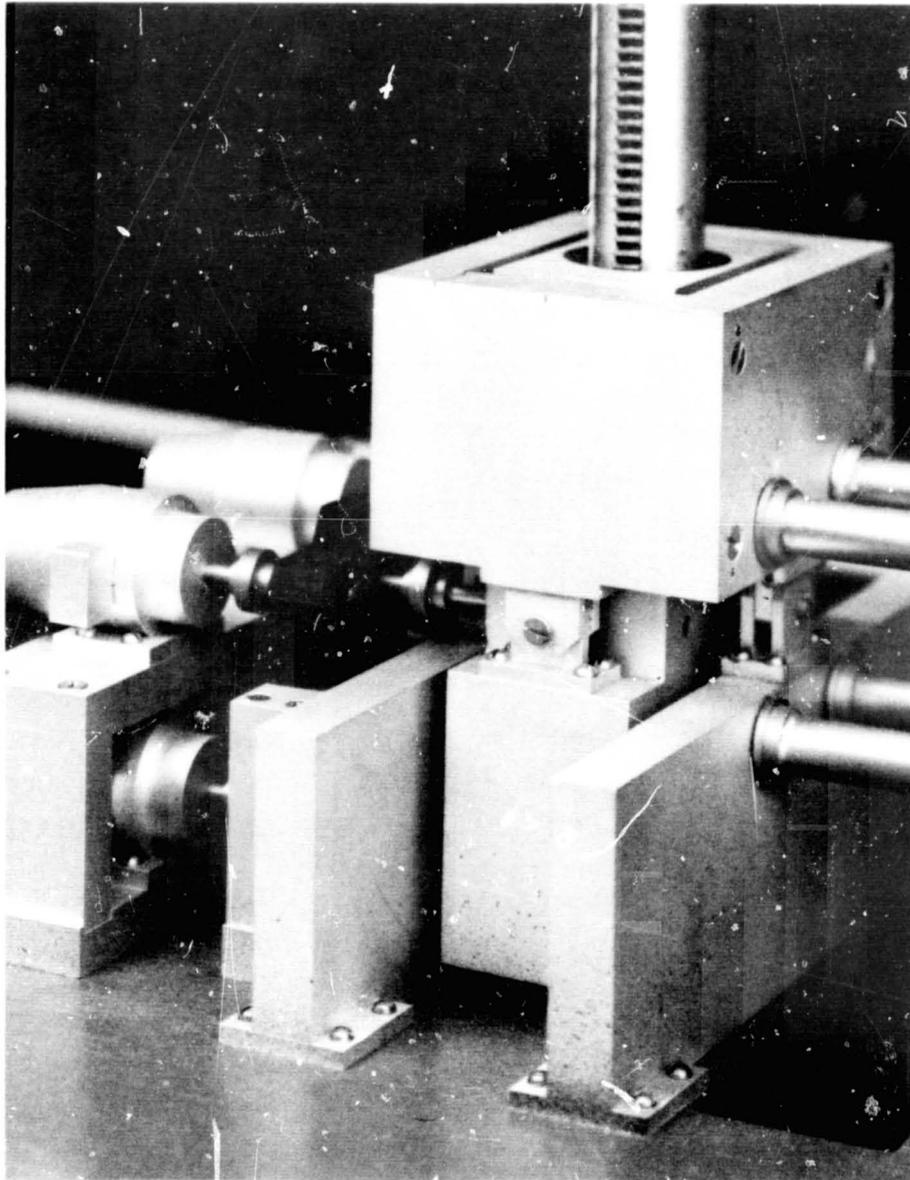
Figure 2. Vertical drive pinion carrier of
Vertical Motion Simulator model

LATERAL SUPPORT
GUIDE WHEELS AT
A, B, AND C

UNDEFORMED SHAPE

DEFORMED MODE SHAPE
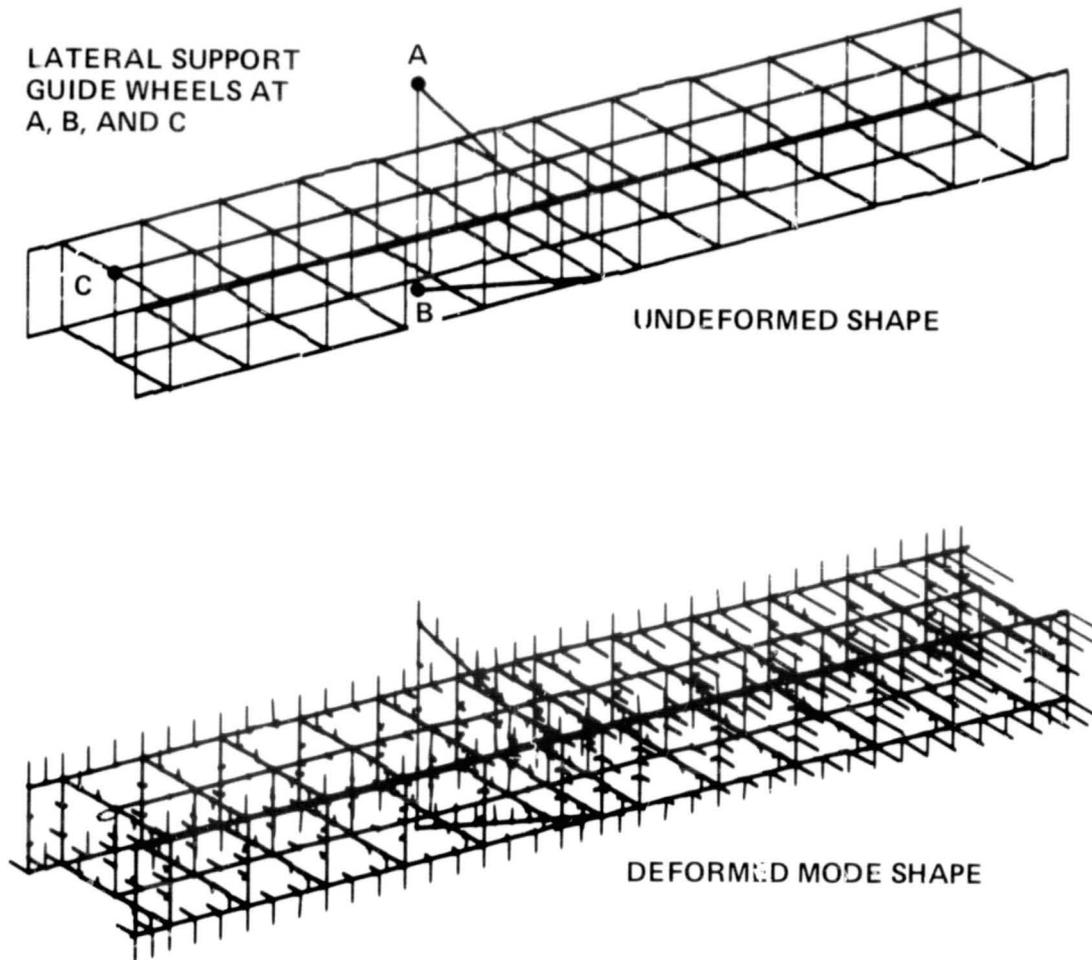
Figure 3.   Structural plots of the vertical platform
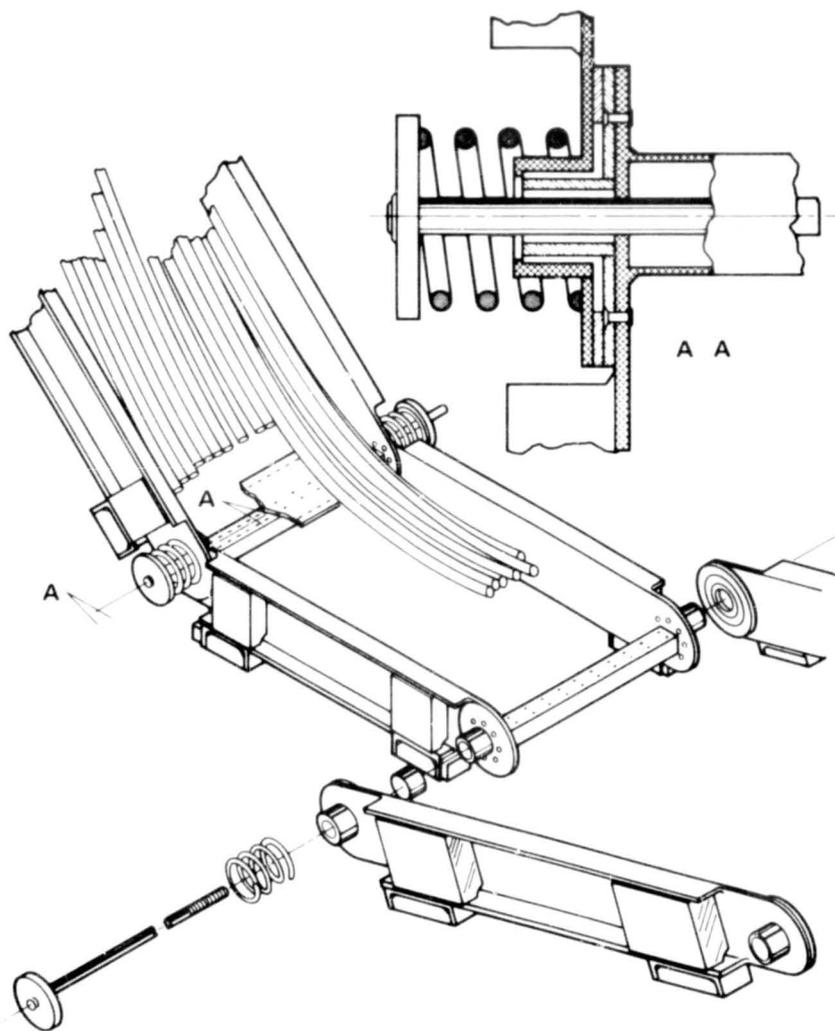
Figure 4. Catenary link detail
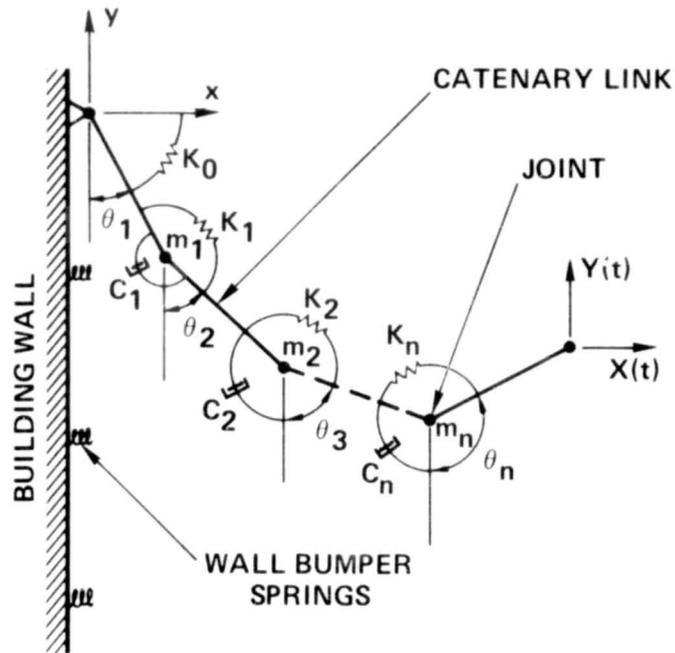
Figure 5. Catenary mathematical model
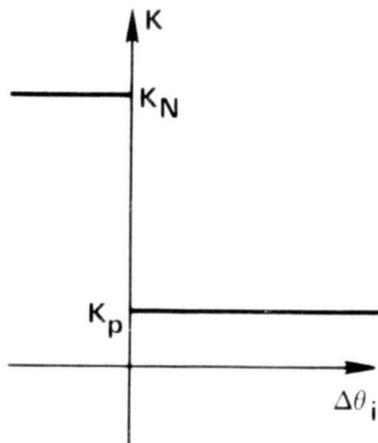
Figure 6. Catenary torsional spring characteristics
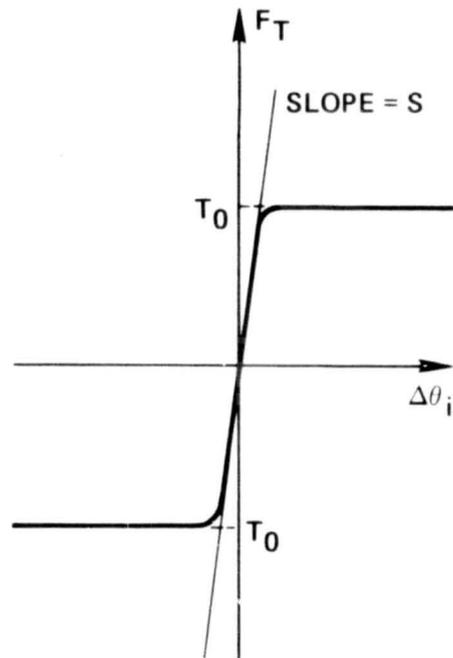
Figure 7. Catenary frictional torque

A SIMULTANEOUS SPIN/EJECT MECHANISM

FOR AEROSPACE PAYLOADS[†]

By G. Dan Palmer, TRW Systems Group
and Tom N. Banks, AVCO Systems Division

ABSTRACT

A simultaneous spin/eject mechanism was developed for aerospace applications requiring a compact, passive device which would accommodate payload support and controlled-release functions, and which would provide a highly accurate spin/ejection motion to the payload. The mechanism satisfied the requirements and is adaptable to other deployment applications.

INTRODUCTION

The simultaneous spin/eject mechanism is an important element of a recently developed system for accurate, efficient, low-cost deployment of aerospace payloads from their final booster stage (Figure 1). Although this is not the first program to employ a mechanical device to impart a simultaneous spin and eject function to a payload, the mechanism is unique because it is extremely compact and lightweight, has a highly efficient energy release, and has excellent, repeatable performance. These features have been confirmed by extensive analytical simulations and ground tests under 1-g and zero-g environments.

For this application, ease of integration with the vehicle, the supporting spacer, and the booster configuration was important; in addition, payload bumping potential and desired system accuracy called for low tipoff effects. The mechanism can be easily adapted to other aerospace deployment applications. Basic design parameters are listed in Table 1.

The successful development of this mechanism involved the joint efforts of three separate contractors: AVCO, TRW, and General Electric. AVCO was responsible for design, development, fabrication, and testing of the mechanism as a subsystem; TRW supplied design analysis, system engineering, and technical support; and GE was responsible for the integrated system (final stage booster with spin/eject mechanisms and vehicles).

SPIN/EJECT MECHANISM

The post-deployment configuration of the mechanism, Figure 2, has three basic elements: (1) a spin/eject device which imparts the desired relative separation velocity and spin rate to the vehicle; (2) a central tie-down system consisting of a structural spacer, a pyrotechnically actuated separation nut, and a high strength tie-down bolt; and (3) two in-flight disconnects (IFD's) that provide the electrical interface between the vehicle and the booster.

Spin/Eject Device

The spin/eject device consists of a spring-actuated guide housing with helical grooves and helix guidepins, with the guidepins also functioning as mechanical stops for the spring guide. The housing, which is fixed to the spacer hub, accommodates the two fixed and diametrically opposite guidepins that ride in matching helix grooves. The force of the spring pushes the spring guide against the guidepins causing simultaneous spin and longitudinal ejection. The selected helix angle determines the amount of rotation in relation to the axial translation of the spring guide and the vehicle. Ejection and spin forces are applied to the vehicle through its rear cover upon which the spring guide bears while simultaneously engaging two torque pins.

The elongated slots at the ends of the helix grooves provide low rebound and self-locking (Figure 2). During the development ejection tests, a change from a completely round pin to a semi-flat pin was made to eliminate local deformations (due to high bearing stresses) which occurred along the helix groove surfaces. These local deformations had contributed to high friction and posed a potential threat to test result repeatability. Friction was further reduced by an application of Molycoat to the guidepin and grooved surfaces. The design change and the coating permitted a reduction of friction forces by a factor of 2, resulting in a realization of 88 percent of the theoretically available energy. The redesigned pin also permitted re-use of ejector hardware without refurbishment for successive ejection tests.

Spin torque is transmitted from the moving spring guide to the vehicle through two torque pins extending aft from the vehicle rear cover to slotted grooves in the spring guide forward face (Figure 2). This interface is critical at the instant of vehicle-to-spring guide disengagement because it not only provides the torque transfer, but also supports and stabilizes the vehicle during the ejection stroke. The latter condition is facilitated by both the flat area and the conical frustum extension on the forward face of the spring guide which matches and centers the mechanism with respect to the flat area and machined indentation in the vehicle rear cover. All ejection tests demonstrated a clean, non-disturbing separation at this interface.

Central Tie-Down System

A central tie-down system was developed that utilizes a mechanical spring deployment device to impart a simultaneous spin/eject motion to the vehicle upon activation of an explosive nut. The structural spacer provides the interface transition between booster and vehicle while accommodating powered flight loads. The tie-down and release device consists of a high-strength separation bolt, under a preload of 37. 8 kN (8500 lb), with an ordnance activated separation nut (SOS114196) located within the vehicle.

The preload magnitude is based on static and dynamic loads and vibration environments associated with the boost phase, and is designed to preclude vehicle-to-spacer "gapping." A simple assembly and preload procedure was developed for integrating the spin/eject mechanism with the spacer and vehicle.

The tapered seat at the aft end of the spring guide housing prevents rebound of the ejected separation bolt. The bolt is trapped in its rearward position prior to spring guide movement providing a protuberance-free interface with the vehicle.

Inflight Disconnects

Electrical requirements for the subsystem were met by providing two IFD's (18-pin standard Bendix connector) at the rear cover/spacer interface (Figure 2). These connections provide checkout, monitoring, and control functions from the launch facility, as well as transmission of the activation current on inflight command to fire the pyrotechnics of the separation nut.

To preclude pin binding during extraction, AVCO designed and developed a connector support device. This device allows three-dimensional adjustment during assembly and adequate freedom for rotation which permits the pin connector to be separated with little or no side load upon preload release and during the initial spin/eject motion. This "floating nut-plate" (Figure 3) prohibits relative motion prior to the separation event and accommodates the rotation required up to the time of IFD physical separation.

SPIN/EJECT REACTIONS

Booster control system capability limits dictate the maximum axial and angular (roll) impulses to the booster at 75. 6 Ns (17 lb-sec) and 13. 6 Nms (10 ft-lb-sec). Booster component responses to the separation nut ordnance shock and to off-center deployments were of concern; however, ground test results verified that the induced environments were within acceptable limits.

Although the deploying vehicle is supported at the forward face of the spring guide, very little transverse moment capability exists at this interface. Consequently, the vehicle tends to hinge, or tip, relative to the moving spring guide if the reaction moments on the booster stage yield

overturning moments to the vehicle greater than the restoring moment
capability. Off-axis deployments, i.e., where the ejection force line of
action does not coincide with the combined booster-vehicle c.g., are sus-
ceptible to this tendency. The degree of hinging is a function of the deploy-
ment reaction moments and the booster-vehicle mass properties.

Because the existing design has limited moment capability at the
vehicle-spring guide interface, and because the booster is relatively massive
for the initial vehicle deployments, only the last few vehicles in multiple
deployments experience significant hinging.

DESIGN EVALUATION

The mechanism's flight performance was verified through extensive
analytic simulations and ground tests. Functional performance specifications
required a separation velocity of 1 ± 0.1 m/sec (3.24 ± 0.3 ft/sec) and a vehi-
cle spin rate of 450 ± 72 deg/sec with a tipoff rate less than 3 deg/sec, while
not exceeding the booster reaction impulse limits. Further, contact with
adjacent equipment or vehicles during boost and deployment was to be avoided.

Analytical Simulation

Both closed-form and computerized solutions were utilized in the func-
tional performance analyses. These simulations involved single-body ejec-
tions (the ejector spacer cantilevered from an infinite mass) and two-body
ejections (the ejector spacer rigidly attached to the booster). Closed-form
terms satisfactorily describe the kinematics of the mechanism because the
helix proportions the ejection energy between spin and axial translation. The
closed-form solution was used in the mechanism parameter/performance
tradeoffs and for support of the early development tests.

To include booster control system and ejector flexibility effects (e.g.,
torque pin/rear cover and guide pin/groove compliances), however, a more
extensive computerized simulation was developed. The simulation was used
in establishing the pre-test predictions and post-test evaluations for both the
system separation tests (zero-g drop) and actual flight tests. Critical areas
of deployment clearance, optimum deployment order and sequence for multi-
ple deployments, and trajectory inputs (targeting biases) were evaluated
based on the computerized simulation. This simulation included two six-
degree-of-freedom bodies (one with a complete control system and logic),
clearance envelope geometry, flexible ejector effects, and provisions for an
approximation to the hinging effect.

Ground Test

Development and verification of the simultaneous spin/eject mecha-
nism, both as a subsystem and as part of a missile system, comprised a

major portion of the overall program testing activity. The ground ejection testing history is briefly summarized in Figure 4.

Ejection Tests (1-g)

Early design verification of the mechanism concept was obtained from a series of fixed-base vehicle downward ejection tests. Several tests were run using a conservative simulation of the hinging environment; a 10-degree vertical tilt induced a transverse moment on the vehicle during the ejection stroke caused by the 1-g gravity vector. Several test configurations underwent preconditioning (shock and vibration) prior to testing. The vehicle was a mass simulated model with actual rear cover hardware; the spacer and the mechanism were full-scale development, or flight-type, hardware configurations.

AVCO developed and employed a computerized data reduction technique for use with the high-speed (400 frames/sec) film coverage. Markings were made on the vehicle model, and the relative positions of these markings and changes in dimensions were measured, frame by frame, using a Vanguard film analyzer. Appropriate geometric relationships and camera optics coded into a computer program were input with measured data from the Vanguard analyzer; velocity, spin rate, and tipoff data were output.

For this test phase, eleven subsystem ejection tests were performed: three checkout tests of early design hardware; five development tests, one with the semi-flat pin reference design; and three engineering demonstration tests, all with design reference hardware (Figure 4).

In addition to verifying the simultaneous spin/eject concept and design approach, the tests were used to: (1) demonstrate functional operational and performance capabilities, (2) determine repeatability, and (3) establish final design performance parameters and compliance with design requirements.

Separation Tests (Zero-g)

The system-level separation tests utilized the mechanism to deploy a vehicle from a booster model under a zero-g environment. The zero-g environment was obtained by simultaneously dropping the vehicle and the booster model prior to initiating the ejection event, and continuing free-fall beyond end of stroke (Figure 4). As part of the flight-proof testing, an additional separation test was conducted with the flight-proof vehicle and spin/eject subsystem in the zero-g environment.

The configurations tested represented different mass properties of the booster, as well as different offsets for the ejection impulse reaction with respect to the system c.g. Corresponding results were predicted for each test from analytic simulations that accounted for specific mass and offset parameters. The correspondence was excellent between predictions and measurements.

Deployment data for the separation tests from the vehicle and booster model rate gyros and accelerometers were hard-wired to the data acquisition system. For the flight-proof test, the dynamics portion of the flight instrumentation system (rate gyros, accelerometers, and PCM telemetry) was utilized.

Results of the four demonstration separation tests and the flight-proof separation test data, including the effects of new hardware and environmental exposure, indicate oustanding agreement with predictions and an excellent degree of repeatability (Table 2).

CONCLUSION

The final design hardware and functional performance of the simultaneous spin/eject mechanism fully meets the subsystem and system requirements as verified by analyses, ground tests, and successful flight tests. Specifically,

- The electrical inflight disconnect design, which accommodates simultaneous rotation and translation, is functionally adequate; no adverse effects were observed.

- The ordnance-activated separation nut is a reliable device for initiating the spin/eject process. The shock environments produced by separation nut activation and spin/eject process are within acceptable limits.

- The mechanism provides predictable, acceptable, and repeatable performance; tipoff effects were consistently less than the 3 deg/sec requirement.

- Deployment reactions generated by the operation of the mechanism were accommodated by the booster without detrimental effects.

The design latitude of this mechanism can readily accommodate a practical range of vehicle mass properties by modification to the helix angle, ejector spring rate, and/or stroke. The design ensures adaptability to future aerospace vehicle or spacecraft deployment subsystem applications.

ACKNOWLEDGEMENT

Table 1. Mechanism basic design data

Parameter	Nominal Magnitude
Mechanism	
Ejection spring rate	26.62 kN/m (1824 lb/ft)
Spring free length	16.6 cm (6.55 in.)
Spring compressed length	9.1 cm (3.59 in.)
Active stroke	5.1 cm (1.99 in.)
Initial spring force	2.13 kN (480 lb)
Torque radius	2.4 cm (0.9488 in.)
Helix angle	9.963 deg
Displacement ratio, angular to linear	4.18 deg/cm (10.608 deg/in.)
Friction coefficient	0.12
Exterior size	6.6 cm (2.6 in.) diameter, 14.0 cm (5.5 in.) height
Weight (including spring)	1.45 kg (3.19 lb)
Spacer	
Spacer size	25.4 cm (10.0 in.) diameter, 20.3 cm (8.0 in.) height
Spacer weight (including separation bolt, nuts, and cable assemblies)	2.97 kg (6.54 lb)

Table 2. Zero-g separation results

Parameters	Test Designation				
	1	2	3	4	Flight-Proof
Axial Velocity, m/sec					
measured	0.98	1.07	1.04	0.94	0.85
predicted	0.95	1.01	1.01	0.88	0.82
Axial Velocity, ft/sec					
measured	3.2	3.5	3.4	3.1	2.8
predicted	3.1	3.3	3.3	2.9	2.7
Angular Rates, deg/sec					
measured pitch	-5.0	-0.1	0.5	-3.0	-3.3
predicted pitch	-3.6	0.1	1.8	-5.2	-5.2
measured yaw	3.2	0.2	-1.1	3.2	2.8
predicted yaw	3.1	0.2	-0.5	3.0	2.4
measured roll	478	483	472	475	472
predicted roll	465	453	456	469	458
Tipoff Rates,[†] deg/sec	1.4	0.2	1.4	2.2	1.9

[†]Mechanism induced, based on vector difference of test and predicted transverse rates.
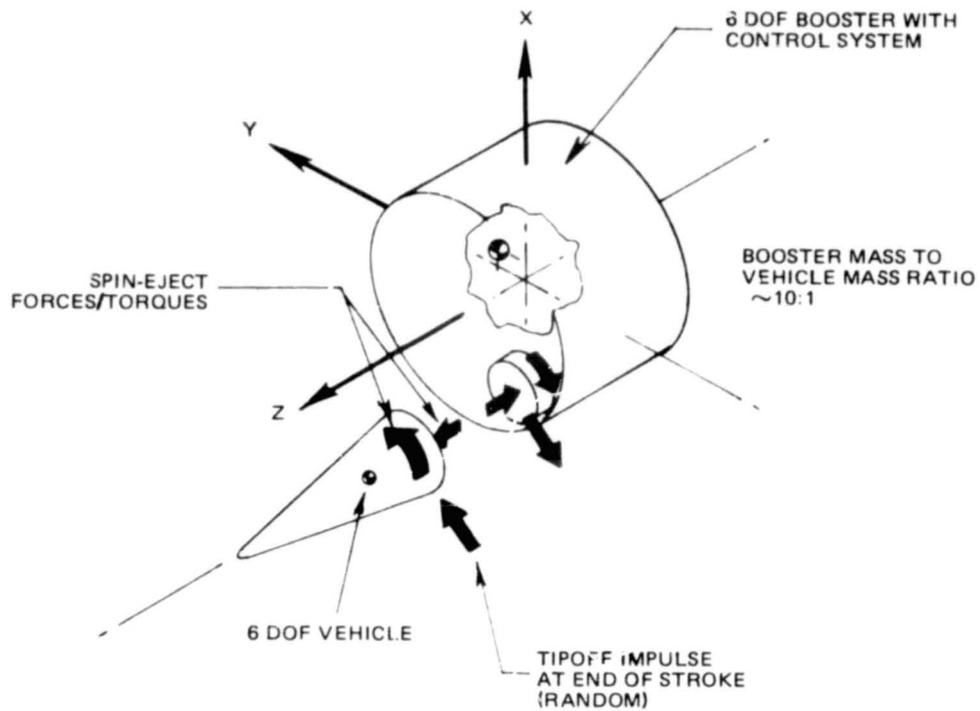
Figure 1. Schematic representation of vehicle deployment
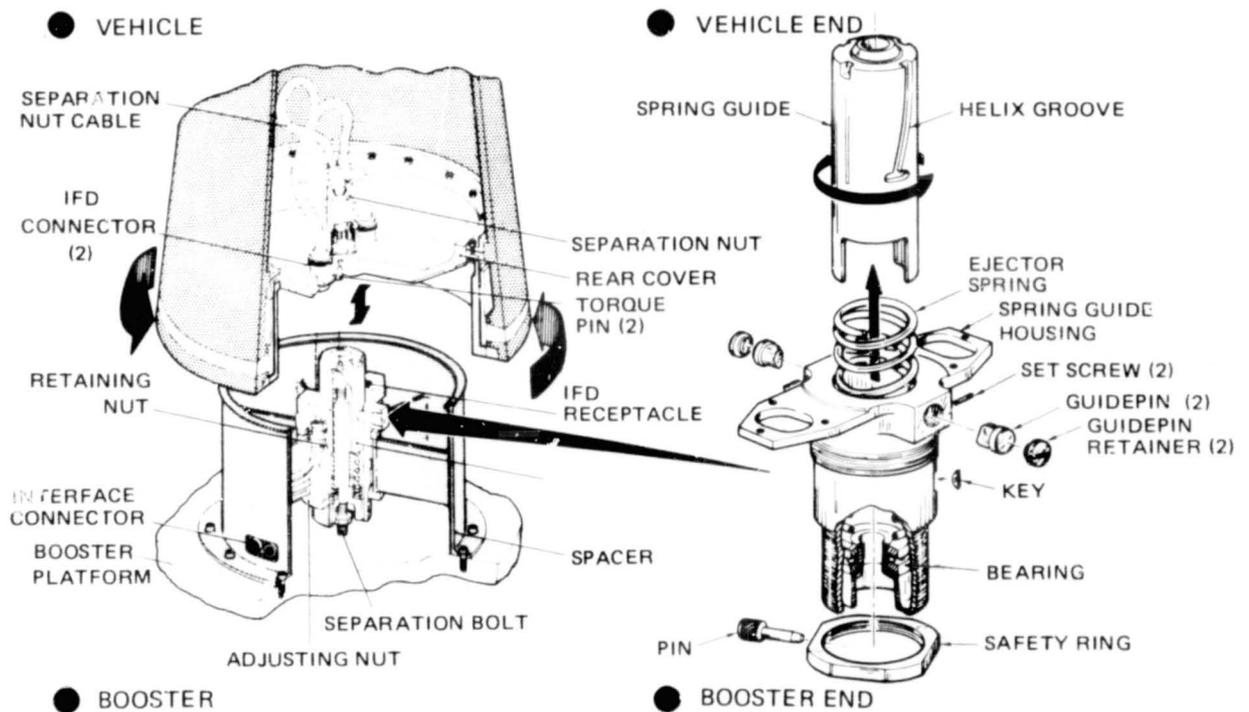
Figure 2. Simultaneous spin/eject mechanism, post-deployed

● ASSEMBLED VEHICLE AND SPACER

GROUNDING FINGERS

ADJUSTING RING

CONNECTOR
(PLUG END)

DIRECTION OF EJECTION

CONNECTOR
AND PIN SEALS

VEHICLE
REAR COVER

ADAPTER

HOUSING

DIRECTION OF SPIN

VEHICLE SIDE ◄——► SPACER/BOOSTER SIDE
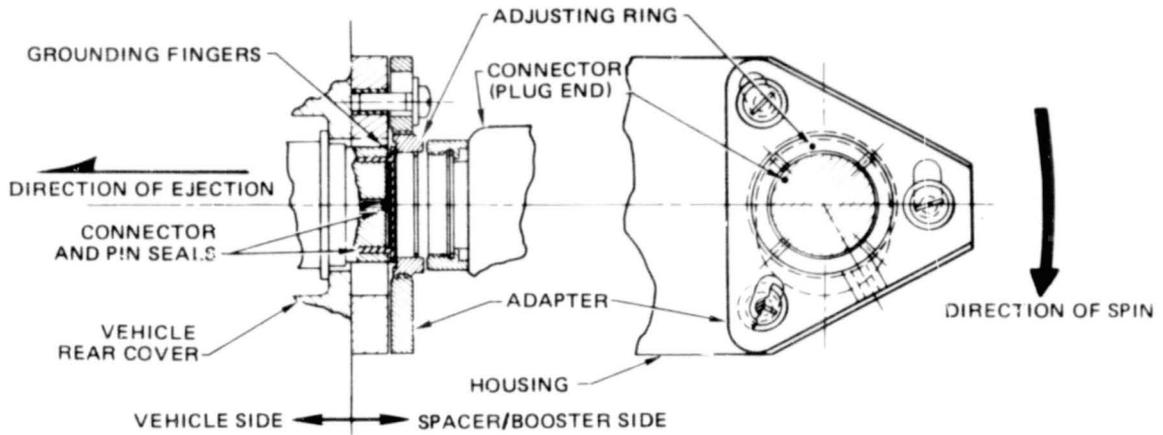
● DISENGAGED VEHICLE AND SPACER

INITIAL POSITION

0.762 CM
(0.300 IN)

4°

ANGULAR DISPLACEMENT
NEEDED FOR 0.762 CM
(0.300 IN) FWD
DISENGAGEMENT
OF CONNECTORS

VEHICLE SIDE ◄——► SPACER/BOOSTER SIDE
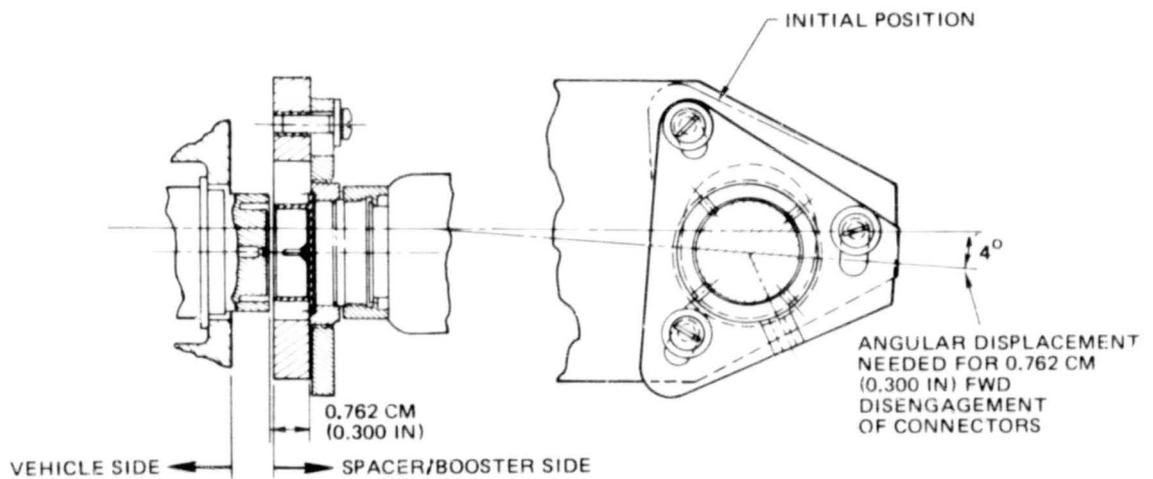
Figure 3. Basic design, inflight disconnect

● EJECTOR TEST SETUP, 1-g
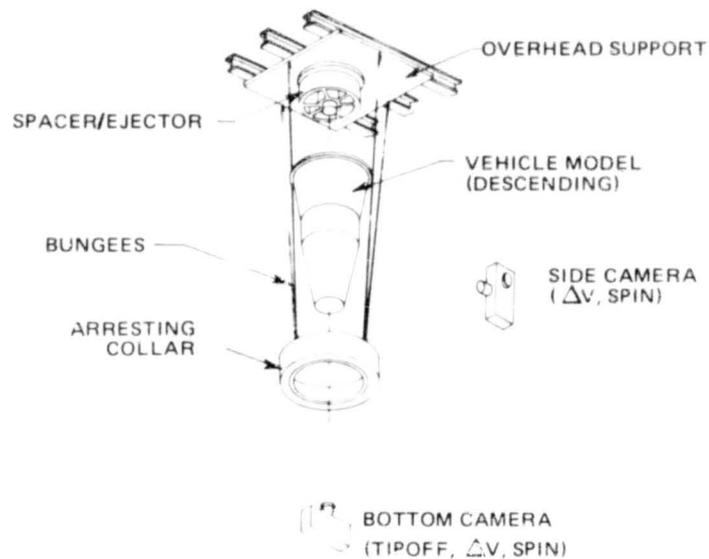
● TEST TYPE:

Fixed base, downward ejection in 1-g field

● NUMBER OF TESTS AND MECHANISM HARDWARE CONFIGURATION:

3 Checkout (early design hardware)

5 Development (1 with final helix pin design)

3 Engineering demonstration (design reference hardware)

RESULTS

● 16 Successful deployments; results and repeatability allowed reduction of planned test program

● Hinging effects predictable and acceptable

● Friction determination:
  $\mu = 0.124$ (7 tests)

● Tipoff rate:
  < 3 deg/sec (10 tests)

● Spin-rate and velocity predictions confirmed: (5 0-g tests)

● SYSTEM SEPARATION TEST SETUP, 0-g
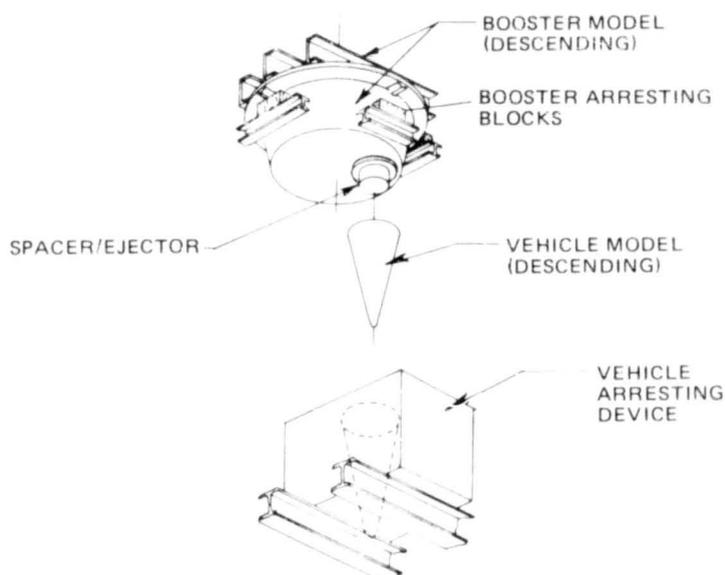
● TEST TYPE:

Two body separation, free-fall in 0-g field

● NUMBER OF TESTS AND MECHANISM HARDWARE CONFIGURATION:

4 Engineering demonstration (design reference hardware)

1 Flight proof (flight configuration)

Figure 4. Ejector and system separation tests

DESIGN EVOLUTION OF A LOW SHOCK RELEASE NUT*

By David H. Otth - Jet Propulsion Laboratory
and
William Gordon - Hi-Shear Corporation

ABSTRACT

Design improvements and detailed functional analyses are reviewed to trace the development of a pyro-actuated release device with segmented thread design from its intermediate design into one that reduces the levels of shock spectra generated during its operation by 50%. Comparisons of shock output and internal load distribution are presented, along with descriptions of mechanical operation for both designs. Results also show the potential areas where design development activity can gain further progress in lowering actuation shock levels.

INTRODUCTION

Pyro-actuated release device configurations with launch load carrying capability for spacecraft or expended-stage separation plane designs characteristically reduce their installed preloads to zero within millisecond function times to complete interface separations. This design feature provides high mechanical and dynamic efficiency for separation but generates high frequency and magnitude shock levels which are transmitted through the interface to the adjacent structure. If electronic packaging, attitude control gyros, or science instruments sensitive to shock are nearby, this side effect may be undesirable depending upon the magnitude of shock spectra received.

Development of the release device for the Viking Orbiter 1975 (VO'75) separation interfaces brought about an understanding of the release forces and internal dynamic action related to shock generation. Subsequent design improvements that significantly reduced shock levels were then incorporated into the release device for the Mariner Jupiter/Saturn 1977 (MJS'77) spacecraft interface. Both designs involve a segmented nut that releases 1/2-20 bolts and, for this report, are individually presented in two sections. Discussions are limited, however, to findings and design improvements that resulted in lowering shock during operation.

RELEASE DEVICE FOR VO'75

Description of Operation and Development Program

The Viking Orbiter 1975 release mechanism was a dual squib segmented nut design that mated with a 1/2-20 strain gaged bolt and was utilized on both Orbiter separation interfaces (Viking Lander adapter and spacecraft adapter). The release nut assembly provided an 11,800-lb tension launch preload at four interface hardpoints coincident with each VO'75 separation plane. Upon simultaneous commands to eight squibs, all four mechanisms functioned within 6 milliseconds to reduce hardpoint preloads to zero and eject bolts, thereby completing interface separation.

The Viking device was a modified version of the segmented nut design used on the Surveyor Program with improvements in areas of materials, configuration, and lubrication. These improvements were made during the development program and were initiated to improve internal load distribution, low-temperature performance, and reusability as related to repeated pneumatic testing. A significant portion of the development program was devoted to understanding the source and distribution of the 100,000-g peak accelerometer shock response generated during its operation and to reducing levels as electronic bays were installed adjacent to the separation plane hardpoints. Reducing the shock output required extensive modification, which was not feasible for VO'75, but an understanding of the source of shock and the distribution of loads was obtained. Design changes that would result in reduced shock levels were implemented on the release nut for MJS'77 and are discussed in detail in the next section.

Referring to Figure 1, the VO'75 release nut basically consists of three threaded segments positioned by the base key seat, locking piston, and separator. When the release nut is preloaded, the bolt load is reacted out within the assembly into axial loads, which are parallel to the bolt axis, and lateral loads, generated by the 60-degree thread angle, which are perpendicular to the bolt axis. The axial portion of the bolt load is transferred to the base key seat and the bolt's lateral load is transferred through the segment lands to mating lands in the locking piston. The bolt ejector is contained in the separator and can add velocity to the bolt only after the bolt has been released. The release nut is operated by pneumatic or squib pressure, which drives the locking piston forward, thereby allowing the segments to move radially outward and release the bolt. The pressurized separator keeps the segments out after release by applying a radial load to the segments through the angled interfaces of the separator and base key seat. The true-arc ring is used for initial positioning of the separator and segments relative to the piston lands during assembly and the O-ring's limit outgassing of squib contaminants.

Distribution of Loads

The significant design changes that resulted in lowering actuation shock levels were based upon an understanding of the preload distribution and stresses on the segments and locking piston within the release nut. For a given bolt preload, the load distribution on a threaded segment is described with the aid of Figure 2. The axial portion of the load is compressive in nature and is reacted out into the base key seat. This component of the load acts along a well defined path and therefore requires little description. However, the 60-degree included angle on the bolt and segment threads generates a large lateral component whose load path is not precisely known.

The exact position and shape of the segment load distribution are only generally known; that is, the first few threads carry the majority of the preload. In addition, the reactive load to the piston is also a distribution, but again shape and exact location are unknown. The end result is the inability to determine a precise value for (1) the maximum bending stress on the segments, which occurs at the minimum thread diameter adjacent to the front lands, shown as point A in the close-up portion of Figure 2, and

(2) the piston hoop and bending stress, as shown in Figure 3. To circumvent the problem of inexact load description, a comparative analysis was conducted using point loading rather than distributions and determining the segment bending stress at point A. The bending stress established was given a value of 1.0 and was compared to recalculated stresses when (1) land areas were increased and moved forward toward the base, (2) the first few threads were moved in line with the center of land areas, and (3) segment thickness was increased in the area of highest bending stress (see Table 1). The main design improvement made for VO'75 was increasing the segment thickness behind the first land to lower bending stresses. Aligning the first few threads with the center of land areas and moving the lands forward required extensive redesign, and both changes were incorporated into the MJS'77 configuration, which also eliminated the lightly loaded rear land. These changes not only reduced internal stresses by 60% but lowered piston deflection and changed the segment configuration, which were key factors in reducing actuation shock, as will be discussed in the second section.

Table 1 also shows that although bending stresses were reduced for VO'75, deflection was not, at least from segment changes. On the other hand, the piston's first land area could be easily increased and was, by 0.050", to decrease piston deflection by 20%. The objective was to lower the open end "belling" of the piston, as shown in Figure 3, and thereby the "ramp effect" configuration between the piston and segment lands. This in turn lowered the threshold of "release pressure" and increased functional margins. Moreover, further reductions in piston deflections were possible and were implemented later for the MJS device to lower the squib energy needed for operation and lower shock.

Another hardware change that resulted in lowering actuation pressures was a combination of materials selected to withstand repeated pneumatic actuation without dimensional changes and an improved moly-disulfide coating. The coating was used on the threaded segments and piston to reduce the coefficient of friction between mating surfaces. The friction coefficient was reduced further by burnishing the land areas prior to assembly and then during two pneumatic actuations prior to flight. A 15% reduction in threshold pressure was obtained by using this process, which again increased functional margin or allowed lower squib energy to be used for operation.

Sources of Shock

The impact of the piston on the base, the strain energy release of the bolt from the segments, and squib firing contribute to the high-level shock generated during operation. The VO'75 development program identified the individual contribution of each source in order to determine those areas where redesign or modification could reduce shock levels. The release device was mounted to a flight-type spacecraft structure with three electronic bays and was instrumented with shock accelerometers located next to the device.

A series of shock signatures were generated by using a number of release nuts actuated with pneumatic, hydraulic, or single and dual squib pressures. The test results have been summarized in Table 2, which gives

the individual contribution of shock sources that result in a 100,000-g peak shock load next to the device. Varying squib loads changed the shock levels by 15%, while hydraulic actuations of the nut which drastically slowed down the piston velocity (compared to squib actuations) indicated that the major shock source was piston impact and represented 60% of the total. This was verified by using Fastax camera coverage that determined the piston velocity in excess of 250 feet per second prior to impact. Using the initial piston velocity and the measured penetration of the piston into a steel base, the deceleration was calculated to be on the order of 60,000 g.

Lowering Shock Levels

Figure 2 shows that shock output can be readily lowered by reducing squib loading and damping piston impact, assuming that methods to reduce the strain energy release are not convenient. By using the load distribution analyses, a new segment configuration was designed having the same preload capability but requiring a more compact and lightweight piston. The new configuration also provided room within the release nut to design a method of reducing piston impact. Damping as well as reversing the direction of piston impact, along with lowering the threshold release forces to permit operation with VO'75 squibs, were the design goals of the low shock release nut.

RELEASE DEVICE FOR MJS'77

Design Features

Concurrent with the effort described for the VO'75 program, the need for an improved release nut design that inherently provided reduced shock levels was recognized. Development work that ensued included design, fabrication, and testing of three different nut configurations that followed the basic bolt retention method used on Surveyor and VO'75. These were tested and evaluated on the basis of several relevant factors, including simplicity, cost, weight, producibility, and the reduction of shock output. The resulting low shock design, depicted in Figure 4, was selected for the MJS'77 program.

The load distribution analyses of the Viking development program led to a further revision of the VO'75 segment, moving the lands toward the base to react against the thread radial loading induced in the first few threads. The second set of lands, located where little or no radial loading exists, were eliminated. The balance of the changes involved those parts which retain the segments and a lighter two-piece piston assembly to mate with the new segment design.

With the primary shock-generating event in the operation of previous release nuts being the impact of the piston with the base, two methods of eliminating this collision were employed. First, the piston was driven away from the base and secondly, it was brought to rest through mechanical and squib gas damping. Reversing the piston direction also aided in lowering threshold release forces as less energy was required to back off the ramp configuration between segment and piston lands caused by "open end" belling. Thus, the same release pressure was obtained with a smaller piston.

Description of Operation

As can be seen in the installed view of Figure 4, the segments are retained by the piston, base key seat, and separator. The separator, similar to that previously used, bears on the upper ends of the segments, helping to stabilize and align them as well as forcing them apart when squib pressure is introduced above the separator. An optional ejector pin is shown that pushes the bolt out of the nut, again when propelled by squib pressure. Unlike the VO'75 design, the pressurized gases are introduced between the separator and piston rather than on top of the piston. This results in the piston being driven away from the base of the nut and allows the segments to move radially outwards. At the same time, gas pressure acts on the separator and ejector, forcing them against the segment and bolt respectively. After the piston has moved sufficiently to release the segments, the lock piston ring contacts the separator. The collision occurs in such a way as to avoid transmitting shock into the adjacent structure as before.

A comparison of the effective pressure area of the piston and separators shows that the separator has more effective area than the piston. This additional area provides a force which acts to decelerate the piston and separator after the piston strikes the separator. The separator is momentarily unseated from the top of the segments due to the inertia of the piston. The major portion of the shock energy in the piston is absorbed during upward motion of piston and separator. The space above the piston is ideally sized such that the two components stop their upward motion due to the pressure area differential, then are forced downward until the separator again seats on the top of the segments. This final seating does generate some shock but significantly less than the direct collision of the piston and base.

Comparison of Shock Levels

The VO'75 device and MJS'77 low shock design were evaluated comparatively on a full-scale flight-type spacecraft structure with electronic bays. Shock signatures were obtained from accelerometers mounted within the electronic bays. The results have been presented as shock spectra, which show peak structural response (G's) versus frequency (Hz). The structural response is derived from the accelerometer peak g time trace, frequency, and a structural amplification factor (Q) of 20. The end result is a convenient representation of total shock content, transferred to the structure in terms of peak G shock and frequency.

Referring to Figure 5, the peak G level of the low shock device is 50% less than that of the VO'75 design as recorded within the electronic bay. If the MJS device was not hard-mounted to the structure but allowed to rebound off the structure after functioning, a 70% reduction in shock spectra was obtained. The same mounting scheme was used for the VO'75 device, but no appreciable reductions were recorded.

CONCLUDING REMARKS

Significant reductions in shock response have been achieved; however, further reductions may be possible by lowering the shock contributions caused by preload release and squib actuation. Although lowering squib energy was not a design goal for MJS'77, reduction of the release force was achieved. Future configurations which are not limited to a specific device diameter can incorporate larger piston diameters and capitalize on the lower release forces. Large areas will allow release pressures to be obtained with less squib energy. As further improvements lower actuation shock, more compact packaging of separation plane hardpoints with electronic bays or science can occur.

Table 1. Segment stresses and piston deflection vs. segment configurations

Configuration	Segment Bending Stress Factors [a]	Open End Piston Deflection, inches
1) Surveyor segment design	1.0	0.00252
2) Increase segment thickness [b]	0.46	0.00252
3) Align first threads with center of land plus (2) above	0.39	0.00194
4) Move land forward plus (2) and (3) above[c]	0.32	0.00173

[a] Represents maximum bending stress comparisons.
[b] Between lands, as was done for VO'75 segment design.
[c] This represents MJS'77 segment design.

Table 2. VO'75 release device shock sources and contribution

Source Item	Accelerometer Response Next to Device	
	g's	Contribution, %
Squib firing	15,000	15
Piston impact	60,000	60
Strain energy release of preload	25,000	25
Total assembly	100,000	100
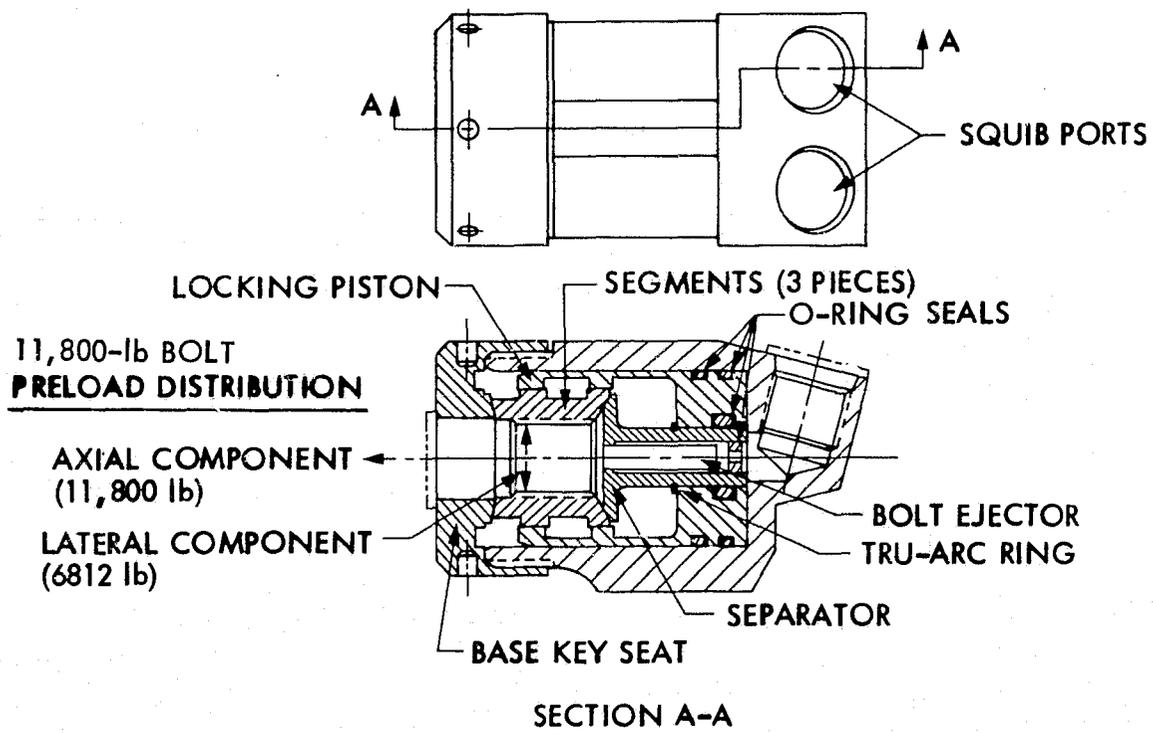
Figure 1. VO'75 release nut assembly cross section

SURVEYOR

SEGMENT LANDS

VO'75 →

MJS'77

MAXIMUM
BENDING

BOLT
PRELOAD
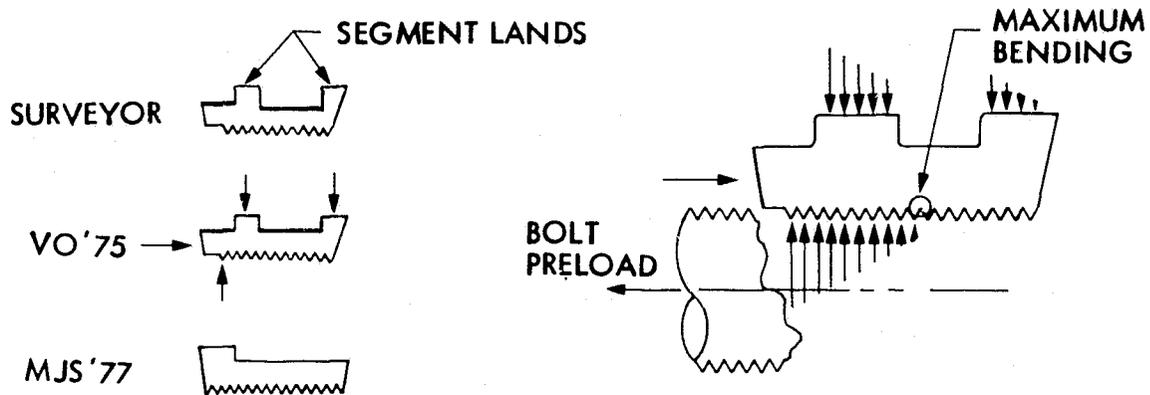
Figure. 2. Cross section of segment designs showing load distribution

HEAVILY LOADED
FRONT LANDS

LIGHTLY LOADED
REAR LANDS

LOADING FROM
SEGMENT LANDS

EXAGGERATED"OPEN END
BELLING" FROM SEGMENT
LOADS
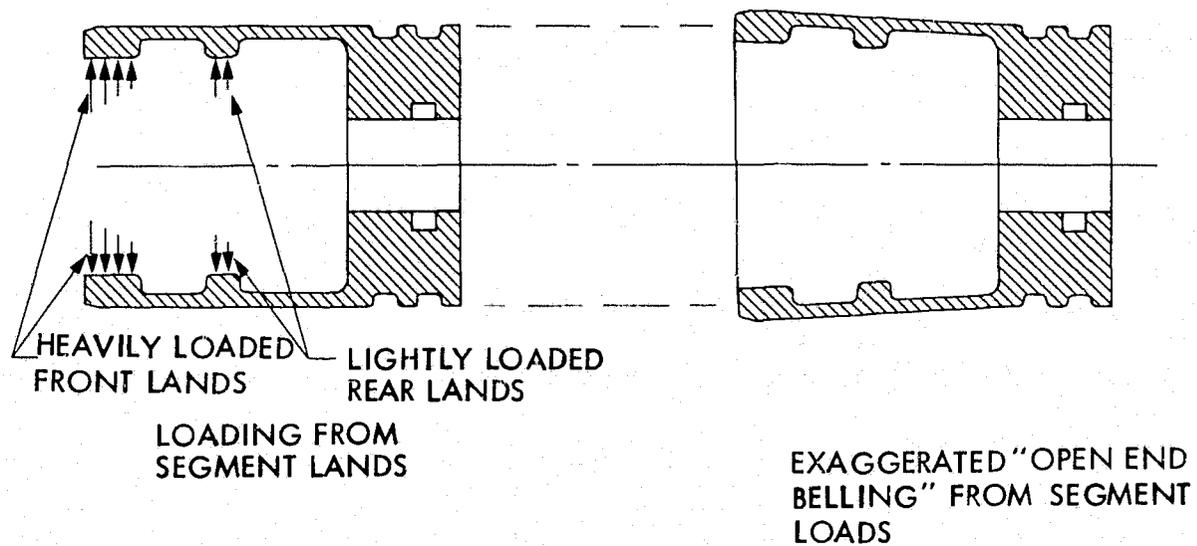
Figure 3. Piston cross sections showing loading and belling

STRUCTURE

KEY SEAT

RETAINING RING

SEALING RING

BOLT

OUTSIDE CASE

THREADED SEGMENT

BASE INSTALLED

LOCK PISTON RING

LOCK PISTON
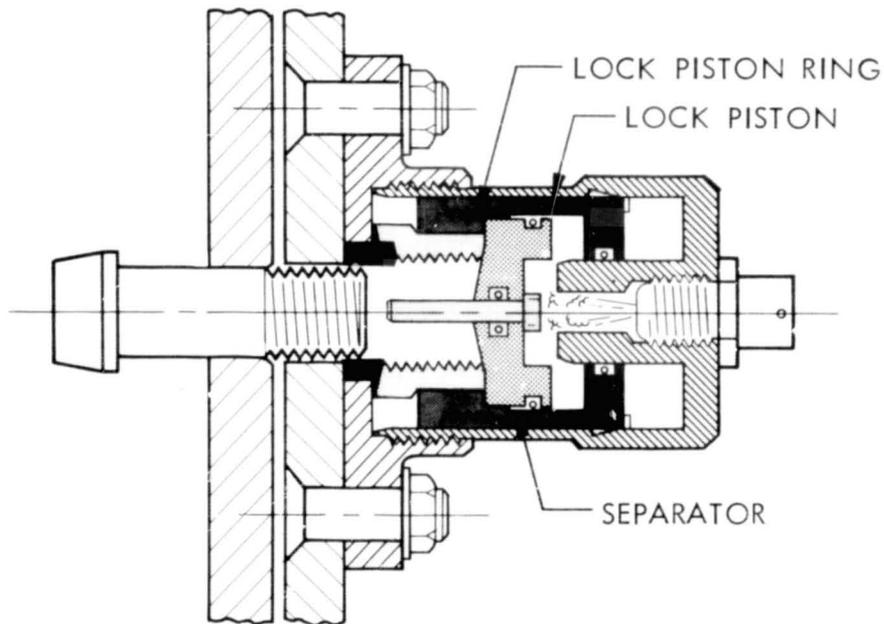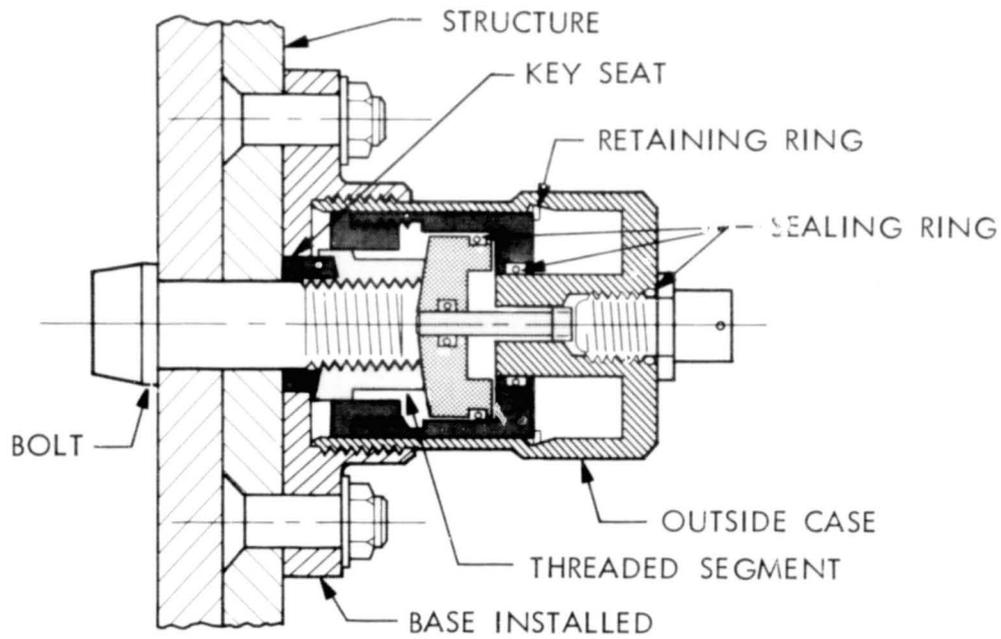
SEPARATOR

SEPARATED

1. LOCK PISTON MOVES AWAY FROM STRUCTURE TO UNLOCK THREADED SEGMENTS.

2. SEGMENTS DISPLACE RADIALLY AWAY FROM BOLT.

3. SEPARATOR PISTON LOCKS SEGMENTS IN OPEN POSITION.

Figure 4. MJS'77 low shock release nut
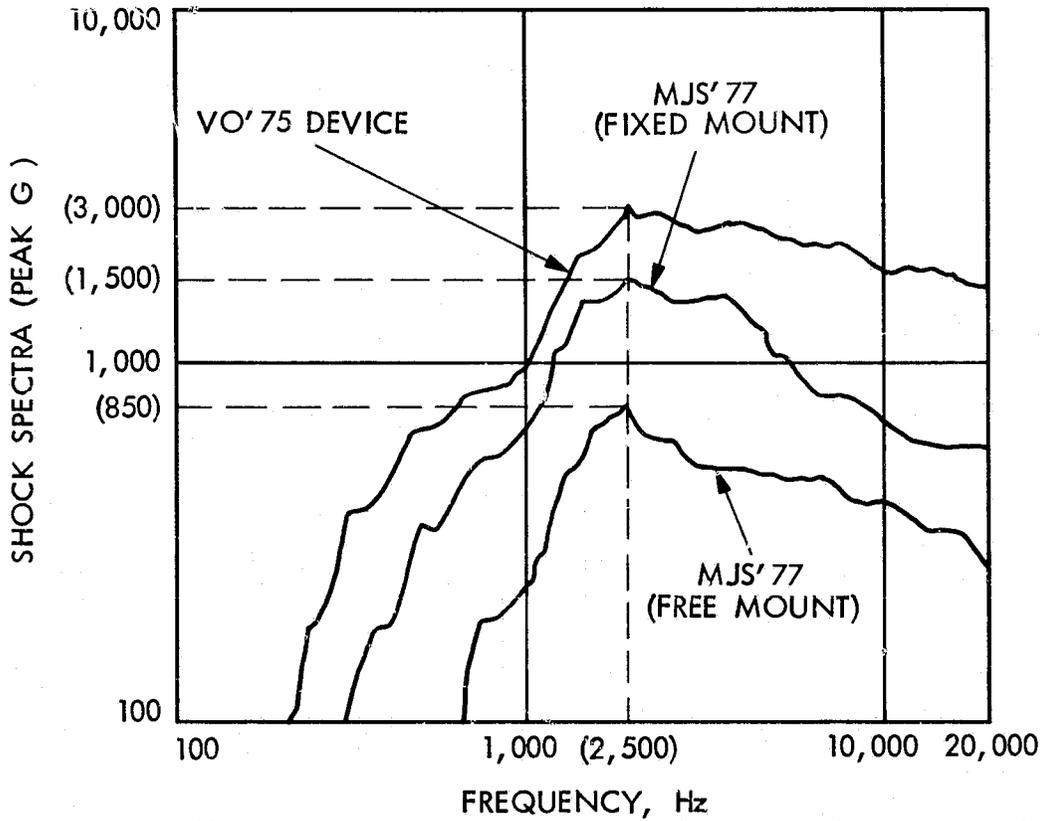
Figure 5. Comparison of peak G shock spectra generated by VO'75 and MJS'77 low shock device vs. frequency

SOLAR ARRAY DRIVE SYSTEM

by Frank D. Berkopec and John C. Sturman
National Aeronautics and Space Administration
Lewis Research Center

and

by R. W. Stanhouse
General Electric
Space Systems Organization, Valley Forge Space Center

ABSTRACT

A solar array drive system consisting of a solar array drive mechanism and the corresponding solar array drive electronics is being developed by the Lewis Research Center of NASA. The principal feature of the solar array drive mechanism is its bidirectional capability which enables its use in mechanical redundancy. The solar array drive system is of a widely applicable design. This configuration will be tested to determine its acceptability for generic mission sets. Foremost of the testing to be performed is the testing for extended duration.

INTRODUCTION

A Solar Array Drive System (SADS) consisting of two elements, a Solar Array Drive Mechanism (SADM) and the corresponding Solar Array Drive Electronics (SADE), is being developed by the Lewis Research Center of NASA (NASA-LeRC). The design of the SADS and the status of the test program are the subject of this paper.

Requirements for the SADS arose from the NASA-LeRC studies of future spacecraft missions (ref. 1, 2, and 3). During conceptual design of spacecraft to fulfill these missions it became apparent that available solar array drive system design and performance data were meager. Also, existing designs did not fulfill the full range of mission requirements. Consequently, specifications for a solar array drive system were formulated from the NASA-LeRC studies and other potential applications (ref. 4 and 5). A set of SADM and SADE hardware was built to these specifications. This hardware is of a quality consistent with its intended use: performance testing, environmental testing, and extended duration testing.

Extended duration testing is perhaps the most meaningful testing to be done. Experience has shown that subsystem and component level testing is essential for detection of defects (ref. 6) and that components must be tested in their correct configuration to minimize flight failures (ref. 7). Specifically, however, motor gear-reduction systems are prone to failures that are not predictable but are unique to a particular design. The only method of determining actual failure modes is by performing an extended duration test of units of flight configuration (ref. 8).

This paper presents a summary of the SADS specifications and descriptions of the design of the SADM and the SADE that were produced to meet these specifications. The status of the SADS test program is presented.

DESIGN REQUIREMENTS

The SADS design requirements were formulated from missions that range from low earth orbit to geosynchronous orbit to planetary missions. Corresponding rotation rates of the spacecraft solar arrays range from 14 revolutions per day (rpd) to 1 rpd to several revolutions per two or three year mission. The rigid-body mass moments of inertia for these solar arrays, about the axis of rotation, are as high as 270 kg-m^2 (200 slug-ft^2) for one wing of a two wing system. Missions are up to six years in length. Mission characteristics thus determine the required life, rate of rotation, and minimum torque for the SADS. Additional requirements for the SADS include bidirectional operation capability, use in parallel for redundancy and/or increased output, and the ability to be completely operated by ground command or by an autonomous spacecraft system.

The SADS specifications are given in Tables 1 through 5. There are several design constraints that should be emphasized so that these specifications are clearly understood. First, some SADM design specifications are based on past test experience with a specific design. Second, it is intended that there be a final 6:1 gear reduction between the SADM output and the solar array; this is noted in the specification. Third, the SADE for each SADM is contained on one 12.7 by 17.7 cm (5 by 7 in.) printed circuit card. This should facilitate use in any spacecraft electronics assembly (attitude control electronics, on-board processor, or housekeeping electronics). The current effort, however, includes packaging two cards in a separate box with conventional connector interfaces.

Principal aspects of the SADS, SADM, and SADE require emphasis. Operation of the SADS is bidirectional. The SADS design permits use of two or more SADM/SADE in parallel for block redundancy and/or increased output. The SADS is operable completely from the ground or completely by an autonomous spacecraft system; thus, the widest range of applications and contingencies is bracketed. The SADM configuration permits single-ended or double-ended output; specifically, the SADM output can be coupled anywhere along the shaft of the driven unit. Loads to the SADM are thus reduced. This also allows more flexibility in the end use of the SADM. The SADE is self-contained on one printed circuit card. The SADE is electrically and mechanically compatible with current spacecraft systems.

SADM DESIGN DESCRIPTION

Background

The SADM developed for the Solar Array Drive System is founded in the General Electric Co. "Long Life" solar array drives extensively life tested in 1972-1974 (ref. 9). Counter-wound wrap springs have been added to the output of this compact

step motor-harmonic drive subassembly to provide bidirectional clutching action. This permits direct coupling of two or more drives to a common solar array shaft gear resulting in a bidirectional block redundant drive assembly.

The two "Long Life" drives were removed from the vacuum chamber in May, 1974 with a total of 60,180 output shaft revolutions and a total time in 1.3×10^{-6} N/m^2 (10^{-8} torr) pressure of 28 months accumulated on both units. The drives were disassembled and thoroughly inspected for evidence of wear or degradation. The condition of the bearings and gears was excellent. Since one of these mechanisms was dry lubricated, the actual cycle life is some measure of "mission life." For a 600-nautical-mile orbit the 60,180 cycles is equivalent to 11.7 years of orbit operation, and for a geosynchronous satellite this is equivalent to 164 years of operation in orbit.

Mechanism Description

The drive mechanism is patterned directly after the General Electric "Long Life" drive mentioned above. The step motor and harmonic drive assembly is identical, using a small angle step motor (1.8° per step), and a 100:1 ratio harmonic speed reducer. A cross-sectional view of the drive is shown in Figure 1. The harmonic drive flex spline is connected to the output pinion shaft through two wrap spring clutches which are counter wound to provide bidirectional overriding clutch action. The clutch energizing torque, which is a requirement for all wrap spring clutches, is provided by a friction drag disc. The friction torque level is adjustable on the exterior of the unit through the action of a wave spring washer and wedge. The smaller wrap spring is wound left-hand and drives when the input shaft rotates clockwise looking at the motor end of the unit, and the larger spring is wound right-hand, making the drive connection when the input shaft is driven counterclockwise.

The net characteristic of the SADM is one of free wheeling at the output in either direction while still maintaining drive capability in either direction from the input side. When driving, a rigid mechanical coupling is established by the spring clutches so that large torques can be transmitted. Hence, two or more units can be directly geared to a common shaft. Clutching from one unit to the other results from switching input power from one drive motor to the other. The interface between the SADM and the driven unit is a keyed output shaft on which a pinion can be mounted to interface with the ring gear of a solar array system.

Design Considerations

The DC step motor is inherently adaptable to space since it does not require mechanical commutation. The small 1.8° steps help to reduce the output step size and to smooth the velocity profile of the driven load. The discrete steps of the motor make the drive readily adaptable to open loop control. A high reserve torque of 8.1 N-m (6.0 ft-lb) can be realized from the drive because of the size 23 motor and the 100:1 gear ratio in the harmonic drive (chosen for its compactness, simplicity, and reliability).

Since the SADM is modular in construction it can be connected to the drive member with a further gear reduction providing any desired output torque up to 40 ft-lb. A preloaded pair of bearings support the clutch input shaft and in turn hold the flex spline in proper alignment. The wrap spring clutches are positioned next in line at an intermediate torque level. At this location the springs can be relatively small and lightweight. Clearances between the shaft and spring are sized to provide the desired overriding clutch action.

Adjustments for the clutch energizing torque are placed radially on the outside of the output housing assembly for easy access. A low gradient wave washer provides an insensitive method of changing the normal force on the friction ring pad. The energizing torque is on the order of 0.1 N-m (3.0 in.-lb) or 4% of the output torque capability.

The mechanism is completely lubricated with dry lubricant throughout for a long life potential. The only exception is the presence of a small quantity of fluorocarbon grease in the harmonic drive. This grease protects the silver plated raceway of the wave generator ball bearing during assembly and run-in. A thin film of grease on the outside diameter of the bearing aids in its insertion into the flex spline. A listing of the types of dry lubrication used in the mechanism is given in Table 6. The lubricants were all chosen on the basis of their performance in the 28-month life test on the "Long Life" drive.

Discussion

A total of six units was fabricated. Following fabrication, all six drives were functionally tested. The drives were mounted on a test stand and flexibly coupled to a hysteresis brake used as a load. The motor was driven with a commercial two-phase, bipolar driver. Measurements were made on rotation rate, output step size, input power, torque output, and clutch performance.

Rotation rate was made to be linear with respect to the input pulse rate for all loads by adjusting the energizing torque level of the clutch (0.2 N-m (2 to 4 in.-lb)) so that full motor torque could be realized without slip. When a no-slip condition exists the output step size is nominally .018° per step. This value was verified to the required accuracy by interpretation of oscillograph data provided by a potentiometer on the test stand output shaft. Power measurements were made on the voltage-current product at the motor input reflecting a 100% duty cycle. This value was typically 6.6 watts. (If the motor driver is designed to remove power after the step has occurred, average power input can be less than 0.5 watt for low orbit rates.)

Temperature tests were performed to determine the drive operating characteristics at low temperature. The drive is operable down to -29° C (-20° F). Below this point the redundant heaters are activated to accommodate the low interface temperature range of -29° C (-20° F) to -46° C (-50° F). The necessity for heaters is the result of the viscous drag of the grease in the harmonic drive wave generator bearing.

The SADM demonstrated the feature of bidirectional drive capability with mechanically coupled redundancy. The SADM were manufactured with flight-type quality controls on critical materials and processes and are considered representative hardware capable of providing long life.

SADE DESIGN DESCRIPTION

Design Considerations

Primary considerations in the design of the SADE were the minimization of circuit complexity and power consumption consistent with maximum operational flexibility. The SADE has command capability sufficient for convenient ground control and the ability to be completely operated from an on-board computer or programmer. This latter mode requires only two inputs. One sets the direction of rotation, the other steps the motor once for each input pulse. Step rate in this mode is independent of any internally set rate.

Three things were done to minimize SADE power consumption. First, drive power is applied to the motor for only 125 milliseconds for each step. This allows sufficient time for any oscillations of the motor armature to damp out completely. Second, the step motor is driven in the bipolar mode with only one winding excited at any time. This doubles the number of output transistors required but provides the best torque to power rating for the motor. A primary advantage of single winding drive is that it reduces the tendency of the motor to make a partial step when power is removed. Third, all internal logic circuits are C/MOS. Low power TTL is used to interface all input and output lines. This provides low impedance interface and transient protection.

Circuit Description

The SADE electronics can be roughly divided into two sections: one section generates and gates a selectable rate pulse train for the 3° step and slew modes, and one section contains decoding and power circuits that drive the step motor. Figure 2 shows a block diagram of this whole system.

Design of the step rate portion was based on the requirement that the step rate be selectable over a wide range to match the dynamic requirements of potential applications. Basic timing is derived from either an internal or external clock. An internal clock of 1024 pulses per second and about 3% stability is provided. If higher accuracy or synchronization between several SADS units is desired, an external clock can be used. The clock signal is divided to provide the required step rate. This is done in a four stage divide-by-N counter, which is programmed by soldered jumpers on the circuit board. It can divide the input by any integer from 1 to 16. For a clock rate of 1024 pulses per second this provides a selectable output from 34 to 512 pulses per second.

For operation in the slew mode, this output is merely gated on or off by a flip-

flop that stores the command. In the 3^0 step mode, an 11 stage counter is used to gate out 1024 pulses each time it is commanded. This corresponds very closely to 3^0 for the 6:1 gearing expected in most SADM applications. In the single step mode, the clock derived output is bypassed, and the external pulse is passed directly to the next stage. This way, there is no rate limitation in the single step mode. The motor step rate equals the single pulse command rate. After being gated, the pulse train drives a 2 bit up/down counter. Its output is decoded to provide the drive signal to the step motor. A convenient means of reversing the direction of the motor is the count up/down mode of the counter, which is controlled by a flip-flop that stores the direction command. The decoder gating circuit is also used to limit the drive pulse to 125 milliseconds. A retriggerable one-shot multivibrator controls this feature, holding the drive output on for pulse rates above eight per second. At lower pulse rates the one-shot multivibrator times out on each pulse, turning off the drive after 125 milliseconds.

One circuit not shown in the block diagram has been incorporated as a diagnostic measure. It monitors the drive current drawn by the motor on each step. If this current either increases or decreases beyond set limits, a flag output is set for telemetry.

SADE Package Description

SADE packaging was considerably simplified by its low power dissipation. Conventional printed circuit card construction was used. Only the eight output transistors and one transistor in the switching regulator had enough dissipation to require heat sinking. This was accomplished by leaving a band of copper along one edge of the card which makes thermal contact with a BeCu spring card retainer.

The completed package houses two circuit boards, one for each SADM. Each circuit board is 12.7 by 17.7 cm (5 by 7 in.). The package contains three MIL-C-38999 type connectors, one for the package input and one for output from each SADE.

Development Testing

A breadboard version of the SADE was operated in air at temperatures from -45^0 C (-49^0 F) to 65^0 C (149^0 F) for a total time of 1800 hours without failure. Measured power consumption at 26 V dc was 75 milliwatts in standby. Maximum power of 4.55 watts occurs at 8 pulses per second step rate. Above this rate power decreases because the inductance of the step motor never allows it to draw dc current. At 60 pulses per second, a typical slew rate, power is 3.6 watts. Below 8 pulses per second the power to the motor is turned off after each pulse and total power therefore decreases linearly to the standby power of 75 milliwatts at zero rate.

TESTING

Current plans for the SADS are outlined in Table 7. This series of tests will serve to verify that the SADM and the SADE will perform as specified. The

component characteristics of the SADM (damping, output torque profile, and other characteristics) will be determined; this will enable complete documentation of the SADM characteristics. The SADM will be tested with simulations of the rigid-body and flexible-body inertias expected in typical applications. Environmental testing of the SADM and the SADE will be performed to specifications that envelope the environments expected in typical applications. Extended duration testing will be performed in a thermal vacuum environment. This testing will consist of SADS operation profiles and thermal profiles that are representative of generic mission sets.

CONCLUDING REMARKS

The SADS has been approached in its design as an integral spacecraft subsystem. Sufficient flexibility has been incorporated into the design of the SADM and the SADE to encourage widespread adoption. The basic elements of the system, the SADM and the SADE, contain the bulk of the complexities that would exist in any given application. Testing, then, of the SADS as it now exists should increase confidence in its applications.

Engineering model units of the SADM and packaged SADE have been completed. These units are of a flight configuration and were manufactured with sufficient quality control to allow engineering and environmental testing of maximum validity consistent with reasonable cost. Performance testing, environmental testing, and extended duration testing are being performed at the NASA-LeRC.

Further optimization of the design of the SADM that reduces weight and volume without compromising the basic drive train has been identified.

Tests to determine the acceptability of the design for generic mission sets have been formulated. Tests currently planned are performance tests, component characterization, applications testing, environmental testing, and extended duration testing.

REFERENCES

1. SERT C Project Study. NASA TM X-71508, 1974.

2. SERT D Spacecraft Study. NASA TM X-71494, 1973.

3. TADPOLE Satellite. NASA TM X-71498, 1974.

4. Concept Definition and Systems Analysis Study for a Solar Electric Propulsion Stage. SD-74-SA-0716, Vols. 1 through 4, Rockwell International, 1975.

5. Low Cost Modular Spececraft. GSFC Document X-700-75-140, Goddard Space Flight Center, 1975.

6. Timmins, A. R.: A Study of Total Space Life Performance of GSFC Spacecraft. NASA TN D-8017, 1975.

7. Butterfield, A. J. and Herz, J. N.: Experience Applicable to the Viking Lander from a Study of Related Space Flight Projects. NASA CR-111876, 1971.

8. Evaluation of Space Station Solar Array Technology and Recommended Advanced Development Programs. LMSC-A981486, Lockheed Missiles and Space Company, 1970.

9. Kirkpatrick, Don L.: The Development and Test of a Long-Life, High Reliability Solar Array Drive Actuator. 8th Aerospace Mechanisms Symposium. NASA TM X-2934, 1973, pp. 69-83.

TABLE 1. - SADS PERFORMANCE SPECIFICATIONS

Life . . . . 2 years storage; 6 years space operation
Operation . . . . bidirectional
Rotation rate[a] . . . . 0 to 150 rpd
Torque output[b] . . . . 8.1 N-m (6.0 ft-lbs)
Step size[a] . . . . 0.018 degree
Motor input power . . . . . 0.5 watt average at 10 watts peak at 6 rpd,
$\qquad\qquad\qquad\qquad\qquad$ 10 watts average at 150 rpd
Electronics input power . . . . 1 watt without motor drive

[a] A further reduction by 6:1 would be typical in application
[b] An increase by 6:1 would be typical in application

TABLE 2. - SADS DESIGN SPECIFICATIONS

Modes of operation . . . . . operation by ground command, input available for operation by an autonomous spacecraft system

Commands available . . . . . 1 System on
$\qquad\qquad\qquad\qquad\qquad$ 2 System off
$\qquad\qquad\qquad\qquad\qquad$ 3 Slew rate on
$\qquad\qquad\qquad\qquad\qquad$ 4 Slew rate off
$\qquad\qquad\qquad\qquad\qquad$ 5 3° step
$\qquad\qquad\qquad\qquad\qquad$ 6 Single step
$\qquad\qquad\qquad\qquad\qquad$ 7 Forward
$\qquad\qquad\qquad\qquad\qquad$ 8 Reverse
$\qquad\qquad\qquad\qquad\qquad$ 9 Heater on
$\qquad\qquad\qquad\qquad\qquad$ 10 Heater off

TABLE 3. - SADM DESIGN SPECIFICATIONS

Elements . . . . consist of: permanent magnet step motor, harmonic drive, wrap-spring clutch, output interface, motor rotation sensor

Configuration . . . . provisions for single or double ended output

Output interface loads . . . 500 pounds radial, 50 pounds axial

Lubrication . . . . predominantly MoS_2; harmonic drive: ion plated silver: bearing parts; gold plate: bearing, mesh; fluorocarbon grease: bearings, mesh
motor: $Ag + WS_2$

Output interface . . . . . . keyed shaft

Clutch . . . . engage and disengage output interface

Motor rotation sensor . . . sense 1/4 motor revolution, direction

Mass . . . . 4.6 kg (10.1 lb) maximum

Envelope . . . . 11 cm dia. by 27 cm long
(4.3 in. dia. by 10.7 in. long) maximum

Mounting interface . . . . Flanged, 4 holes of 0.64 cm dia. (0.25 in. dia.)

TABLE 4. - SADE DESIGN SPECIFICATIONS

Communications interface . . all signals TTL compatible

Electrical interface . . . . . input voltage 26 to 30 vdc

Signals processed . . . . . SADM motor current flag, 5 (SADM plus SADE) temperatures, SADM heater current flag

Size . . . . one 12.7 by 17.7 cm (5 by 7 in.) printed circuit card per SADM

Package (option) . . . . . . two cards per box, MIL-C-38999 type connectors, bolted flange mounting

TABLE 5. - SADS ENVIRONMENTAL SPECIFICATIONS

Temperature

Radiative and conductive heat sinks at the SADM and SADE radiative and conductive interfaces will range from -46° C (-50° F) to 66° C (150° F).

Acceleration

The following qualification acceleration is to be applied 5 minutes:
16. 0 g thrust with +3 g lateral applied simultaneously

Sinusoidal Vibration

The following is qualification sinusoidal vibration to be applied to each axis at a sweep rate of 2 octaves per minute:

Frequency	Amplitude
5 to 15 Hz	0. 75 in. double amplitude
15 to 100 Hz	9. 0 g 0 to peak
100 to 200 Hz	6. 4 g 0 to peak
200 to 2000 Hz	5. 0 g 0 to peak

Random Vibration

The following is qualification random vibration to be applied to each axis for 4 minutes:

Frequency	Amplitude
20 to 100 Hz	+3db/octave to 0. 10 g^2/Hz
100 to 200 Hz	0. 10 g^2/Hz
200 to 300 Hz	slope to 0. 16 g^2/Hz
300 to 700 Hz	0. 16 g^2/Hz
700 to 2000 Hz	−3db/octave from 0. 16 g^2/Hz

TABLE 6. – BEARINGS AND LUBRICATION

Location	Type	Lubricant
Motor	Deep Groove Crown Retainer	Feuralon AW $(Ag + WS_2)$
Harmonic Drive	Ball Bearing (Braze Machined Retainer) Flex Spline	Silver plated race (Gold plated retainer) stn. stl., gold plated
Input Shaft	Ball Bearing (Angular Contact)	Ceramic Bonded MoS_2
Output Shaft	Ball Bearing Deep Groove Bronze Retainers	Ceramic Bonded MoS_2

TABLE 7. – SADS TESTS

Performance	Performance testing of the SADM and the SADE to verify conformance to performance and design specifications.
Characterization	Determine the component characteristics of the SADM and the SADE that are necessary for complete documentation of component performance.
Applications	Testing with simulations of rigid-body and flexible-body inertia
Environment	Testing consists of the following environmental exposures: 1. Temperature testing 2. Sinusoidal and random vibration testing 3. Acceleration testing 4. Thermal vacuum testing
Extended duration	Thermal vacuum testing for an extended duration; testing consists of operation and temperature profiles representative of generic mission sets
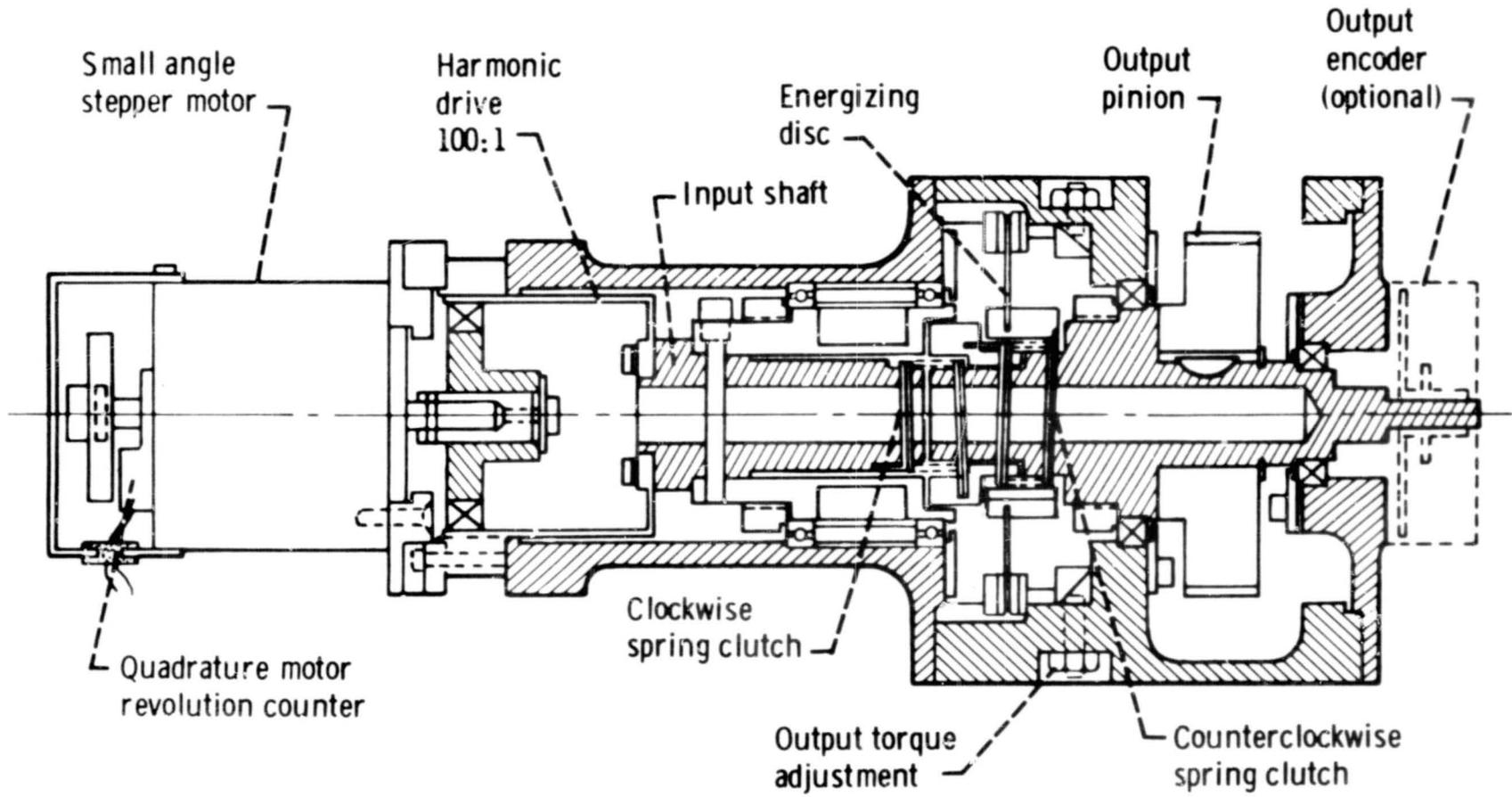
Figure 1. - Solar Array Drive Mechanism

Commands
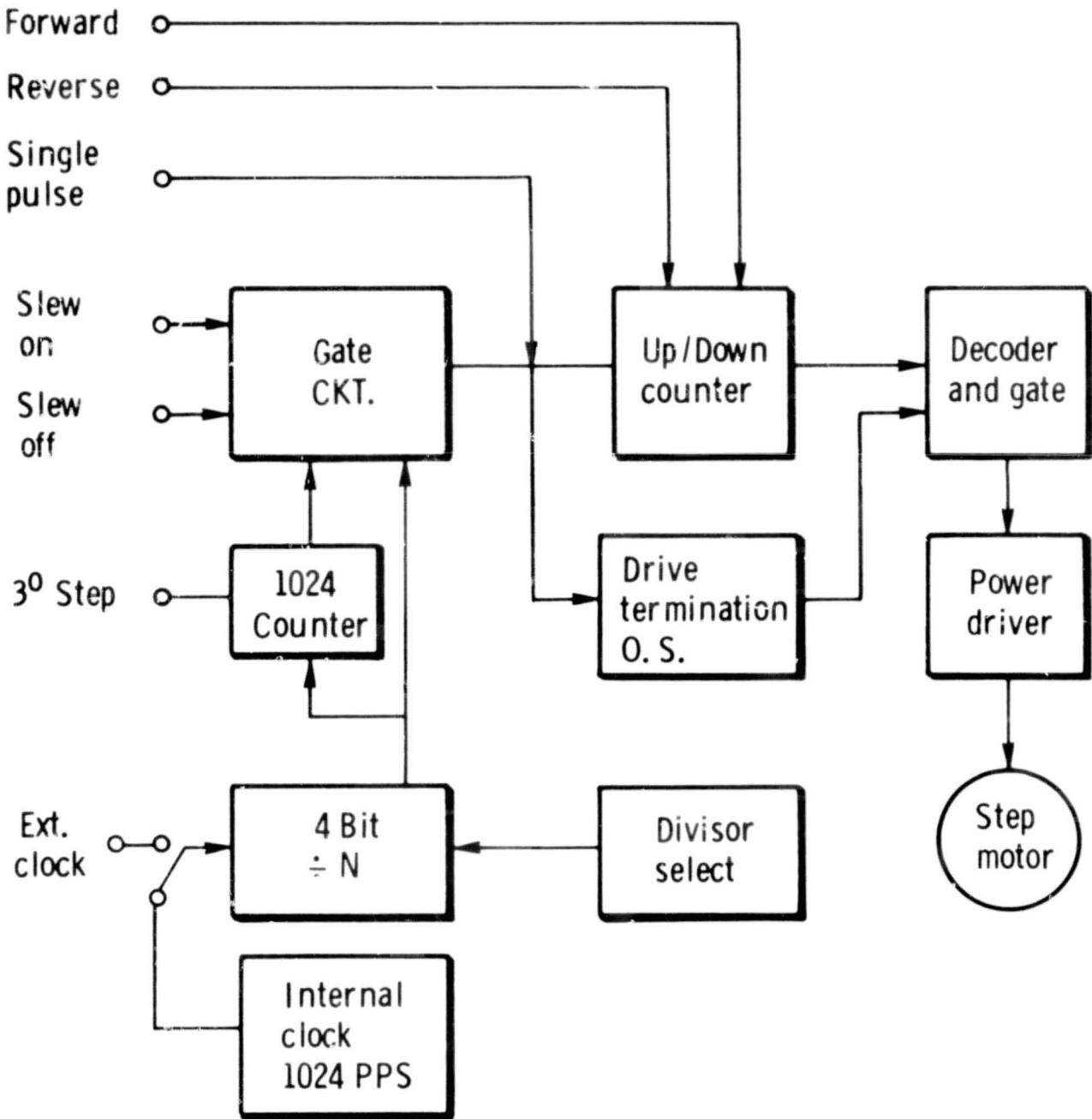
Figure 2. – Solar Array Drive Electronics

VISCOUS ROTARY VANE ACTUATOR/DAMPER*

By   JACK D. HARPER

MARTIN MARIETTA CORP.

SUMMARY

JPL has developed a compact viscous rotary actuator/damper for use on the Mariner '71 and Viking Programs. Several functions have been combined into this single mechanism to control the deployment, latching and damping of the solar panel arrays used on these space vehicles. The design, development and testing of the actuator/damper are described, and major problems encountered are discussed.

INTRODUCTION

The Jet Propulsion Laboratory's Mariner Mars spacecraft, launched in 1971, and the Viking Orbiter spacecraft, launched in mid 1975, required the use of panels of solar cell arrays for electrical power generation. Because of the size of these solar panel arrays, they were folded parallel to the spacecraft's longitudinal axis to fit within the launch vehicle shroud. After launch and shroud removal, they were rotated to their flight position. Deployment of the solar panels from their launch position, latching of the solar panels in their proper flight position and damping of solar panel perturbations caused by the spacecraft engine firings were functionally controlled at the hinge line of the panels. These three main functions were incorporated into a single unique fluid-filled viscous rotary vane actuator/damper. The concept was originally developed for Mariner '71 and then modified and improved for use on the larger solar panels on Viking Orbiter. This paper will deal primarily with the design configuration flown on the Viking Orbiter spacecraft.

DEPLOYMENT AND LATCHING

Deployment of the solar panels is accomplished by the release of stored energy from a torque spring. This was a clock spring design on Mariner '71 and later modified, because of weight and reliability considerations, to a pair of constant torque multi-leaf springs for Viking. The torque level for the deployment springs was set by a design goal of maintaining a torque margin of four times the maximum resistive torque.

This resistive torque comprises the friction of the hinge joint, the tare torque of the deployment device, plus the items that bridge the hinge joint such as electrical wire bundles, attitude control gas lines and the coaxial

---

cable for the relay antenna. These torque values and the deployment torque margin can be seen in Figure 1. The variations in available deployment torque are from the mounting of the actuator; its crank and linkage to the solar panels form a four-bar linkage that has an increasing mechanical advantage that approaches one to one at the deployed position.

Under free running conditions, this excess torque margin would drive the solar panel assemblies too fast and cause high shock loads to the system at latching; therefore the springs are configured to drive the panels in parallel with the fluid actuator. This causes compression of the fluid between the vanes of the actuator pumping the fluid through the orifice gap formed between the stationary vanes and the outer rotating wall. This can be seen in the cross section of Figure 3. The actuator in this case acts as a rotary rate-limiting device that is velocity sensitive and will, for a constant torque input, maintain a constant deployment velocity. The device can be adjusted to control the rate of deployment independently of the input driving torque. The input torque is based on the resistive torques and the required torque margin; then the fluid viscosity and the orifice gap are selected to balance the input torque for the deployment rate desired.

After deployment, the solar panels are latched in their flight position by either or both redundant lock pins located in the rotating vanes. The lock pins are spring loaded taper pins that engage conically reamed holes. This configuration allows for a gradual entry of the lock pins into the holes and near-zero backlash when engagement is complete. When coupled with the controlled deployment velocity, this arrangement provides for small or negligible impact loads at latching.

To insure that the solar panels are in the proper position at latching, the solar panels must be aligned to actuator's locking pin locations. This adjustment is made at the flight assembly by means of the turnbuckle linkage assembly connecting the panels to the rotating portion of the actuator. This linkage and its attach points are shown in Figure 2.

DAMPING

After deployment and latching, it was necessary to have a damper in the system to minimize any interaction between solar panel perturbations and the spacecraft's attitude control system (ACS). The requirements to decouple the solar panel assemblies' resonant response from any known pulses of the spacecraft ACS system were determined to be a minimum undamped natural frequency of .5 Hz and at least 30% damping. To meet the damping requirements, the actuator/damper had to have a dual spring rate, one for deployment and one, much higher, for system frequency control. This was accomplished in the device by the action of the latching pins. As the pins stop the system deployment, they lock out the deployment springs and couple the actuator/damper's outer rotating body to the inner stationary base through the center shaft, which is a tuned torsion bar. The torsion bar had to be configured stiff enough to meet the frequency requirement but flexible enough to allow sufficient panel rotation at engine firings and shut-off for the damper to be effective. For the Viking solar panel assemblies, the

torsion bar provided an undamped natural frequency of .87 Hz. The flexing of the torsion bar allows relative motion between the damper vanes, displacing fluid through the orifice gap. It is the work required for this fluid displacement that damps the solar panel vibrations.

The damping of a rotary device like this is dependent upon the geometry of the vane configurations, the working fluid viscosity and the orifice size and shape. The parameters easiest to adjust to meet the damping requirements are the fluid viscosity and the orifice size. To meet the damping requirements of the Viking spacecraft with its larger, heavier solar panels as compared to the solar panels on Mariner '71, it was necessary to increase the working fluid viscosity and decrease the orifice gap. The combination finally selected was a dimethyl silicone oil, because of its relative flat viscosity vs. temperature curve, with a kinematic viscosity of 178,000 centistokes and an orifice gap of 0.015 in. With this combination, the damper was able to provide the required 30% damping over the predicted temperature range of -10° F to +115° F, with damping ranging from 30% to 53%. Although this fluid and orifice size did provide the needed damping, they presented a problem to the deployment function of the actuator/damper. With the input torque of the deployment springs set and this high fluid viscosity and small orifice, the deployment time became unacceptably long. To shorten the deployment time, a step, shown in Figure 3, was added to the inside wall of the body to increase the orifice gap. This gives a faster rate at the beginning of the deployment and a gradual decrease to the slower rate about halfway through the deployment.

Another problem that had to be considered is the fluid expansion and contraction with temperature. At high temperatures, the fluid expansion causes high internal pressure, increasing the possibility of leakage or a structural failure of the pressure vessel. At low temperatures, the fluid contraction can cause a void within the fluid. This vacuum "bubble" allows relative vane motion without forcing the fluid to be pumped through the orifice and greatly reduces the damping capabilities of the device. To prevent these problems from occurring, a temperature compensator was used to provide an additional spring-pressurized reservoir that supplies the expansion volume needed at high temperatures and the make-up fluid needed at low temperatures. The temperature compensator, shown in Figure 3, consists of a sealed piston, a compression spring of conical washers and a small orifice connection to the working fluid chamber.

DEPLOYMENT TESTING

For the deployment testing, the solar panel assemblies were positioned with the hinge axis vertical to minimize the gravitational effects. All of the development testing was performed using a pair of simulated solar panels shown in Figure 4. Deployment tests were conducted to check the actuator's deploying, rate limiting and latching functions. Because the Viking system was a double folded panel pair, with the outboard panel deployed and latched during the deployment of the inboard panel, the effect of this two-panel deployment was investigated during the deployment and latching tests.

The flight solar panel structure was not capable of supporting the cantilevered weight of the outboard panel, so the panels could not be free-deployed in the flight-like manner. To minimize the complexity and cost of the testing equipment and the risk to flight hardware, it was decided to deploy the flight panels in steps using a mid-hinge support for the deployment of the outboard panel. Testing of the flight panels is shown in Figure 5. By running tests with both the simulated panels and the flight panels, a collation of the deployment times was assembled for evaluation of preflight checks and a prediction of flight deployment times.

DAMPING TESTING

Damping tests were performed on the test setup shown in Figure 6. It consisted of a simulated solar panel assembly, the actuator/damper in an insulated box shroud and a liquid nitrogen/hot air temperature control system. To simulate the maximum .16 g force on the solar panels from a main engine firing, the simulated panel and actuator/damper are assembled in the deployed position (latch pins engaged) and mounted at an angle of 9° from vertical. When released from this position, the horizontal component of the weight will approximate the load the torsion bar and damper will see in flight.

All dampers were tested in this manner at various temperatures from -19°F to 124°F, with the damping ranging from 30% to 53% for all flight units. A typical damping curve taken at room temperature is represented in Figure 7.

Certain problem areas were identified from the development and acceptance tests conducted. Early damping tests showed that the temperature compensator must be decoupled from the damper or the pressure on the fluid would force it into the compensator and not past the damper vanes. This was corrected by making the fluid passages between the compensator and damper a pair of .006-in. diameter holes. A suddenly applied load would not drive fluid through this small orifice, but a gradual change in temperature would allow fluid to flow between the damper and compensator. Also the device had to be pressure filled to a level that would remove any axial play within the unit and completely seat the "O" ring seals so that they would not move or "breathe" when a load was applied.

VIKING FLIGHT PERFORMANCE

During the launch and early flight of the Viking missions, data was transmitted that allowed evaluation of the flight performance of the actuator/damper assemblies. With four assemblies per spacecraft and two successful launches, the data received gives a good indication of the actuator/damper's flight characteristics. The data gave direct readings for deployment times and latching but not for the damping function; this was interpreted from data of other spacecraft subsystems.

Solar panel deployment times were estimated, based on pre-flight testing and the predicted flight temperature range, to be between 2 minutes to 2 1/2 minutes, with the bay 1 panel being the slowest because of increased inertia due to a relay antenna attached to the outboard panel.

The last ground tested deployments and flight actuals are shown below:

TABLE 1. VIKING SOLAR PANEL DEPLOYMENT TIMES

Location	Last Preflight Test	Launch A Time +6.7 sec -0.0 sec	Launch B Time +6.7 sec -0.0 sec
Bay 1	2 min 2.8 sec	2 min 11 sec	
Bay 5	1 min 39 sec	2 min 2 sec	
Bay 9	1 min 43 sec	1 min 55 sec	
Bay 13	1 min 39.7 sec	1 min 55 sec	
Bay 1	1 min 49 sec		2 min 10 sec
Bay 5	1 min 48 sec		2 min 1 sec
Bay 9	1 min 41 sec		1 min 54 sec
Bay 13	1 min 39.5 sec		1 min 47 sec

It can be seen from the flight deployments that all actuators functioned quite well, giving a uniform deployment within a small time variation. Actual flight deployment times were slightly faster than predicted because of the fluid's sensitivity to temperature. The flight devices were close to nominal temperature, and the predicted times were based on the low temperature predicts.

Based on the ACS gas usage, the actuator/dampers functioned properly, preventing any adverse interaction between the solar panel natural frequency and the ACS gas jet firings. Confirmation of the latching and damping functions of the devices was given by the midcourse engine firing in that there was no discernible c.g. shift, indicating a free or non-latched panel; in addition, the ACS system showed normal operation after the engine firing.

CONCLUDING REMARKS

This viscous rotary damping device has been developed, tested and successfully proven on two spacecraft programs. The major unexpected phenomena encountered with the design and their solutions have been discussed; however, there has been no attempt to describe all of the problems, pitfalls and agonies encountered with a design effort of this nature from concept to a proven flight-ready mechanism. Because of the nature and complexities of this type of fluid actuator/damper, the design does not come only from careful analysis but must be gained from testing and experimentation. This device has the advantage of being designed and developed for one program, then re-evaluated and expanded to requirements greater than the original design goals. This additional work and testing have increased the knowledge of the device's performance characteristics and capabilities.

Because of the device's versatility, it has been considered for many applications where panels, booms or other appendages have to be deployed and/or damped in a space environment. It is currently being used on JPL's Mariner Jupiter/Saturn Program and Rockwell International's Global Positioning Satellite. It has also been included by Martin Marietta and General Electric Space Division in proposals for other spacecraft and satellites.
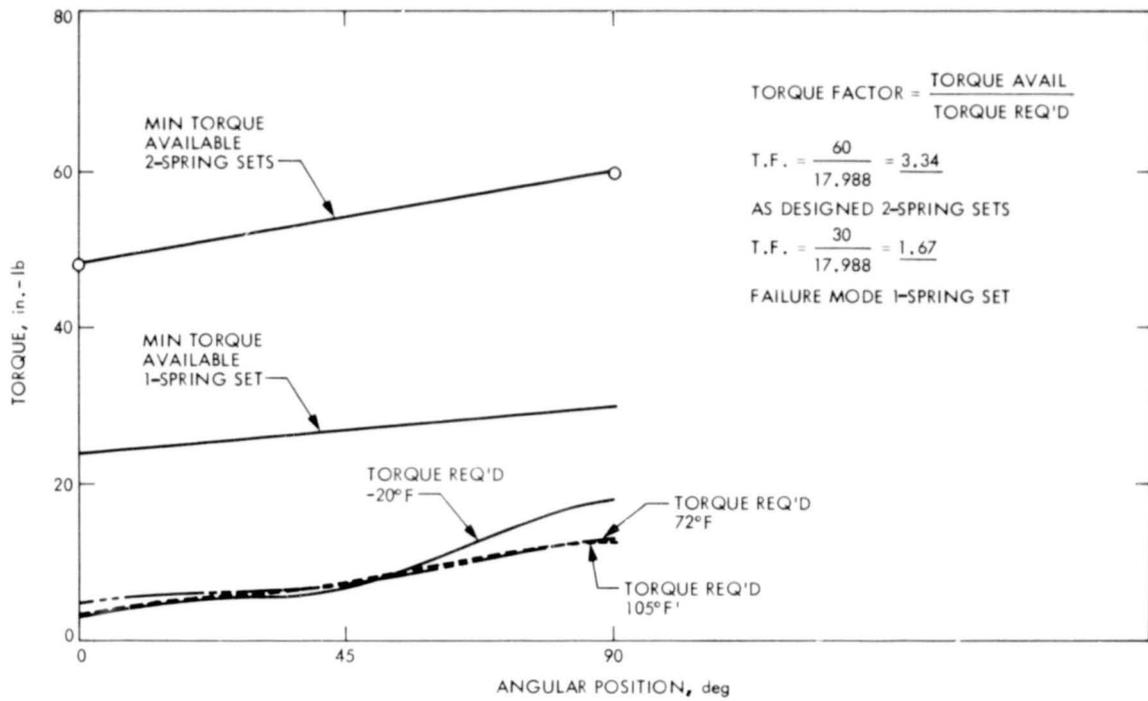
Figure 1. Input Torque Available and Resistive Torques
Compared to Panel Angular Position
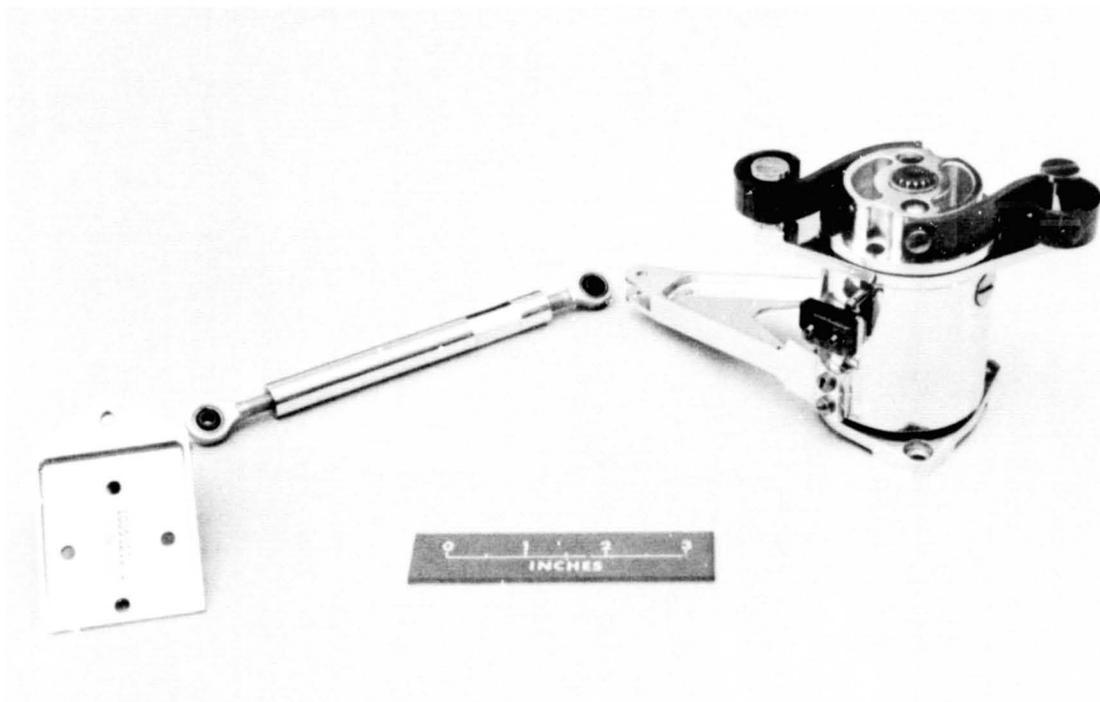
Figure 2. Actuator/Damper, Turnbuckle Linkage and
Solar Panel Attach Bracket
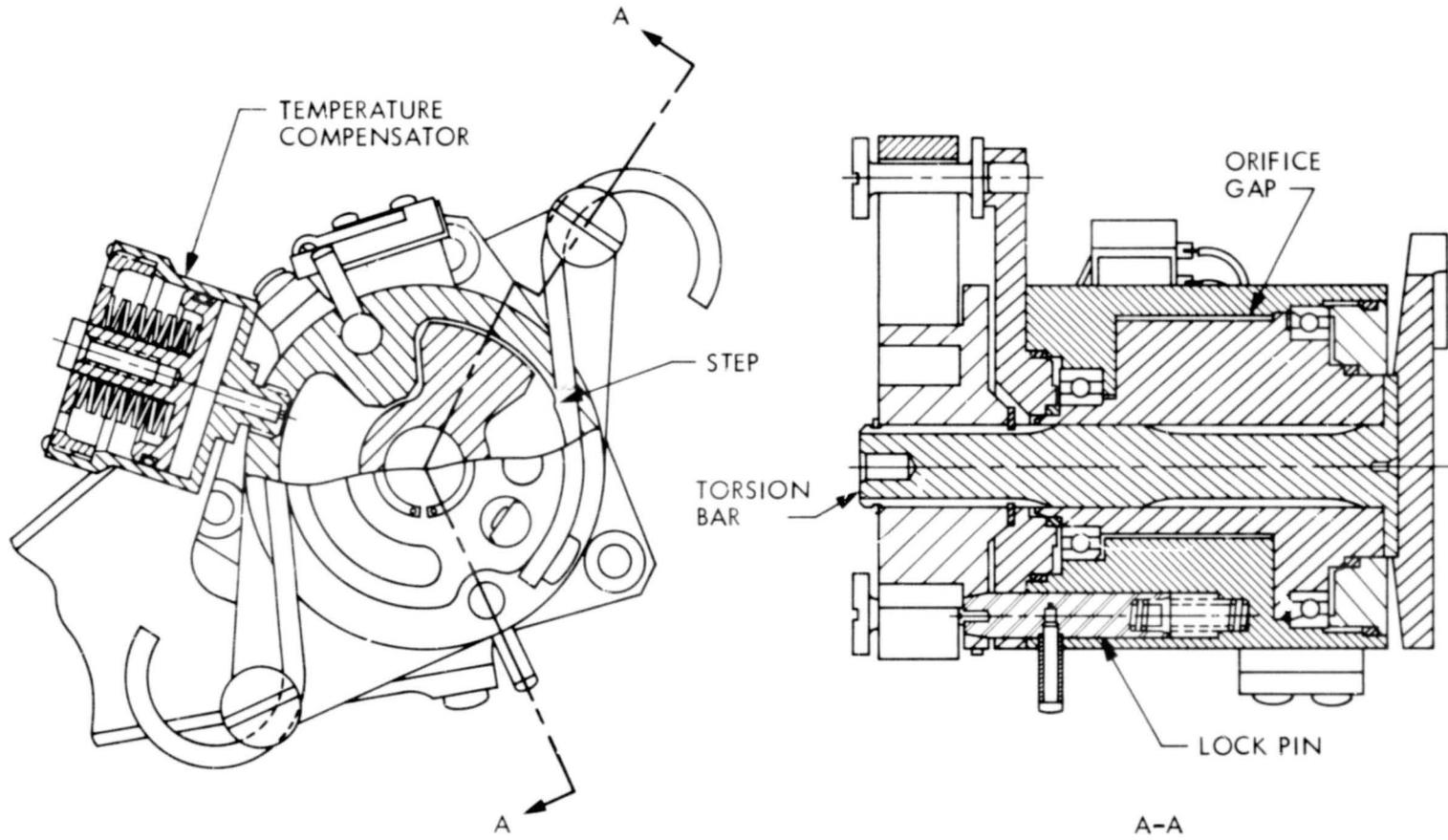
Figure 3.   Rotary Vane Actuator/Damper Assembly
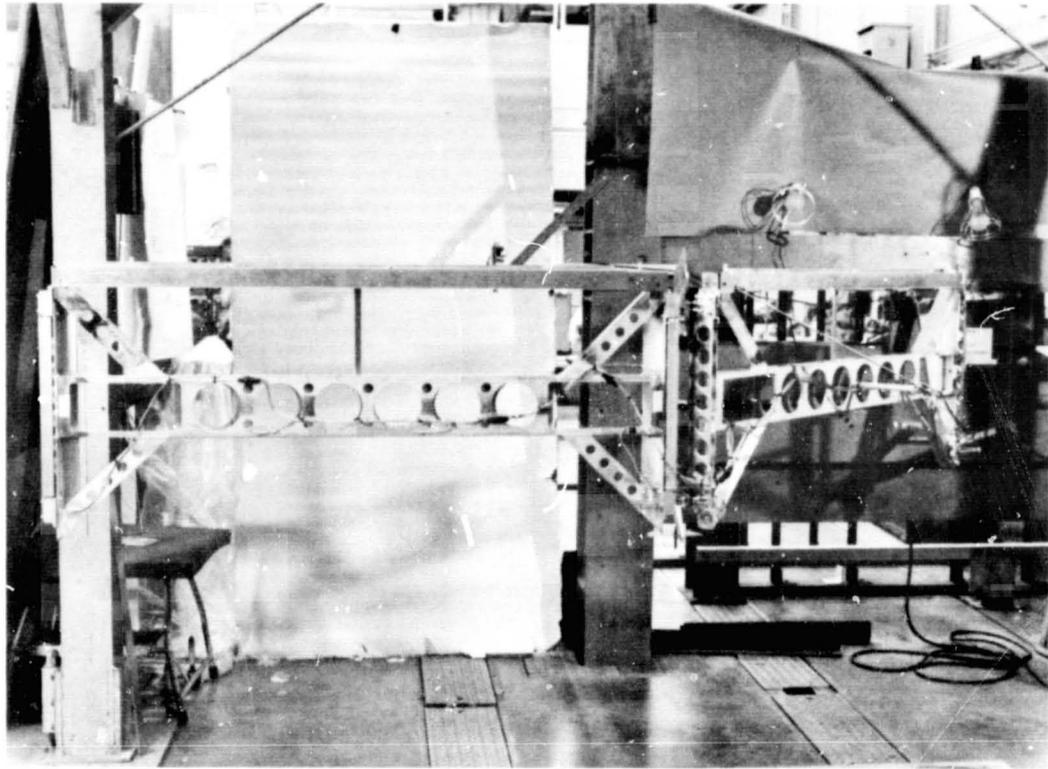
Figure 4.   Deployment Test Setup With Simulated Solar Panels
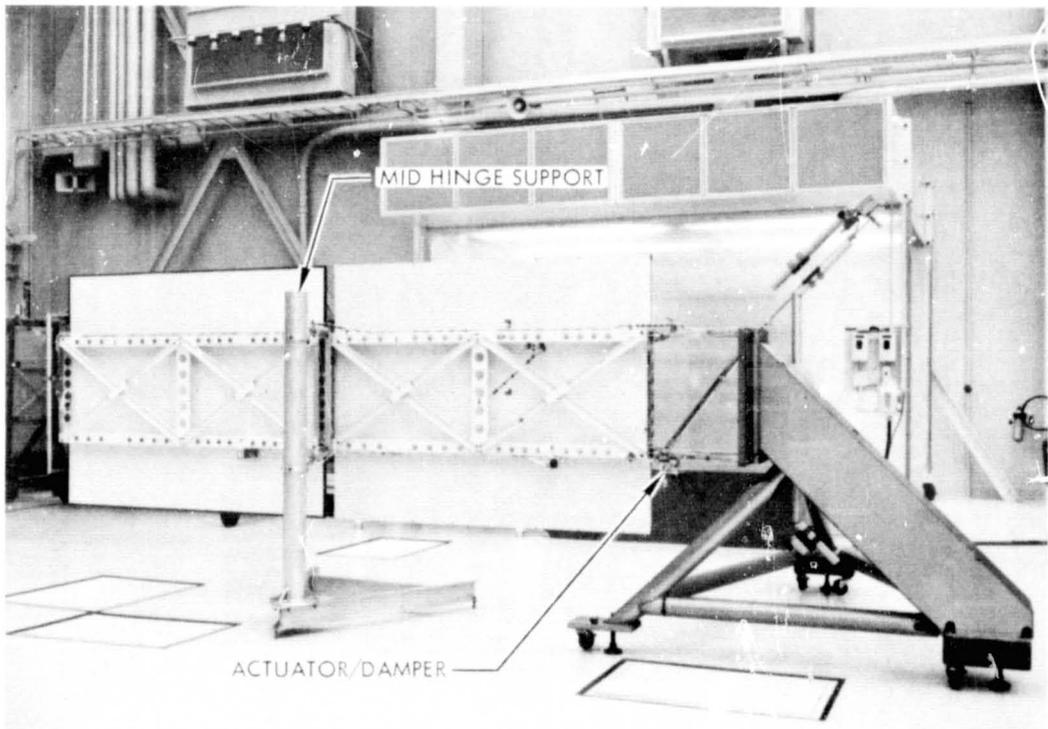
Figure 5.   Final Testing of Flight Solar Panels and Actuator/Damper
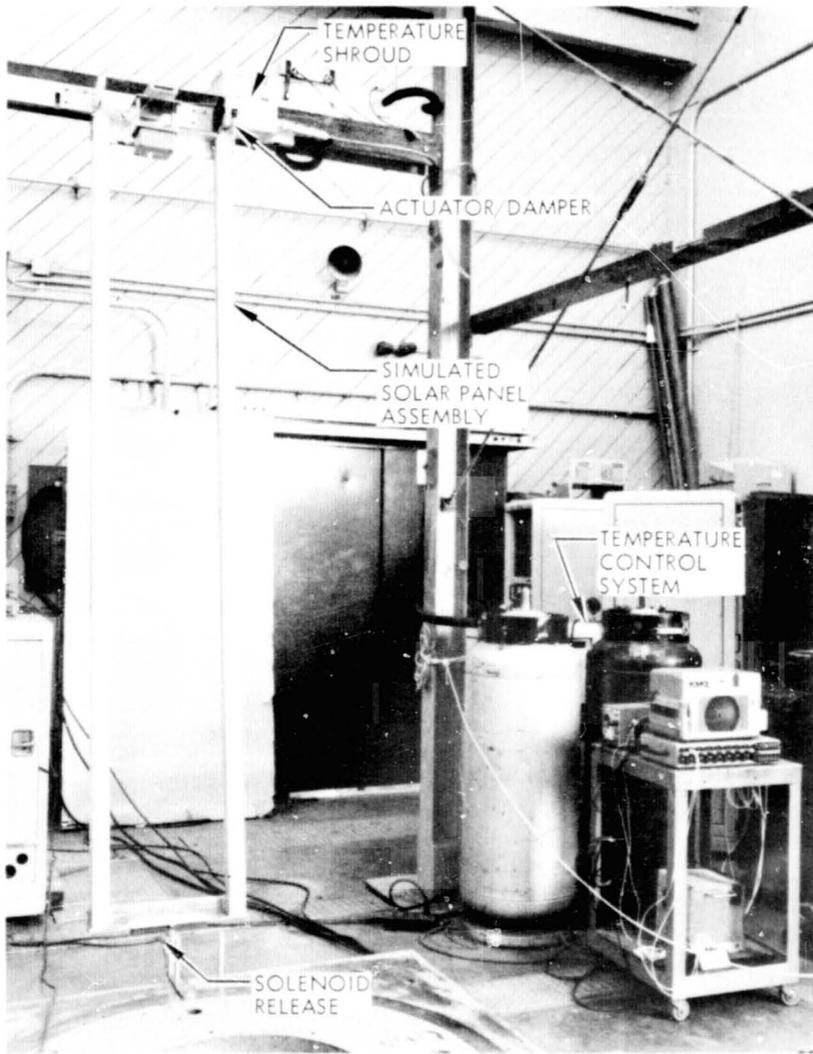
Figure 6. Damping Test Equipment

δ = LOGARITHMIC DECREMENT

ζ = DAMPING FACTOR

$\delta = L_N \dfrac{x_1}{x_2}$

$\delta = \dfrac{2\pi\zeta}{\sqrt{1 - \zeta^2}}$

$\zeta = 0.53$
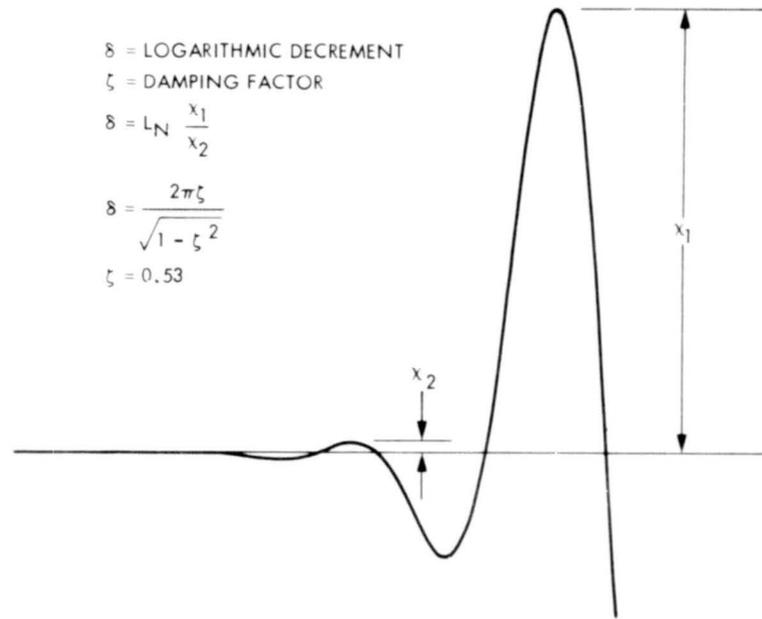
Figure 7. Representative Damping Curve

VIKING GC/MS MECHANISMS DESIGN AND PERFORMANCE

By C. Peter Chase and August O. Weilbach

Advanced Technology Operations
Beckman Instruments, Inc.

N76-98292

ABSTRACT

The Viking Lander Gas Chromatograph/Mass Spectrometer will analyze pyrolyzed samples of the Martian surface for organic content. The Surface-Sample Loader and Pyrolyzer Assembly (SSLPA) is described, along with the major problems encountered during design and testing. Three mechanisms were developed to implement the required SSLPA functions: (1) a soil loader that forces soil from a filled rotating funnel into each of three ovens located on a carriage, (2) a Geneva drive for rotating and precisely indexing the ovens to receive sample, and (3) a toggle-clamp mechanism for sealing the ovens by forcing circular double knife edges into gold sealing surfaces.

INTRODUCTION

The "laboratory" launched the afternoon of 20 August 1975 from Kennedy Space Center contained sophisticated instruments for experiments on Mars. Newspaper accounts of the mission focused on these experiments, especially those for detecting evidence of life. Some accounts mentioned the instruments themselves. None described the intricate mechanisms that made the experiments possible. This paper describes one such mechanism--the Surface-Sample Loading and Pyrolyzing Assembly for the gas chromatograph/mass spectrometer (GC/MS) instrument.

THE GC/MS EXPERIMENT

The basic concept of the GC/MS experiment is to perform analyses on organic matter in soil samples by pyrolyzing the soil sample (i.e., heating the sample to a high temperature, causing the breakdown of organic matter to volatile products) and then separating the components of the pyrolyzed organic matter with a gas chromatograph. As each separated component elutes from the gas chromatograph, it is identified by a mass spectrometer using the known fragmentation pattern of the component. The results of these analyses will be a guide in determining the presence of biological organic matter. Also, because the pyrolysis of each class of biological compounds gives characteristic and predictable products, it is possible to deduce what classes of organic material were originally present in the soil and to obtain an indication of how much was present.

The crucial part of the experiment is sample handling and pyrolysis, which is carried out by the Surface-Sample Loading and Pyrolyzing Assembly (SSLPA).

SSLPA FUNCTIONAL DESCRIPTION (Figure 1)

The SSLPA consists of a soil loader, an oven carriage and indexing mechanism, an oven-seal clamping mechanism, two prime movers, and the necessary drive systems. The principal functions of the SSLPA are to:

- Receive a soil sample from the Viking Lander Sample Processor.

- Load and pack the soil into one of three ovens suspended in the oven carriage.

- Rotate and index the oven carriage.

- Clamp and seal the oven.

- Pyrolyze the soil in the oven at a selected temperature, while flushing the effluents to the gas chromatograph.

- Dump and clean out the excess soil from the soil loader and repeat on command the above functions for the other two ovens.

The soil loader rotates and taps the soil inlet funnel as a reciprocating plunger directs and packs the soil sample through the funnel exit into one of three 60-$\mu\ell$ ovens. All these movements are achieved by an arrangement of a pair of helical gears, a spur gear pair, a slider crank, and a spring-loaded tapping follower. The carriage then rotates, indexing the filled oven to the next station and bringing a dump cavity under the inlet funnel. The soil loader mechanism cleans out the soil remaining in the funnel, dumping it into the reservoir in preparation for receiving another soil sample.

The ovens and dump cavities are located on a rotating carriage indexed by a Geneva drive. The carriage has seven stations--six for oven and dump reservoirs and one non-operating station for transit to Mars.

Oven-seal clamping is achieved by a four-bar toggle-clamp mechanism operated by a motor-driven cam. The linkage forces a set of circular knife edges into gold discs at both ends of the ovens, plastically deforming the discs to form a seal with a leak rate less than 1×10^{-9} scc/s helium at one atmosphere. Only 1.1 kg (2.5 lb) input force is required at the cam to impart 20 kg (45 lb) force into the gold discs.

The ovens are suspended by triangular stainless steel spring washers, which thermally isolate the ovens and apply a preload for holding them in place under vibration and g loads. All power and sensor connections to the ovens are hard wired using a flexible cable that permits unrestrained rotation of the oven carriage through one full cycle.

All precision mechanisms are susceptible to failure from particulate contamination. To prevent failure of the GC/MS mechanisms from sample contamination, the motors are sealed, the one-way clutch uses a labyrinth seal, and shielded ball bearings are used to minimize friction.

SOIL LOADER MECHANISM (Figure 2)

The soil loader receives soil sample from the Lander Sample Processor via a simple gravity feed. However, once sample is in the inlet funnel of the soil loader, a mechanism is needed to load the sample into the three ovens and clean the funnel between loadings to prevent sample cross contamination in excess

of 10 percent. The main problems encountered were: (1) maintaining sample flow through the narrow funnel exit opening--1.5 mm (0.058 inch)--and into the ovens through their matching 1.5 mm opening without plugging; (2) cleaning the funnel of residual sample; and (3) loading the ovens with a reproducible amount of sample. These problems were further complicated by the range of sample particle size, particle configuration, and moisture content that had to be accommodated.

The original design used an oscillating rod tangential to the inside of the funnel for poking the soil into the ovens. The funnel was rotated, causing the rod to scrape the soil from the sides of the funnel. However, even though the rod was close-fitted to the wall of the funnel, soil packed underneath it, forcing it away from the wall and defeating its use as a scraper. Additionally, the 90-degree end surface of the rod caused plugging at the funnel exit opening, preventing reliable, complete filling of the ovens.

Two simple design changes solved both problems. First, the poker cross section was changed from circular to triangular, providing a sharp edge for scraping the inside wall of the rotating funnel and adding rigidity to prevent any lifting action. Second, the poker end was tapered to a 30-degree angle, allowing excess sample to flow back over the face of the poker tip as it penetrated the narrow exit opening. This design change eliminated plugging and improved oven loading and sample packing consistency.

In its original concept the poker was guided and supported by a complex linkage. During tests of the soil loader, it became apparent that an improved mechanism was needed. The new mechanism had to provide better alignment of the poker rod with the funnel and work with less friction and less effect from soil induced interference. A small ball bushing was selected as an alternative support and low friction was obtained. During testing of the engineering model it became apparent that the bushing idea worked but new soil testing requirements required more force on the poker mechanism. Within permissible space a next larger bushing was installed, solving the problem.

Another problem was filling the very narrow 60-$\mu\ell$ ovens with a known and reproducible amount of sample. It was initially believed that this could be accomplished by sensing the resistance of the poker to sample packing force and turning the loader mechanism off at a predetermined resistance force. This approach turned out to be unduly complex and unreliable. The approach finally selected was simply to load for a fixed time sufficient to guarantee loading a worst-case sample.

As shown in Figure 3, the soil loader mechanism is driven by a 150-r/min motor on whose shaft is attached a helical gear. This gear drives another helical gear at right angles and at the same speed of 150 r/min. The second helical gear is fixed to the crank shaft. The crank drives a connecting rod which, in turn, drives a shaft guided by a linear bearing. Rigidly attached to the guided shaft is the poker, which reciprocates at 150 cycles per minute in the funnel. The first helical gear has, on the same shaft, a spur pinion and a four-lobed cam. The pinion drives another gear attached to the funnel. The funnel thus rotates at approximately 27 r/min. The funnel tapper is spring-loaded against the cam, causing it to tap the funnel wall as the funnel rotates.

OVEN CARRIAGE AND INDEXING MECHANISM (Figure 3)

The oven carriage holds three sample ovens and a flight oven, two dump cavities, and a flush tube--seven stations in all. Indexing precisely positions the seven stations for each operation.

The primary design feature is the indexing mechanism. Initially, it was conceived as a spring-loaded ratchet and pawl mechanism, but this design was discarded because of its complexity, high power requirements, and inadequate accuracy and reliability. A Geneva drive mechanism was selected since its inherent characteristics closely matched the design requirements. It is extremely simple, requires very little power, provides precise indexing, and is highly reliable. It was the ideal mechanism for the application.

The Geneva drive is powered by the same motor used for the soil loader. On command, an electrical clutch engages and a gear set transmits the motion to the Geneva drive. The actuator drives the Geneva wheel, which is an integral part of the carriage. It takes two revolutions of the drive wheel to index the carriage one station. This arrangement, because of the inherently-accurate position capability of a Geneva drive, assures a smooth and positive transition from one station to another.

Position status indication is provided by a 3-bit binary code on a thin disc attached to the carriage. The encoder head is implemented with light-emitting diodes and photosensitive detectors. The functional sequence (see Figure 4) is as follows:

- An oven is readied for receiving the sample by a preheat cycle at 500°C for about 1 minute in order to clean out possible residual contamination.

- With the oven placed under the loader, soil is fed from the loader and compacted by the poker of the soil-loading mechanism.

- The oven is indexed to the pyrolysis station, where it is clamped and sealed.

- Simultaneously, a dump cavity is positioned to receive the residual sample from the loader.

As a loaded oven is indexed to the pyrolysis station, residual soil on the surface of the oven seal is removed by the wiping action of a set of thin flexible metal blades. Any remaining fine particles--down in the 5 μm size or less--do not interfere with hermetic closure of the oven.

OVEN-SEAL CLAMPING MECHANISM (Figures 4 and 5)

Sealing the ovens to attain a leak rate no greater than 2×10^{-5} scc/s of helium presents several problems. The seal has to be effective in the presence of soil particles up to 5 μm that might not be wiped away by the metal blades, it has to be maintained at high temperatures, and there has to be a mechanism for applying sufficient force to attain the seal and maintain it during analysis.

The initial design approach to sealing was to force circular knife edges into gold discs brazed to both ends of the ovens. Although a satisfactory seal was obtained at the shearing surfaces between the knife edge and the disc under ideal conditions, when soil particles were present they caused leak rates in excess of the requirement. Also, the gold tended to cold-flow away from the knife edge, deteriorating the seal.

The solution was a two-edged knife (see Figure 4), which solves both the cold-flow and particle problems. The two edges prevent the entrapped gold from extruding and they provide a redundant seal that increases reliability and reduces leakage to an acceptable rate.

There were a number of possible implementations explored for applying a sufficient force to the circular knife edges to obtain the required seal. But in addition to the force required to make the initial seal, there was also the problem of maintaining the seal as the gold softened during oven heating. This required a controlled spring rate that would cause additional knife penetration as required to maintain the seal.

The toggle-clamp mechanism (Figure 5) selected is ideal for applying force. It is simple, fits the space available for clamping movement, and attains its greatest clamping force as it approaches its 180-degree stop position. The corresponding force imparted to the eccentric is only about 1.1 kg (2.5 lb)--a force easily achieved with the drive system used. Additionally, by selecting a flexing arm design and using it as a spring for the top and bottom clamp arms, the required uniform spring rate is attained to maintain the seal throughout the oven heating cycle.

PRIME MOVERS

Actuation of the pyrolyzer mechanisms is performed by two geared hysteresis synchronous motors enclosed in beryllium housings. One motor, rotating at approximately 8 r/min, drives the oven-seal clamp mechanism. The second motor drives the soil loader at 150 r/min. An electric clutch with a reducing gear train couples the second motor to the Geneva drive for indexing the oven carriage.

The selection of this type of prime mover permits a low profile package with a relatively high stall and high drive torque; the latter is needed especially for the clamping mechanism. Reduction of the rotor speed down to the output shaft is achieved by an integral gear train.

Potential contamination from the motor into the pyrolyzer assembly is prevented by using chevron-type seals at the drive shaft exit. Since this type of device seals well, balancing of internal to external pressure is achieved through a 2-μm filter built into the lower end of the motor case.

OTHER PROBLEMS

Contamination control requirements for the final assembly were extremely stringent. During the cleaning procedure the dry lubricant applied in small quantity to the gears and ball bearings did not survive the original cleaning process applied at the White Sands clean room facility. This process was eventually modified for particular components.

The size and weight requirements for the SSLPA necessitated the use of such materials as beryllium, titanium, and magnesium. Custom miniaturization of electrical connectors, plumbing components, clutches, and motors was also required.

During thermal vacuum testing, Vespel* shrank up to 10 percent and future design efforts were required to take this unexpected performance into consideration.

CONCLUSION

The mechanisms described, although not unique, have been implemented to meet the system environmental and performance requirements. The problems of lubrication, material limitations, and severe environments made the design a challenge. The final design takes advantage of these simple mechanisms with relatively few moving parts to maintain a highly reliable system. The extensive testing program, which included soil loading with various soil models, oven sealing after loading, and environmental testing, has validated this design approach. There were several significant outcomes of this design and testing effort. First, the ability to eliminate conventional lubricants when compatible materials are used as wear surfaces was tested. Even though extensive cleaning was performed on the pieces and the finished assembly, no "cold welding" or galling problems were encountered during testing. Second, it is possible to design precision mechanisms that are tolerant of particulate contamination, such as excess soil. Third, the repeated assembly and disassembly of the unit in the clean room can be accomplished without impact on the system performance.

---

*Registered trademark of duPont.
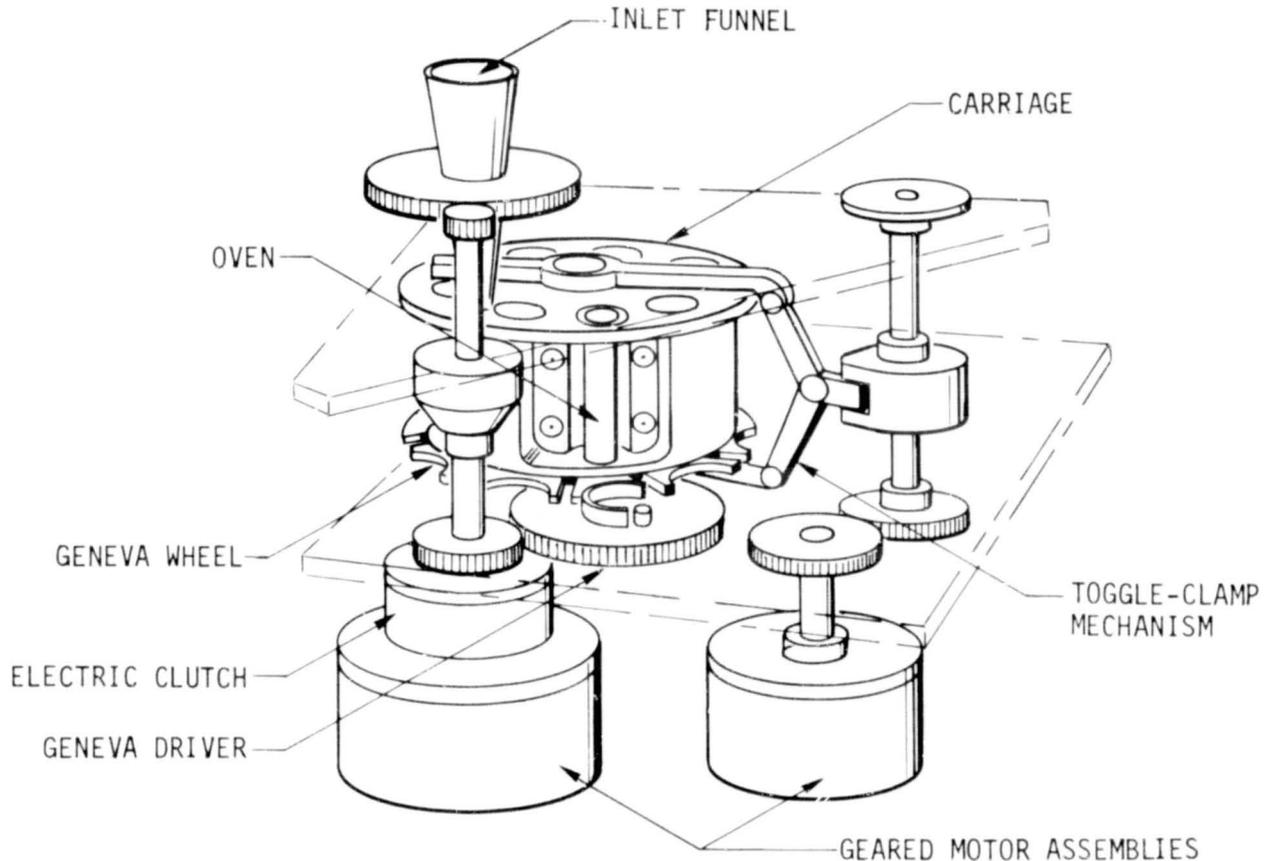
Figure 1a. Diagram of Surface-Sample Loading and Pyrolyzing Assembly (SSLPA)
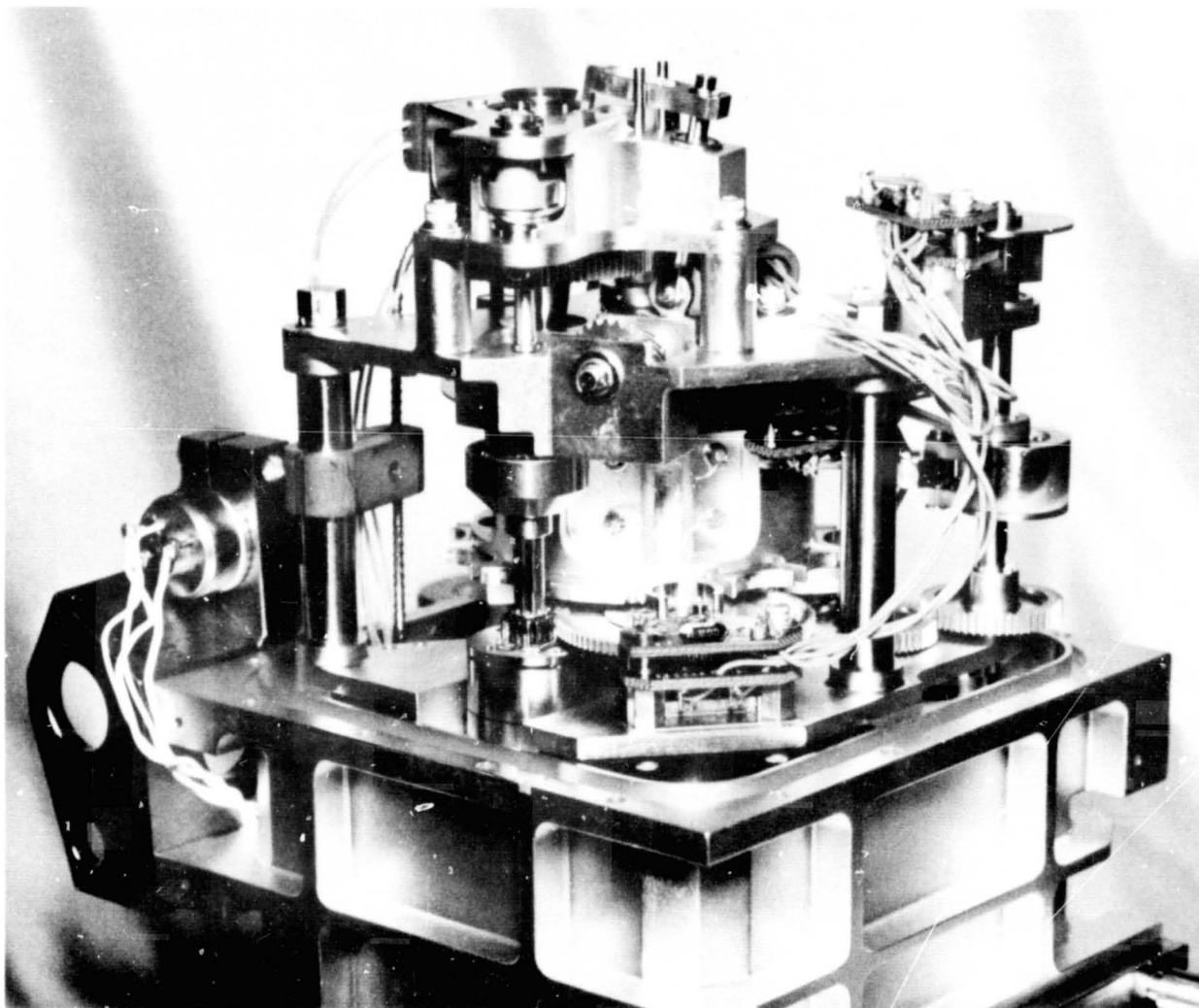
Figure 1b. Complete SSLPA Without Cover
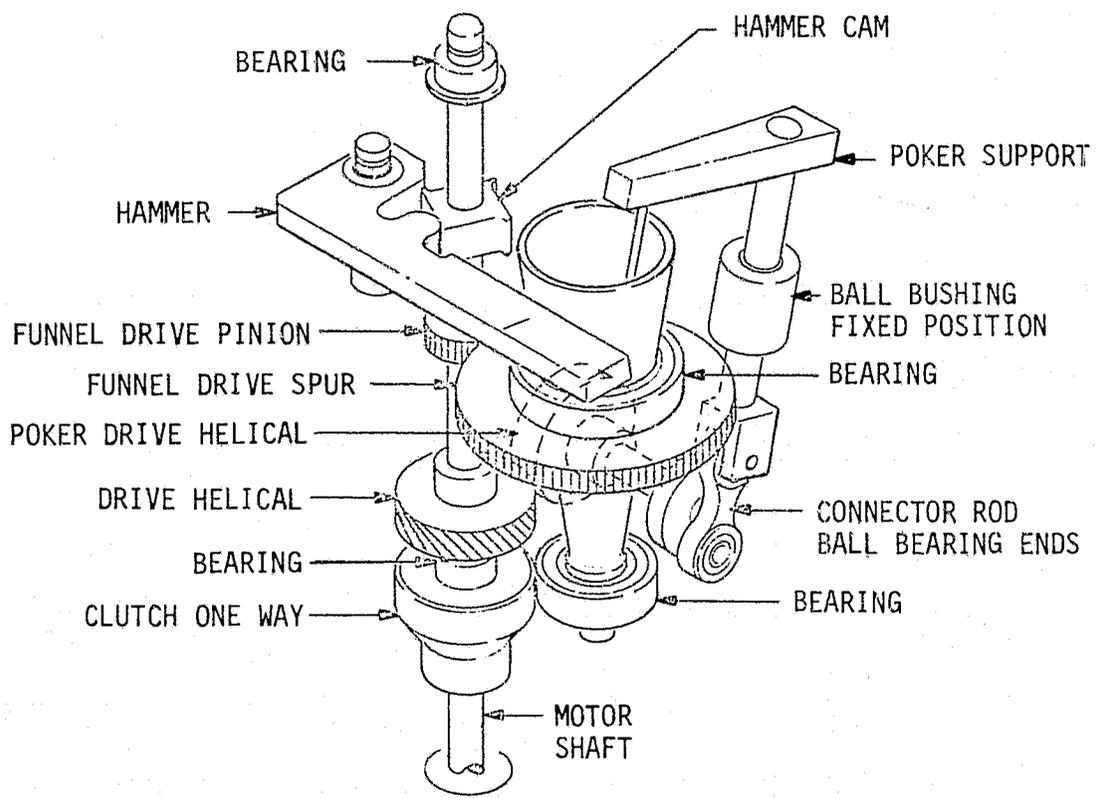
Figure 2. Soil Loader Mechanism
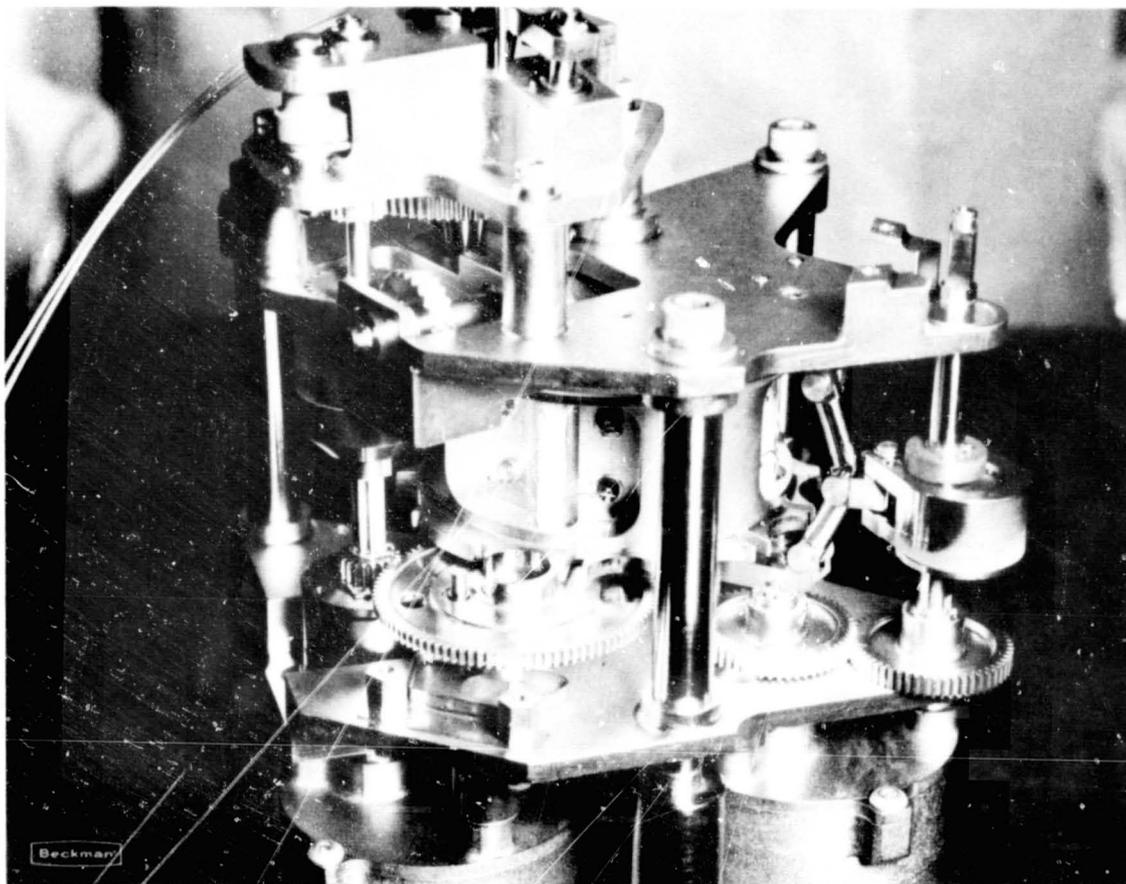
Figure 3a. Oven Carriage and Indexing Mechanism
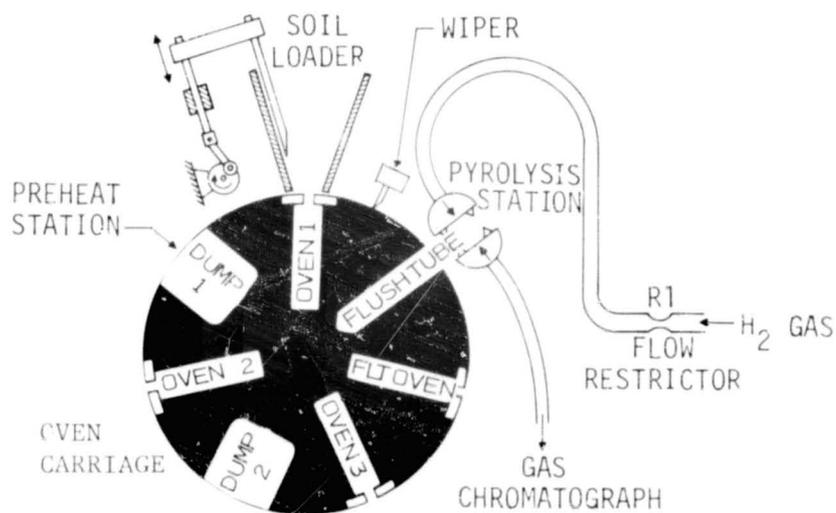

Figure 3b. Functional Sequence Diagram
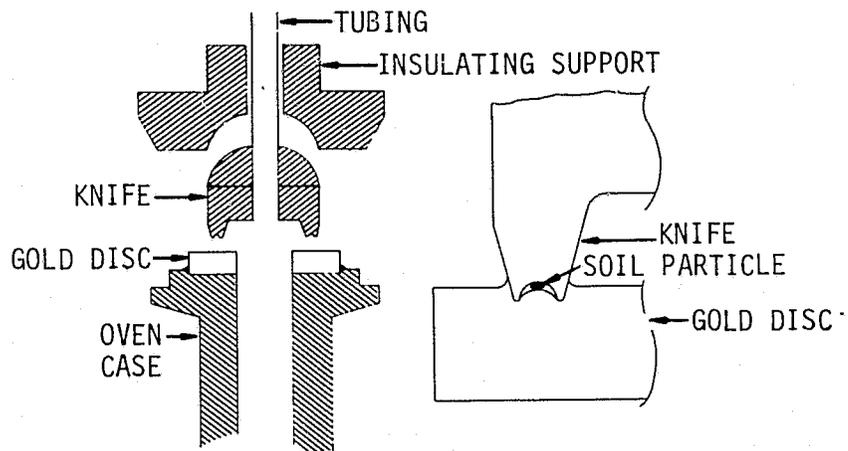
Figure 4.   Oven Sealing Concept
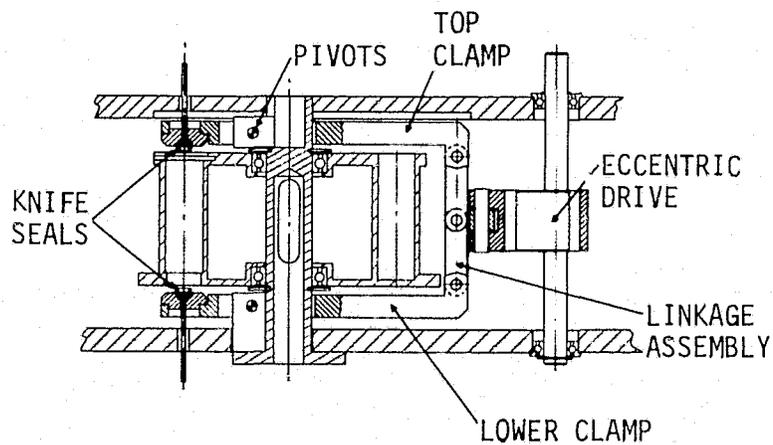
Figure 5.   Oven-Seal Clamping Mechanism

THE EVOLUTION OF THE VIKING LANDING GEAR[a]

JOE C. POHLEN[b]
BRUCE D. MAYTUM[c]
IRA W. RAMSEY[d]
U. J. BLANCHARD[e]

N76-28293

ABSTRACT

The primary function of the landing gear is to dissipate touchdown energy in a controlled fashion that minimizes the landing shock for onboard components while maximizing ground clearance and the probability of landing stability over the range of possible surface and touchdown parameter variations. Many other mission requirements and constraints were translated into the evolving Viking landing gear design as they arose. Hence, design considerations included such factors as prelaunch heat sterilization and non-contamination of the Martian landing site, gear stowage and deployment, terminal descent engine shutdown initiation, structural load attenuation, hard/soft landing surface capability, reliability, weight, and post-landed stability.

The landing gear, which was selected on the basis of proposal-phase trade studies, consisted of three inverted-tripod legs with crushable honeycomb elements in the main struts and omnidirectional crushable footpads, both for energy absorption and strut load attenuation. The gear design evolved through several intermediate configurations during early analytical studies and development test programs as the functional specifications for the landing gear were definitized. The final flight-design landing gear consists of three inverted-tripod landing legs, with optimized crushable honeycomb elements having return-stroke load capability in the main struts, deformable load limiters for the attachment of the split bipod struts to the lander body, and a footpad having both hard surface capability and soft surface bearing load enhancement.

INTRODUCTION

The configuration of the Viking landing gear at the time of contract award in May 1969 was conceptually similar to the Surveyor gear. A crushable/shearable footpad was fastened to the end of the tripod. The original footpad is shown in Figure 1. The main strut for Viking utilized crushable honeycomb with multiple force levels instead of the pressurized oleo strut of Surveyor. Component footpad, attenuator and limiter development tests, vehicle stability analyses, and sub-scale model tests were conducted through 1970, '71, and '72 with full scale vehicle structural model drop tests in 1973 and three system-level vehicle drop tests on a "flight type" lander in 1974. The flight gear, following one of these drop tests, is pictured in Figure 2. The requirements which were imposed on the landing system during the course of the program are listed in Table 1.

Table 1. Viking Landing Gear Design Criteria

Parameter	Contract Go Ahead	As Flown
Vertical Velocity	3 ± 1.5 m/sec (10 ± 5 fps)	2.44 ± .9 m/sec (8 ± 3 fps)
Horizontal Velocity	± 1.8 m/sec (± 6 fps)	± 1.22 m/sec (± 4 fps)
Engine Cut-Off Altitude	3 ± 1.5 m (10 ± 5 feet)	at touchdown
Engine Cut-Off Sensor	by Radar	switches in legs
Stability	all 19° slopes	99.7% stable
Package Loads	80 g's	30 g's
Clearance	22 cm (8.66 in.)	22 cm (8.66 in.)
Coeff. of Friction	1.0 for stability 0.2 for clearance	1.0 for stability 0.2 for clearance

FOOTPAD/LOAD LIMITER DESIGN

The primary function of the crushable footpad employed in the original gear design (circa 1969) was to limit the lateral loads applied to the lander. This design concept relied on the fact that the shear strength of the pad honeycomb is less than the longitudinal crush strength. The footpad was fastened to the inverted tripodal gear by means of a "U" joint to prevent bending moments in the main strut and the secondary bipods, in the event that the pad hit an uneven surface. A footpad rollover problem was uncovered early (1970) in testing conducted at Langley Research Center. The problem shown in the photo of Figure 1, was especially evident when landing on a hard, high-friction surface. These tests showed that the crushing force dropped drastically for loads applied at angles to the honeycomb cell axes, so that the omnidirectional capability of the crushable honeycomb footpad was very poor and unpredictable. Also, sharp or protruding immovable rocks easily penetrated the honeycomb while providing little or no energy absorption. These results led to the deletion of the crushable rotating footpad and prompted the development of a fixed conical footpad design. A solid spherical nosecap was selected to keep high load, hard surface landings from "dumping" high moments into the bipods. The soil penetration tests pictured in Figure 3 dictated the addition of an integral reverse flange skirt on the cone. This thin flange could not carry point loads, and therefore could not cause excessive moments in the bipods. The impact velocity for all the tests shown in Figure 3 was 2.5 m/sec. The soil density was 1.4 g/cm^3 for $\underline{a}$ and $\underline{b}$ (sand), 1.45 g/cm^3 for $\underline{c}$ and $\underline{d}$ (lunar nominal), and 1.6 g/cm^3 for $\underline{e}$ and $\underline{f}$ (also lunar nominal). Drops pictured in $\underline{a}$, $\underline{c}$, and $\underline{e}$ were conducted with a bare conical pad, while $\underline{b}$, $\underline{d}$, and $\underline{f}$ had the reverse flange. The final flight design is shown in Figure 2.

At the time that the conical pad was implemented, the secondary struts (bipods) were conceived to be telescoping members, permitting both tension and compression stroke and having load limiting capability while carrying significant moment and axial loads. Another haunting requirement, that of post-landed stability, stood a chance of loosing ground. While yet in the paper phase of the above nightmare, the project "invented" the idea of fastening a load limiter to the body of the lander. A very simple H-beam type bipod could be fastened to this and when the axial load in the bipod member exceeded the bending capability of the limiter, it "stroked." A significant analytical and development test program took place to get the actual limiter performance characteristics now employed on the lander. At about the time the initial limiter hardware was being delivered, significant site alteration test results allowed the lander to be flown all the way to the surface. This change reduced the maximum touchdown kinetic energy by a factor of four. As a result, the load limiter design went from the one pictured at the top of Figure 4, which weighed 1.5 kg , to that of the other three limiters shown in the same figure with a weight of 0.45 kg. The limiter on the right is shown

as-built with the center one tested and exhibiting approximately 2 cm of stroke and the limiter on the left has been stroked 6.0 cm. The flight configuration limiter design fabricated from fully annealed stainless steel had load requirements shown in Figure 5, with typical test performance as shown.

MAIN STRUT ATTENUATOR DESIGN

The primary strut transmits the majority of the vertical load to the lander body, and hence, the landing deceleration applied to on-board components is controlled by the selection of attenuator crushing force levels. More importantly, the main strut attenuator must dissipate most of the touchdown energy, particularly in the event that the footpad can slide out across the landing surface with little frictional resistance. The force levels carried in each of the strut members, and the changing gear geometry during landing determine the stabilizing (and destabilizing) moments which act about the lander center of gravity.

Crushable aluminum honeycomb (H/C) tubecore was selected at the outset to provide the necessary landing energy absorption for several reasons: the desired crushing force levels can be obtained by varying the core cross-sectional area and the skin thicknesses; the core is very lightweight; the core can be stroked over 80% of its initial length before bottoming; and the crushing behavior is unaffected by long-term exposure to the interplanetary thermal/vacuum environment. These performance advantages were demonstrated on the Apollo project, where crushable H/C tubecore and hexagonal cell H/C elements were used in the primary and secondary struts, respectively, of the Lunar Excursion Module landing gear.

Tubecore attenuator elements are formed by wrapping alternating layers of corrugated skin and face-sheet skin on a circular mandrel to obtain the desired ID/OD dimensions. The initial elements which were built and tested as part of the attenuator development program were fabricated in this manner from sheets of corrugated/flat skins, where the corrugated skin was brazed at each "wavelength" to the face sheet. The layers were not able to be brazed together during wrapping. This all-metal attenuator was designed to meet the requirement that the landing site not be contaminated with any organic compounds. At that point in time, the primary strut attenuator was composed of five separate stages of tubecore, which were to crush at prescribed step-wise increasing force levels. The attenuator was assembled by bonding a spacer disc between each stage; the entire assembly was about 40.6 cm long (four 1 in. stages and one high-force 12 in. stage). Crushing force of the stages increased progressively from 8230 nt. (1850 lbs) to 21360 nt. (4800 lbs).

These initial H/C attenuators, and several early variants, exhibited

column instability problems during static and dynamic testing due to the absence of brazing between wrapped layers. This behavior caused very erratic fluctuations in the crushing strength and unpredictable energy absorption capability.

On the basis of subsequent testing, it was concluded that a fully-bonded tubecore attenuator design would perform properly. At about the same time, site alteration testing indicated that descent engine shutoff at touchdown was feasible. Extensive "worst-case" and statistical landing dynamics studies, similar to those conducted earlier, provided new H/C attenuator design requirements which optimized the trade-offs between landing stability, shock, and post-landed ground clearance. These new design requirements called for attenuators whose crushing load-vs-stroke characteristics would follow a ramped curve for the first 8.9 cm (3.5 in) of stroke, initially crushing at 4448 nt. (1000#), and then crushing at a constant 11200 nt. (2500#) force level for at least another 21.6 cm (8.5 in.); these requirements are depicted in Figure 6. The tubecore vendor (Hexcel Corp.) was able to supply attenuators whose static and dynamic crushing performance (also depicted in Figure 6) satisfied these design requirements. These attenuators were fabricated from fully bonded tubecore cylinders whose cross-section was tapered for 8.9 cm (3.5 inches) by machining; the elements were slightly pre-crushed, and then bonded to machined end-fittings for installation in the primary strut. The final flight-design attenuator assembly is about 53 cm (21 in.) long. These flight attenuators also have limited return-stroke capability to resist tension loads up to about 445 nt. (100 lbs). Figure 7 is a photo of flight-type attenuators; the upper assembly is shown compressed approximately 18 cm.

To conform with site non-contamination requirements, it was necessary to completely enclose these organically-bonded H/C attenuators. A laminate Kapton cloth contamination fairing, identified on Figure 2, was used for this purpose. An O-ring was used to seal off the enclosed attenuator as the primary strut strokes; in addition, a microfilter was fitted to the top of the primary strut housing to provide venting during launch and landing. A long spring in the main strut tube is used to deploy the leg from its stowed configuration (Figure 8) after a pyrotechnic pin-puller releases the leg about fifteen seconds following aeroshell jettison. The main strut tube is treated with a Tufram coating to minimize deployment friction. A terminal engine shutdown switch (TESS) was fitted to each leg to provide shutdown commands to the lander computer. These switches are activated on touchdown as the leg compresses a weak spring a distance of 1.3 cm (1/2 in.) before any attenuator stroking has occurred.

CONCLUSIONS

The final flight-design Viking landing gear geometry is shown in Figure 8. The evolution of this gear design has been described in terms of functional requirements defined primarily from analytical studies, and in terms of hardware performance (and problems) determined from test programs. The more innovative features of this design are the footpad, the honeycomb main strut attenuators and the secondary strut load limiters. Their consistent performance, demonstrated in component development tests and in lander verification drop tests, permitted landing dynamics analyses to be conducted with certainty.

The stringent and challenging mission requirements imposed on the landing gear have been satisfied by this design.

In particular:

--- Probability of stability exceeds 99. 7% ;
--- Statistical ground clearance exceeds 22 cm;
--- Three-sigma component landing shock is less than 30 g;
--- The energy absorption capability of the gear elements permits landings at greater than three-sigma velocities;
--- Site non-contamination and engine-shutdown requirements have been satisfied; and
--- The footpad design permits landing on surfaces ranging from impenetrable to very soft soils.

Furthermore, the total landing gear has evolved from an early design weighing over 45 kg (100 lbs) to the flight-design, which weighs only 20 kg (44 lbs), less than 3.5% of the lander touchdown weight.
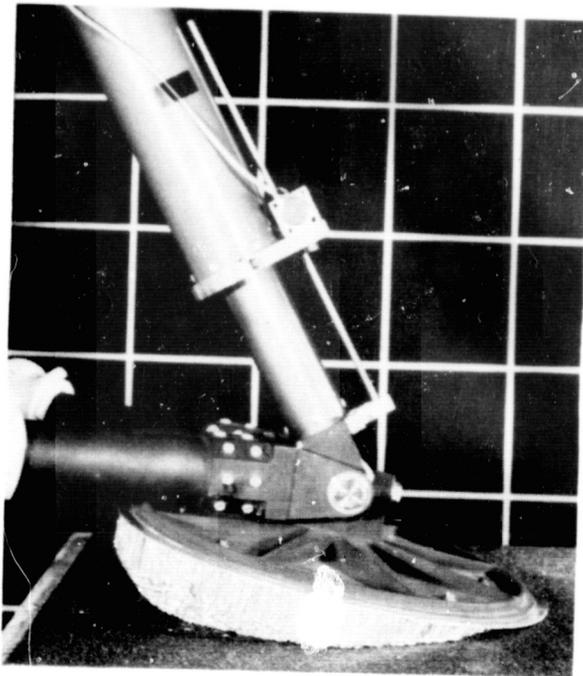
Figure 1 - Original Gear Design

TESS

Main strut
Contamination
fairing

Load
Limiter

Pin
puller

Skirted
Footpad
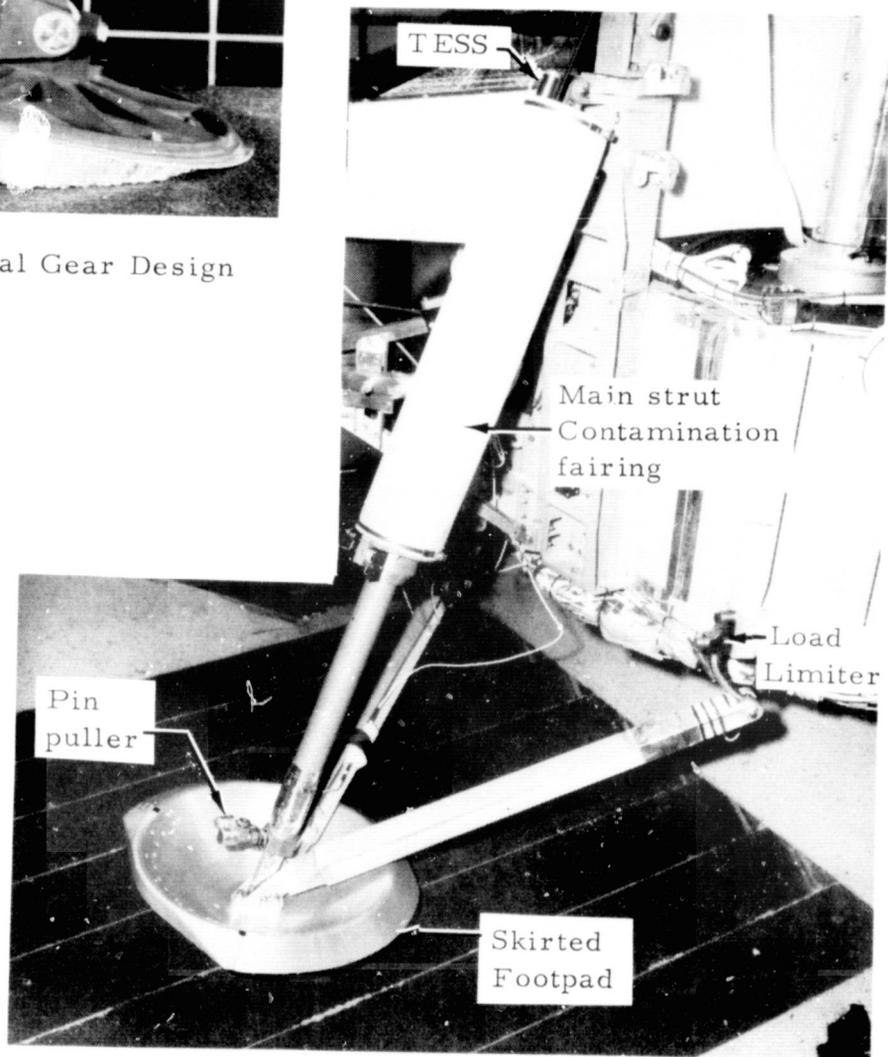
Figure 2 - Final Flight Gear
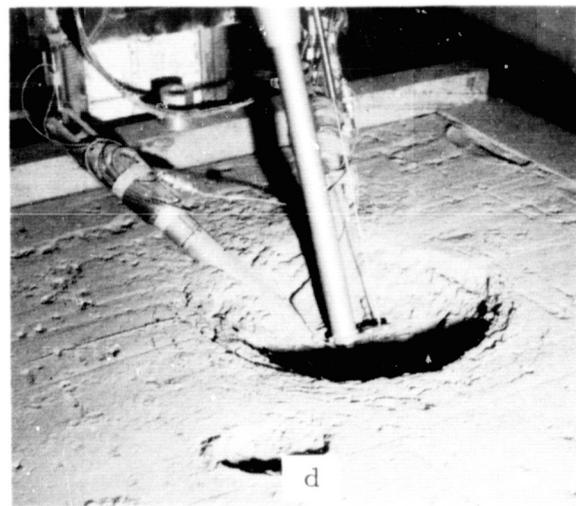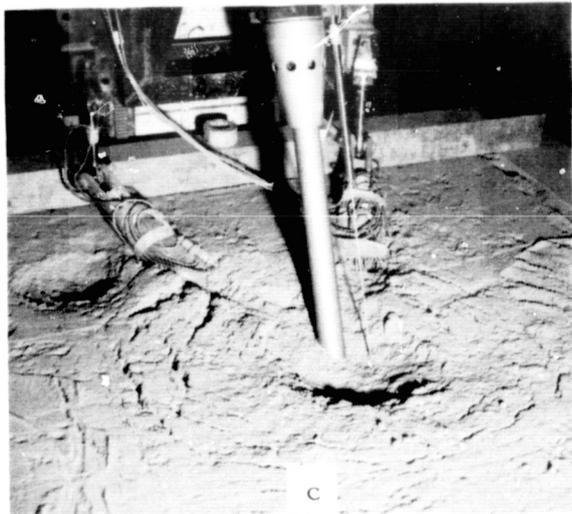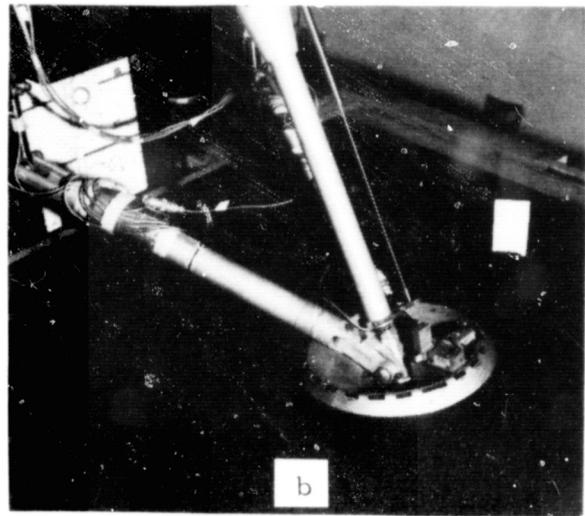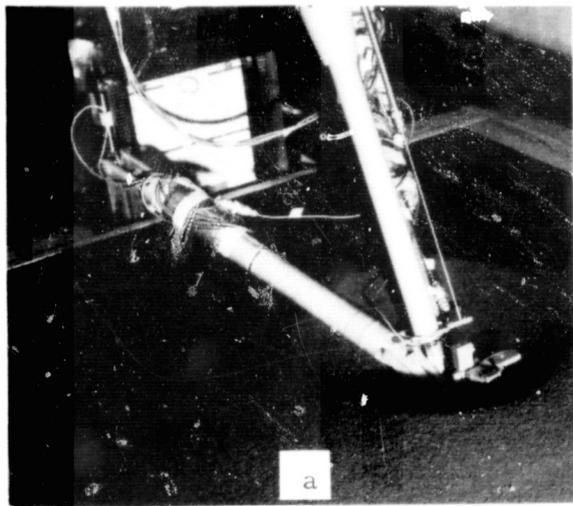
Figure 3 - Footpad Soil Penetration Tests
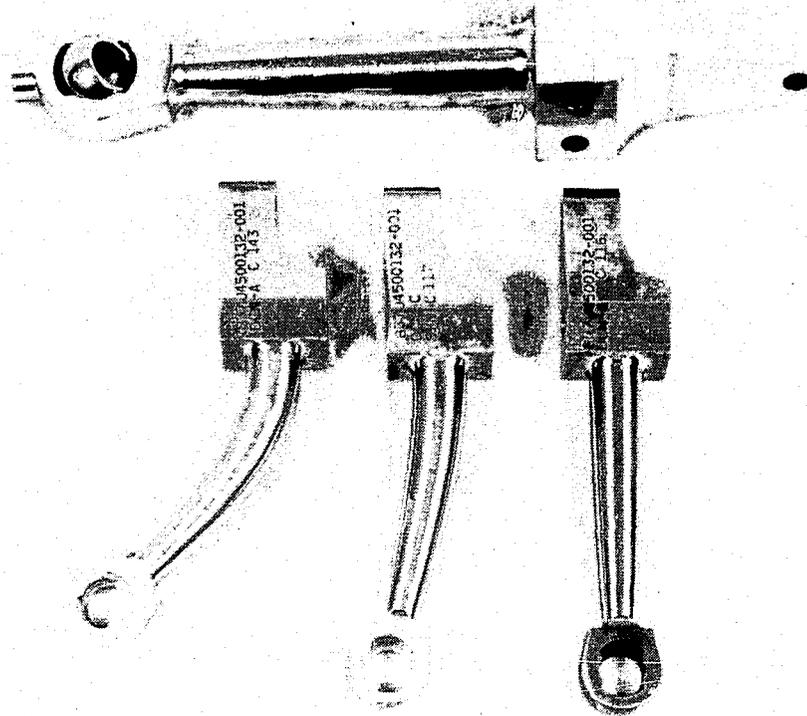
Figure 4 - Load Limiters
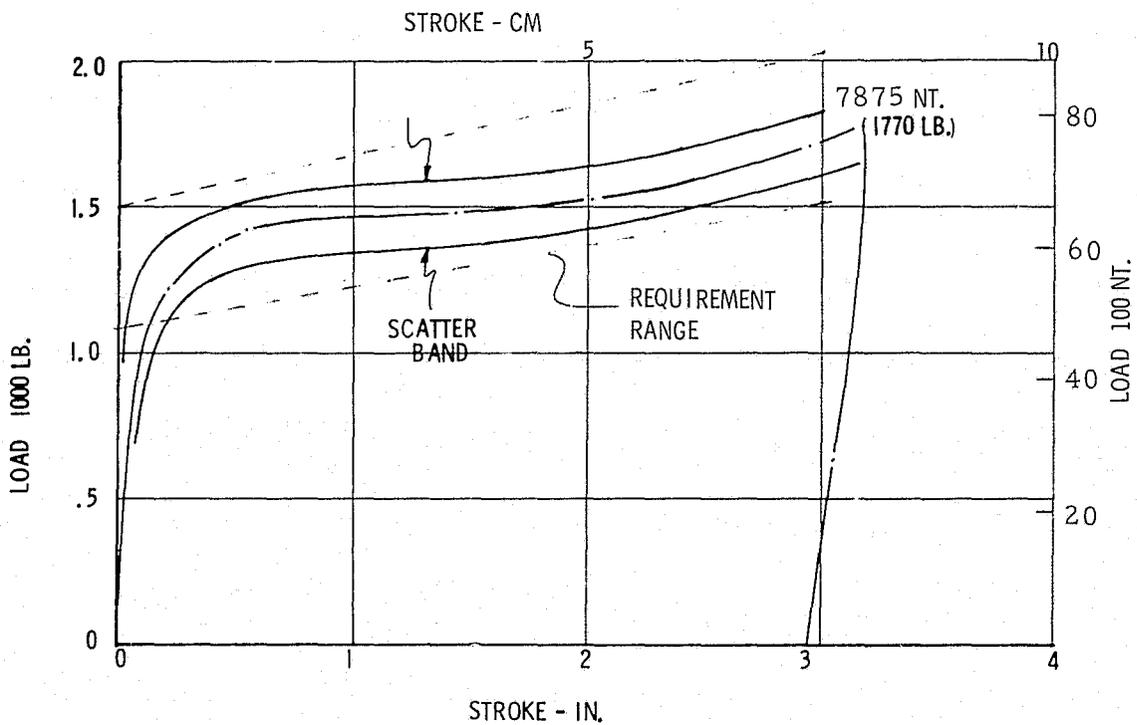
Figure 5 - Load Limiter Requirement and Test Data
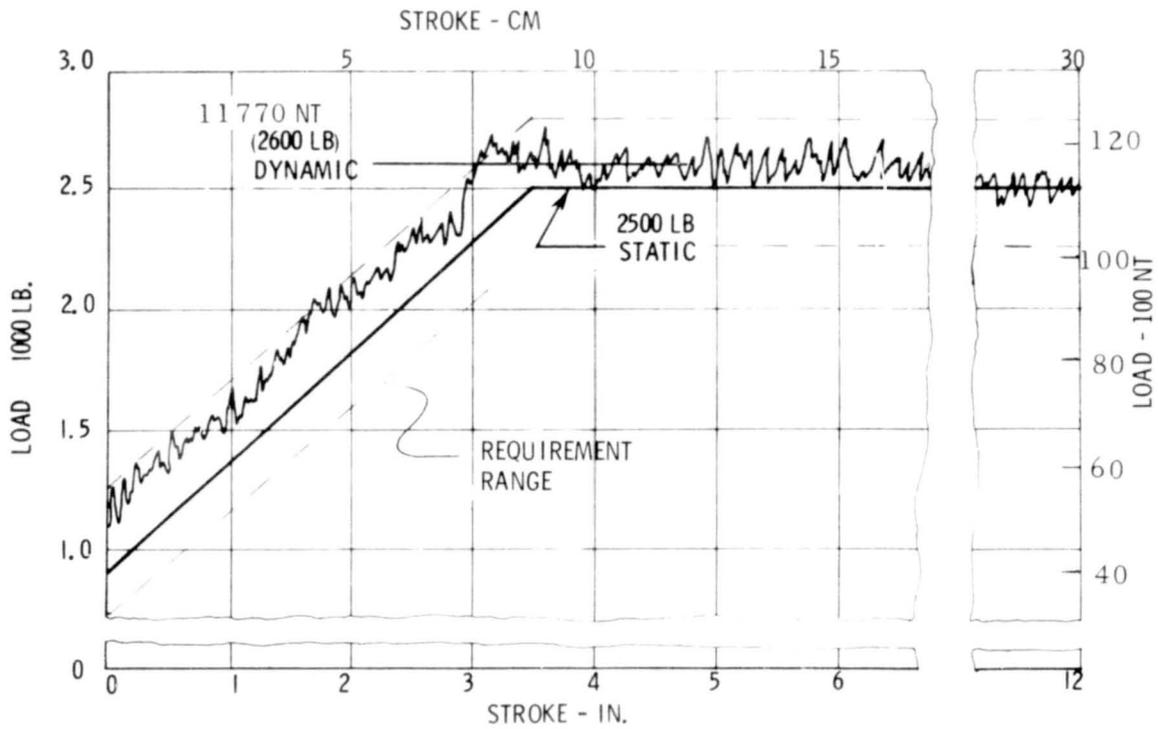
Figure 6 - Attenuator Requirement and Test Data
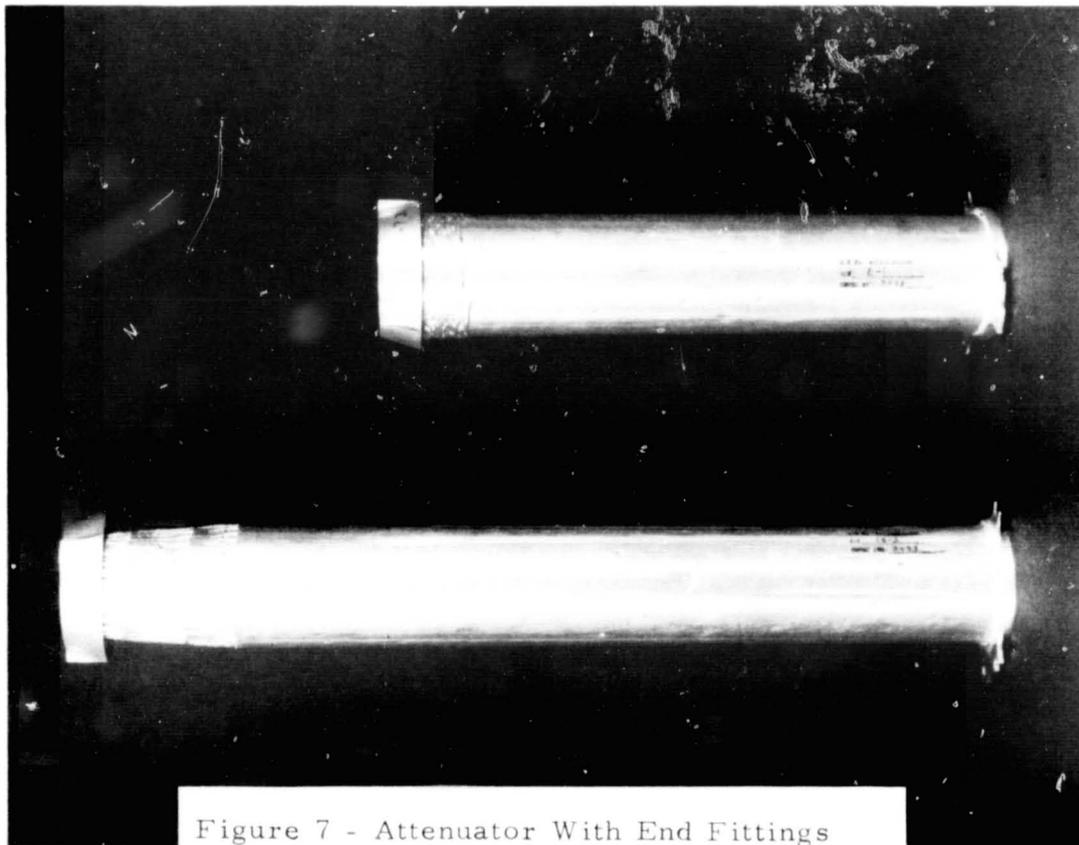
Figure 7 - Attenuator With End Fittings
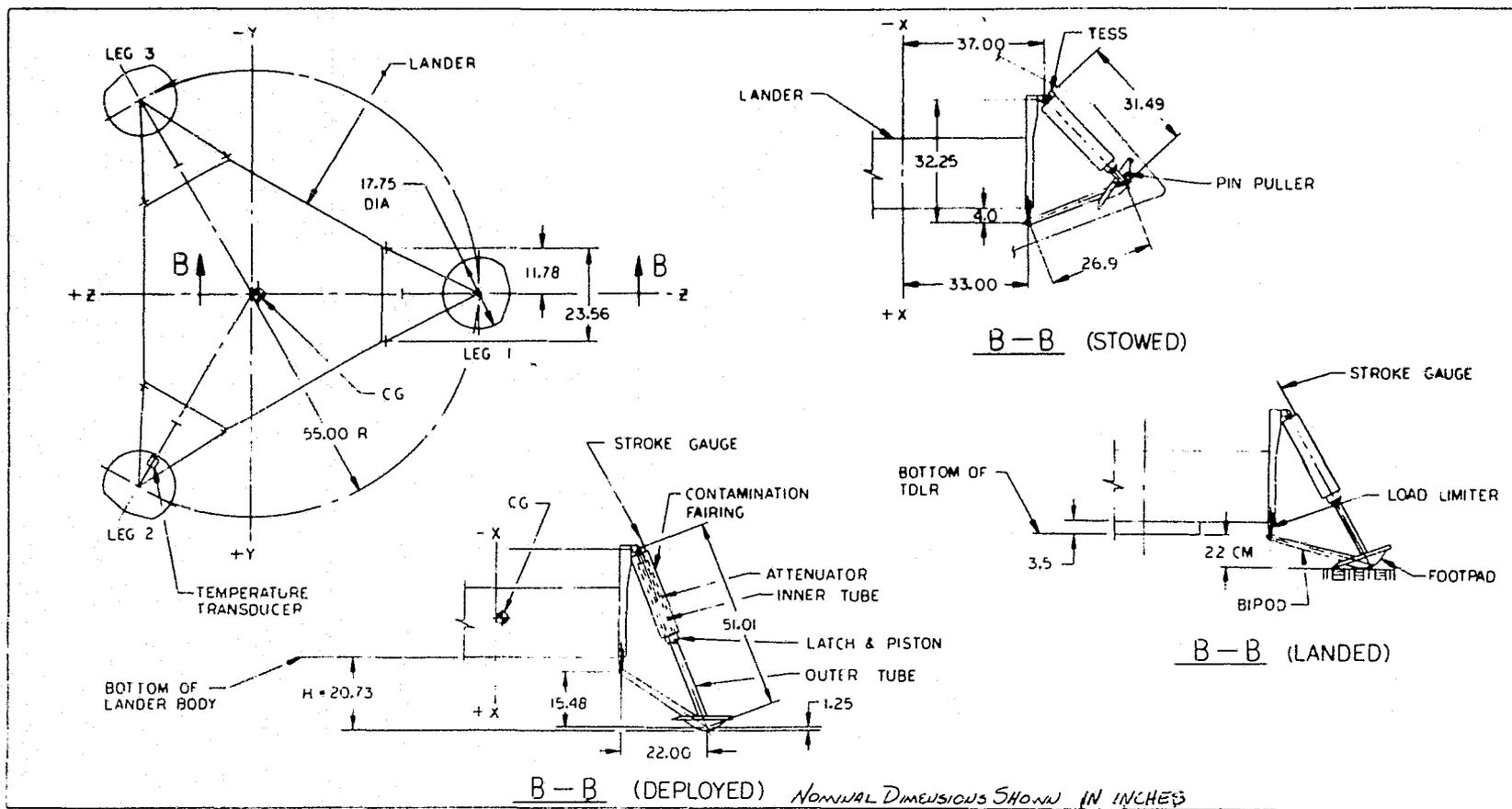
Figure 8 - Flight Design Configuration